ORBIT ESTIMATION OF NON-COOPERATIVE MANEUVERING

SPACECRAFT

DISSERTATION

Gary M. Goff, Captain, USAF

AFIT-ENY-DS-15-J-051

AFIT-ENY-DS-15-J-051

ORBIT ESTIMATION OF NON-COOPERATIVE MANEUVERING SPACECRAFT

DISSERTATION

Presented to the Faculty

Graduate School of Engineering and Management

Air Force Institute of Technology

Air University

Air Education and Training Command

in Partial Fulfillment of the Requirements for the

Degree of Doctorate of Philosophy in Space Systems

Gary M. Goff, B.S., M.E.

Captain, USAF

June 2015

AFIT-ENY-DS-15-J-051

ORBIT ESTIMATION OF NON-COOPERATIVE MANEUVERING SPACECRAFT

Gary M. Goff, B.S., M.E.
Captain, USAF

Committee Membership:

Dr. Jonathan T. Black
Chair

Dr. Benjamin F. Akers
Member

Dr. Joseph A. Beck
Member

Dr. Richard G. Cobb
Member

ADEDEJI B. BADIRU, PhD
Dean, Graduate School of Engineering
and Management

AFIT-ENY-DS-15-J-051

Abstract

Due to the ever increasing congestion of the space environment, there is an increased demand for real-time situation awareness of all objects in space. An unknown spacecraft maneuver changes the predicted orbit, complicates tracking, and degrades estimate accuracies. Traditional orbit estimation routines are implemented, tested, and compared to a multiple model format that adaptively handles unknown maneuvers. Multiple Model Adaptive Estimation is implemented in an original way to track a non-cooperative satellite by covariance inflation and filtering-through a maneuver. Parameters for successful instantaneous maneuver reconstruction are analyzed. Variable State Dimension estimation of a continuously maneuvering spacecraft is investigated. A requirements based analysis is performed on short arc orbital solutions. Large covariance propagation of potential maneuvers is explored. Using ground-based radars, several thousand simulations are run to develop new techniques to estimate orbits during and after both instantaneous and continuous maneuvers. The new methods discovered are more accurate by a factor of 700 after only a single pass when compared to non-adaptive methods. The algorithms, tactics, and analysis complement on-going efforts to improve Space Situational Awareness and dynamic modeling.

To my wife and parents for their constant support. To my dog for her proofreading help.

Acknowledgments

Dr. Black was absolutely key to this research. He constantly pushed me to present my work to peers, seek feedback, and become confident in my abilities. Thanks for supporting me and making this work a truly awesome experience. Thanks to Dr. Beck as well for his dedication and help. His feedback was direct, supportive, and sometimes just plain hillarious. Thanks to Dr. Akers and Dr. Cobb for serving as committee members and helping me along the way. Finally, thanks to the CSRA team. Our weekly meetings and brainstorming sessions helped keep me on track.

Gary M. Goff

Table of Contents

List of Figures

Figure   Page

List of Tables

List of Algorithms

List of Symbols

Symbol	Definition
A	Jacobian
A	Square Root of **P**
a	Acceleration
a	Semi-major Axis
b	Locus of Points
deg	Degree
E	Expectation Operator
E	Eccentric Anomaly
$\mathcal{E}$	Ellipsoid
e	Error
e	Eccentricity
$e_\oplus$	Earth's Eccentricity
el	Elevation
f	Nonlinear Function
f_X	Probability Density Function
G	Nonlinear Transformation of States to Observations
H	Linearized State to Observation Matrix
h	Sine Component of Eccentricity Vector (Equinoctial Element)
h_{ellp}	Height Above Reference Ellipsoid
IJK	Coordinate Frame
i	Counter
i	Inclination
I	Identity Matrix

Symbol	Definition
J	Cost function
$\mathbf{K}$	Kalman gain
k	Monte Carlo Samples
k	Cosine Component of Eccentricity Vector (Equinoctial Element)
L	Start of Smoothing Window
M	Mean Anomaly
$\mathcal{M}$	Mahalanobis Squared Distance
m	Dimensions of Observation Vector
m	Meters
N	Total Observations in Batch
N	Components in Gaussian Mixture
N	Number of Models in IMM
$\mathcal{N}$	Gaussian (Normal) Distribution
n	Dimensions of state vector
$\mathbf{P}$	Covariance
$\bar{\mathbf{P}}$	Propagated Covariance
$\hat{\mathbf{P}}$	Estimated Covariance
$\underline{\mathbf{P}}$	IMM Covariance Estimate
$\mathbf{P}^s$	Smoothed Covariance
Pr	Probability
$\mathbf{Pr}_{j|k}$	IMM Jump Probability Matrix
p	pdf and σ Sizing
p_e	Sine Component of Ascending Node Vector (Equinoctial Element)
$\mathbf{Q}$	Process Noise Covariance
q_e	Cosine Component of Ascending Node Vector (Equinoctial Element)

Symbol	Definition
R	Observation Noise Covariance
$R_{\oplus}$	Radius of Earth
ROT	Rotation
r	Position
S	Predicted Observation Covariance
S/N	Signal to Noise Ratio
T	Translation Matrix
T	Orbital Period
t	Time
th	Thrust
u	Splitting Direction
$\mathcal{U}$	Uniform Distribution
V	Eigenvector Matrix
v	Observation Noise Vector
v	Velocity
v	Eigenvector
Δ**v**	Velocity Change (Maneuver)
w	Process Noise Vector
w	Gaussian Mixture Weights
w	IMM Model Weight
w	Unscented Transform Weights
x	State
$\bar{\mathbf{x}}$	Propagated State
$\hat{\mathbf{x}}$	Estimated State
$\underline{\mathbf{x}}$	IMM State Estimate

Symbol	Definition
$\mathbf{x}^s$	Smoothed State
$\dot{\mathbf{x}}$	State Derivative (Dynamics)
$\mathbf{y}$	Observation
$\hat{\mathbf{y}}$	Observation Estimate
α	Unscented Transform Weighting Parameter
β	Azimuth
γ	Unscented Transform Weighting Parameter
δ	Small Deviation
ε	Specific Mechanical Energy
η	Covariance Inflation Constant
Θ	Generalized Distribution Parameter Set
Θ	Filter-Smoother Consistency Test
θ	Earth's Rotation Angle
κ	Unscented Transform Weighting Parameter
Λ	Eigenvalue Matrix
λ	Eigenvalue
λ	Unscented Transform Weighting Parameter
λ_{long}	Longitude
$\boldsymbol{\mu}$	Mean
$\mu_{\oplus}$	Earth's Gravitational Parameter
$\boldsymbol{\nu}$	Residual
υ	True Anomaly
ξ	Covariance Inflation Factor
ρ	Range
$\dot{\rho}$	Range rate

Symbol	Definition
σ^2	Variance
σ	Standard deviation
$\hat{\sigma}$	Mixture Splitting Input
τ	Time Constant
$\Phi\left(t_f, t_0\right)$	State Transition Matrix from Initial to Final
ϕ	Latitude
χ^2	Chi-squared distribution
Ψ	Maneuver Detection Scalar
ψ	Standard Normal Distributed Vector
ψ_{th}	Maneuver End Detection Scalar
Ω	Right Ascension of the Ascending Node
ω	Argument of Perigee
ℓ	Mean Longitude (Equinoctial Element)

List of Acronyms

Acronym	Definition
AFIT	Air Force Institute of Technology
AFSPC	Air Force Space Command
ASAT	Anti-Satellite
BLS	Batch Least Squares
CMS	Continuously Maneuvering Spacecraft
COE	Classical Orbital Elements
CR	Carlton-Rauch
ECEF	Earth Centered Earth Fixed
ECI	Earth Central Inertial
EKF	Extended Kalman Filter
EM	Expectation Maximization
FES	Fixed Epoch Smoother
GPS	Global Positioning System
HPOP	High Precision Orbit Propagator
IE	Input Estimation
IOD	Initial Orbit Determination
IMM	Interacting Multiple Model
INS	Inertial Navigation System
JPDA	Joint Probabilistic Data Association
JSpOC	Joint Space Operations Center
KF	Kalman Filter
KOMPSAT	Korean Optical Satellite
LEO	Low Earth Orbit

Acronym	Definition
MFA	Multiple Frame Assignment
MHT	Multiple Hypothesis Tracking
MMAE	Multiple Model Adaptive Estimation
NTW	Radial, In-track, Cross-track
ODTK	Orbit Determination Tool Kit
pdf	probability density function
RK	Runge Kutta
RMS	Root Mean Squared
RSW	Radial, Along-track, Cross-track
RV	Random Variable
SEZ	South, East, Zenith
SGP	Simplified General Perturbations
SOCRATES	Satellite Orbital Conjunction Reports Assessing Threatening Encounters in Space
SOD	Statistical Orbit Determination
SSA	Space Situational Awareness
SSN	Space Surveillance Network
SSNAM	Space Surveillance Network Analysis Model
STK	Systems Tool Kit
STM	State Transition Matrix
TLE	Two Line Element
UCT	Uncorrelated Target
UKF	Unscented Kalman Filter
UT	Unscented Transform
US	United States
USAF	United States Air Force

Acronym	Definition
VSD	Variable State Dimension

ORBIT ESTIMATION OF NON-COOPERATIVE MANEUVERING SPACECRAFT

I.   Introduction

1.1   Motivation

It is no secret today that space is a congested, contested, and competitive environment. The United States (US) National Security Space Strategy highlights that space-based assets are vital for conducting military operations. Additionally, it states that the US will support information sharing for the purposes of characterizing the space environment [1]. United States Air Force (USAF) leadership echoes the fact that the space challenges will continue to grow as more commercial and foreign governments own and rely on space assets. In an interview with SpaceNews, the Commander of USAF Space Command, General Hyten, stated "I would hope three years from now, what you see is a more real-time ability to deal with the challenges of today [2]." Additionally, he stated: "Where we are lacking is our ability to fully immerse and deal with the command and control of capabilities in a real-time fashion in a contested scenario [2]." Recent space activities, especially Anti-Satellite (ASAT) demonstrations, have perpetuated the need for fast and accurate situational knowledge [3:1].

The problem of congestion is not slowing down, nor will it fix itself as more satellites retire and become debris. There are roughly 500,000 pieces of space debris the size of a marble or larger of which only 22,000 objects are actively tracked [4; 5]. There are approximately 1000 active satellites performing space missions and the USAF must maintain a robust posture through tactical, predictive, and intelligence driven Space Situational Awareness (SSA) [6]. The congestion of space will continue especially as the cost of acquiring capabilities drives design changes. The days of large expensive satellites

1

are over as new trends lean towards smaller satellites and disaggregated networks [7]. These trends makes the mission of achieving situational awareness in space even more difficult for the USAF in the future.

Political pressures and national security postures prevent nations from openly sharing information about the locations and maneuver plans of space assets. This posture emphasizes the need to increase sensor collections and improve techniques to track, predict, and estimate the orbits of non-cooperative spacecraft. In a perfect world, all parties would maintain full accountability of their assets and share precise orbital information that reveals the locations of their satellites. They would share this information with all interested parties and international collaboration could occur to avoid satellite collisions. Entities would remain responsible to de-orbit and track non-functional satellites as well. Unfortunately these actions do not always occur. Space is becoming a contested environment and future space operations are dependent upon accurate and up-to-date information on the locations of other space objects.

1.1.1 Problem.

To maintain a clear picture of space and the operating environment, the USAF focuses efforts and resources on the SSA mission. SSA is based on the notion that to conduct peaceful operations in space, it is necessary to understand where everything is all the time. SSA is officially defined as "the current and predictive knowledge of the space environment and the operational environment on which space operations depend [8]." SSA focuses on three basic classes of space objects: non-cooperative actively controlled, cooperative actively controlled, and un-controlled/debris. Active spacecraft often maneuver to maintain a mission orbit and unknown maneuvers disrupt the ability of the USAF to accurately track and predict the orbits of these spacecraft.

Air Force Space Command (AFSPC) leads the mission of using ground-based assets to track and estimate the location of space objects. They manage 20+ ground sites that

compose the Space Surveillance Network (SSN) [3:9]. The Joint Space Operations Center (JSpOC), reporting to the Joint Forces Component Command, performs the SSA mission [8]. A portion of this mission also includes assessing a realistic confidence in the error in each object's orbital estimate. Overall, the JSpOC manages the tasking of ground sites to collect orbital data, processes the data to predict future satellite and debris locations for the entire space catalog, estimates the confidence in each prediction, and publishes the results. There is a shared interest among the research communities of collision avoidance, debris removal, spacecraft servicing, and SSA to quickly and accurately estimate the state and covariance of all objects.

With the effectiveness of Global Positioning System (GPS) receivers on satellites for precise orbit ephemeris, many active cooperative satellites provide detailed orbital state estimates that the JSpOC can use for its orbital maintenance mission. However, these satellites comprise only a small subset of the catalog as the majority of objects are debris and the other smaller portion consists of non-cooperative active satellites. The mission of tracking satellites is additionally complicated by congested volumes of space, lack of perfect accuracy in orbital propagation, and lack of perfect measurements. A large portion of the JSpOC mission is to associate a collection with a specific item in the space catalog. Often times, the collection fails to fall within the required confidence to associate it with a cataloged item, in which case an Uncorrelated Target (UCT) is created. One goal of improving the SSA mission is to reduce the number of UCTs and mis-tagged observations (collection associated with the wrong satellite) [3:30].

1.1.2 Research Question.

As satellites decrease in average size and more are placed aboard a single launch vehicle, the potential for shorter tactical missions increases. It is feasible to imagine mission profiles in the near future in which spacecraft no longer utilize maneuvers for just station-keeping or achieving a permanent orbit location. The Center for Space

3

Research and Assurance at the Air Force Institute of Technology (AFIT) investigates short term tactical spacecraft missions [9; 10]. The Center investigates tactics in which satellites maneuver often to perform specific missions such as decreasing over-flight times, avoiding cluttered areas, and performing rendezvous and proximity operations. This research necessitates completing work to develop techniques to track, predict, and estimate the orbital states of non-cooperative tactical spacecraft that perform multiple unknown maneuvers at unknown times with unknown thrusts. Determining the orbits of these spacecraft requires adapting known orbital estimation techniques to handle unplanned maneuvers. When certain active objects peak interests in the SSA community, use of adaptive estimation and multiple model estimation can greatly increase orbital estimate accuracies. The non-cooperative maneuvering satellite case motivates the research question for this dissertation. **What are the best tactics and techniques to track, predict, and estimate the orbital state for non-cooperative satellites that perform unknown maneuvers at unknown times with unknown magnitudes in unknown directions?**

1.2 Assumptions and Limitations

The chances for UCTs and mis-tagged observations grows every time an active satellite performs an unknown or unplanned maneuver. There are two divisions of research for reducing UCTs: association and real-time tracking. Solving the problem of the likelihood that an observation belongs to a certain spacecraft is not investigated in this dissertation; instead, heavy focus is placed on assuming observations pertain to a certain spacecraft and estimating post-maneuver states. Furthermore, an unrealistic estimate of the error in an orbital prediction creates association difficulties. This research also investigates methods to preserve underlying error distributions in estimates and uses this information to detect maneuvers.

The primary focus of the research is on objects maneuvering in Low Earth Orbit (LEO). Maneuvers undoubtedly occur in every orbital regime, but LEO is the focus of

this study due to the timeliness and accuracy of ground-based radars. While the results are limited to LEO, the techniques and methods developed are applicable to any orbital regime.

During testing, simulation results are compared to a known truth solution that is propagated using the same orbital propagation routine as the estimator. This approach places the focus of the study on the estimation routine and not the accuracy of the orbital propagation. Highly accurate orbital propagation routines are studied and tested frequently throughout the operational community [3:20]. For longer propagation times, a higher-order fidelity propagation routine is implemented in this research to mimic operational propagation routines. The multiple model methods developed in this research require accurate propagation methods for operational implementation.

1.3 Contributions

An unknown satellite maneuver creates issues when attempting to associate collected observations to a known orbit reference. There are three methods to recover a post-maneuver orbit: a new Initial Orbit Determination (IOD) fit, filtering-through, and performing maneuver reconstruction [11]. This dissertation dedicates a chapter or more to each of these approaches. This work seeks to improve real-time SSA of maneuvering spacecraft and error covariance estimation through Multiple Model Adaptive Estimation (MMAE) techniques. Specifically, this research addresses techniques for real-time tracking of the orbital state during and across maneuvers. The use of MMAE techniques is motivated by the National Research Council's evaluation of areas of improvement for the USAF space mission. They specifically mention using MMAE for maneuver detection, "because it can take some time for a filter to settle down, such 'state-augmented' or 'multiple model' filtering techniques can be particularly valuable for converging sooner with limited data [3:39]."

The methods developed and analyzed in this work are designed to directly aide SSA efforts especially in calculating realistic orbit and accuracy estimates for high-

priority maneuvering spacecraft. Improved accuracy directly supports increased abilities in associating tracks with cataloged items thereby reducing UCTs and mis-tagged orbits. Reducing UCTs also decreases the need for the future collects to characterize a new orbit and frees sensors to collect on other targets. Since maneuvering tactical satellite missions are not prevalent today, many of the techniques discussed suggest new ways to estimate orbital solutions and ways to handle active maneuvering satellites in future plans. To handle maneuvers, the focus shifts from static orbit propagation to dynamic real-time multiple model estimation using techniques to converge on changing orbital parameters. Filtering across maneuvers assists in realistic estimates and requires adapting techniques from the aircraft and missile tracking disciplines for the SSA mission. Evaluating these techniques provides a clear picture of the future capabilities necessary to handle a dynamic contested space environment.

Until complete transparency of all satellite orbital data and maneuver schedules is achieved, there is a need to accurately predict error growth, detect maneuvers, and converge on new orbits. The research herein provides methods and techniques to improve SSA of maneuvering satellites. As tactical maneuvering satellites become more prevalent, the research provides improved operational estimation routines for effective tracking and prediction. It is a sobering fact that the difficulty in achieving realistic SSA grows at the same pace as space congestion. The reliance of everyday operations on space assets keeps pace with this growth solidifying the fact that battlespace awareness is a must. The mission of non-cooperative tracking, prediction, and estimation of active satellites is a key pillar in future battlespace awareness and paramount to preserving space as a platform for peaceful international, military, and commercial operations.

1.4 Document Overview

To understand the development of the ideas and concepts, this dissertation presents a review of other works and development methodologies followed by chapters of simulations

and results. Overall, this dissertation is the archival of five specific research papers organized into a logical flow of information. Chapter 2 is primarily a literature review and covers the background information pertaining to past and current research in related areas. Chapter 3 provides a methodology overview focusing on the necessary equations and algorithms used to support the research reviewed in Chapter 2. Chapter 4 discusses filtering-through an instantaneous maneuver. Chapter 5 provides simulations and results for reconstructing an instantaneous maneuver. Chapter 6 details detecting and estimating a continuous maneuver in real-time. Chapter 7 investigates short arc orbital fits for covariance requirements. Chapter 8 reviews techniques to transform between Equinoctial and Cartesian error covariances. Chapter 9 provides simulation and results for using Gaussian mixtures to estimate potential maneuvers. Finally, Chapter 10 addresses relevant conclusions and potential future work.

Throughout the entire document, many different techniques are implemented and developed for tracking maneuvering satellites. Figure 1.1 provides a flow chart to map out the different techniques and the relevant chapters in which the techniques are implemented. The top line in the flow chart provides a general timed sequence of events implemented in the research to perform state estimation of a non-cooperative maneuvering satellite. Each box below the top line action contains an implemented technique or approach that is color coded to signify the corresponding chapters.
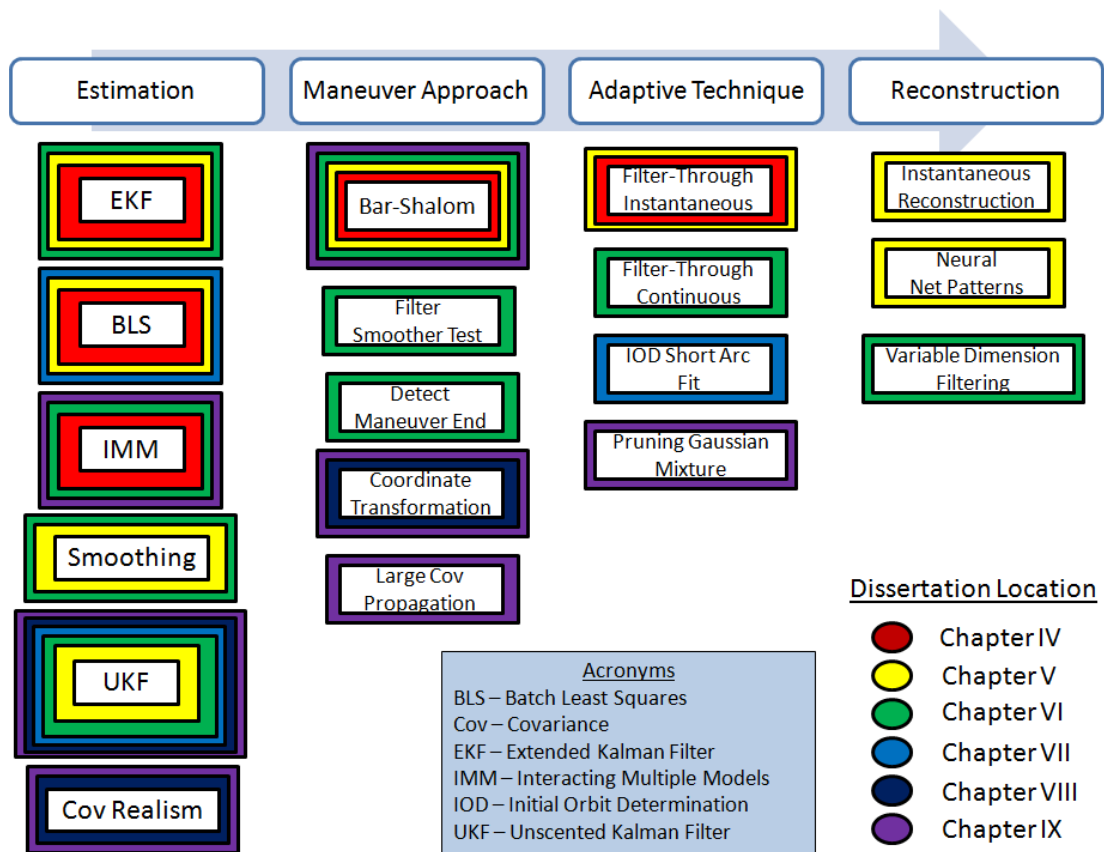
Figure 1.1: Flow Chart of Techniques and Relevant Chapters

II.   Background

Meeting SSA mission needs for estimating the orbit of a maneuvering spacecraft requires dedicated research in methodologies of Statistical Orbit Determination (SOD), adaptive modeling, multiple models, error estimation, maneuver detection, and track association. This chapter reviews relevant literature in each topic area and discusses its applicability to tracking maneuvering satellites. Overall, this chapter reviews the state-of-the-art and sets the stage that the research in future chapters builds upon.

2.1   Statistical Orbit Determination

SOD is a general term that describes using estimation theory principles to handle errors in measurements and errors in orbital dynamics. Estimation theory uses statistics principles to estimate the true error in a measurement and calculate the confidence of the estimate. In satellite estimation theory, the confidence in the estimation is represented by the covariance matrix which describes the correlation between the estimation of the error amongst the state variables. Aerospace engineering is one of many fields that uses estimation theory as the basis for filtering observations to generate estimates and minimize errors. The fields of electronics engineering, computer engineering, etc. also utilize similar tools that are worthwhile to review for understanding and applicability to maneuvering spacecraft.

Several people throughout history searched for the perfect orbit equation that captured the motion of planets, while others tried to create the perfect telescope to observe the orbit of planets. The work of estimation theory began with Carl Friedrich Gauss in the late 1700s and early 1800s. He realized that instrument measurements and equations describing nature had errors. Gauss developed a new approach that focused on minimizing errors instead of achieving a perfect solution. His work was continued hundreds of years later when the

Kalman filter was introduced as an optimal estimator to handle white noise. Presently, we adapt these techniques to perform orbit determination for active satellites and debris using ground-based radars. Vallado's text develops the necessary theory for orbital mechanics and contains an entire chapter on estimation theory [12]. This text is heavily used and cited in orbit estimation and provides much of the fundamental theory development for the research herein. The two other widely used texts in SOD are written by Wiesel and Tapley et al. [13; 14]. Wiesel covers implementation of the common estimation algorithms which are relied heavily upon for this research [13]. Schutz et al. provide an in-depth look at filtering and develop pseudocode which greatly aides in understanding the fundamental algorithms used for estimating the state of a maneuvering spacecraft [14].

Other texts are used as well when developing this research's mathematical methodologies. Wiesel's texts provide necessary background methodologies in orbital mechanics [15; 16]. The combination of these texts with supporting math texts lay the foundation for the SOD methods of estimating orbital states and errors through ground sensor collections [17; 18].

2.1.1 State and Covariance Estimation.

SOD combines the stochastic approaches of minimizing instrument and dynamics model errors with predicting spacecraft orbits and locations. There are several fundamental algorithms implemented to transform observations from a sensor into an estimate of a satellite's state alongside an estimate of the error in the state estimate. The error in the state estimate is represented by a multi-dimensional Gaussian distribution with the same dimensions as the state. This state error matrix is referred to as the covariance [13:26]. When no prior information is known about an object and observations are collected, the first algorithm used is called an IOD [12:457-463]. Then, a Batch Least Squares (BLS) filter (often called Bayes filter) solves the least squares problem to estimate both a state and covariance. The BLS algorithm is also used to update a state and covariance estimate

when additional observations are processed [14:196-197]. The BLS filter is used most often by the USAF for determining orbits. This method is chosen because of the sparsity of cataloged observations for each item tracked. The BLS filter is used operationally to provide orbit estimates as it combines batched observations to minimize errors [3:11].

The Kalman Filter (KF) is an alternative algorithm to solve the linear least squares problem in the framework of optimal control [19; 20]. The original KF when applied to a nonlinear, sequential implementation is referred to as the Extended Kalman Filter (EKF) [21]. While BLS filtering is designed for a small number of observations over longer periods; the EKF is suited for a larger number of observations over a short period of time [13:102].

Traditionally, the BLS approach is used when tracking foreign objects due to its long performance history and abilities to categorize unknown observations. New tracks are associated with objects based on their fit to a determined orbit and a BLS filter is run with a large number of data points to appropriately weight new observations. More recent work by Wright states that the BLS filter is not always the best way to perform operations [22]. Wright details that an optimal method to perform orbit determination for a new object is:

1. Perform IOD

2. Perform BLS filter on data to refine the epoch state and covariance

3. Run an EKF sequentially on previous and incoming data

Wright defends the assertion that a properly configured EKF is adaptable to most situations and is well suited for SOD [22]. Configuring the filter routine requires accounting for measurement errors in the ground sites and the dynamics model through modeling both stochastic errors and correlated errors [23; 24]. Orbit Determination Tool Kit (ODTK) is one type of commercial software that was built on estimation theory principles to model

11

expected errors based on trends seen with operational data [25]. It allows for the estimation of additional states to include both satellite parameters (Coefficient of Drag, mass, etc.) and ground station parameters (bias, error standard deviation, etc.). The techniques used in the software apply to tracking a maneuvering satellite and the software was used in initial research as a baseline for nominal estimation.

After the conclusion of a filter, a backwards smoother can further improve past filter estimates. A Fixed Epoch Smoother (FES) pairs well with the discrete nature of satellite observation, and there are two forms: the Carlton-Rauch (CR) and the Frazer. These smoothers process new observations one at a time and then recursively use this new information to update the state and covariance at the epoch. The fixed interval smoother is a different approach that updates all estimates within an interval. It works backwards from the last filter estimate in an interval and improves estimates in a backwards sequential fashion. Wright and Woodburn et al. discuss the combination of an EKF with different smoothers [26; 27]. If the post-maneuver state and covariance are assumed known from a declared maneuver, a smoother can provide improved estimates of the actual maneuver based on the difference between the pre- and post-maneuver smoothed states. Smoothers provide considerable improvement when reconstructing maneuvers.

2.1.2 Unscented Kalman Filter.

While the BLS and EKF are commonly used for orbit determination, others are experimenting with different filters for predicting the orbital state and covariance. Raol, Sinha, Li, and Jilkov provide an outline of multiple filter types and their applicability to the orbit estimation problem [28; 29]. Due to advances in computational speed, the Unscented Kalman Filter (UKF) has grown in popularity. The EKF is well known and perhaps the most applied method of estimation for a nonlinear system; however, it is often difficult to tune when the system nonlinearities are severe. The EKF algorithm uses a first order Taylor series fit to approximate the nonlinear dynamics. The UKF reduces linearization

errors in the EKF by using point distributions to approximate how means and covariances change under a nonlinear transformation. Julier and Uhlmann developed the Unscented Transform (UT) using thirteen sigma points which preserve the statistics of the initial estimate through a nonlinear transformation. After transformed, the points are used to recalculate statistical values [30]. Simon shows through a simplified polar coordinates example how the first order assumption of EKFs can cause errors in mean and covariance calculations while the UKF avoids these errors [31:434-437]. The EKF works under the assumption that a linearized transformation of means and covariance approximates the true transformation. The UKF is based on two principles:

1. It is easier to transform a single point than a probability density function (pdf)

2. Points selected properly create a pdf that approximates the true pdf of the state vector [32]

The big advantage of the UKF is that the differentiation of the observation transformation is no longer necessary to linearize the system. Additionally, the UKF reduces errors associated with developing a linear State Transition Matrix (STM) for an inherently nonlinear system [30; 32].

The use of the UKF in SOD is growing in popularity as parallel processing becomes more frequent, since the UKF more accurately estimates error covariance matrices. Teixeira et al. compares the performances of the EKF and UKF in orbit determination [33]. Lee and Alfriend evaluates scenarios with the UKF and compares its performance to a divided difference filter [34]. Pardal et al. compares the ability of an EKF and UKF to process GPS-based orbital solutions with pseudo range observations [35]. Pardal shows the UKF outperforms other filters when observations are less frequent. Teixeira et al., Lee, and Alfriend both show different cases in which each filter is superior based on the scenario. In general, the EKF is faster computationally and performs better when the noise is more Gaussian, while the UKF is slower and better at calculating realistic covariances

when the dynamics contain non-Gaussian errors. Cheon discusses using the UKF when processing data from satellite on-board magnetometers [36]. The software routine was flown on Korean Optical Satellite (KOMPSAT)-1 and proved with actual flight data that a UKF can use magnetometer readings for orbit determination. In general, the UKF is applicable to many different fields of estimation theory and is proven as a viable filter for orbit determination. Just as smoothers improve EKF outputs, UKF estimates are also improved via backwards smoothing. Smoothers are developed for the UKF by Särkkä and are adaptable for use in SOD [37; 38]. The use of an adaptive UKF with a smoother is a new application for tracking maneuvering spacecraft and explored in Chapters 5 and 6.

2.1.3 Additional States.

When using a filter to estimate an orbit, the state variable need not only contain position and velocity components. Often times additional states such as radar bias and drag coefficients are estimated by the filter. When using a KF, the algorithm must adapt all vectors and matrices to account for any additional states. Each additional state must have its own estimate at each discrete observation and an associated covariance. Additionally, each state must include a method to estimate the dynamics between observations. Finally, in SOD the process noise matrix must account for any errors associated with the dynamics of the additional states. The practice of using additional states to monitor parameters dates back to earlier space operations when lunar gravity terms were calculated with BLS routines [13:54].

Recent literature shows this practice continues with KFs and ground sites. Hough uses filter states to estimate radar range, angle, and Inertial Navigation System (INS) biases [39]. In this work, the initial state error covariance does not include correlation factors. Hough utilizes a different error matrix to account for the correlations between state and bias errors to improve filter performance [40]. Ichikawa uses the process of estimating thrust components as additional states [41]. The paper evaluates the ability to estimate the

14

state of an interplanetary satellite that maneuvers with a continuous low thrust. The concept of using additional states to estimate a thrust is discussed further in section 2.2.4. Using additional states to track a non-cooperative satellite while estimating long duration thrust accelerations is investigated in Chapter 6.

2.2   Multiple Model Adaptive Estimation

The National Research Council advised the USAF consider MMAE for maneuver detection and specifically mentioned using state-augmented filtering techniques [3:39]. As discussed in the motivation, the focus of the research is not on the data association problem but instead on the real-time tracking of high-priority maneuvering spacecraft assuming the observations correlate to the object of interest. For these missions, there is an abundance of observations at frequent intervals. A KF is preferred for tracking a maneuvering spacecraft due to its speed and forward-moving (sequential) prediction capabilities [42]. Many adaptive maneuver estimation research papers focus on linear state propagation in simple coordinate frames and assume a constant maneuver [43–45]. Tracking a maneuvering spacecraft is much more complex as it is a nonlinear problem with multiple coordinate frame rotations and variable thrust maneuvers.

Once a filter is selected for use, it is best to tune and adapt the filter to meet mission demands and objectives while improving performance. One motivation for adaptive filters is to prevent the covariance from reaching zero. This side-effect of KFs results in a smug filter which ignores all future inputs as the KF mathematically has gained complete knowledge of the state at all times. A smug filter creates a serious issue as new observation data is not included in the estimation process. Additionally, non-adaptive filters diverge quickly when there is an unknown change in the dynamics caused by a maneuver. The filter keeps the covariance low and does not heavily weight the information in new observations. When tracking maneuvering satellites it is necessary to prevent filter smugness and divergence through adaptation of process noise and inclusion of multiple

models. These methods are implemented in Chapters 4 - 9 for estimating the state of a maneuvering spacecraft and a background of relevant sources in these areas is provided in the subsequent subsections.

MMAE approaches are at times referred to as sub-optimal filtering since they deviate from the traditional optimal control KF. While MMAE approaches are sub-optimal, in practice they are more robust and equipped to handle changes in the dynamics, non-Gaussian noise, and estimate additional state parameters. The term MMAE encapsulates any formulation that considers a multiple model framework consisting of either static models, adaptive models, or both. A MMAE framework allows for various models to adapt certain parameters in different ways to account for updates in noise, residuals, dynamics, etc. There are a multitude of different ways to implement MMAE techniques based on the estimation problem of interest. The approach is general enough to use any type of filter to model any type of dynamics and combine the outputs of multiple models to improve the overall estimate. Of specific interest for maneuvering spacecraft estimation are MMAE implementations that solve for additional states, adapt noise parameters, and combine the outputs of all models at each time step.

2.2.1   Fading Memory Filters.

A well known method to handle the issue of a shrinking covariance in SOD is to use fading memory filters as an adaptive model. Gelb introduced this idea as a method to prevent an unrealistically small covariance by increasing the weight of new measurements and de-weighting older measurements [46:285-288]. A fading memory filter inflates the optimal covariance allowing for incorporation of un-modeled accelerations in the dynamics process. Inflating the covariance prevents a smug filter, adds uncertainty, and forces the filter to minimize recent dynamics modeling errors by increasing the weight of new observations on the estimate. Sorenson and Sacks prove that the fading memory filter is asymptotically stable and prevents filter gains from becoming unjustifiably small [47].

Also, the idea of transitioning between a fading filter and non-fading filter when residuals fail to meet the zero mean white noise assumption is introduced in this work. Lee expands upon Sorenson and Sacks' work with the development of several theorems based on a stability analysis of a general fading memory filter [48]. The work focuses on designing a bandpass filter composed of two fading memory filters to determine the precession motion of a spinning top and shows with proper bounds that adaptive filters do not degrade stability. The fading memory approach is a simplified and stable method to handle unknown and un-modeled changes in the dynamics that is applicable for any tracking mission [49:415-419]. All fading memory approaches harness the strategy of adding noise to inflate the covariance and prevent filter divergence. This approach is implemented in Chapters 4 - 6 to estimate the state of a maneuvering spacecraft in real-time.

2.2.2 *Multiple Model Framework.*

It is often advantageous to use several models to estimate the state and covariance of a dynamic system. This method allows for increased performance by transitioning between models as conditions change. The simplest approach to using multiple models for state estimation is to allow each model to act independently on a set of data and then select the model that most closely matches the observations. This simple approach originated in Magill's work in which a bank of KF models vary the start time of an applied acceleration [50]. This initial theory predicts that with enough filters, one filter could capture the timing and magnitude of the unknown applied acceleration accurately enough to result in an ideal state estimate and covariance. This idea is applicable to a bank of KFs with varying noise characteristics and/or varying dynamics run in parallel in a multiple model framework. This pioneering work was improved in future MMAE formulations with the development of the Interacting Multiple Model (IMM).

2.2.3   Input Estimation.

The Input Estimation (IE) routine is one method to estimate an unknown thrust within a MMAE framework. The IE approach uses residuals as a measurement added to the state and solves for the thrust states in a BLS routine. Chan et al. and Bogler began the work in IE to determine the acceleration input for an augmented model when tracking a maneuvering target [51; 52]. Lee and Tahk improve the IE approach by estimating a varying magnitude unit step function input [53]. Wang and Varshney expand upon Bogler's work by developing a real-time recursive routine to solve for an input as opposed to using the batched IE approach [52; 54]. The recursive routine is centered on minimizing the error covariance associated with the thrust. Input estimation routines are similar to a Variable State Dimension (VSD) KFs in that each tracking approach solves for a maneuver [55]. Most IE routines use post processing least-squares iteration to solve for a thrust, and the VSD approach is more robust and estimates the thrust in real-time. While IE is considered for maneuver reconstruction, the instantaneous case requires solving only for a single specific acceleration as discussed in Chapter 5 and the continuous case is best solved using additional states as discussed in Chapter 6 and the next subsection.

2.2.4   Variable State Dimension.

In opposition to the IE technique, the VSD approach uses additional states within a KF to sequentially solve for the thrust of a maneuvering vehicle. While this approach adds complexity to the filter, it allows for the maneuver to vary according to known dynamics equations or observations. The differences between IE and VSD routines are similar to the differences between BLS and EKF routines in that one inverts a matrix the size of the observation vector while the other inverts a matrix on the order of the state vector. For the Continuously Maneuvering Spacecraft (CMS) mission, a multitude of observations are received and a KF approach is preferred for its speed and sequential estimation.

The literature reveals that VSD estimation began with Bar-Shalom and Birmiwal's work that simulates using the VSD approach in a hypothetical tracking problem [56]. The VSD approach is further detailed in the authors' text [57:431-434]. VSD estimation is based around adaptively augmenting the state variables when necessary to capture new dynamics through a modified model with added states. This method is slightly different from the approach of using filtering to estimate additional states throughout a scenario. VSD estimation adds states in response to large residuals and then removes these states when observations reveal that the dynamics has returned to a nominal pattern. For the VSD method to remain effective, it is critical to determine when to estimate using additional states and when to estimate using the nominal states and model. When estimating thrusts, this approach helps ensure the thrust itself is estimated and not some other dynamics parameter or noise that occurs during non-maneuver times. The VSD method works well provided the additional states are added at that proper time and are not added to compensate for a bad observation [58]. The Bar-Shalom-Birmiwal's model uses a fading memory filter parameter and a maneuver detection statistic to determine when to switch between a nominal KF model and the augmented filter with acceleration states [59:191-209]. In Chapter 6, a VSD is implemented, tested, and analyzed for estimating the state of a maneuvering spacecraft.

2.2.5 *Adaptive Noise.*

Many MMAE formulations adapt added noise parameters within models to properly account for dynamics uncertainties. Both the EKF and UKF have adaptable noise parameters which are either set to known values or adapted to handle system dynamic uncertainties (e.g. process noise) and measurement uncertainties (e.g. observation noise) [60]. Early work in this field by Mehra discusses how to make residuals consistent with the filter's predicted covariance by directly solving for either the process noise covariance or the measurement noise covariance [61]. Assuming one is known, the other is directly

solved for in the linear KF application. Another adaptive approach detailed by Myers and Tapley estimates the process and observation noise along with the process and observation noise covariance at each time step [62]. The residuals are used to solve for the noise and associated covariance at each time step and the results are averaged over previous observations. Frequently, the observation noise covariance is rather well known based on sensor calibration testing.

Adaptive filtering cannot estimate both the process and observation noise covariances at the same time, so most work focuses on adapting the process noise covariance [63]. Burkhart, Bishop, and Kumar et al. use different adaptive techniques to estimate noise covariances and other parameters [64; 65]. Wright and Hujsak tune the process noise in orbit propagation routines to reflect the true error in the estimate [23; 24]. Wright et al. develops detailed methods using autocorrelation functions and polynomial coefficients to calculate the covariance for errors in non-spherical gravity modeling [66]. Hujsak discusses how to estimate certain perturbing acceleration errors by using an exponentially correlated stationary process based on Singer's work [67; 68]. Essentially, Wright and Hujsak develop accurate models to capture the error in the dynamics of orbital predictions through a properly formulated process noise covariance. The adaptive noise techniques reviewed are implemented in this dissertation to prevent divergence when unknown changes in the dynamics occur. In Chapter 4, adaptive techniques are applied in real-time to modify process noise covariances and filter-through unknown spacecraft maneuvers.

The UKF contains additional parameters that many have tuned for improved filter performance. Since the UKF uses sigma points to estimate the state and covariance, it is possible to adaptively change the sigma points or weighting of each point. Adaptively changing these affects higher order terms of the nonlinear estimation and can slightly modify the estimation accuracy and stability of the UKF [69]. The weighting factors within the UT are investigated in Chapter 8.

Li et al. uses the exact same method as Myers and Tapley with sliding factors to estimate the noise covariance in a UKF [60]. This method uses a sliding window as a way to limit the filter memory and scale the impact of the previous measurements and covariance matrices. In a similar fashion, Lee and Alfriend discuss using process noise covariance estimation based on a window size to control the covariance update. However, they use a numerical optimization routine to properly select the window length based on a Monte Carlo simulation average [70]. The approach of optimizing parameters to minimize residuals is applicable to post-maneuver SOD; however, the window size parameter depends on when the maneuver occurred and the frequency of observations. Early testing revealed that these approaches are extremely sensitive to selection of the window sizes and not robust for orbit determination with large residuals. These results are supported by Busse et al. who discusses the limited effectiveness of using a weighted sliding window UKF. Instead, they recommend a fading memory parameter in the process noise covariance within the EKF [71]. A related method was implemented in Chapter 6 for the continuous maneuver case.

Recently, adaptive UKFs are becoming more prominent in on board estimation routines. Shi et. al uses a modified Sage-Husa estimator to adapt the process noise covariance by weighting coefficients in an adaptive UKF [63; 72]. The process noise covariance is calculated recursively based on scaling factors and differences between the propagated state and state estimate. The scaling factor adjusts both the process noise covariance and a process noise vector at each time step. The Sage-Husa adaptation of process noise covariance is effective, but only for small errors in the dynamics. Soken and Hajiyev adapt process noise covariance by modifying the UKF gain for the purpose of diminishing the input of a failed sensor in attitude estimation [58]. Mohamed and Schwarz use a sliding window KF to determine position based on inputs from a precision INS [73]. The multitude of literature on adaptive filtering shows not only its promise, but

more importantly the need to selectively choose an adaptive routine to fit the mission goals. In Chapters 4 - 6, EKF and UKF routines are adapted to improve performance in estimating a maneuvering spacecraft's state.

2.2.6 Interacting Multiple Models.

The IMM is a specific type of MMAE that allows for a statistically effective way to combine the inputs of several models at each time step. This approach uses multiple models and relies on the statistics of the residuals to weight the impact of each model at each time step. Li and Jilkov discusses several methods to combine model estimates in the IMM framework [74]. The benefit of the IMM approach is that it is simply a framework and different models with different techniques are customized to support the application. IMM and VSD formulations are commonly used when solving the tracking problem with classic kinematic equations of motion. Often times, both methods are merged and the IMM approach is used with augmented state models, IE routines, and switching logic.

Amirzadeh et al. uses the IMM framework composed of a standard and augmented model KF for tracking an aircraft [75]. This approach required pre-determining the jump transition probabilities within the IMM. Rago and Mehra uses a 3 model IMM framework for missile guidance [76]. This work shows the versatility of using multiple models instead of fully solving for the noise characteristics. The real-time tracking branch of research begins with the assumption that the identity of the tracked spacecraft is known. With this assumption, techniques from missile and aircraft tracking are adaptable for use in estimating the orbits of maneuvering spacecraft.

In other work, Xiong et al. uses an IMM format with a constant velocity model, constant acceleration model, and a non-zero mean time-correlated acceleration model [77]. The work shows a method to use multiple UKFs in an IMM framework. Also, Hanlon and Maybeck use the IMM approach and time correlated residuals from a KF bank to calculate conditional probabilities [78]. This updated hypothesis testing algorithm allows for more

accurate model probabilities within the IMM framework and was applied to detect flight control actuator failures. Bizup and Brown approach the problem of maneuver detection using a two model IMM with uniform motion KFs [79]. The models have different noise parameters based on a fading memory average of residuals and a predetermined Markov chain is used for the jump transition in the IMM. Shetty and Alouani show the benefit of using multiple sensors in calculating the transition statistic for maneuver detection [80]. This work fuses optical and radar methods to determine when to switch to a VSD model for target tracking. Similar to other filters, many have developed smoothers for the IMM [81–83]. Together, these works prove the versatility of the IMM approach when paired with particular models to account for specific dynamics. Also, these works show the importance of choosing the proper filters and filter configurations within an IMM framework to fit a specific scenario.

When developing covariance inflation strategies to filter-through unknown maneuvers, a trade-off occurs. The larger the covariance inflation, the less likely the probability of divergence; however, the greater the errors. Conversely, a smaller post-maneuver covariance inflation reduces errors but increases the probability of divergence. The IMM filter provides a method to mix Gaussian models in real-time and weight the results from the most likely model [83; 84]. The IMM approach prevents the need to determine an optimal covariance inflation size and run optimization routines that are typically only valid for a specific maneuver type and orbit. Although the IMM is considered sub-optimal, the results in Chapter 4 show its effectiveness in post-maneuver orbit estimation. Additionally, the research shows that a predetermined jump probability model is unnecessary to detect maneuvers and is also not recommend as it adds the assumption that the probability of a certain maneuver is known at each time step.

2.3 Error Estimation

A baseline assumption of the BLS and KF routines is that the state error covariance is captured by a multi-dimensional Gaussian. Due to the nonlinearities in orbital dynamics, covariances may not capture the true error in the state estimate. For longer propagations, covariance estimates are often times inaccurate and optimistic. Many have studied the covariance output from filtering routines to determine its effectiveness in representing the underlying error distribution.

2.3.1 Covariance Realism.

The covariance of an orbit estimation routine is realistic only when sensors are properly calibrated and error distributions are well understood. Vallado and Seago discuss ways to test if the predicted satellite location fits a normal distribution and whether the error spread is consistent with the covariance [85] . A realistic, propagated covariance from a filter should match errors experienced during actual tracking and simulated Monte Carlo testing. Folcik et al. and Aristoff et al. conclude that mean or Equinoctial element representations of states and covariances better capture underlying distributions when compared to Cartesian elements [86; 87]. Horwood et al. expands upon Vallado and Seago's work and develops specific goodness of fit statistical tests to address whether or not realism is achieved. Specifically, a formulation of the Cramér-von Mises test is developed using the Mahalanobis distance [88]. In Chapters 7 and 9, covariance realism techniques are adapted for use in estimating potential orbital maneuvers. Additionally, Horwood et al. shows that the output of a convergent BLS filter achieves covariance realism [89]. This result was confirmed and further analyzed when performing short arc orbit estimation in Chapter 7. Overall, the covariance realism research proves that representing the error covariance in different element sets can impact covariance realism. If covariance realism is not achieved, a different pdf is necessary to capture the underlying distribution [87; 88].

2.3.2   *Gaussian Mixtures.*

When a single Gaussian no longer captures the underlying error distribution, a pdf composed of a mixture of Gaussian components is often used. Pioneering work in the area proves that given enough components, a mixture can model any distribution arbitrarily close for a specific distance metric [90]. To preserve an accurate representation of the error distribution, deMars et al. splits a single Gaussian into a mixture when differences in entropy grow beyond a threshold [91]. Vishwajeet et al. continue this work by implementing a convex optimization formulation to determine mixture components [5]. The work of Terejanu et al. shows an approach to propagate each Gaussian component of a mixture individually and then reform the mixture after propagation [92]. Horwood et al. develops routines to split a Gaussain a sufficient number of times to meet covariance realism requirements [93]. Aristoff et al. highlights that a far greater number of mixture components are needed to achieve realism using Cartesian elements compared to Equinoctial elements [87]. The methods discussed above are tested, analyzed, and adapted for the maneuver estimation cases in Chapter 9.

2.3.3   *Collision Avoidance.*

Collision avoidance and certain data association routines need realistic covariance information to deliver accurate results. A common method to predict satellite collisions involves determining when propagated covariance error ellipsoids intersect [94]. Gottlieb et al. simulate collision probabilities by altering orbital knowledge [95]. Yim et al. evaluate Two Line Element (TLE) sets to predict actual errors measured against the predicted covariance for collision avoidance purposes [96]. Alfano, one of the originators of the Satellite Orbital Conjunction Reports Assessing Threatening Encounters in Space (SOCRATES) tool, has published multiple articles on predicting collision probabilities [97; 98]. The groundwork laid by Alfano is adapted for an SSA focused mission evaluation in Chapter 7.

The missions of space debris removal and satellite servicing also require accurate state and error estimation. Kahle et al. evaluate relative non-cooperative orbit determination methods to asses errors during rendezvous operations for debris removal [99]. Similarly, Xu et al. describe a full algorithm for guidance, navigation, and control to rendezvous with a target as well as additional algorithms to predict the orbital state of an object [100]. The research in Chapter 7 addresses the timeline prior to a precise orbit rendezvous and focuses on a fast way to arrive in the proper vicinity of a non-cooperative target.

Vallado and Carter investigate a reliable way to use numerical integration to evaluate dense operational data from geographically separated sites [101]. The BLS approach is used to fit dense data and predict the covariance of actual satellite data compared to precision orbit ephemeris data. In Chapter 7, this work is continued as dense orbital data describes an orbit with a BLS filter and a UKF propagates covariance estimates to calculate intersection probabilities.

2.3.4 Pattern Matching.

While analyzing certain estimation approaches for non-cooperative maneuvering satellites, additional techniques from computer vision and machine learning prove useful. Fitting an unknown propagated orbit state error distribution with a mixture is synonymous with pattern matching routines. The sub-optimal Expectation Maximization (EM) routine can fit a mixture to any arbitrary set of points [102:18-28]. The EM algorithm is a clustering method similar to k-means [103]. The iterative EM algorithm is fast and effective in convergence on a solution [104]. However, the approach is highly dependent upon the initial guess. Arthur and Vassilvitskii recommends using k++ means seeding to begin the EM algorithm as this approach outperforms a random initial guess [105]. In Chapter 9, these approaches are implemented and analyzed to develop propagated mixtures that meet covariance realism requirements.

2.4   Responsive Orbits

As the space environment becomes more crowded, the USAF stresses the need for resiliency and flexibility in mission profiles. Additionally, as space becomes a more contested environment, maneuvering spacecraft are a solution to achieving mission requirements amidst contention. These solutions include maneuvering satellites often to improve latency, dodge keep-out zones, and maintain an optimal formation [9; 10; 106]. Research in these areas motivates development of orbit estimation strategies to track maneuvering spacecraft and reconstruct maneuvers of non-cooperative spacecraft.

2.4.1   *Maneuver Reconstruction.*

Often times a satellite maneuvers outside of view of a ground site or radar. The first post-maneuver observation vastly differs from the predicted non-maneuver orbit and a maneuver is detected. Once the post-maneuver orbit is known, a conventional straight forward deterministic approach is used to determine the maneuver that connects the pre-maneuver orbit to the post-maneuver orbit. By propagating the post-maneuver orbit backwards in time and the pre-maneuver orbit forward in time, the point where the two orbits touch is determined as the time of an instantaneous maneuver. The benefit of numerical integration and STM routines is that they are easily adapted to run backwards in time. These matrix properties permit transfer of the state and covariance to any time based on initial conditions and known dynamics. This approach allows for a simple method to calculate the differences between pre- and post-maneuver orbital solutions. For the instantaneous thrust case, the thrust is estimated as the change in the velocity vector from the pre- to post-maneuver orbit at the time of closest approach [11; 12]. Chapter 5 uses this approach to analyze the accuracies of a reconstructed maneuver based on the covariances of the pre and post-maneuver orbit solutions.

In other works, Woodburn et al. use a smoother to improve estimates of the reconstructed maneuvers and covariance [27]. Wright discusses using a fixed epoch

smoother that begins at the centroid of the maneuver [26]. The maneuver estimate is improved based on the differences between the pre- and post-maneuver smoothed states. Hujsak develops a method using filtering and smoothing to reconstruct a maneuver with an EKF, additive process noise, and smoothers [25]. He develops an impulsive form of the fading memory filter by adding process noise covariance at regular intervals. This methodology assists in convergence upon a reconstructed maneuver solution within an EKF and smoothing iterative loop [24; 25]. Hujsak et al. use a similar loop with additional state variables during post processing to estimate a low-thrust long-duration spacecraft maneuver [107]. Once the velocity is initially estimated, the filter and smoother are re-run until convergence is achieved. Convergence is achieved when an orbit solution is found that estimates the time, duration, magnitude, and direction of maneuver well enough to keep residuals within non-maneuver limits [24]. In Hujsak's approach, thrust values are added to the state vector and the thrust errors are estimated using Singer's dynamics model solution [67]. The Singer solution involves modeling the acceleration state errors as exponentially time-correlated processes with zero mean Gaussian noise. Li and Jilkov also discuss the use of the Singer model for unknown time-varying accelerations as a mean adaptive acceleration method for tracking in a traditional kinematic system [108]. Chapter 5 describes an alternative approach to determine how variables and parameters of the orbit estimation impact the ability to reconstruct maneuvers.

There are several other works that develop different methodologies for the maneuver reconstruction problem. Oltrogge uses a software called Orbit Detective to propagate orbital solutions back to an epoch and then uses a low pass filter to determine potential cross-tagging events and maneuvers [109]. Kelecy and Jah use the ODTK software to evaluate the detection of very small maneuvers using operational data [110]. Additionally, Kelecy et al. investigate TLE sets to detect maneuvers [111]. This effort involved filtering TLE data and evaluating the difference between two consecutive TLEs. Maneuver time

and magnitudes are determined based on the closest approach of the orbits and the change in the orbital element sets. In a similar fashion, Lemmens and Krag examine TLE histories to detect maneuvers and patterns of behavior [112].

Patera uses TLEs to calculate the energy per unit mass over a sliding window [113]. This information is used to fit a cubic polynomial and maneuvers are detected based on changes in the energy curve. Mehrotra and Mahapatra implement Singer's dynamic model for estimating the jerk of a maneuver in the traditional kinematic tracking case [114]. This work develops a KF model for the thrust acceleration and its derivative for the three-dimensional case. Oltrogge uses dual level optimization to solve for a thrust profile that includes jerk components [115]. The optimization routine implements variation equations with a line searching routine based on known characteristics of the satellite engine. Johnson evaluates the filter convergence based on uncertainty in planned maneuvers using ODTK and displays how errors in thrust calculations affect the state covariance [116]. In a different approach, Storch develops a close proximity linear STM to determine relative motion maneuvers for satellites in geosynchronous orbits [117]. Huang et al. performs maneuver reconstruction through the maximum a posterior probability that two orbits are connected by a single in track maneuver [118].

The reviewed methods show different approaches to attack the problem of reconstructing a maneuver with post-maneuver data. For the high-priority maneuvering spacecraft research that this dissertation addresses, the developed methods use near real-time approaches. In Chapters 5 and 6, filter and smoothing techniques are improved from the resources above for use in high-priority near real-time maneuver reconstruction.

2.4.2   *Neural Networks.*

When data sets are highly nonlinear and variable correlations are not easily visible, neural networks can provide additional insights. Neural network pattern recognition serves as a high fidelity method to predict an output based on a given input [119:116-161]. A

trained set of neural network rules learn patterns within the data and can drive event based decisions for space operations [120]. Training a neural network framework involves customizing a set of network layers composed of sigmoid functions with weights and biases [121]. Training a neural network framework is analogous to an optimization problem and there are multiple different methods to train a network [122:11.1-12.50]. The number of hidden and output neurons are also customizable. Typically, the initial data set is divided into sets for training, validation, and performance testing [121]. Furthermore, signal to noise implementations of neural network patterns can determine the weight that each variable contributes toward the output classifications [123]. There are many different variables to consider when reconstructing an instantaneous maneuver. To aide in determining the most critical variables during maneuver reconstruction, neural network rules are trained, implemented, tested, and analyzed in Chapter 5.

2.5 Space Situational Awareness

The JSpOC conducts the SSA mission, publishes TLE data, and issues collision warnings. The SSN is a set of ground sites (radar, optical, and phased array) the JSpOC uses to track active satellites, missiles, and debris [8]. The location and mission of each of these sites are available for modeling [124]. Furthermore, some performance metrics are also available to simulate operational data [12:258-259]. Overall, the JSpOC manages the tasking of the SSN and the performance of the radar used to track an object impacts the orbital estimate as discussed in Chapter 5.

As the number of space objects increases, so does the demand for more observations. At this rate, the current SSN will likely become over tasked with requests. To improve SSA, some advocate for increased international data sharing and open architectures. Weeden and Cefola discuss the fact that both USA and Russia lead the world in SSA software. They advocate a common set of algorithms and standards for all to use [125]. The work discusses how uncertainty modeling requires detailed knowledge on the calibration of the sensors and

dynamics model perturbations. Furthermore, Cefola et al., highlight the need for using an open software system to track orbital objects. They frown upon the USAFs stance to remain fixed to a Simplified General Perturbations (SGP) model with BLS correction, while not using large data sets available from improved sensors [126]. In other works, Richmond discusses data fusion methods to improve the SSA mission by incorporating orbital data and maneuver detection routines [127]. The article proposes a service oriented architecture to support SSA information dissemination. Butkus et al. discuss a tool to improve SSN performance [128]. The work details using the Space Surveillance Network Analysis Model (SSNAM) to evaluate the effects of losing certain ground sites due to maintenance. The software determines effects on orbital estimates when certain ground configurations are used. These sources support the research herein as sensor variations are assessed using KF routines with maneuver detection and reconstruction capabilities in Chapters 4-7.

2.5.1 Uncorrelated Targets.

One of the main motivations of maneuver detection and reconstruction is that it can reduce UCTs and properly associate a set of observations to a satellite. While association is not a focus of the research, the techniques used in this research prove valuable for estimating the state of a maneuvering spacecraft in near real-time. The literature reveals several different data association focus areas including "nearest-neighbor", Multiple Hypothesis Tracking (MHT), and Joint Probabilistic Data Association (JPDA) filters [129–133]. These efforts typically run during post-processing of large data sets and each method has certain benefits as discussed in the literature.

Nearest neighbor simply associates an observation with the satellites whose predicted track is closest to the sensor observation and any unassigned sensor observations are classified as UCTs. Blackman suggests that IMMs composed of KFs with different target maneuvers are best to use with nearest neighbor association techniques when tracking maneuvering objects [134]. The IMM construct increases performance by sequentially

predicting and mixing models for future associations. A similar approach is used in Chapters 4 and 6 to determine the proper dynamics model to use while filtering-through maneuvers.

The JPDA method propagates satellite covariance matrices and matches observations to satellites if the observation lies within the predicted covariance volume. This approach allows for pairing observations to multiple satellites and multiple observations simultaneously to the same satellite. Unknown maneuvers further complicate the problem resulting in assigning an observation to the wrong satellite because the actual state does not match the filter prediction. Benoudnine et al. evaluate combining an IMM with KFs to capture maneuver profiles within a JPDA framework for the mission of tracking with a phased array radar [135]. Measurements are validated within the IMM only if they are within a threshold based on the output of the residual and measurement covariance. Chapter 5 builds upon this work by removing the assumption that a specific maneuver profile is known ahead of time.

MHT is also known as Multiple Frame Assignment (MFA) and delays association until enough statistical information is available. It allows for propagating candidate satellite tracks forward in time to compare to multiple frames of observations. Reid's hypothesis filter creates tracks for each possible observation association, then actual association occurs only when tracks have no observations in common in that frame [136]. Cox and Hingorani evaluate visual tracking data using a "k-best" Reid's MHT approach [137]. The work uses residuals to determine and propagate the top "k" hypotheses for potential association. Poore and Horwood develop a methodology called Multiple Hypothesis Correlation for incorporation into an MHT framework [138]. This work uses an adaptive Gaussian sum filter for orbit estimation in a sliding batch window format for prediction. It also handles bias correction and calculates the probability of correct data association through a "k-best" approach. Similarly, Singh et al. investigate calculating maneuver size to connect discrete

tracks and association of tracks are made through selection of the satellite with the least fuel cost distance [139]. This method also includes estimating uncertainty through a UT to approximate the probability distribution. The research in this dissertation builds upon these MHT efforts by incorporating similar methodologies within a pruning IMM in Chapters 4 and 9. Also, the IMM approaches in Chapter 9 are rooted in using likelihood weights to determine the most relevant mixture components which is similar to most association techniques.

2.5.2   Sensor Tasking.

The research completed in this dissertation can help improve SSA tasking when faced with estimating the state of a high-priority maneuvering spacecraft. Others have researched methods to configure network collections to improve catalog accuracies. In an effort to develop a decision engine for collection prioritizing, Erwin et al. develop a methodology for a set of sensors to minimize the covariance for an entire catalog of objects through proper sensor tasking [140]. Williams et al. continue research in this area by determining a visibility matrix matching objects and sensors at a given time, and they also study sensor tasking metrics based on information theory [141; 142]. Miller looks at sensor tasking in a similar way to solve the resource constrained problem of using low altitude satellite collections to update the special perturbations catalog [143]. The focus of the article is on organizing the network to collect on passes with favorable signal to noise ratios. While these efforts consider the entire network, the research herein focuses on real-time immediate tasking of radars for collection on a target once a maneuver is detected. Chapter 5 investigates required ground site tasking and a specific number of passes necessary to reconstruct an orbit based on the quality of the site observations.

2.6   Optimization

Optimization is a large field full of literature, methodologies, algorithms, and space specific examples that find the optimal input to minimize a scalar cost function. Several

portions of the research within this dissertation implemented optimization algorithms. Specifically, Chapters 5, 8, and 9 all involve solutions to optimization problems. In a survey paper, Betts reviews a multitude of different approaches to optimization and the advantages and disadvantages to each [144]. Most approaches are rooted in solving a specified two-point boundary problem using calculus of variations [145:1-43]. For several of the topics reviewed, there are specific works that use optimization routines in coordination with other methods discussed thus far.

With the increase in computational speed and parallel processing, some MMAE combine optimization with filtering. Jiang et al. and Han et al. use the approach of optimizing a cost function with gradients to adaptively change the process noise covariance [69; 146]. These adaptive approaches improve filter performance and prevent divergence by optimizing process and observation noise. In other optimization efforts, Holzinger et al. formulate the maneuver data association problem as an optimization problem. They discuss a methodology for associating UCT tracks with a maneuver. The goal of the work was proper association through minimization of the distance between the optimally maneuvered spacecraft and the UCT [147; 148]. Similarly, a local search routine is implemented to determine an optimal maneuver solution in Chapter 5.

2.7 Conclusion

Overall, this section reviews current literature research as well as methodology development from a wide variety of academic disciplines. The sources provide the necessary background developments to justify that the research methodology in the following chapter is consistent with works in the field. Additionally, the literature review reveals an absence of research pertaining to estimating the orbit of a non-cooperative maneuvering satellite in near real-time using MMAE. Specifically, the research herein adapts filters to detect maneuvers, inflates the state covariance to increase convergence speeds, expands state dimensions to estimate maneuvers, and incorporates an IMM

framework to reduce errors. The review provides evidence that the results in Chapters 4- 9 is new in its approach and application. Additional sources are discussed as well in subsequent chapters and are consistent with themes discussed thus far.

III.   Methodology

3.1   Introduction

The previous chapters provide a motivation and background for incorporating the tracking and estimation of non-cooperative maneuvering spacecraft into the overall SSA mission. This chapter develops the methodologies and the mathematical formulations common in the subsequent chapters. Additional specific methodologies are further developed in each chapter as required for certain scenarios. This chapter pulls from textbooks and articles to arrange the development of key algorithms used throughout the dissertation. This chapter assumes knowledge of math techniques and orbital dynamics. Reference supporting texts for any necessary background information [12; 13; 31].

3.2   Orbit Estimation

In state notation, define the state vector of the spacecraft, $\mathbf{x}$, as the combination of the position from the center of the Earth to the spacecraft, $\mathbf{r}$, and velocity, $\mathbf{v}$, of the spacecraft in the I, J, K, Cartesian Earth Central Inertial (ECI) coordinate frame [12:159, 772-797]

$$\mathbf{x} = \left[\begin{array}{cccccc} r_I & r_J & r_K & v_I & v_J & v_K \end{array} \right]^T \tag{3.1}$$

Under the influence of Earth's gravity where $\mu_\oplus$ is Earth's gravitational parameter and r is the magnitude of the spacecraft position vector, the time derivative of the state and the two-body equations of motion are

$$\dot{\mathbf{x}} = \left[\begin{array}{cccccc} v_I & v_J & v_K & -\frac{\mu_\oplus r_I}{r^3} & -\frac{\mu_\oplus r_J}{r^3} & -\frac{\mu_\oplus r_K}{r^3} \end{array} \right]^T \tag{3.2}$$

Additional higher fidelity dynamics are described in 3.14. Using the equation of variation define the Jacobian matrix, $\mathbf{A}(t)$

$$\mathbf{A}(t) = \frac{\partial f(\mathbf{x})}{\partial \mathbf{x}} = \frac{\partial \dot{\mathbf{x}}}{\partial \mathbf{x}} = \left[\begin{array}{cc} 0 & \mathbf{I} \\ \Lambda & 0 \end{array} \right] \tag{3.3}$$

where

$$\Lambda = \begin{bmatrix} \frac{-\mu_\oplus}{r^3} + \frac{3\mu_\oplus r_I^2}{r^5} & \frac{3\mu_\oplus r_I r_J}{r^5} & \frac{3\mu_\oplus r_I r_K}{r^5} \\[2mm] \frac{3\mu_\oplus r_I r_J}{r^5} & \frac{-\mu_\oplus}{r^3} + \frac{3\mu_\oplus r_J^2}{r^5} & \frac{3\mu_\oplus r_K r_J}{r^5} \\[2mm] \frac{3\mu_\oplus r_I r_K}{r^5} & \frac{3\mu_\oplus r_K r_J}{r^5} & \frac{-\mu_\oplus}{r^3} + \frac{3\mu_\oplus r_K^2}{r^5} \end{bmatrix} \tag{3.4}$$

Expanding $\dot{\mathbf{x}}$ in a first order Taylor series and solving the differential equations produces a STM, $\mathbf{\Phi}(t, t_0)$, where t_0 is the initial time and t is the final time. The STM propagates based on the differential equation

$$\dot{\mathbf{\Phi}}(t_i, t_0) = \mathbf{A}(t_i)\mathbf{\Phi}(t_i, t_0) \tag{3.5}$$

with initial conditions such that $\mathbf{\Phi}(t_0, t_0)$ is the identity matrix, $\mathbf{I}$.

3.3 Stochastic Estimation

Carl Friedrich Gauss developed the formulation for normal "Gaussian" distributions and the method of least squares to minimize errors. In SOD, the true error, $\mathbf{e}$, is never truly known, since the true state is never known [13:4]. Gauss developed the techniques to estimate the true error of the state, $\mathbf{e}$. Define the univariate Gaussian pdf

$$f_X(x) = \left(\frac{1}{\sigma\sqrt{2\pi}}\right) e^{\frac{-(x-\mu)^2}{2\sigma^2}} \tag{3.6}$$

where $x \in [-\infty, \infty]$, X is a Random Variable (RV), μ is the mean, and σ is the variance [17:102]. Describe evaluating the Gaussian at a single value x as $\mathcal{N}\left(x; \mu, \sigma^2\right)$ and describe the distribution of X as $X \sim \mathcal{N}\left(\mu, \sigma^2\right)$. Orbit estimation pertains to the multivariate case where n defines the number of dimensions (variables) in the Gaussian:

$$\mathcal{N}(\mathbf{x}; \boldsymbol{\mu}, \mathbf{P}) = \frac{e^{-\frac{1}{2}(\mathbf{x}-\boldsymbol{\mu})^T \mathbf{P}^{-1}(\mathbf{x}-\boldsymbol{\mu})}}{(2\pi)^{n/2} |\mathbf{P}|^{1/2}} \tag{3.7}$$

Applying a non-deterministic approach in discrete time and state form at time t_i [31:107-114]

$$\overline{\mathbf{x}}_{i+1} = f_i \hat{\mathbf{x}}_i + \mathbf{w}_i \tag{3.8}$$

where $\mathbf{x}_i$ is the state vector of length n. The bar above $\bar{\mathbf{x}}$ represents the state propagated to the next observation; whereas, $\hat{\mathbf{x}}$ represents the estimate after considering observations at t_i. f_i represents either a linear transformation or the numerical integration of nonlinear dynamics to update the state variable to the next time step. For orbit estimation, f_i is the numerical integration of the dynamics in Equation 3.2 and Equation 3.5. In the update, $\mathbf{w}_i$ is the n-dimensional process noise $\mathbf{w}_i \sim \mathcal{N}(0, \mathbf{Q}_i)$ where $\mathbf{Q}_i$ is the process noise covariance [31:68-73]. To compare the predicted state to an actual observation, the statistical model of the measurement process is defined as

$$\hat{\mathbf{y}}_i = G_i \bar{\mathbf{x}}_i + \mathbf{v}_i \tag{3.9}$$

where G_i is the observation mapping function which transforms the state into a predicted observation, $\hat{\mathbf{y}}_i$ is an m-dimensional calculated observation, and $\mathbf{v}_i$ is the m-dimensional observation noise, $\mathbf{v}_i \sim \mathcal{N}(0, \mathbf{R}_i)$ where $\mathbf{R}_i$ is the observation noise covariance [31:150-156].

The error in a state estimate is captured in the state covariance matrix, $\mathbf{P}$. The covariance provides the confidence in a particular state estimate detailing how the predicted error in the estimate varies. $\mathbf{P}_i = E\left[\mathbf{e}_i \mathbf{e}_i^T\right]$ where $\mathbf{e}$ is a vector of length n representing the true error in the state estimate and E is the expectation function [13:26].

Filtering methods are designed to minimize the error between the actual observation and the predicted observation

$$\nu = \mathbf{y}_{ob} - \mathbf{y}_{calc} = \mathbf{y} - \hat{\mathbf{y}} \tag{3.10}$$

where ν is the residual of length m and $\mathbf{y}$ is the actual measurement vector [13:60-61].

3.4 Numerical Integration

Without a closed form solution of certain dynamics, numerical integration can solve for the orbit at a future time. Numerical integration requires knowledge of the state at a

certain time, $\mathbf{x}_i$, its analytical derivative, $\dot{\mathbf{x}}$, and a time span to evaluate, t_k to t_l. The fourth-order Runge Kutta (RK) numerical integration approach is used for numerical integration in this research and uses a step size Δk to determine the future value of the state using Algorithm 1 [18:398].

Algorithm 1: Runge-Kutta 4 Algorithm [18:398]

Data: $\mathbf{x}_k, \dot{\mathbf{x}}, t_k, t_l, \Delta k$

Result: $\mathbf{x}_l$

for $t_i = t_k$ **to** $t_{l-\Delta k}$ **do**

$\quad$ $t_1 = t_i + \frac{\Delta k}{2}$

$\quad$ $\Delta \mathbf{x}_1 = \dot{\mathbf{x}}(\mathbf{x}_i, t_i)\,\Delta k$

$\quad$ $\Delta \mathbf{x}_2 = \dot{\mathbf{x}}\left(\mathbf{x}_i + \frac{\Delta \mathbf{x}_1}{2}, t_1\right)\Delta k$

$\quad$ $\Delta \mathbf{x}_3 = \dot{\mathbf{x}}\left(\mathbf{x}_i + \frac{\Delta \mathbf{x}_2}{2}, t_1\right)\Delta k$

$\quad$ $\Delta \mathbf{x}_4 = \dot{\mathbf{x}}(\mathbf{x}_i + \Delta \mathbf{x}_3, t_i + \Delta k)\,\Delta k$

$\quad$ $\mathbf{x}_{k+\Delta k} = \mathbf{x}_k + \frac{\Delta \mathbf{x}_1 + 2\Delta \mathbf{x}_2 + 2\Delta \mathbf{x}_3 + \Delta \mathbf{x}_4}{6}$

end

This RK4 approach is implemented using MATLAB's ode45 numerical integration routine [149]. In Chapter 9, Microcosm's High Precision Orbit Propagator (HPOP) routine is used which implements a Runge-Kutta-Fehlberg method of order 7-8 [150]. A higher order integrator is implemented to account for the larger contribution of perturbations when propagating orbits over longer periods of time.

3.5 Coordinate Frames

In observing and predicting orbits it is very important to understand reference and coordinate frames. A coordinate frame is described by three features: origin, fundamental plane, and preferred direction. The most common coordinate frame for satellite orbit

determination is the Cartesian ECI frame and is described with unit vectors I, J, K whose origin is the center of the Earth. The I vector points towards the vernal equinox, the K vector points towards the North Pole, and the J vector completes the orthogonal right handed coordinate system. The fundamental plane is the Earth's equator. This frame is not perfectly inertial and requires additional rotations and standardized epochs which are described by Vallado with pictures of each coordinate frame [12:153-244].

The Earth Centered Earth Fixed (ECEF) frame is similar to the ECI frame except that I points to 0 deg longitude (Prime Meridian) and rotates with the Earth. In Chapters 4-7, epoch seconds are used for scenario time and it is assumed that the ECI and ECEF frames are aligned at the start of the scenario. This assumption is implemented to prevent the need for complex epoch based rotations. The results are easily convertible to epoch based scenarios using orbit analysis software to perform the rotations.

Ground-based radar measurements of satellites are traditionally performed in the Topocentric Horizon Coordinate Frame, also known as the South, East, Zenith (SEZ) frame. This frame consists of unit vectors that point due South, S, due East, E, and radially outward along the local vertical, Z. The SEZ frame is dependent upon the origin which is described by the latitude, ϕ, and longitude, λ_{long}, of the observation site.

When describing satellites and the accuracy of their locations, the Radial, Along-track, Cross-track (RSW) frame is used. The RSW is a coordinate frame that follows the satellite with the origin at the center of the satellite. $\hat{R}$ points from the center of the Earth along the radius vector towards the satellite as it moves in orbit. $\hat{W}$ is normal to the satellite's orbital plane and $\hat{S}$ points in the direction of the velocity vector (but not necessarily parallel to it). In the very similar Radial, In-track, Cross-track (NTW) frame, $\hat{W}$ still points orbit normal, $\hat{T}$ points in the velocity vector direction, and $\hat{N}$ completes the right-handed coordinate system. In a perfectly circular orbit, the RSW and NTW frames are equivalent [12:163-166].

3.6 Coordinate Rotations

When describing satellite motion, it is important to maintain the ability to freely transform a vector expressed in one coordinate frame to another. Rotating the position requires only a single matrix rotation, but rotating the velocity and acceleration vectors must account for the motion of the rotating coordinate frame. Define **ROT** as the rotation matrix between the given coordinate frame and the coordinate frame of choice.

The SEZ to ECEF transition is based on the location of the observation site and is completed through two rotations. Geodetic latitude (traditional use of the term latitude) is based on the angle between the vector perpendicular to the surface and equatorial plane vector. Using the geodetic latitude, ϕ_{gd}, longitude, λ_{long}, and multiplying the two transition matrices together [12:427]

$$\mathbf{ROT}_{SEZ \to ECEF} = \begin{bmatrix} \sin\left(\phi_{gd}\right)\cos\left(\lambda_{long}\right) & -\sin\left(\lambda_{long}\right) & \cos\left(\phi_{gd}\right)\cos\left(\lambda_{long}\right) \\ \sin\left(\phi_{gd}\right)\sin\left(\lambda_{long}\right) & \cos\left(\lambda_{long}\right) & \cos\left(\phi_{gd}\right)\sin\left(\lambda_{long}\right) \\ -\cos\left(\phi_{gd}\right) & 0 & \sin\left(\phi_{gd}\right) \end{bmatrix} \quad (3.11)$$

Since both coordinate frames rotate at the same speed, there is no need to account for the angular rotation of the Earth when rotating the velocity vector

$$\mathbf{r}_{ECEF} = \mathbf{ROT}_{SEZ \to ECEF}\mathbf{r}_{SEZ} \quad (3.12)$$

$$\mathbf{v}_{ECEF} = \mathbf{ROT}_{SEZ \to ECEF}\mathbf{v}_{SEZ} \quad (3.13)$$

During simulations, scenarios begin with the ECEF and ECI axes aligned. This implementation allows for a simplified axis three rotation through the angle the Earth has rotated at that time. Define $\theta = \omega_{\oplus}t_i$ that considers the average rotation speed of the Earth and the elapsed scenario time of interest.

$$\mathbf{ROT}_{ECI \to ECEF} = \begin{bmatrix} \cos\left(\theta\right) & -\sin\left(\theta\right) & 0 \\ \sin\left(\theta\right) & \cos\left(\theta\right) & 0 \\ 0 & 0 & 1 \end{bmatrix} \quad (3.14)$$

The average rotation speed of the Earth is $\omega_\oplus = 7.29212 \cdot 10^{-5} \; rad/s$. The rotation in Equation 3.14 is only valid for the position vector as the coordinate frames are moving in relation to each other. Additionally, recall that a fundamental property of a rotation matrix is that its inverse and/or transpose reverses the direction of the rotation.

$$\mathbf{ROT}_{ECEF \to ECI} = \mathbf{ROT}_{ECI \to ECEF}^{-1} \tag{3.15}$$

To rotate the velocity use

$$\mathbf{r}_{ECI} = \mathbf{ROT}_{ECEF \to ECI} \mathbf{r}_{ECEF} \tag{3.16}$$

$$\mathbf{v}_{ECI} = \mathbf{ROT}_{ECEF \to ECI} \mathbf{v}_{ECEF} + \dot{\mathbf{ROT}}_{ECEF \to ECI} \mathbf{r}_{ECEF} \tag{3.17}$$

where $\dot{\mathbf{ROT}}$ is the time derivative of the rotation matrix [12:174].

Finally, the RSW to ECI and NTW to ECI transformations are based on the following relations

$$\hat{R} = \frac{\mathbf{r}_{ECI}}{|\mathbf{r}_{ECI}|_2} \qquad\qquad \hat{T} = \frac{\mathbf{v}_{ECI}}{|\mathbf{v}_{ECI}|_2} \tag{3.18}$$

$$\hat{W} = \frac{\mathbf{r}_{ECI} \times \mathbf{v}_{ECI}}{|\mathbf{r}_{ECI} \times \mathbf{v}_{ECI}|_2} \tag{3.19}$$

$$\hat{S} = \hat{W} \times \hat{R} \qquad\qquad \hat{N} = \hat{T} \times \hat{W} \tag{3.20}$$

$$\mathbf{ROT}_{RSW \to ECI} = \left[\; \hat{R} \; \vdots \; \hat{S} \; \vdots \; \hat{W} \; \right] \qquad \mathbf{ROT}_{NTW \to ECI} = \left[\; \hat{N} \; \vdots \; \hat{T} \; \vdots \; \hat{W} \; \right] \tag{3.21}$$

It is assumed that the RSW frame is fixed to the orbit at each point in time and the transition process is the same for position and velocity (as in SEZ to ECEF) [12:172].

3.7 Observations

Similar to many other systems, instruments used for satellite operations do not directly observe the state itself. A ground radar used for tracking satellites typically provides measurements of the satellite's range, ρ, azimuth, β, elevation, el, and range rate, $\dot{\rho}$. Range is a measure of the distance from the radar to the satellite. Range rate is a measure of the velocity magnitude and is the time rate of change of the range. Azimuth is the angle of

the position vector measured clockwise from North and elevation is measured up from the local horizon [14:81].

To update an orbit estimate, the predicted state is transformed to a predicted observation and compared against an actual observation as in Equation 3.10. Define the actual observation vector reported from the radar as

$$\mathbf{y} = \begin{bmatrix} \rho & \beta & el & \dot{\rho} \end{bmatrix}^T \tag{3.22}$$

This dissertation is primarily focused with ground-based radars and considers only Equation 3.22 for observation vectors; however, the approaches developed can incorporate any sensor type and observation vector.

3.8 State to Observation

To update the state estimate with information from the radar observation, it is necessary to transform the state to an estimated observation vector, $\hat{\mathbf{y}}$. Define a function G to represent all operations necessary to convert the state to an observation. The state is converted to an observation using a series of equations [12:269]. First, rotate the state in inertial coordinates to ECEF.

$$\begin{bmatrix} \hat{\mathbf{r}}_{sat,ECEF} \\ \cdots \\ \hat{\mathbf{v}}_{sat,ECEF} \end{bmatrix} = \bar{\mathbf{x}}_{ECEF} = \begin{bmatrix} \mathbf{ROT}_{ECI \to ECEF} & 0 \\ \dot{\mathbf{ROT}}_{ECI \to ECEF} & \mathbf{ROT}_{ECI \to ECEF} \end{bmatrix} \bar{\mathbf{x}}_{ECI} \tag{3.23}$$

Next, create a full state observation vector in ECEF.

$$\widetilde{\boldsymbol{\rho}}_{ECEF} = \begin{bmatrix} \hat{\mathbf{r}}_{sat,ECEF} - \mathbf{r}_{site,ECEF} \\ \hat{\mathbf{v}}_{sat,ECEF} \end{bmatrix} \tag{3.24}$$

where $\mathbf{r}_{site,ECEF}$ is the position vector from the center of the Earth to the ground site. Define this position vector using the Earth's equatorial radius, $R_\oplus$, and the eccentricity of the Earth,

$e_\oplus$; both known constants.

$$C_\oplus = \frac{R_\oplus}{\sqrt{1 - e_\oplus^2}} \qquad S_\oplus = C_\oplus \left(1 - e_\oplus^2\right)$$

$$r_\delta = \left(C_\oplus + h_{ellp}\right) \cos\left(\phi_{gd}\right) \qquad r_K = \left(S_\oplus + h_{ellp}\right) \sin\left(\phi_{gd}\right)$$

$$\mathbf{r}_{siteECEF} = \begin{bmatrix} r_\delta \cos\left(\lambda_{long}\right) \\ r_\delta \sin\left(\lambda_{long}\right) \\ r_K \end{bmatrix} \tag{3.25}$$

and h_{ellp} is the height of the ground site above the reference Earth ellipsoid [12:426].

Next, rotate this vector into the SEZ frame.

$$\widetilde{\boldsymbol{\rho}}_{SEZ} = \begin{bmatrix} \mathbf{ROT}_{ECEF \to SEZ} & 0 \\ 0 & \mathbf{ROT}_{ECEF \to SEZ} \end{bmatrix} \widetilde{\boldsymbol{\rho}}_{ECEF} \tag{3.26}$$

Define the vector elements of $\widetilde{\boldsymbol{\rho}}_{SEZ}$.

$$\widetilde{\boldsymbol{\rho}}_{SEZ} = \begin{bmatrix} \boldsymbol{\rho}_{SEZ} \\ \dots \\ \dot{\boldsymbol{\rho}}_{SEZ} \end{bmatrix} = \begin{bmatrix} \rho_S & \rho_E & \rho_Z & \dot{\rho}_S & \dot{\rho}_E & \dot{\rho}_Z \end{bmatrix}^T \tag{3.27}$$

For ease of notation, define a new variable.

$$\varpi = \boldsymbol{\rho}_{SEZ} \cdot \dot{\boldsymbol{\rho}}_{SEZ} \tag{3.28}$$

Perform the final operations to determine the predicted observation.

$$\hat{\mathbf{y}} = \begin{bmatrix} \sqrt{\rho_S^2 + \rho_E^2 + \rho_Z^2} \\ \tan^{-1}\left(\frac{-\rho_E}{\rho_S}\right) \\ \sin^{-1}\left(\frac{\rho_Z}{\rho}\right) \\ \frac{\varpi}{\rho} \end{bmatrix} \tag{3.29}$$

To implement an EKF, it is necessary to take partial derivatives of all operations and rotations in the state to observation transformation. Define the partials as matrix $\mathbf{H}$.

$$\mathbf{H} = \frac{\partial \hat{\mathbf{y}}}{\partial \widetilde{\boldsymbol{\rho}}_{SEZ}} \frac{\partial \widetilde{\boldsymbol{\rho}}_{SEZ}}{\partial \widetilde{\boldsymbol{\rho}}_{ECEF}} \frac{\partial \widetilde{\boldsymbol{\rho}}_{ECEF}}{\partial \overline{\mathbf{x}}_{ECEF}} \frac{\partial \overline{\mathbf{x}}_{ECEF}}{\partial \overline{\mathbf{x}}_{ECI}} \tag{3.30}$$

$$\frac{\partial \overline{\mathbf{x}}_{ECEF}}{\partial \overline{\mathbf{x}}_{ECI}} = \begin{bmatrix} \mathbf{ROT}_{ECI \to ECEF} & 0 \\ \dot{\mathbf{ROT}}_{ECI \to ECEF} & \mathbf{ROT}_{ECI \to ECEF} \end{bmatrix} \tag{3.31}$$

$$\frac{\partial \widetilde{\boldsymbol{\rho}}_{ECEF}}{\partial \overline{\mathbf{x}}_{ECEF}} = \mathbf{I} \tag{3.32}$$

where $\mathbf{I}$ is a 6-D identity matrix.

$$\frac{\partial \widetilde{\boldsymbol{\rho}}_{SEZ}}{\partial \widetilde{\boldsymbol{\rho}}_{ECEF}} = \begin{bmatrix} \mathbf{ROT}_{ECEF \to SEZ} & 0 \\ 0 & \mathbf{ROT}_{ECEF \to SEZ} \end{bmatrix} \tag{3.33}$$

Define $\frac{\partial \hat{\mathbf{y}}}{\partial \widetilde{\boldsymbol{\rho}}_{SEZ}}$ as a 4 x 6 matrix using two matrix variables.

$$\frac{\partial \hat{\mathbf{y}}}{\partial \widetilde{\boldsymbol{\rho}}_{SEZ}} = \begin{bmatrix} \boldsymbol{\Upsilon} & \boldsymbol{\Omega} \end{bmatrix} \tag{3.34}$$

$$\boldsymbol{\Upsilon} = \begin{bmatrix} \frac{\rho_S}{\rho} & \frac{\rho_E}{\rho} & \frac{\rho_Z}{\rho} \\ \frac{\rho_E}{\rho_E^2 + \rho_S^2} & \frac{-\rho_S}{\rho_E^2 + \rho_S^2} & 0 \\ -\frac{\rho_S \rho_Z}{\rho^2 \sqrt{\rho^2 - \rho_Z^2}} & -\frac{\rho_E \rho_Z}{\rho^2 \sqrt{\rho^2 - \rho_Z^2}} & \frac{\sqrt{\rho^2 - \rho_Z^2}}{\rho^2} \\ \frac{\dot{\rho}_S}{\rho} - \frac{\rho_S \varpi}{\rho^3} & \frac{\dot{\rho}_E}{\rho} - \frac{\rho_E \varpi}{\rho^3} & \frac{\dot{\rho}_Z}{\rho} - \frac{\rho_Z \varpi}{\rho^3} \end{bmatrix} \tag{3.35}$$

$$\boldsymbol{\Omega} = \begin{bmatrix} 0 & 0 & 0 \\ 0 & 0 & 0 \\ 0 & 0 & 0 \\ \frac{\rho_S}{\rho} & \frac{\rho_E}{\rho} & \frac{\rho_Z}{\rho} \end{bmatrix} \tag{3.36}$$

3.9 Initial Orbit Determination

The BLS and KF methods require an initial state estimate. For orbit estimation, this requires defining an initial position and velocity. When no prior information is known

about a tracked object, an IOD is performed to determine the initial state. For closely spaced observations, the Herrick-Gibbs IOD method uses a Taylor series to estimate an initial state, $\mathbf{v}_2$, given: $\mathbf{r}_1, \mathbf{r}_2, \mathbf{r}_3$, and the time lapse between each vector, Δt_{ji} [12:457-463]

$$
\begin{aligned}
\mathbf{v}_2 = &-\Delta t_{32} \left(\frac{1}{\Delta t_{21} \Delta t_{31}} + \frac{\mu_\oplus}{12 r_1^3} \right) \mathbf{r}_1 + \Delta t_{21} \left(\frac{1}{\Delta t_{32} \Delta t_{31}} + \frac{\mu_\oplus}{12 r_3^3} \right) \mathbf{r}_3 \\
&+ (\Delta t_{32} - \Delta t_{21}) \left(\frac{1}{\Delta t_{21} \Delta t_{32}} + \frac{\mu_\oplus}{12 r_2^3} \right) \mathbf{r}_2
\end{aligned}
\tag{3.37}
$$

This approach is used throughout the research and requires transforming a radar observation into a position vector. Performing the reverse of the operations in Section 3.8 a satellite position is determined from a radar observation.

$$
\boldsymbol{\rho}_{SEZ} = \begin{bmatrix} -\rho \cos(el) \cos(\beta) \\ \rho \cos(el) \sin(\beta) \\ \rho \sin(el) \end{bmatrix}
\tag{3.38}
$$

$$
\boldsymbol{\rho}_{ECEF} = \mathbf{ROT}_{SEZ \to ECEF} (\boldsymbol{\rho}_{SEZ})
\tag{3.39}
$$

$$
\mathbf{r}_{sat,ECEF} = \mathbf{r}_{siteECEF} + \boldsymbol{\rho}_{ECEF}
\tag{3.40}
$$

$$
\mathbf{r}_{sat,ECI} = \mathbf{ROT}_{ECEF \to ECI} \mathbf{r}_{sat,ECEF}
\tag{3.41}
$$

3.10 Estimation Algorithms

In estimation routines, measurements are weighted based on their accuracy. This information is captured in the matrix $\mathbf{R}$. As discussed in Section 3.3, it is assumed that each measurement error is uncorrelated and distributed $\mathcal{N} \sim \left(0, \sigma^2\right)$. Define the observation error matrix for the observation vector $\mathbf{y}$ defined in Equation 3.22 as

$$
\mathbf{R} = \begin{bmatrix} \sigma_\rho^2 & 0 & 0 & 0 \\ 0 & \sigma_\beta^2 & 0 & 0 \\ 0 & 0 & \sigma_{el}^2 & 0 \\ 0 & 0 & 0 & \sigma_{\dot\rho}^2 \end{bmatrix}
\tag{3.42}
$$

Estimation routines such as KFs and BLS filters were derived as least squares error solutions. The methods are composed of two parts: propagation and update. Each method

46

propagates an orbital state and covariance. Then, the errors between the actual observation and the predicted observation are minimized. This result is then used to update the state and covariance estimate. The KF and BLS filters solve the minimization problems by inverting different matrices [13:101]. The BLS filter uses an iterative process to determine the initial covariance matrix at an epoch, while the EKF and UKF sequentially solve for a new state and covariance as each observation is processed. Table 3.1 highlights the differences between each SOD algorithm.

Table 3.1: SOD Filter Characteristics

Filter	Obs Processing	$\mathbf{x}$ & $\mathbf{P}$ Update	Linearize G	Estimate with STM
BLS	Batch	At epoch	Yes	$\mathbf{x}_0$ and $\mathbf{P}_0$
EKF	Each ob	Each time step	Yes	$\mathbf{x}_i$ and $\mathbf{P}_i$
UKF	Each ob	Each time step	No	None

3.10.1 *Batch Least Squares Filter.*

The BLS process is also referred to as a Bayes' filter and applies the solution of the nonlinear least squares method in repetition to process data, provide state estimates, and produce covariance estimates at epoch times. To begin the process a state reference is required, $\mathbf{x}_{ref,0}$ at time t_0, and represents the initial conditions at a specific epoch. Additional initial conditions of the covariance $\mathbf{P}_0$ are utilized by the filter but not necessary. The BLS filter for orbit estimation is provided in Algorithm 2 and the specifics of each variable are discussed in Section 3.2 and Section 3.8 [14:196-199].

The BLS filter is iterative and requires a convergence criteria to exit the loop and determine a state and covariance solution. The reference orbit, $\mathbf{x}_{ref,t}$, differs from the unknown theoretical true state by a state error, $\delta\mathbf{x}$. Given the assumption that $\delta\mathbf{x}$ is small, the variations of parameters approach is used to approximate the observation residual. Using the STM, propagate the error at the epoch to the observation and correlate the residual to

47

Algorithm 2: Batch Least Squares Filter [14:196-199]

---

1 Propagate state and covariance (if known) to an epoch t_0 resulting in $\mathbf{P}_0, \mathbf{x}_{ref,0}$

2 Set $\mathbf{\Lambda} = \mathbf{P}_0^{-1}$ and $\mathbf{\Xi} = 0$; **if** $\mathbf{P}_0$ unknown **then** $\mathbf{\Lambda} = 0$

3 Read in the next observation: $t_i, \mathbf{y}_i, \mathbf{R}_i$

4 Propagate reference trajectory $\mathbf{x}_{ref,i-1}$ to t_i and calculate $\mathbf{x}_{ref,i}$ and $\mathbf{\Phi}(t_i, t_0)$

    Initial condition: $\mathbf{x}_{ref,i-1}$ Differential equation: $\dot{\mathbf{x}}_{ref} = f(\mathbf{x}, t)$

    Initial condition: $\mathbf{\Phi}(t_{i-1}, t_0)$ Differential equation: $\dot{\mathbf{\Phi}} = \left[\frac{f(\mathbf{x},t)}{\partial \mathbf{x}}\right]\mathbf{\Phi}(t, t_0)$

5 Accumulate observations:

$$\mathbf{H}_i = \left[\frac{\partial G\left(\mathbf{x}_{ref,i}, t_i\right)}{\partial \mathbf{x}}\right] \qquad \mathbf{\nu}_i = \mathbf{y}_i - G\left(\mathbf{x}_{ref,i}, t_i\right)$$

$$\mathbf{T}_i = \mathbf{H}_i \mathbf{\Phi}(t_i, t_0) \qquad \mathbf{\Lambda} = \mathbf{\Lambda} + \left(\mathbf{T}_i^T \mathbf{R}_i^{-1} \mathbf{T}_i\right) \qquad \mathbf{\Xi} = \mathbf{\Xi} + \mathbf{T}_i^T \mathbf{R}_i^{-1} \mathbf{\nu}_i$$

6 Return to step 3; increment counter ($i = i + 1$), continue until last observation

    ($i = N$)

7 Solve: $\hat{\mathbf{P}}_0 = \mathbf{\Lambda}^{-1}$ $\delta\hat{\mathbf{x}}_0 = \hat{\mathbf{P}}_0 \mathbf{\Xi}$

8 **if** converged **then** set epoch state and covariance estimate:

    $\hat{\mathbf{x}}_0 = \mathbf{x}_{ref,0} + \delta\hat{\mathbf{x}}_0$ $\hat{\mathbf{P}}_0 = \hat{\mathbf{P}}_0$

    else update $\mathbf{x}_{ref,0} = \mathbf{x}_{ref,0} + \delta\hat{\mathbf{x}}_0$ and $\mathbf{P}_0 = \hat{\mathbf{P}}_0$; return to step 1.

---

the initial error [13:69]

$$\delta\mathbf{x}_k = \mathbf{\Phi}(t_k, t_0)\,\delta\mathbf{x}_0 \tag{3.43}$$

$$\mathbf{\nu}_k = \mathbf{y}_k - G\left(\mathbf{x}_{ref}, t_k\right) \approx \mathbf{H}_k \delta\mathbf{x}_k = \mathbf{H}_k \mathbf{\Phi}(t_k, t_0)\,\delta\mathbf{x}_0 \tag{3.44}$$

Next, define the best estimate of the observation error at any point

$$\hat{\mathbf{e}}_i = \mathbf{\nu}_i - \mathbf{H}_i \delta\mathbf{x}_i \tag{3.45}$$

Then, define the Root Mean Squared (RMS) error as

$$RMS = \sqrt{\frac{\sum_{i=1}^{N} \hat{\mathbf{e}}_i^T \mathbf{R}^{-1} \hat{\mathbf{e}}_i}{M}} \tag{3.46}$$

48

where N is the total number of observation vectors in the batch, m is the number of measurements in the observation vector, $M = Nm$ where M is the total number of measurements in the batch, and $\hat{\mathbf{e}}_i$ and $\boldsymbol{\nu}_i$ are $m \times 1$ vectors [14:198]. Two convergence criteria used are to terminate the loop when the RMS error is below a threshold or when the RMS difference between two successive iterations is below a threshold.

3.10.2 *Extended Kalman Filter.*

The EKF solves the nonlinear least squares problem at the time of each observation and uses the propagation and update steps to estimate an orbital state and covariance. Similar to the BLS filter, the EKF linearizes the dynamics and observation to state transformation. The orbit estimation EKF is provided in Algorithm 3 [14:212].

Algorithm 3: Extended Kalman Filter [14:212]

1 Define or update previous reference: $\hat{\mathbf{P}}_0, \hat{\mathbf{x}}_0$

2 Read in the next observation: $t_i, \mathbf{y}_i, \mathbf{R}_i$

3 Propagate state from t_{i-1} to t_i to determine $\overline{\mathbf{x}}_i$ and $\boldsymbol{\Phi}(t_i, t_{i-1})$

    Initial condition: $\hat{\mathbf{x}}_{i-1}$ Differential eq: $\dot{\mathbf{x}} = f(\mathbf{x}, t)$

    Initial condition: $\boldsymbol{\Phi}(t_{i-1}, t_{i-1}) = \mathbf{I}$ Differential eq: $\dot{\boldsymbol{\Phi}} = \left[\frac{f(\mathbf{x},t)}{\partial \mathbf{x}}\right] \boldsymbol{\Phi}(t, t_{i-1})$

4 Update covariance:

    $\overline{\mathbf{P}}_i = \boldsymbol{\Phi}(t_i, t_0)\hat{\mathbf{P}}_{i-1}\boldsymbol{\Phi}(t_i, t_0)^T + \mathbf{Q}_i$

5 Accumulate observations finding partial derivatives and residuals:

    $\mathbf{H}_i = \left[\frac{\partial G(\overline{\mathbf{x}}_i, t)}{\partial \mathbf{x}}\right]$ $\boldsymbol{\nu}_i = \mathbf{y}_i - G(\overline{\mathbf{x}}_i, t_i)$

6 Calculate observation covariance and maneuver metric:

    $\mathbf{S}_i = \mathbf{H}_i \overline{\mathbf{P}}_i \mathbf{H}_i^T + \mathbf{R}_i$ $\Psi_i = \boldsymbol{\nu}_i^T (\mathbf{S}_i)^{-1} \boldsymbol{\nu}_i$

7 Calculate Kalman gain; estimate state and covariance:

    $\mathbf{K}_i = \overline{\mathbf{P}}_i \mathbf{H}_i^T (\mathbf{S}_i)^{-1}$ $\hat{\mathbf{x}}_i = \overline{\mathbf{x}}_i + \mathbf{K}_i \boldsymbol{\nu}_i$ $\hat{\mathbf{P}}_i = (\mathbf{I} - \mathbf{K}_i \mathbf{H}_i) \overline{\mathbf{P}}_i$

8 Return to step 1, process next observation

3.10.3 Unscented Kalman Filter.

Julier and Uhlmann invented the UKF as an improved method to estimate transformations that are poorly represented by a linearized EKF [30]. The UKF uses sigma points to estimate a transform instead of finding partials and linearizing the transform as is done with an EKF. The UKF implements the UT in the KF estimation routine.

3.10.3.1 Unscented Transform.

The UT uses 13 sigma points to transform a mean and covariance and preserves the first two moments of a distribution (mean and covariance) [32]. There are different scaling factors and weighting approaches to consider when using the UT. In general, the UT is one method of a general numerical integration. Quadrature methods use sample points and weights to evaluate an integral and different sampling schemes can preserve a specified number of moments. Besides the UT, other point sampling methods include Monte Carlo, Gaussian-Hermite Quadrature, and Conjugate Unscented transforms [89; 151]. Since the first two moments are of most interest for orbit determination, only the UT is considered in this dissertation.

The UT has two common weighting methods. The first approach is referred to as the symmetric method [32]. The symmetric weighting method requires defining the number of dimensions, $n = 6$, and also declaring a value for κ. Symmetric weights are calculated using the following equations

$$w_m^0 = w_c^0 = \frac{\kappa}{n + \kappa} \tag{3.47}$$

$$w_m^{(j)} = w_c^{(j)} = \frac{1}{2(n + \kappa)} \quad \text{for } j = 1, .., 2n \tag{3.48}$$

For normal distributions, it is possible to match fourth order terms if $\kappa + n = 3$; therefore, $\kappa = -3$ is recommended for orbital elements [32]. The UT formulation does not allow for complex sigma points; therefore, a lower bound exists and $\kappa > -n$. The second weighting method requires defining additional terms [34]. The additional parameter method uses tuning parameters: $\alpha, \gamma,$ and λ. Define α only on the interval $0 < \alpha \leq 1$. Allow

50

γ to take on any real value. Finally, λ can only take on values that generate real sigma points; therefore, $\lambda > -n$. The additional weighting scheme is outlined in the following equations

$$\kappa = \alpha^2 (n + \lambda) - n \tag{3.49}$$

$$w_m^0 = \frac{\kappa}{n + \kappa} \tag{3.50}$$

$$w_c^0 = \frac{\kappa}{n + \kappa} + \left(1 - \alpha^2 + \gamma\right) \tag{3.51}$$

$$w_m^{(j)} = w_c^{(j)} = \frac{1}{2 (n + \kappa)} \quad \text{for} \ \ j = 1, .., 2n \tag{3.52}$$

For the UKF a STM is not used during propagation as the UT estimates the propagated mean and covariance. The UT requires taking the square root of the covariance matrix. For a symmetric, positive definite matrix (which an orbital covariance is by definition) this operation is performed via a Cholesky decomposition [18:117-118]. The UKF for orbit estimation is detailed in Algorithm 4 [31:447-452].

3.10.4 Interacting Multiple Model.

In an effort to combine the estimates of several models, Blom and Bar-Shalom designed the IMM [84]. The IMM combines the inputs of multiple models and weights each model's contribution to the solution based on the residual likelihood. In this research, the IMM is implemented to determine the resulting solution from banks of EKFs and UKFs processing observations. To formulate a general IMM, consider N total models are provided at time $t_i = t_0$. Each kth model has an initial probability $\mathbf{w}_i^k$. Each model also has an initial state, $\hat{\mathbf{x}}_i^k$, and covariance, $\hat{\mathbf{P}}_i^k$. In the original formulation, there is a square matrix, $\mathbf{Pr}_{j|k}$, that is defined to contain memoryless static mixing probabilities of transition from model j to k at each time step. This matrix is determined a priori and requires knowledge on the probability of transitioning between models. This matrix is not updated with any residual information, but instead represents a heuristic-based approach on the potential for

---

Algorithm 4: Unscented Kalman Filter [31:447-452]

Given: κ, w_m^j and w_c^j for $j = 1, .., 2n$

1 Define or update previous reference: $\hat{\mathbf{P}}_0, \hat{\mathbf{x}}_0$

2 Read in the next observation: $t_i, \mathbf{y}_i, \mathbf{R}_i$

3 Perform decomposition $\mathbf{P}_{i-1} = \mathbf{A}^T \mathbf{A}$; denote $\mathbf{a}^{(j)}$ as column $j = 1, .., n$ of $\mathbf{A}$

4 Calculate sigma points:

$$\widetilde{\mathbf{x}}_{i-1}^{(j)} = \mathbf{x}_{i-1} + \breve{\mathbf{x}}^{(j)} \quad \text{for } j = 0, .., 2n \qquad \breve{\mathbf{x}}^{(0)} = 0$$

$$\breve{\mathbf{x}}^{(j)} = \mathbf{a}^{(j)} \sqrt{n+\kappa} \quad \text{for } j = 1, .., n \qquad \breve{\mathbf{x}}^{(n+j)} = -\mathbf{a}^{(j)} \sqrt{n+\kappa} \quad \text{for } j = 1, .., n$$

5 Propagate all sigma points using numerical integration:

Initial condition: $\widetilde{\mathbf{x}}_{i-1}^{(j)}$ Differential eq: $\dot{\mathbf{x}} = f(\mathbf{x}, t)$ Integration results: $\widetilde{\mathbf{x}}_i^{(j)}$

6 Calculate propagated state and covariance:

$$\overline{\mathbf{x}}_i = \sum_{j=0}^{2n} w_m^{(j)} \widetilde{\mathbf{x}}_i^{(j)} \qquad \overline{\mathbf{P}}_i = \sum_{j=0}^{2n} w_c^{(j)} \left(\widetilde{\mathbf{x}}_i^{(j)} - \overline{\mathbf{x}}_i\right)\left(\widetilde{\mathbf{x}}_i^{(j)} - \overline{\mathbf{x}}_i\right)^T + \mathbf{Q}_i$$

$$\overline{\mathbf{C}}_i = \sum_{j=0}^{2n} w_c^{(j)} \left(\widetilde{\mathbf{x}}_{i-1}^{(j)} - \hat{\mathbf{x}}_{i-1}\right)\left(\widetilde{\mathbf{x}}_i^{(j)} - \overline{\mathbf{x}}_i\right)^T$$

7 Transform sigma points and calculate predicted observation

$$\widetilde{\mathbf{y}}_i^{(j)} = G\left(\widetilde{\mathbf{x}}_i^{(j)}, t_i\right) \qquad \hat{\mathbf{y}}_i = \sum_{j=0}^{2n} w_m^{(j)} \widetilde{\mathbf{y}}_i^{(j)}$$

8 Calculate predicted observation covariance, residuals, and Ψ:

$$\mathbf{S}_i = \sum_{j=0}^{2n} w_c^{(j)} \left(\widetilde{\mathbf{y}}_i^{(j)} - \hat{\mathbf{y}}_i\right)\left(\widetilde{\mathbf{y}}_i^{(j)} - \hat{\mathbf{y}}_i\right)^T + \mathbf{R}_i$$

$$\boldsymbol{\nu}_i = \mathbf{y}_i - \hat{\mathbf{y}}_i \qquad\qquad \Psi_i = \boldsymbol{\nu}_i^T \left(\mathbf{S}_i\right)^{-1} \boldsymbol{\nu}_i$$

9 Use Kalman Filter equations to update estimates:

$$\mathbf{V}_i = \sum_{j=0}^{2n} w_c^{(j)} \left(\widetilde{\mathbf{x}}_i^{(j)} - \overline{\mathbf{x}}_i\right)\left(\widetilde{\mathbf{y}}_i^{(j)} - \hat{\mathbf{y}}_i\right)^T \qquad\qquad \mathbf{K}_i = \mathbf{V}_i \left(\mathbf{S}_i\right)^{-1}$$

$$\hat{\mathbf{x}}_i = \overline{\mathbf{x}}_i + \mathbf{K}_i \boldsymbol{\nu}_i \qquad\qquad\qquad\qquad \hat{\mathbf{P}}_i = \overline{\mathbf{P}}_i - \mathbf{K}_i \mathbf{S}_i \mathbf{K}_i^T$$

10 Return to step 1, process next observation

---

transition. The IMM approach is provided in Algorithm 5. For the orbit estimation of a maneuvering spacecraft, each model consists of a KF from Algorithms 3 and 4.

Algorithm 5: Interacting Multiple Model [84]

---

1 Determine mixing probabilities at time of next observation t_i

$$\bar{\mathbf{c}}_k = \sum_{j=1}^{N} \mathbf{Pr}_{j|k}\mathbf{w}_{i-1}^{j} \text{ for each model } k \text{ up to } N \text{ total}$$

$$\mathbf{w}_{i-1}^{j|k} = \frac{1}{\bar{\mathbf{c}}_k}\mathbf{Pr}_{j|k}\mathbf{w}_{i-1}^{j} \text{ for all } N^2 \text{ model combinations}$$

2 Determine mixed state and covariance for each model k up to N

$$\widetilde{\mathbf{x}}_{i-1}^{k} = \sum_{j=1}^{N} \hat{\mathbf{x}}_{i-1}^{j}\mathbf{w}_{i-1}^{j|k}$$

$$\widetilde{\mathbf{P}}_{i-1}^{k} = \sum_{j=1}^{N} \mathbf{w}_{i-1}^{j|k}\left\{\hat{\mathbf{P}}_{i-1}^{j} + \left[\hat{\mathbf{x}}_{i-1}^{j} - \widetilde{\mathbf{x}}_{i-1}^{k}\right]\left[\hat{\mathbf{x}}_{i-1}^{j} - \widetilde{\mathbf{x}}_{i-1}^{k}\right]^{T}\right\}$$

3 Input $\widetilde{\mathbf{x}}_{i-1}^{k}$ and $\widetilde{\mathbf{P}}_{i-1}^{k}$ into filter k, propagate and update each estimated state, covariance, residual, and predicted observation covariance: $\hat{\mathbf{x}}_{i}^{k}$, $\hat{\mathbf{P}}_{i}^{k}$, $\mathbf{\nu}_{i}^{k}$, and $\mathbf{S}_{i}^{k}$.

4 Update the modal probability for each model via the likelihood function

$$\Lambda_{i}^{k} = \mathcal{N}\left(\mathbf{\nu}_{i}^{k}; 0, \mathbf{S}_{i}^{k}\right) \qquad\qquad \mathbf{w}_{i}^{k} = \frac{\Lambda_{i}^{k}\bar{\mathbf{c}}_k}{\sum_{j=1}^{N}\Lambda_{i}^{j}\bar{\mathbf{c}}_j}$$

5 Calculate IMM estimate

$$\underline{\mathbf{x}}_i = \sum_{k=1}^{N} \hat{\mathbf{x}}_{i}^{k}\mathbf{w}_{i}^{k} \qquad\qquad \underline{\Psi}_i = \sum_{k=1}^{N} \mathbf{w}_{i}^{k}\Psi_{i}^{k}$$

$$\underline{\mathbf{P}}_i = \sum_{k=1}^{N} \mathbf{w}_{i}^{k}\left\{\hat{\mathbf{P}}_{i}^{k} + \left(\hat{\mathbf{x}}_{i}^{k} - \underline{\mathbf{x}}_i\right)\left(\hat{\mathbf{x}}_{i}^{k} - \underline{\mathbf{x}}_i\right)^{T}\right\}$$

6 Return to step 1, process next observation.

3.10.5   Smoothers.

As discussed in Chapter 2, the output of each KF is improved via a smoother that propagates backwards in time and modifies estimates. For the research herein, a fixed interval smoother is implemented and adapted for the EKF, UKF, and IMM orbit determination routines. Each epoch smoother begins at the end of a batch of filtered observations, L. At this point, the counter is defined as $i = L$ and the time of the last observation is defined as $t_i = t_L$. To begin the fixed interval smoother, set $\hat{\mathbf{P}}_{L}^{s} = \hat{\mathbf{P}}_L$ and $\hat{\mathbf{x}}_{L}^{s} = \hat{\mathbf{x}}_L$ where s represents a smoothed estimate. Next, work backwards to each observation

in the batch and solve for the smoothed state and covariance. The fixed interval EKF smoother uses the following equations [26]

$$\mathbf{Z} = \hat{\mathbf{P}}_{i-1} \mathbf{\Phi}(t_i, t_{i-1}) \overline{\mathbf{P}}_i^{-1} \tag{3.53}$$

$$\hat{\mathbf{x}}_{i-1}^s = \hat{\mathbf{x}}_{i-1} + \mathbf{Z}(\hat{\mathbf{x}}_i^s - \overline{\mathbf{x}}_i) \tag{3.54}$$

$$\hat{\mathbf{P}}_{i-1}^s = \hat{\mathbf{P}}_{i-1} + \mathbf{Z}\left(\hat{\mathbf{P}}_i^s - \overline{\mathbf{P}}_i\right)\mathbf{Z}^T \tag{3.55}$$

Continue propagating backwards until the start of the batch is reached and $t_{i-1} = t_0$. The UKF smoother is extremely similar, except that the definition for $\mathbf{Z}$ differs [152]

$$\mathbf{Z} = \overline{\mathbf{C}}_i \left(\overline{\mathbf{P}}_i\right)^{-1} \tag{3.56}$$

The IMM smoother requires more rigor. Begin by setting the smoother equivalent to the filter output at the last observation of the interval, $t_i = t_L$. For all N models set each kth model filter output equivalent to the smoother: $\mathbf{w}_L^{s^k} = \mathbf{w}_L^k$, $\hat{\mathbf{x}}_L^{s^k} = \hat{\mathbf{x}}_L^k$, and $\hat{\mathbf{P}}_L^{s^k} = \hat{\mathbf{P}}_L^k$. Also, set the overall IMM filter output equivalent to the IMM smoother: $\underline{\mathbf{x}}_L^s = \underline{\mathbf{x}}_L$ and $\underline{\mathbf{P}}_L^s = \underline{\mathbf{P}}_L$. Then, perform the operations in Algorithm 6 to implement an IMM mode matched smoother [82; 83].

3.10.6 Maneuver Detection.

If a spacecraft maneuvers unknowingly and a nominal filter is used to process observations, the residuals in Equation 3.10 will eventually reveal a maneuver occurred. There is a forward moving detection approach that can often times detect maneuvers faster by taking advantage of the relationship between post-maneuver covariance and residuals. The EKF, UKF, and IMM algorithms (Algorithms 3, 4, and 5) are adapted to track the magnitude of Ψ. This scalar determines whether or not the filter is properly capturing the system, modeling the dynamics, and generating normally-distributed residual vectors. Provided that the residual is zero mean (which it is) and using the predicted observation covariance, Ψ is the m dimensional Mahalanobis squared distance which is discussed in detail in Section 3.12.

Algorithm 6: Interacting Multiple Model Mode Matched Smoother [82; 83]

1 Calculate backwards transition probabilities

$$\bar{\mathbf{e}}_k = \sum_{j=1}^{N} \mathbf{Pr}_{j|k} \mathbf{w}_{i-1}^{j} \text{ for each model } k \text{ up to } N \text{ total}$$

$$\mathbf{B}_{j|k} = \frac{1}{\bar{\mathbf{e}}_k} \mathbf{Pr}_{j|k} \mathbf{w}_{i-1}^{j} \text{ for all } N^2 \text{ possibilities}$$

$$\bar{\mathbf{d}}_k = \sum_{j=1}^{N} \mathbf{B}_{j|k} \mathbf{w}_{i}^{s^j} \text{ for each model } k \text{ up to } N \text{ total}$$

$$\mathbf{w}_{i}^{s^{j|k}} = \frac{1}{\bar{\mathbf{d}}_j} \mathbf{B}_{j|k} \mathbf{w}_{i}^{s^j} \text{ for all } N^2 \text{ model combinations}$$

2 Calculate mode matched mixed smoothing:

$$\widetilde{\mathbf{x}}_i^{s^k} = \sum_{j=1}^{N} \hat{\mathbf{x}}_i^{s^j} \mathbf{w}_i^{s^{j|k}} \qquad\qquad \widetilde{\mathbf{P}}_i^{s^k} = \sum_{j=1}^{N} \mathbf{w}_i^{s^{j|k}} \left\{ \hat{\mathbf{P}}_i^{s^j} + \left[\hat{\mathbf{x}}_i^{s^j} - \widetilde{\mathbf{x}}_i^{s^k} \right] \left[\hat{\mathbf{x}}_i^{s^j} - \widetilde{\mathbf{x}}_i^{s^k} \right]^T \right\}$$

$$\mathbf{U}_{i-1}^k = \hat{\mathbf{P}}_{i-1}^k \mathbf{\Phi}_i^{k^T} \left(\bar{\mathbf{P}}_i^k \right)^{-1}$$

$$\hat{\mathbf{x}}_{i-1}^{s^k} = \hat{\mathbf{x}}_{i-1}^k + \mathbf{U}_{i-1}^k \left(\widetilde{\mathbf{x}}_i^{s^k} - \bar{\mathbf{x}}_i^k \right) \qquad\qquad \hat{\mathbf{P}}_{i-1}^{s^k} = \hat{\mathbf{P}}_{i-1}^k - \mathbf{U}_{i-1}^k \left(\widetilde{\mathbf{P}}_i^{s^k} - \bar{\mathbf{P}}_i^k \right) \left(\mathbf{U}_{i-1}^k \right)^T$$

3 Find smoothed mode probability:

$$\mathbf{\Lambda}_{i-1}^k = \sum_{j=1}^{N} \mathbf{Pr}_{j|k} \left(\mathcal{N} \left(\hat{\mathbf{x}}_i^{s^j} ; \bar{\mathbf{x}}_i^j, \bar{\mathbf{P}}_i^j \right) \right) \qquad\qquad \mathbf{w}_{i-1}^{s^k} = \frac{\mathbf{\Lambda}_{i-1}^k \mathbf{w}_{i-1}^k}{\sum\limits_{j=1}^{N} \mathbf{\Lambda}_{i-1}^j \mathbf{w}_{i-1}^j}$$

4 Estimate IMM smoothed state and covariance:

$$\underline{\mathbf{x}}_{i-1}^s = \sum_{k=1}^{N} \hat{\mathbf{x}}_{i-1}^{s^k} \mathbf{w}_{i-1}^{s^k} \qquad\qquad \underline{\mathbf{P}}_{i-1}^s = \sum_{k=1}^{N} \mathbf{w}_{i-1}^{s^k} \left\{ \hat{\mathbf{P}}_{i-1}^{s^k} + \left(\hat{\mathbf{x}}_{i-1}^{s^k} - \underline{\mathbf{x}}_{i-1}^s \right) \left(\hat{\mathbf{x}}_{i-1}^{s^k} - \underline{\mathbf{x}}_{i-1}^s \right)^T \right\}$$

5 Return to step 1; continue until $t_{i-1} = t_0$

A maneuver is declared within a forward moving KF or IMM once Ψ grows above a predefined level [57:421-488]. The scalar Ψ indicates how well the orbit is fit using filter predictions and radar observations. Once a maneuver occurs, the orbit changes and Ψ grows quickly highlighting a disparity between residuals and the covariance. Using Ψ for real-time spacecraft post-maneuver orbit determination and tracking is a focus of this dissertation for the filter-through process. Another detection routine leverages the backwards running smoother to detect maneuvers and is discussed further in Chapter 6.

3.10.7 *Covariance Inflation Adaptive Estimation.*

When using a sequential filter to track a spacecraft that performs an unanticipated maneuver, the residuals in Equation 3.10 clearly show a maneuver occurred, yet the state covariance, $\mathbf{P}$, remains unaffected. The filter has diverged and is no longer accurately tracking the spacecraft. After a maneuver is detected, increasing the filter's state covariance can prevent divergence. Using this approach, an MMAE routine can detect the maneuver with Ψ, filter-through unknown dynamics, and quickly re-converge on the orbital solution. There are two ways to inflate the state covariance after a maneuver. First, the process noise covariance, $\mathbf{Q}$, is adaptable to larger values that are added directly to the state covariance. Second, a direct method to increase the covariance is to multiply $\mathbf{P}$ by a constant, similar to a fading memory filter [47]. In Chapters 4, 5, and 6 the covariance is inflated using a multiplication constant ξ until the covariance grows to a desired size. The size of the covariance is measurable several ways including the trace, eigenvalues, and determinant. The logic for the filter-through inflation approach implemented for this research uses the trace due to its simplicity and effectiveness. The following logic is implemented to filter-through maneuvers for the single model cases as well to populate models within an IMM

$$\textbf{if } \ \Psi_i > \text{threshold} \ \textbf{ then } \ \overline{\mathbf{P}}_i = \xi\overline{\mathbf{P}}_i \ \textbf{ until } \ \text{trace}\left(\overline{\mathbf{P}}_i\right) > \text{threshold} \qquad (3.57)$$

When performing this logic with the UKF, it is necessary to recalculate the sigma points with the inflated covariance prior to updating any estimates. The two specific thresholds that determine when to declare a maneuver and how much to inflate the covariance are discussed in detail in subsequent chapters. As stated in the motivation, the research assumes that the post-maneuver observations are known to pertain to the satellite of interest; therefore, maneuvers in which $\Delta\mathbf{v} < 1$ *km/s* are the focus of this research.

3.11 Performance Analysis

When evaluating the abilities of any estimation routine, the true error between a known simulated solution and estimate is an effective way to quantify performance. The position and velocity errors at each observation time, t_i, are defined

$$RMS_r = \left|\hat{\mathbf{r}}_{est_i} - \mathbf{r}_{true_i}\right|_2 \qquad RMS_v = \left|\hat{\mathbf{v}}_{est_i} - \mathbf{v}_{true_i}\right|_2 \qquad (3.58)$$

Additionally, if the true location is not known, Ψ and the residuals serve as a method to evaluate the orbital fit.

In order to generalize the results to other orbital regimes besides LEO, consider describing the length of the pass as the percentage of the orbit. Define the orbital period

$$T = 2\pi \sqrt{\frac{a^3}{\mu_\oplus}} \qquad (3.59)$$

where a is the orbit's semi-major axis. Also, it is possible to normalize the thrust about a known spacecraft bus. The Orbital ATK A200 is a Responsive Space Modular Bus that houses the TacSat-3 mission which flies in a LEO orbit [153]. The bus is customizable for up to a 300 m/s $\Delta\mathbf{v}$ capacity. Define a maneuver in terms of its percentage of the ATK A200 capacity

$$\Delta\mathbf{v}_{norm} = \frac{\Delta\mathbf{v} \; m/s}{300 \; m/s} \qquad (3.60)$$

3.12 Covariance Realism

The output of an estimation routine is a multidimensional Gaussian with mean, $\boldsymbol{\mu}_{est}$, and covariance $\mathbf{P}_{est}$. A given state at time t_i is $\mathbf{x}_i \sim \mathcal{N}(\boldsymbol{\mu}_{est}, \mathbf{P}_{est})$. A proper estimation routine must preserve covariance realism such that the underlying error distribution is Gaussian and captured by the covariance. Often times, $\mathbf{P}$ is viewed as a 3-Dimensional position ellipsoid at a specified σ of the distribution.

Determining the probability of lying within a n-dimensional (n-D) Gaussian requires integrating the multidimensional pdf over the interval $[-p\sigma, \; p\sigma]$. The integration is

simplified by changing to the principal axis frame and transforming to the N-sphere via an axis scale change. Then, the integration becomes dependent on only the radius of the sphere [13:25-26]. The analytical solution of the integral provides the probability of lying within $p\sigma$ n-D ellipsoids. For the $n = 3$ and $n = 6$ dimension cases, the solutions are

$$Pr_3(p) = erf\left(\frac{p}{\sqrt{2}}\right) - \sqrt{\frac{2}{\pi}}pe^{-\frac{p^2}{2}} \tag{3.61}$$

$$Pr_6(p) = 1 - \frac{1}{8}e^{-\frac{p^2}{2}}\left(p^4 + 4p^2 + 8\right) \tag{3.62}$$

in which erf is the error function defined when integrating the normal distribution and is available in most numerical analysis packages. Table 3.2 describes the probabilities for common $p\sigma$ values.

Table 3.2: Probability Values Based on Dimensions

Dimensions	1σ	2σ	3σ	4σ	5σ
1	0.683	0.954	0.997	0.99994	0.9999994
3	0.199	0.739	0.971	0.9989	0.99998
6	0.014	0.323	0.826	0.986	0.9997

Achieving covariance realism involves a statistical test that uses the six dimensional probability, Equation 3.62, to determine if a set of points fits a Gaussian distribution [88]. Define a set of Monte Carlo state samples as $\mathbf{x}_{mc}$. The distance metric that is equivalent to $(p\sigma)^2$ is referred to as the squared Mahalanobis distance and defined for a single Gaussian as

$$\mathcal{M} = m^2 = (\mathbf{x}_{mc} - \boldsymbol{\mu})^T \mathbf{P}^{-1} (\mathbf{x}_{mc} - \boldsymbol{\mu}) \tag{3.63}$$

The first portion of the covariance realism metric uses the averaged Mahalanobis squared distance, $\bar{\mathcal{M}}$, of a set of samples and tests if $\bar{\mathcal{M}} \sim \frac{1}{nk}\chi^2(nk)$ where n is the dimension and k is the number of trials. The second (more stringent) covariance realism test uses the

Cramér-von Mises goodness of fit test statistic. Sorting the Mahalanobis squared distance of the samples, $\mathcal{M}_i$, from smallest to largest, the test evaluates

$$F(\mathcal{M}_i) = 1 - \frac{1}{8}e^{-\frac{\mathcal{M}_i}{2}}\left(\mathcal{M}_i^2 + 4\mathcal{M}_i + 8\right) \tag{3.64}$$

$$Q = \frac{1}{12} + \sum_{i=1}^{k}\left[\frac{2i-1}{2k} - F(\mathcal{M}_i)\right]^2 \tag{3.65}$$

in which i is the sorted sample number. Confidence interval bounds for specified sample sizes are available in the literature [87]. At times, a single Gaussian may not capture the underlying error distribution after a long propagation period. To implement the realism statistical tests, it is necessary to generalize the squared Mahalanobis distance. For any other type of distribution with a pdf defined as $f(\Theta)$ where Θ is a parameter set, the metric is generalized to

$$\mathcal{M}(\mathbf{x}_{mc}; \Theta) = -2\ln\left(\frac{f(\mathbf{x}_{mc}; \Theta)}{f(\hat{\mathbf{x}}; \Theta)}\right) \tag{3.66}$$

where $\hat{\mathbf{x}}$ is the mode such that

$$\hat{\mathbf{x}} = \operatorname{argmax}\ f(\mathbf{x}; \Theta) \tag{3.67}$$

Now, it is possible to sort the Mahalanobis squared distance of the samples from smallest to largest and test for realism using Equations 3.64 and 3.65 for any distribution.

Specifically, this realism test evaluates whether or not all the propagated Monte Carlo states fit the distribution predicted by the filter propagated state and state covariance. Just as this test measures the distance of points from a mean according to a covariance, so does Ψ. Within a Kalman Filter, the residuals are assumed zero mean Gaussian according to a predicted observation vector and observation covariance. Given that the orbit is properly fit, Ψ determines the "distance" of the predicted observation from the actual observation according to the predicted covariance. Therefore, when given a good observation vector and a large associated Ψ value, the orbit is no longer properly fit and a maneuver is detected.

59

3.13 Element Sets

In Equation 3.1, the ECI Cartesian state notation is presented as a way to represent the state and dynamics of spacecraft. All coordinate frames describing an orbit consist of six quantities. The Equinoctial orbital elements are described by the variables

$$\mathbf{x}_{Eq} = \begin{bmatrix} a & h & k & p_e & q_e & \ell \end{bmatrix}^T \tag{3.68}$$

For certain applications, Equinoctial elements are preferred over Cartesian as there is only one fast moving variable [154]. For the two-body orbital solution, all Equinoctial elements remain fixed except for the mean longitude angular variable, ℓ. The Equinoctial elements are a variation of the Classical Orbital Elements (COE). The COEs provide a visually appealing set of six quantities with only a single moving variable for the two body solution. Define the classical orbital elements as

$$\mathbf{x}_{COE} = \begin{bmatrix} a & e & i & \Omega & \omega & \upsilon \end{bmatrix}^T \tag{3.69}$$

The explanation of the elements are available in most astrodynamics textbooks [12:104-113]. The COEs suffer from inequalities in common orbits (circular, non-inclined). While difficult to visualize, the Equinoctial elements shift the undefined quantities to a true retrograde equatorial orbit. Some introduce a retrograde value into the equations to prevent a singularity all together [12:116-117]. Since no operational spacecraft fly in a non-inclined retrograde orbit, the Equinoctial elements are often preferred. To implement Equinoctial element formulations, it is necessary to freely transform states between all three coordinate systems.

Consider the function $F_{ECI \rightarrow Eq}$ that transforms an element set in Cartesian ECI to Equinoctial elements. The transformation is eased by using the COEs such that

$$\mathbf{x}_{Eq} = F_{COE \rightarrow Eq} \left(F_{ECI \rightarrow COE} \left(\mathbf{x}_{ECI} \right) \right) \tag{3.70}$$

The transformations between element sets are provided in Appendix A.

60

3.14 Perturbations

In Section 3.2, the two-body orbital solution is outlined. For precise applications, higher order physics models are applied to capture a more detailed set of dynamics. Short propagations are subject to perturbations, but these are relatively small compared to the dominant two-body accelerations. The special perturbations formulation adds additional accelerations in the dynamics to account for perturbation models. For simulations in Chapter 7, a J2 gravity and exponential drag atmosphere model is used to propagate the state and covariance

$$\dot{\mathbf{x}} = \left[\begin{array}{cccccc} v_I & v_J & v_K & -\frac{\mu_\oplus r_I}{r^3} + a_{pert_I} & -\frac{\mu_\oplus r_J}{r^3} + a_{pert_J} & -\frac{\mu_\oplus r_K}{r^3} + a_{pert_K} \end{array} \right]^T \tag{3.71}$$

The details for calculating $\mathbf{a}_{pert}$ for perturbation modeling are provided in astrodynamics texts [12:515-604]. There are also multiple available software orbit estimation routines with high-fidelity orbit propagators that use complex gravity, drag, and other perturbations models (Systems Tool Kit (STK), Orekit, OCEAN, etc.). In Chapter 9 when long propagation times are tested with large covariance solutions, the HPOP algorithm is used within STK for high-accuracy, high-fidelity perturbation modeling.

3.15 Pruning

Within an IMM, each model's solution is weighted when each observation is processed as discussed in Section 3.10.4. To prevent singularities in weighting and discard poor models, pruning operations are performed within the IMM. Pruning can prevent undue influence on the solution from a model that is clearly not capturing the dynamics. Pruning models is captured by the following logic

$$\textbf{if } \mathbf{w}_i^k < \text{tolerance, remove model } k \textbf{ set } N = N - 1; \text{ re-normalize weights} \tag{3.72}$$

Pruning logic is implemented within the IMM in Chapters 4 and 9.

3.16 Conclusion

This chapter reviewed all required supporting methodology for orbit estimation techniques that are applied to tracking maneuvering satellites in the next chapters. The methodology combines traditional orbit determination with current adaptive and multiple model estimation approaches. Overall, the methodology requires further tuning for certain applications and maneuver types. The baseline methodology is further improved and adapted in each subsequent chapter.

IV. Filter-Through Instantaneous Maneuvers with IMM

4.1 Introduction

For real-time tracking problems using sequential filtering, an unplanned change in dynamics corresponding to a maneuver may cause filter divergence. To compensate for this problem, MMAE approaches are used to handle changes in the dynamics, non-Gaussian noise, and estimate additional state parameters. Adaptive estimation allows models to change parameters based on collected observations and residuals. In this chapter, an approach is presented to use covariance inflation after an impulsive maneuver is detected to prevent filter divergence and re-converge on the new orbit all while progressing continually forward in time. This research effort provides a method to handle unplanned maneuvers in high-priority spacecraft tracking. It overcomes the shortfall of filter divergence and the need for post-processing reconstruction. Algorithms are implemented to detect the maneuver in real-time, inflate the state covariance, transition to an IMM and continually track the spacecraft. These techniques are designed to directly aide the SSA effort by providing a real-time tracking methodology for maneuvering spacecraft. Specifically, this chapter researches filtering-through an instantaneous maneuver that occurs with an unknown magnitude at an unknown time outside of view of the radar.

4.2 Covariance Inflation Interacting Multiple Model

Once the maneuver is detected, the covariance is inflated using several different thresholds. While the fading memory filter applies a constant level of process noise and the shotgun approach is implemented by periodically adding process noise covariance, this filter-through approach inflates the covariance and allows for filter re-convergence using the new data from the new orbit. The only cause of the filter divergence in this application is the presence of the unknown maneuver. Therefore, it is not necessary to continually inflate the

covariance as is done in fading memory approaches. Provided the maneuver is relatively small, only a single covariance inflation is needed; whereas, shotgunning adds noise at intervals to allow the filter to accept and process observations. For larger maneuvers, or for smaller maneuvers from spacecraft that have gone unobserved over long periods of time, additional process noise is required to prevent divergence and false detection of maneuvers.

Because the maneuver occurs outside of view, the maneuver is easy to detect using Ψ within an EKF as discussed in Chapter 3 and Algorithm 3. Once a maneuver is detected, a forward moving IMM is kicked off in which each model has the same dynamics but a differing covariance inflation threshold. This logic is captured in Algorithm 7. The details for the maneuver threshold and the covariance inflation limits, η^k, are discussed in 4.3.

Algorithm 7: Maneuver Detection Covariance Inflation IMM EKF

---

1 **if** $\Psi_i >$ maneuver threshold **then** begin covariance inflation IMM:

    for each model k to N **set**

        $\hat{\mathbf{x}}_i^k = \hat{\mathbf{x}}_i$ and $\hat{\mathbf{P}}_i^k = \hat{\mathbf{P}}_i$

        while $\mathrm{trace}\left(\hat{\mathbf{P}}_i^k\right) < \eta^k$: $\hat{\mathbf{P}}_i^k = 10\hat{\mathbf{P}}_i^k$

    else continue

2 Process next observation with IMM

In Algorithm 7, the initial states and covariances are defined for N models. The IMM provides a sub-optimal method to merge models. In this application, the model, k, with the best inflation covariance limit, η^k, is most heavily-weighted. As the IMM progresses forward in time and processes observations, certain models are weighted near zero when mixed to determine the overall IMM estimate. A pruning IMM discards unfit models as their estimates do not contribute to the overall estimate. Pruning assists in preventing unnecessary computations while preventing any divide by zero instances within the IMM

algorithm. Discarding unfit models is necessary in maneuver tracking if the overall IMM is broad and contains a large number of models. Since the maneuver size is unknown, the IMM must contain a wide-range of inflation covariance models to handle large and small state discrepancies. Therefore, when filtering-through smaller deviations, models suited for larger maneuvers are unfit and require pruning. The nominal IMM framework is updated with pruning capabilities for the covariance inflation filter-through approach as detailed in Equation 3.72. The nominal IMM is also modified to output the weighted maneuver detection metric, Ψ, which is necessary to continually check the IMM outputs for additional maneuvers or false positives (Algorithm 5).

4.2.1 Filter Process Noise Covariance Considerations.

Larger maneuvers require more than the initial covariance inflation for the filter-through approach. Without the inclusion of additional process noise, the filters tend to converge on an inaccurate solution or develop numerically unstable weights as each model in the IMM is very unlikely. To compensate for this issue, a tiered approach is developed to add process noise in a step-scale fashion. Remembering the trade-off between added process noise and reduced accuracy, the step-scale approach adds enough noise to allow the filter-through approach to handle large maneuvers, while reducing estimate errors. $\mathbf{Q}$ is a 6×6 diagonal matrix. The upper left 3×3 quadrant contains the diagonal matrix $q_r \cdot \mathbf{I}$ while the lower right 3×3 quadrant is composed of $q_v \cdot \mathbf{I}$.

$$\mathbf{Q} = \begin{bmatrix} q_r\mathbf{I} & 0 \\ 0 & q_v\mathbf{I} \end{bmatrix} \tag{4.1}$$

The maneuver detection metric, Ψ, provides a factor of the orbit fit prediction verses observation errors. If a maneuver is large or if a small maneuver occurred during a long observation gap, then Ψ increases in size accordingly. Therefore, it provides an ideal factor with which to scale additional process noise. The step scale approach is detailed in Algorithm 8.

Algorithm 8: Step Scale **Q** Application		
1	Given Ψ **set Q** from Table 4.1 **set** $t_q = t_i + \Delta q$	
2	Process observations until $t_i > t_q$	
	set Q $= 0.1 \cdot$ **Q** **reset** $t_q = t_i + \Delta q$ repeat step 2	

Table 4.1: **Q** Values Based on Ψ Bounds for Use in Algorithm 8

Ψ <	10^5	$5 \cdot 10^5$	10^6	$5 \cdot 10^6$	10^7	$5 \cdot 10^7$	10^8	$5 \cdot 10^8$	∞
Ψ ≥	0	10^5	$5 \cdot 10^5$	10^6	$5 \cdot 10^6$	10^7	$5 \cdot 10^7$	10^8	$5 \cdot 10^8$
q_r	0	0.05	0.1	0.5	1	5	10	50	100
q_v	0	$5 \cdot 10^{-5}$	10^{-4}	$5 \cdot 10^{-4}$	10^{-3}	$5 \cdot 10^{-3}$	0.01	0.05	0.1

The filter-through method for larger cases has a tendency to falsely detect maneuvers during the first observation after a coverage gap. The false detections are a result of the covariance propagation within the EKF and the solution quality after filtering-through a single post-maneuver pass. Ψ spikes when the first observation indicates a larger residual with a smaller covariance. Two ways to counter the false detections are to decrease the coverage gap or modify the covariance propagation over the gap. Since shortening the gap is often not an option, a covariance modification scheme is necessary. Once again, consideration is taken to inflate the covariance only as large as necessary to avoid increasing state errors. In the EKF in Algorithm 3 step 4, **Q** is added once during the propagation step. Given that **Q** $\neq 0$ (larger cases scale **Q** based on Algorithm 8) then **Q** is also scalable over coverage gaps to prevent false maneuver detections. Given the time of the coverage gap, t_{gap}, define

$$\mathbf{Q}_{gap} = \left(\frac{t_{gap}}{\tau} \cdot \xi_q \right) \mathbf{Q}_i \qquad (4.2)$$

where τ is a time constant to scale the length of the coverage gap and ξ_q is a scalar that determines the amount to increase the covariance. This approach purposefully uses the

current **Q** value, the covariance **P**, and the length of time without observations to mirror how a fading memory filter works [46:285-288]. Increasing the covariance over coverage gaps, Equation 4.2 modifies the fading memory filter for use in high-priority maneuvering spacecraft tracking. This method scales covariance inflation based on pass length, and prevents false detections while keeping state errors small.

4.3   Simulation

To test the reliability and performance of the filter-through covariance inflation IMM EKF for maneuvering spacecraft, many different orbits, maneuvers, and ground configuration scenarios are necessary. The primary focus of this research effort is tracking maneuvering LEO spacecraft. For each orbit configuration, 14 maneuvers are simulated and listed in Table 4.2 and the normalized thrust cases (Equation 3.60) are provided in Table 4.3. The maneuvers occur both in- and out-of-plane five seconds after the end of a pass. Maneuvers occur with varying magnitudes to modify the time and magnitude of the detection. The simulations consider four different combinations of orbit types: circular non-inclined, circular inclined at 98.1°, elliptical non-inclined, and elliptical inclined at 98.1°. Each of these four configurations are tested at eight different orbital altitudes each with an associated eccentricity as detailed in Table 4.4. The average percentage row of Table 4.4 captures the percentage of the total orbit observed during the average daily pass for the non-inclined elliptical cases. Passes under two minutes are removed from the average daily percentage calculation to prevent small passes from perturbing the metric. Finally, three different ground antenna configurations are evaluated: four sites, two sites, and a single site all placed at a 5° latitude and equally spaced longitudinally. In total, 14 different maneuvers are simulated with three different antenna configurations, four different orbit shapes, and eight different orbit altitudes resulting in 1344 simulation cases. The parameters are intentionally varied to test the IMM's abilities in handling delayed

detection of maneuvers for the small cases and filtering-through large deviations caused by substantial maneuvers.

Table 4.2: Scenario Maneuver Cases

In velocity dir (m/sec)	0.01	0.05	0.1	0.5	1	5	10
Out of plane (m/sec)	0.5	1	5	7.5	10	25	50

Table 4.3: Scenario Maneuver Cases Normalized $\Delta\mathbf{v}_{norm}$

In velocity dir	3.3×10^{-5}	1.7×10^{-4}	3.3×10^{-4}	0.0017	0.0033	0.017	0.033
Out of plane	0.0017	0.0033	0.0167	0.025	0.033	0.083	0.17

Table 4.4: Orbital Altitudes and Eccentricities

Altitude (km)	300	400	500	600	700	800	900	1000
Eccentricity	0.02	0.03	0.04	0.05	0.06	0.07	0.08	0.09
Period (min)	90.5	92.6	94.6	96.7	98.7	100.9	103.0	105.1
Avg. %	4.7	7.5	9.0	10.7	11.9	12.8	14.3	14.6

The two-body equations of motion are used, as in Equation 3.2, with RK 4 numerical propagation (Algorithm 1) to integrate the state. To simulate ground observations, perfect observations of range, azimuth, elevation, and range rate and perturbed with zero mean random noise. Simulating current radar capabilities the following standard deviation noise parameters are used: 5 m for range, $0.02°$ for azimuth and elevation, and 0.5 m/sec for range rate. Within Algorithm 3, **R** is populated with the noise variance along the diagonals. Each radar collects observations once every five seconds while the spacecraft is above $1°$ of elevation. This configuration allows for full collection of observations verses a small subset of three observations in a typical track. The tracking of high-priority spacecraft demands

an increase in the number of observations and the number of radar collections to prevent poor estimates.

Within the covariance inflation pruning IMM, initially 23 models are initiated with the following inflation values: $\eta_k = \{0.001, 0.005, 0.01, 0.05, 0.1, 0.5, 1, 5, 10, 50, 10^2, 5 \cdot 10^2, 10^3, 5 \cdot 10^3, 10^4, 5 \cdot 10^4, 10^5, 5 \cdot 10^5, 10^6, 5 \cdot 10^6, 10^7, 5 \cdot 10^7, 10^8\}$. The initial values for $\mathbf{w}_k$ are all set to 1/23 to allow for equal weighting of each possible inflation value. It is possible to add more or less models within the IMM, but for the test cases considered 23 was sufficient to span the ranges of necessary inflation values. Inflation values less than 0.001 are ineffective at adding enough uncertainty to converge on the new orbit, while values above 10^8 often result in too large of an inflation and numerical stability issues.

The matrix $\mathbf{Pr}_{j|k}$ is set to identity to allow each model weighting in the solution to pertain purely to its likelihood. The pruning model weight tolerance is set to 10^{-10} to remove any models that are clearly not contributing to the IMM weighted mean and covariance. To capture a wide-variety of maneuver types, a multitude of covariance inflation models are included within the IMM. Since the IMM prunes unfit models at every time step, models with much larger or smaller covariance inflation than necessary are thrown out within the first couple of observations. This wide-range prevents the need of directly solving for a suitable set of values, or singular inflation value based on some function of Ψ.

A threshold value of 30 is used with Ψ to detect a maneuver. This value is determined through testing and previous research efforts using the filter-through technique [155]. Out of the > 1000 scenarios run, the threshold of 30 was low enough to detect all maneuvers simulated and large enough to allow for only seven false positive detections of an early maneuver due to a large residual. After re-running all seven cases and re-simulating the added noise, the maneuver was detected at the proper time. If there is grave concern with

early false positives, raise the Ψ threshold; however, this in-turn results in delayed detection of smaller maneuvers.

Finally, for the larger maneuver cases, the descending step sizes of $\mathbf{Q}$ are selected according to Table 4.1. The Δq window size is set to 10 observations in Algorithm 8 and this value was determined through extensive testing. Choosing this step size decreases the number of false positives and instances of a numerically unstable IMM while reducing errors. For Equation 4.2, the values of $\tau = 40000$ s and $\xi_q = 10^5$ are set for similar reasons. The values are carefully selected based on testing with the discussed simulation cases and evaluating the trade-space between reducing errors and preventing false positives.

The simulations are designed to test the developed approach to filter-through a maneuver, converge on the new orbit, and minimize estimation errors. Since the true orbit is known, the metric used for comparison is RMS position and velocity errors as detailed in Equation 3.58. The filter estimate is the IMM state output and errors are summed over all post-maneuver observations.

As discussed in the Chapter 2, traditional methods for handling post-maneuver orbits include performing a new IOD which is later corrected by a BLS filter to update the epoch, and then an EKF is run across all observations. The purpose of the filter-through approach is to eliminate the need for performing a new IOD or updating past epochs as is done in the BLS. The BLS filter is dependent on the number of observations included in the routine. The more observations included, the more accurate the epoch update, and in turn the more accurate the EKF estimates. Even though the filter-through approach does not update epochs in an iterative fashion, it should still provide comparable accuracy. To evaluate the IMM's performance, the IOD $\rightarrow$ BLS $\rightarrow$ EKF approach is compared to the filter-through approach. The details of the IOD, BLS, and EKF routines are provided in Chapter 3. The IOD is run immediately after the maneuver is detected based on the same

Ψ logic, and the BLS filter considers all observations in the pass. The EKF begins with the state and covariance output from the BLS and runs until the end of the scenario.

4.4   Results

4.4.1   Covariance Analysis.

The orbit determination EKF quickly reduces the covariance when a full pass worth of observations are collected. In Figure 4.1, the largest and the smallest in-plane maneuvers are compared for the non-inclined circular case with two ground supporting antennas. By design, the larger maneuver requires greater covariance inflation, while the smaller maneuver requires less covariance inflation in the filter-through approach. The trace is one method to evaluate the size of the covariance matrix and it is plotted with a logarithmic scale on the ordinate in Figure 4.1. This evaluation reveals that the covariance decreases approximately an order of magnitude every pass. The responsiveness of the EKF to quickly reduce the covariance allows the IMM filter-through approach to re-converge on the orbit quickly and begin accurately estimating the true error in the states. Even with the added tiered process noise, the covariance for the large case still decreases quickly. This figure provides added confidence that the filter-through approach can quickly recover from the covariance inflation and return to smaller, more accurate levels of covariance. For both orbits, the pre-maneuver covariance trace is on the order of 10^{-5}, and for the smaller maneuver case this accuracy is achieved again after three post-pass orbits. For the larger case, pre-maneuver covariance levels are achieved after the fourth pass of observations.

It is not critical to drive the trace of the covariance as small as possible, but instead ensure consistency between the covariance and the residuals resulting from observations. Ψ is key in ensuring this consistency. When elevated, Ψ highlights the discontinuity between the covariance and the residuals. When driven low, there is stable agreement between the covariance and residuals. In Figure 4.2, Ψ is plotted for the two cases discussed in the

71
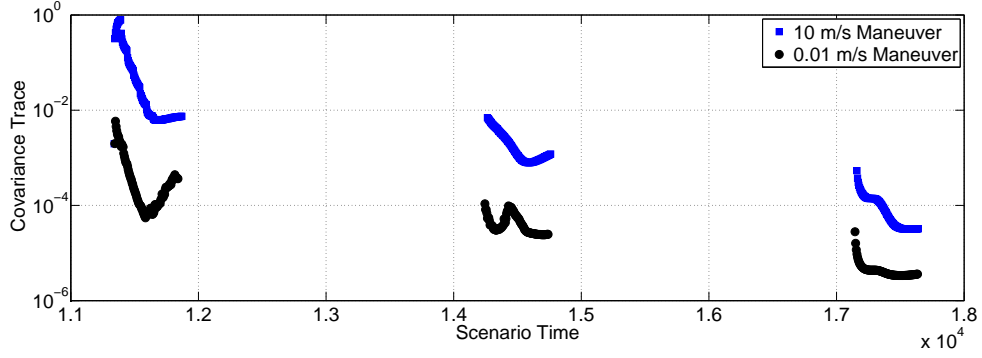
Figure 4.1: Post-Maneuver IMM Covariance

previous paragraph. The first post-maneuver pass is displayed in Figure 4.2 to highlight the covariance inflation effect on the maneuver detection metric. For the larger maneuver case, Ψ is initially much greater at the time the maneuver is detected. This relation is anticipated as the larger the maneuver, the greater the residuals, and the bigger Ψ grows. After the larger covariance inflation from the IMM, Ψ drops lower than the smaller maneuver case. Within the equation for Ψ, the covariance is inverted which results in smaller values of Ψ for larger inflations. The covariance inflation approach ensures consistency in the calculation for Ψ allowing the filter to re-converge on the proper orbit prior to greatly reducing the covariance. Approximately at the half way point of the pass, the values of Ψ reach the same order of magnitude for both cases. Although, the covariances are clearly different in Figure 4.1, both cases keep Ψ between 0 and 20 after quickly settling. Overall, Figure 4.2 shows how the covariance inflation filter-through approach quickly achieves a stable, consistent, and accurate estimate of the orbit.

4.4.2   IMM Analysis.

Within the IMM, the value of $\mathbf{w}^k$ determines the weight of the influence each model has on the total IMM state and covariance estimate. The mixture of a wide variation of Gaussian models within the IMM results in heavily weighting some models while quickly

72
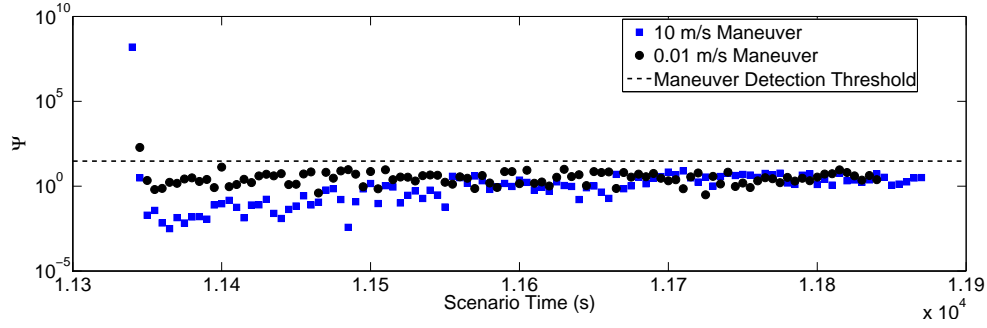
Figure 4.2: Ψ During First Post-maneuver Pass

pruning others. As discussed previously, Ψ is a scalar value of the goodness-of-fit of the orbit estimate and jumps to large values for large discrepancies between the covariance and residuals. It is expected that larger maneuvers require a larger amount of covariance inflation to filter-through, and this trend is captured in Figure 4.3. The figure highlights the model that received the largest weighting throughout the entire scenario and captures all simulated cases. In general, the shape of the plot is as anticipated - large deviations require heavily weighting large η models. There are, however, a few outliers of larger deviations with smaller amounts of associated initial covariance inflation. Two noticeable outliers occur at the smallest η values and around Ψ values of 10^5 and 10^7. Both these outliers are from the same orbit configuration: elliptical, inclined, 600 km, in-plane maneuver. The similarity of the orbit shapes resulted in a similar model weighting. Additional cases of this orbit type also resulted in heavily weighting smaller η value models. It is important to realize that this model weighting did not result in larger than normal errors, nor did a false positive occur. These outliers are simply a product of the large variety of cases simulated and the IMM weighting the best models based on their likelihood. Overall, the results show the abilities of the IMM to heavily weight larger covariance models for larger deviations.
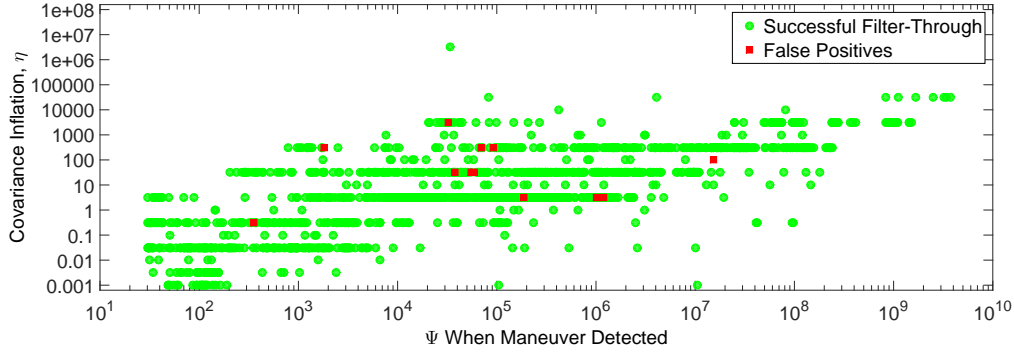
Figure 4.3: Maneuver Detection Ψ Compared to Most Heavily-weighted Model

The breakdown of cases in Figure 4.3 also highlights the performance of the IMM approach in preventing false positive maneuver detections. False positive maneuver detections refer to incidents when the IMM identifies a second maneuver when there is not one present in the scenario. The first maneuver is properly identified in every scenario, but there are cases when the IMM falsely predicts a second maneuver. Overall, only 12 cases have false positives where Ψ grows larger than 30 after the maneuver is detected. The false positive cases happen for three different reasons. The first type of false positive occurs for two cases at exactly the first observation of the second post-maneuver pass. Prior to the inclusion of Algorithm 8, there were more than 40 false positives of this type. It is clear that the inclusion of additional process noise during long coverage time gaps improved the model's performance. Further increases in constants within Equation 4.2 could prevent these two instances of false positives; however, they are deemed acceptable to keep overall state errors low for other cases. The next cause of false positives result from the filter recovering immediately after the covariance inflation. For seven cases, false positives occur one to three observations after the initial covariance inflation. These results show that while the covariance inflation filter-through approach is effective for the majority of maneuvers, there are cases in which the larger covariance models are not weighted heavily

enough. Although the filter eventually converges on the new orbit after the maneuver, a false positive occurs along the way. This type of false positive is preventable by reducing the models in the IMM to include only certain models tailored to the maneuver size. This change is discarded as it is contrary to the approach developed within this paper to keep the IMM broad and include a wide-range of models. The last type of false positive occurs three times when there is an outlier that produces a short small spike in Ψ. This issue is resolvable by increasing the threshold; however, increasing the threshold decreases the speed with which maneuvers are detected. Overall, the specific false positives are not correlated to the size of the maneuver nor the covariance inflation value as shown in Figure 4.3.

Given the true location of the spacecraft during simulation, the position RMS observation error, RMS_r, is known at all times. Similar to Figure 4.3, Figure 4.4 compares the most heavily-weighted filter within the IMM to the average position error through two post-passes. First and foremost, the shape of the curve in Figure 4.4 is very similar to the curve in Figure 4.3 showing that Ψ is an adequate substitute for error in the non-cooperative case. Next, it is seen again that the level of error caused by the maneuver does not correlate to false positives. Finally, the plot confirms the IMM's ability to, in general, opt for larger covariance inflation when larger errors are caused by maneuvers.
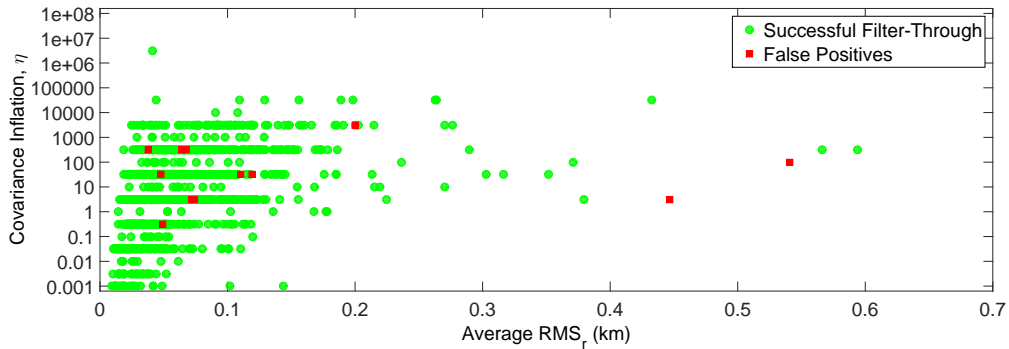
Figure 4.4: Average Position Error Compared to Most Heavily-weighted Model

While developing the IMM approach, the number of post-covariance inflation observations left within the pass was an initial concern. Reviewing Figure 4.1, the greater the number of observations during the pass, the faster the covariance is driven down to pre-maneuver levels. Without sufficient observations prior to a coverage gap, there is a possibility of not achieving sufficient accuracy to prevent filter divergence. To analyze this effect, Figure 4.5 displays the average error compared to the observations remaining in the pass. The figure shows the false positives are not correlated to the number of post-covariance inflation observations remaining in the pass; therefore, filter divergence is not a concern. However, the errors are noticeably larger for the cases with fewer post-inflation observations. This effect is related to how the filter uses longer pass times to drive down the covariance and associated errors prior to a coverage gap. A mediocre orbit fit prior to a coverage gap increases errors during the gap; whereas, filtering-through and driving the covariance down with sufficient observations results in a good orbit fit and decreases errors over gaps. Figure 4.5 emphasizes that the performance of the IMM filter-through approach is dependent upon using as many observations during a pass as possible.
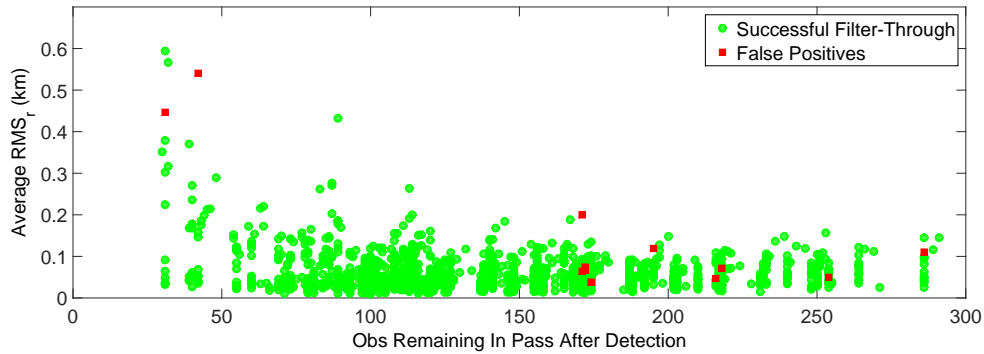
Figure 4.5: Observations in Pass Compared to Average Position Error

The coverage gap is a concern as the accuracy of the estimate deteriorates over large gaps leading to a potential for false positives. The approach outlined in Equation 4.2 adds additional process noise to prevent false positives over large gaps. Figure 4.6 shows the effect of the added noise in Equation 4.2 in preventing false positives as the time between passes is uncorrelated to false positives. Including Equation 4.2 within each active model of the IMM prevents the need for optimizing the amount of added process noise necessary. Since each model has different covariance sizes within the IMM prior to adding coverage gap noise, each has different sizes after the addition. With a large number of models there is a large variety of covariances and state estimates. The process of mixing Gaussians will weight the best model based on likliehood and heavily weight the proper solution after the coverage gap. This approach of using a broad range of models within the IMM allows for flexibility in the amount of added process noise.
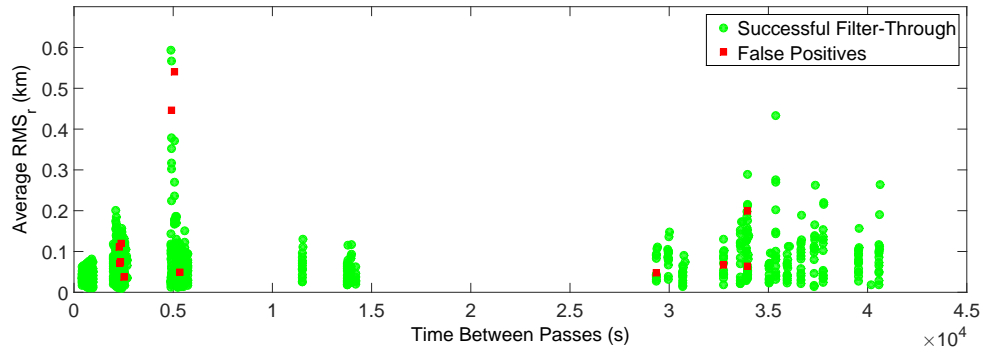
Figure 4.6: Time Between Passes Verses Average Position Error

Besides false positives, there are also three specific cases that result in a failure of the IMM. For the 700 km, 0.06 eccentricity, 98.1° inclined case with in-plane maneuvers of sizes 0.01, 0.05, and 0.1 m/sec, a rare error occurs. The IMM quickly prunes away many of the larger covariance inflation models. Then, after a coverage gap, the remaining models

no longer properly capture the orbit dynamics. The IMM algorithm pruned selections too quickly and eliminated models that were actually better suited to capture the dynamics. While these cases point out a flaw, the instances of failure are extremely low. One goal of the developed IMM is to make the approach as general as possible by including a wide variety of 23 different covariance inflation models to capture an abundance of different orbits and maneuvers. These failure cases are preventable by using a specific IMM tuned for this orbit type. Tailoring the models within the IMM to specific orbits boosts performance, but also limits the model's applicability to only certain orbits. For this reason, the failures are absorbed to maintain the model's usability for a multitude of other cases.

Of the 1344 cases simulated, 0.2% resulted in model failure and 0.9% of cases produced false positives. With both shortfalls below 1%, there is confidence that this approach is effective for the real-time tracking of high-priority maneuvering spacecraft.

4.4.3   IOD Comparison.

It is not expected that the filter-through IMM approach will outperform an IOD $\rightarrow$ BLS $\rightarrow$ EKF method as it updates an epoch in a iterative post processing fashion. However, after the covariance inflation and re-convergence on the orbit, the IMM should perform similarly with the added benefit that it runs forward in real-time. Allowing the filter to settle by processing 30 observations after the maneuver, Table 4.5 compares the average total sum of the error for each approach. As anticipated, the IOD on average outperforms the filter-through approach, and the IOD maintains consistent performance across all maneuver sizes. The IOD approach starts anew by performing an initial orbit fit, then uses a full pass of observations to update the epoch. Next, errors are further reduced using the EKF once the epoch is updated with the BLS filter. This method is an offline approach as it requires using future data to update an epoch; the estimate of the orbit at the beginning of the pass is not calculated until the end of the pass. The IOD approach has the added advantage of averaging errors and iterating to convergence to find the best solution. The goal of the

filter-through method is to avoid waiting for a full pass of observations and estimate the new orbit in real-time. Table 4.5 also reveals that the filter-through approach becomes less and less accurate the more the value for Ψ at detection grows. This result is expected as the filter-through approach requires nearly a full pass of observations to drive down errors after larger maneuvers. Also, the approach is designed for use in real-time orbit determination for spacecraft that are considered high-priority and tracked often. Tracking a maneuvering spacecraft frequently prevents larger values of Ψ from occurring as maneuvers are quickly detected.

Table 4.5: Comparison of IOD to IMM Approach

$\Psi <$	10^3	10^4	10^5	10^6	10^7	
$\Psi \geq$		10^3	10^4	10^5	10^6	10^7
Cases eval'd	279	196	256	261	157	192
IMM RMS$_r$	6.461	7.444	7.642	11.558	13.414	17.200
IOD RMS$_r$	6.062	6.411	6.150	5.886	5.888	5.997
IMM RMS$_v$	0.0219	0.0252	0.0306	0.0890	0.1699	0.2795
IOD RMS$_v$	0.0177	0.0198	0.0179	0.0181	0.0189	0.0198

Examining the cases in which $\Psi < 1000$, the first column of Table 4.5 reveals that the IMM approach performs similarly to the IOD method. Looking at each case when $\Psi < 1000$, Figures 4.7 and 4.8 show the specific errors. These figures reveal that there are instances in which the IMM is actually the better choice. These results are very encouraging as the IMM runs forward in time and does not benefit from iterating on a batch of estimates to update an epoch. Although the IOD→BLS→EKF is better on average, the IMM can process observations in real-time and perform nearly as well. The IMM and IOD methods are also further improved during post-processing through the use of smoothers. However, the focus of this chapter is on real-time forward moving estimation techniques. Overall, the

IMM filter-through approach can handle a large variety of orbits, maneuvers, and coverage gaps with minimal false positives and errors. The method is best suited for real-time orbit estimation of high-priority spacecraft.
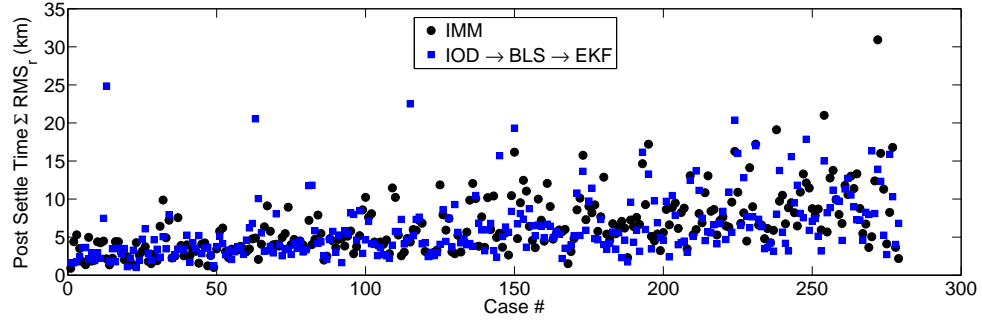
Figure 4.7: IMM verses IOD Total Position Errors When $\Psi < 10^3$ at Detection
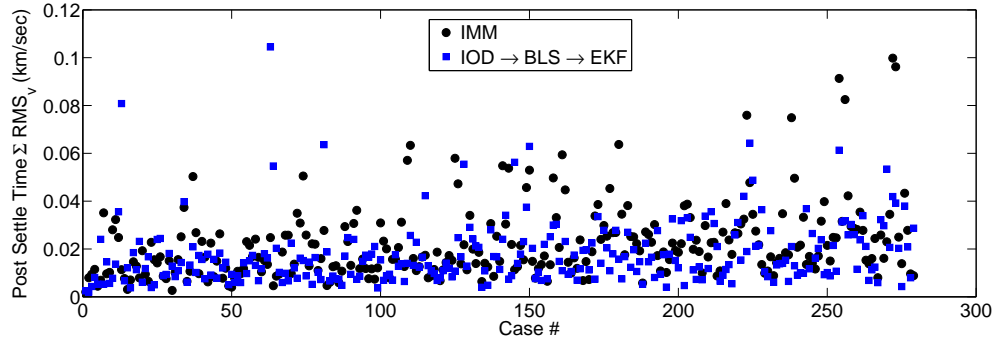
Figure 4.8: IMM Verses IOD Total Velocity Errors When $\Psi < 10^3$ at Detection

4.5 Conclusion

The results show the abilities of using an IMM coupled with covariance inflation models to filter-through maneuvers and re-converge on the orbital solution for the real-time tracking of high-priority assets. This newly developed algorithm and approach separates

80

itself from IOD and BLS methods since it runs in real-time without the need to update epochs. Using the approach requires association knowledge that the item tracked is the spacecraft of interest. Given this correlation, the approach is general enough to work with any orbit propagator. Additionally, it is general enough to handle any size maneuver and coverage scheme, but works best when Ψ remains low. The combination of all the algorithms developed herein provide a way to improve SSA when tracking high-priority maneuvering spacecraft.

In summation, the results in this chapter showed an original approach to handling spacecraft maneuvers while avoiding the need to perform a new IOD. While some have mentioned using process noise to help with orbit estimation errors, this chapter provided an all-in-one real-time approach to filter-through unknown maneuvers and avoid the need to run offline post-processing iterations to converge on a solution.

V.   Parameter Requirements for Maneuver Reconstruction

5.1   Introduction

As discussed previously, there are three basic ways to handle a maneuver when performing SOD: filter-through the maneuver, begin again with an IOD, and reconstruct the maneuver [11]. The methodology of the first two approaches are detailed in Chapters 3 and 4. Using adaptive filtering, this chapter focuses on three routines: an adaptive EKF, an adaptive UKF, and an adaptation of Wright's method [22]. To adapt Wright's approach, the same maneuver detection method uses Ψ to determine a maneuver has occurred. Then, an IOD followed by a BLS filter of observations in that pass is performed to update the epoch. Next, an EKF and smoother is run starting with the BLS initial state and covariance estimates. This chapter specifically addresses the instantaneous maneuver cases. For these cases, it is assumed that the maneuver occurred at a single instant in time, t_{man}, with a defined thrust vector $\Delta\mathbf{v}$ with corresponding magnitude Δv_{mag}. There are different ways to reconstruct an instantaneous maneuver, but all require knowledge of the pre-maneuver and post-maneuver orbit.

5.2   General Reconstruction

The most general approach is to propagate the pre-maneuver orbit forward in time and the post-maneuver orbit backward in time. Next, determine the time when the orbits intersect, touch, or come closest together (minimum separation distance). This instance is the time of the maneuver, t_{man}, and the difference of the velocity vectors is the instantaneous maneuver, $\Delta\mathbf{v}$, shown in Equations (5.1) and (5.2).

$$r_{min_k} = \min \left| \mathbf{r}_{pre} - \mathbf{r}_{post} \right|_2 \tag{5.1}$$

$$\Delta\mathbf{v} = \mathbf{v}_{post_k} - \mathbf{v}_{pre_k} \tag{5.2}$$

This method of reconstruction is the most general and works on any form of maneuver. However, this method tends to work better for some types of orbit changes than others as shown in Section 5.9.2.

5.3   Circular-to-Elliptical Maneuvers

When certain details are known about the maneuver based on the pre- and post-maneuver orbits, a more specific method of reconstruction is possible. If it is determined that the pre-maneuver orbit was circular and that the post-maneuver orbit is elliptical and in the same plane, then it is highly likely that the satellite performed an efficient in-plane Hohmann-type initial transfer maneuver. The assumption is that if the pre-maneuver orbit was circular and now the orbit has a noticeable eccentricity, the following approach is applicable. The magnitude of the maneuver, Δv_{mag}, is determined using the specific mechanical energy, ε, of the estimated orbits. The time of the maneuver is determined by calculating when the satellite was at perigee or apogee of the post-maneuver elliptical orbit. The transition from a circular to elliptical orbit is known to occur at either perigee or apogee of the new orbit since a satellite traveling in a circular orbit has a velocity vector tangent to the orbit at all times. Determining the specific mechanical energy for both orbits reveals whether or not the maneuver occurred at apogee or perigee

$$\varepsilon = \frac{1}{2}v^2 - \frac{\mu_\oplus}{r} \tag{5.3}$$

If the energy of the post-maneuver orbit is larger, assume the transfer occurred at perigee and t_{man} is the time at perigee. If the energy of the second orbit is smaller, assume t_{man} is the time at apogee.

The distance from the Earth at which the maneuver occurred, r_{man}, is either the radius of perigee or apogee depending on the specific mechanical energy change. Determining the radius of apogee and perigee for an orbit are well known procedures [12:105]. Calculating

83

the magnitude of velocity for each orbit at r_{man} and the Δv_{mag}

$$\Delta v_{mag} = \sqrt{2\left(\frac{\mu_\oplus}{r_{man}} + \varepsilon_{post}\right)} - \sqrt{2\left(\frac{\mu_\oplus}{r_{man}} + \varepsilon_{pre}\right)} \tag{5.4}$$

This Δv_{mag} is assumed to occur in the velocity vector direction. In the NTW frame,

$$\Delta \mathbf{v} = \begin{bmatrix} 0 & \Delta v_{mag} & 0 \end{bmatrix}^T \tag{5.5}$$

Using the time of perigee or apogee and the velocity vector, a maneuver is reconstructed using a method pertaining specifically to the circular-to-elliptical transformation.

5.4 Elliptical-to-Elliptical Maneuvers

For the case in which a transfer is made from an elliptical to elliptical orbit, it is no longer valid to assume the maneuver occurred at perigee or apogee. An efficient maneuver would occur at these locations tangent to the position vector, but when performing maneuvers to avoid detection or improve fly over times during short duration missions, the maneuvers may not occur at perigee or apogee. There are two general types of coplanar maneuvers for elliptical-to-elliptical transfers. Either the maneuver occurs only in the velocity direction or some combination of the velocity vector and radial vector directions. Reconstructing these maneuvers requires rotating coordinate frames and using the NTW and RSW coordinate frames (Section 3.5). If it is not evident from the pre- and post-maneuver orbits as to whether the maneuver was purely in the velocity vector direction or some combination of the radial and velocity vector directions, then it is necessary to run both coplanar approaches. The overarching assumptions for these approaches is that the pre- and post-maneuver orbits are coplanar and that the pre-maneuver orbit has a noticeable eccentricity.

5.4.1 Velocity Vector.

For the purely velocity vector direction specific reconstruction approach, a similar method is used as the circular-to-elliptical case. The main difference is that now, the r_{man}

is not at perigee or apogee, but instead dependent on both the pre- and post-maneuver orbit radii at that time. When performing non-deterministic reconstruction, the radii are never exactly the same, so both variables are used at the time of closest approach to determine the velocity. Equation 5.4 becomes

$$\Delta v_{mag} = \sqrt{2\left(\frac{\mu_\oplus}{r_{post}} + \varepsilon_{post}\right)} - \sqrt{2\left(\frac{\mu_\oplus}{r_{pre}} + \varepsilon_{pre}\right)} \tag{5.6}$$

The maneuver vector, $\Delta \mathbf{v}$, is the same as Equation 5.5 for this case. The time of closest approach is considered the time of the maneuver, t_{man}.

5.4.2 Coplanar.

For the coplanar general maneuver, it is known the maneuver occurs only in plane, and the maneuver vector now has components in two directions within the plane. Using the RSW coordinate frame, it is possible to narrow down the general reconstruction to one fewer dimension. The general approach assumes that the maneuver could occur in any of three inertial directions, whereas the coplanar specific approach constricts the maneuver to occur only in the orbital plane. The time of the maneuver is determined using the general case approach in Equation 5.1 where the time of closest approach is the maneuver time, t_{man}. Then, the pre- and post-maneuver position and velocity vectors at that time are rotated into the RSW frame. The maneuver is calculated using only the coplanar directions

$$\Delta \mathbf{v} = \left[\begin{array}{ccc} v_{R_{post}} - v_{R_{pre}} & v_{S_{post}} - v_{S_{pre}} & 0 \end{array} \right]^T \tag{5.7}$$

Once calculated, the maneuver is converted back to the inertial frame for use in the orbit propagation and reconstruction routine. This approach uses the coplanar assumption and a coordinate rotation to avoid including any unnecessary out of plane velocity changes into the maneuver vector $\Delta \mathbf{v}$ calculation.

5.5 Plane Change Maneuvers

The final case to investigate is when an inclination change occurs. This approach is used only if the orbit size and shape are the same for both the pre- and post-maneuver

orbits and the inclination is different. If this is the case, a specific reconstruction method must determine the out of plane velocity component difference between the pre- and post-maneuver orbits. From the general case, Equation 5.1 is used to determine the time of the maneuver, t_{man}, and the magnitude of the velocity vector is determined via $\Delta v_{mag} = |\Delta \mathbf{v}|_2$. Using the RSW frame again, the reconstructed maneuver for this specific case occurs only in the orbit normal, W, direction.

$$\Delta \mathbf{v} = \begin{bmatrix} 0 & 0 & \Delta v_{mag} \end{bmatrix}^T \tag{5.8}$$

Once again, the maneuver is rotated back to the inertial frame after it is calculated.

5.6 Optimization

In all reconstruction approaches, the calculation of $\Delta \mathbf{v}$ depends on a singular estimate of the pre- and post-maneuver orbit solutions. In non-cooperative orbit determination, the type of radar, length of coverage, and time between collected passes affect the accuracy of the orbit solutions. In turn, these variables affect the accuracy of the maneuver reconstruction. Small differences in orbit positions and velocities for the pre- and post-maneuver solutions couple and amplify into errors for the estimated maneuver time and vector. Since each reconstruction method results in a single calculation of the maneuver and time, position uncertainties may distort the time when the pre- and post-maneuver position vectors are closest together. To add robustness and improve the reconstruction solution, a local neighborhood search method is used to find the best maneuver solution [144].

For each reconstruction method, the full time between passes when the maneuver was detected is evaluated as the neighborhood and centered on the initially calculated time of closest approach as described in Equation 5.1. Then, surrounding combinations of pre- and post-maneuver position vectors are used to calculate different reconstructed maneuvers. Each maneuver solution is run through a propagator and the absolute value of the residuals

86

are calculated at discrete observation times. The weighted residuals for range, azimuth, elevation, and range rate are summed. Then, summed weighted residuals at observations times are averaged to form a cost function

$$J_{cost} = \frac{\sum_{i=1}^{l} \sum_{k=1}^{m} \left| \left(\sqrt{\mathbf{R}_i} \right)^{-1} \nu_i \right|_1}{l} \tag{5.9}$$

where i are five specific observation times for each pass occurring equally spaced between the beginning and end of the pass and m is the size of the observation vector. Five observations are chosen to span the length of the pass and capture the performance of the reconstruction while reducing the computational time required within the optimization routine. The more passes that occur prior to the reconstruction attempt, the more points evaluated.

The averaged summed weighted residual cost is compared amongst the calculated possible maneuver solutions. The maneuver solution with the smallest cost is selected as the reconstructed maneuver for that particular case. Since the cost varies across the observations in a parabolic fashion, a local search routine described in Figure 5.1 is used to find the best solution. The dotted boxes represent the best solution for that Δt size. Then, Δt decreases at each level and the pattern continues down until $\Delta t = 1$ s and the best solution is determined. If the best solution is found on the either edge, the evaluations are performed again using a larger window size to ensure the best solution is captured in the middle of the bounds.

Determining the sample space of possible solutions (t_{man}, $\Delta \mathbf{v}$, and J_{cost}) varies between approaches. For the general reconstruction case, times surrounding the initial solution are evaluated and the maneuver is determined using Equations 5.1 and 5.2 at times when the position vectors were not closest together. For the elliptical velocity vector maneuver case, the same approach of varying time is used except that Equation 5.6 is repeated for different combinations to determine solutions. Similarly, the approach of varying the time of the maneuver and calculating separate $\Delta \mathbf{v}$'s is repeated for the elliptical coplanar and plane

change cases. The optimization approach for the circular-to-elliptical case differs. The minimum velocity calculated in Equation 5.5 is applied at different times during the pre-maneuver circular orbit to fill the solution space. This case differs because the $\Delta\mathbf{v}$ calculated for most pre- and post-maneuver combinations was nearly identical; therefore, the timing of the maneuver is the more important variable to consider.

This optimization approach adds flexibility to evaluate reconstructed solutions at other times to find the best solution. Additionally, it provides a format to evaluate both general and specific reconstruction routines to determine which is best. Using the adaptive filtering and smoother algorithms to converge on a new orbit, maneuver reconstruction is optimized using the reconstruction methods discussed previously.
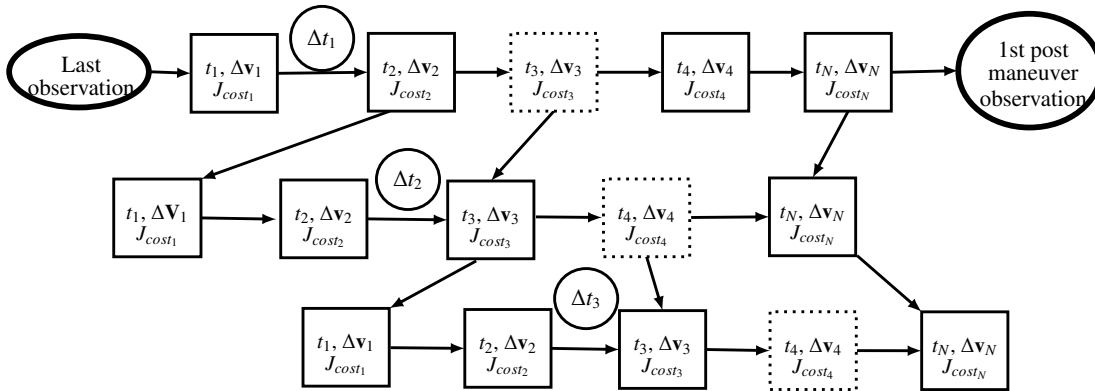
Figure 5.1: Flow-chart for Local Search Optimization Routine

5.7 Variable Analysis

When using a large number of inputs to determine binary outputs, it is critical to analyze each variable's impact on the output. In maneuver reconstruction, an attempt is either successful or unsuccessful based on a classification metric. Using all the known

variables pertaining to a maneuver reconstruction, a classification test is performed to determine the most critical variables in the decision.

Neural network pattern recognition serves as a high fidelity method to predict an output based on a given input [121]. Because the neural network approach can analyze any type of variable and the weighting scheme allows for effective variable reduction, this approach was selected instead of other multivariate analysis techniques. Applying the pattern recognition tool to maneuver reconstruction is a new application. Given a test set, validation set, and a specified number of hidden neurons, a complex set of weights are applied to each input to produce an output [123]. The outputs predicted by the neural network are compared to the actual outputs and the percentage of proper classifications is determined. Appending a normally-distributed random variable to the inputs creates a way to determine the signal to noise ratio of each variable. By running all variables (including the random noise) through the pattern recognition, each variable weight, $var_{i_{weights}}$, and noise weights, $noise_{weights}$, combine to determine the signal to noise ratio [123]

$$S/N_i = 10 \log_{10} \left(\frac{var_{i_{weights}} var_{i_{weights}}^T}{noise_{weights} noise_{weights}^T} \right) \tag{5.10}$$

The neural network pattern recognition classifier results and Equation 5.10 are used to determine the most important variables during the classification. The largest ratio, in absolute value, of the S/N vector is the most influential variable and the smallest is the least influential. When the goal is reducing the dimensionality of the inputs, the neural network pattern recognition tool is re-run on a data set with the least influential variable removed. Then, if the percent correctly classified is within tolerance, the next least influential variable is removed. Continuing this process, the most important variables in the classification are determined and their combined ability to classify is known.

5.8 Simulation

Oftentimes simulation is a beneficial tool when testing maneuver reconstruction performance as many different types of maneuvers are easy to simulate and test the robustness of the different methods. For non-cooperative orbit determination, the true orbit state is never known, only estimated. However, in simulation the truth state is known and simulations evaluate the errors in proposed orbit and maneuver solutions. Scenarios are developed that simulate observations to test reconstruction methods.

To examine the parameters necessary for maneuver reconstruction, four specific maneuvers are simulated each with an associated starting orbit. The specific maneuvers detailed above are circular-to-elliptical, elliptical-to-elliptical in the velocity vector direction, elliptical-to-elliptical-coplanar, and inclination (plane) change. The circular-to-elliptical maneuver simulated is 4 m/s in the anti-velocity vector direction. The elliptical-to-elliptical velocity vector maneuver simulated is 4 m/s in the velocity vector direction. The elliptical-to-elliptical-coplanar maneuver is 4 m/s in both the radial and velocity vector directions. The inclination change is 50 m/s in the orbit normal direction.

This analysis effort focuses on LEO tracking. For the pre-maneuver orbit, circular, circular inclined, elliptical, and elliptical inclined orbits are evaluated. For the starting circular orbit an altitude of 500 km is used and the two specific cases evaluated contained 0 and 60 deg inclinations. The starting orbit for the elliptical cases has an altitude of 2500 km and an eccentricity of 0.2. The elliptical orbits evaluated are inclined at 0 and 60 deg also. The simulation cases are summarized in Table 5.1. The $\Delta\mathbf{v}_{norm}$ values associated with the two maneuver magnitudes in Table 5.1 are 0.013 and 0.17. For each orbit, the average daily pass lengths and percentage of the orbit viewed during the average pass are captured in Table 5.2.

For each case, the maneuver occurs at approximately the middle of a gap in coverage of the ground antennas. If an observation resulted in a Ψ value greater than 250, a maneuver

90

is declared and the covariance is inflated according to the algorithm, or a new IOD is performed for the IOD→ BLS→ EKF/smoother approach. In the adaptive filter routines (Equation 3.57), the covariance is inflated until its trace is greater than 10^6. The UKF parameters are set to $\alpha = 0.1$, $\gamma = 2$, and $\kappa = -3$ for Equations 3.49 - 3.52 . For the BLS algorithm, the first 100 observations in that pass are used. If less than 100 observations are available in the pass, then all the observations of the pass are included in the BLS routine. BLS algorithms occasionally have convergence problems, but these are minimized by restricting observations to only the pass of interest.

To evaluate varying the length of the pass captured by an antenna, partial and full coverage cases are created. The partial cases contain 1/4 of the observations that a full pass contains and are taken at the beginning of the post-maneuver passes. The partial cases are evaluated for only the non-inclined cases. For the partial coverage cases, the reduction in the pass length occurs only during post-maneuver tracking. For all cases, four full pre-maneuver passes are used to determine the pre-maneuver orbit. Additionally, four post-maneuver passes are considered in the analysis for the reconstruction. An attempt to reconstruct is made after each of the four post passes.

There are three different types of antennas used with varying performances. The antennas are described as either good, medium, or poor. The good antennas have similar performance characteristics as a newer mechanical antenna. The medium antennas have performance characteristics of a phased array radar used to track satellites. Finally, the poor antennas have characteristics similar to a 1960s mechanical radar [12:259]. Table 5.3 describes the error standard deviation σs for each radar. For the simulation, zero bias normal random errors are added to (simulated) perfect observations according to the antenna's performance.

Each antenna collects observations at 5 second intervals when the elevation is above 1 deg for all degrees of azimuth. Furthermore, cases are created that vary the pre- and

post-maneuver antennas used for tracking. The breakdown of the simulated combinations are captured in Table 5.4. For the full coverage simulations, two antennas of the specified quality are placed at a longitude of ±62 deg. For the inclined cases, the antennas are placed at a latitude of 17.4 deg whereas for the non-inclined cases the antennas are placed at a latitude of 5 deg to ensure coverage. For the partial coverage cases during post-maneuver tracking, a single antenna is placed at a latitude of 5 deg and a longitude of 62 deg.

Table 5.1 and Table 5.4 combine to form 160 simulated test cases for full coverage. The partial coverage cases are simulated for only the non-inclined cases and comprise an additional 80 test cases. To test all methods, 240 cases are analyzed to evaluate when a maneuver reconstruction is effective.

Using a neural network pattern recognition tool all cases are evaluated. A two-layer feed-forward network with sigmoid and output neurons is used to classify cases. The network is trained using the scaled conjugate gradient back propagation method. 10 hidden neurons are selected for the hidden layer and two for the output layer. The network sets aside 15% of the data for training, 15% for validation, and the remaining 70% for performance. Each run of the classifier is performed at least three times allowing for random re-selection of training and validation cases for the network. The average output is selected as the result to avoid outliers. Using four maneuver types, five antenna combinations, three types of antenna coverage, and four post-maneuver passes, variables are evaluated on their impact in classifying a successful reconstruction. Seven variables are considered: the number of post-maneuver passes, the sum of the largest eigenvalues of the smallest position covariance estimate during the last pre-maneuver pass and smallest position covariance estimate of the post-maneuver pass considered, the type of antennas used for tracking after the manuever, the average weighted σ over all passes experienced using the given antenna performance (cost function Equation 5.9), the summed average weighted residuals based on the good antenna performance characteristics, the type of

coverage, and the type of maneuver. All seven variables are known quantities when performing non-cooperative orbit determination.

Table 5.1: Orbit and Maneuver Cases Simulated

Maneuvers			Starting Orbits			Reconstruction Parameters		
Type	Dir	Mag (m/s)	Alt (km)	Ecc	Inc (deg)	Ant Combos	Post Passes	Coverage
Circ→Ellip	Vel	-4	500	0	0	All	1, 2, 3, 4	Full, Partial
Circ→Ellip	Vel	-4	500	0	60	All	1, 2, 3, 4	Full
Ellip→Ellip	Vel	4	2500	0.2	0	All	1, 2, 3, 4	Full, Partial
Ellip→Ellip	Vel	4	2500	0.2	60	All	1, 2, 3, 4	Full
Ellip→Ellip	Vel & Rad	4	2500	0.2	0	All	1, 2, 3, 4	Full, Partial
Ellip→Ellip	Vel & Rad	4	2500	0.2	60	All	1, 2, 3, 4	Full
Inc Change	Normal	50	500	0	0	All	1, 2, 3, 4	Full, Partial
Inc Change	Normal	50	500	0	60	All	1, 2, 3, 4	Full

Table 5.2: Orbit Percentages

Alt (km)	Ecc	Inc	Avg. Pass Length (s)	Avg. Orbit %
500	0	0	684	12.1
500	0	60	582	10.3
2500	0.2	0	2213	26.6
2500	0.2	60	2279	27.4

Table 5.3: Antenna Measurement Errors

Antenna Type	Range σ (m)	Azimuth σ (deg)	Elevation σ (deg)	Range Rate σ (m/s)
Good	5	0.01	0.01	0.05
Medium	25	0.03	0.03	0.2
Poor	100	0.05	0.05	10

Table 5.4: Antenna Combinations

Pre Antenna Type	Good	Good	Good	Medium	Bad
Post Antenna Type	Good	Medium	Bad	Medium	Bad

5.9 Results

5.9.1 Filter/Smoother Analysis.

For each case described in Table 5.1 all the filters in Table 3.1 are used to determine the post-maneuver orbit. Specifically, an adaptive EKF, adaptive UKF, and the combination of IOD $\rightarrow$ BLS $\rightarrow$ EKF are used. Each filter is coupled with a fixed interval smoother that runs at the completion of each pass (Section 3.10.5). For all the simulated cases, each filter is able to detect the maneuver that occurs outside of the view of the radar at the first post-maneuver observation. Specifically, the purpose of this section is to run the EKF, UKF, and the IOD $\rightarrow$ BLS $\rightarrow$ EKF all with fixed interval smoothers, then perform a maneuver reconstruction and determine which approach produced the estimate with the least cost as defined in Equation 5.9.

Since the truth is known, it is worthwhile to evaluate and compare each filter's performance after every post pass. The research by Showalter and Black is focused around altering arrival times over a radar [9]. Adaptive filtering provides a method to determine the effectiveness of these types of maneuvers given the assumption that the satellite is found and tracked by the radar. Looking specifically at the circular-to-elliptical maneuvers in Showalter and Black's work, the error after each pass is calculated using the minimum covariance state estimate of the smoother for that pass. The best filter/smoother is selected as the filter/smoother with the smallest position covariance estimate during the pass.

Figure 5.2 shows the error for each antenna for the full coverage non-inclined cases. The results are from adaptive filtering/smoothing without attempting to reconstruct. Figure 5.2 shows how quickly the error decreases in the first three passes. The slight upward trend for the bad antenna in the third pass is due to the fact that the filter/smoother

94

combination will fluctuate slightly with observations and that the least covariance point does not always directly correlate to the least true position error. However, the smoother's smallest covariance point is always very close to the best overall estimate of both position and velocity. The results show that if a 4 m/s maneuver occurs outside of view, adaptive filtering for good antennas reduces the position error to 25 m within 1 pass and even with older antennas the error is below 80 m. A traditional non-adaptive filter/smoother produces errors of 18 km, 24 km, 39 km, and 43 km after each pass. Thus, the adaptive approach is more accurate by a factor of 700 after only a single pass. These large errors highlight the importance of using adaptive filters when tracking maneuvering spacecraft.
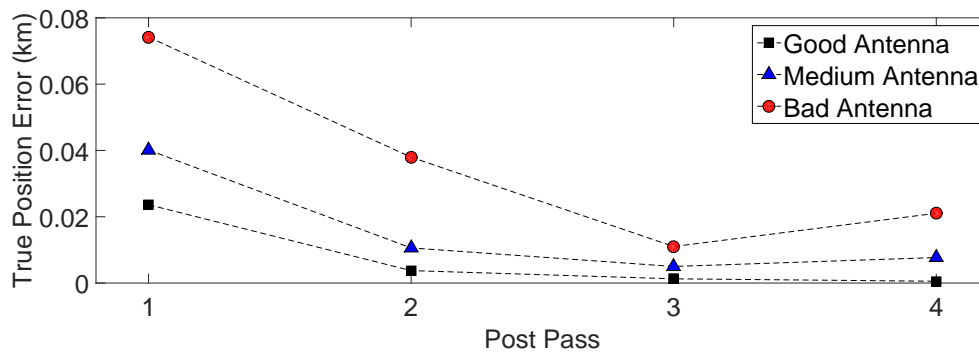
Figure 5.2: RMS of Filter/Smoother with Smallest Covariance

Each of the filter/smoothers provide a different way of estimating the state and covariance and each tends to perform better for certain orbits and maneuvers. After the optimal reconstruction is performed, the filter/smoother with best cost function is selected and its maneuver, state, and covariance estimates are used. It is worth comparing which filter/smoother combinations are selected depending on the case as is done in Figure 5.3. These results show that the adaptive filter/smoothers perform differently for each maneuver type. The results of this study show that the IOD is effective for coplanar maneuvers in

general, but an adaptive filter is preferred for plane changes. Additionally, these results support using all filter/smoother combinations when available as a diversified selection of filtering approaches improves reconstruction accuracy.
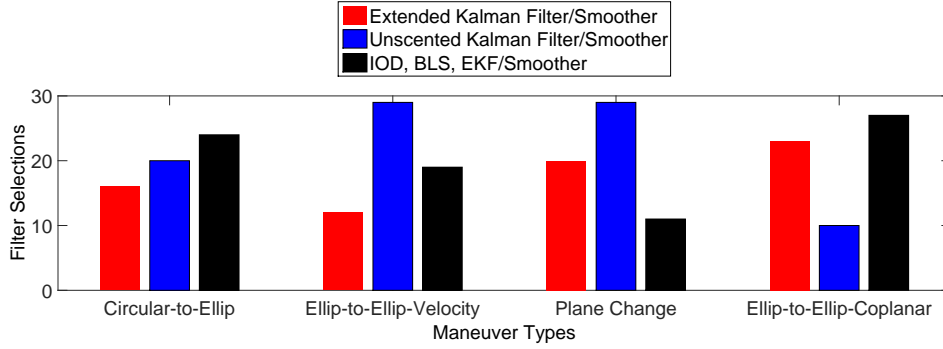
Figure 5.3: Best Filter/Smoother Combination Based on Maneuver Types

5.9.2 Reconstruction Method Analysis.

In Section 5.1, a general method for all types of maneuvers (Equation 5.2) is discussed. In Sections 5.3 - 5.5 a specific method for each type of maneuver simulated is presented. During simulation, each type of reconstruction is attempted for all 240 cases. The best maneuver reconstruction approach is selected as the method with the least average weighted residual cost function. This comparison serves as a way to select the best guess of the maneuver from the best filter/smoother. For each case, each filter/smoother is run and both reconstructions attempted; hence, the final solution is the best of six options. As in the filter selection, it is also worthwhile to investigate which reconstruction method is optimal. Figure 5.4 shows the comparison between general and specific methods. The results show that both a general and specific method are necessary for the elliptical cases, but not as necessary for the other cases. Therefore, if handling elliptical maneuver reconstructions, both approaches are necessary. When handling plane changes, the specific maneuver

96

approaches are the more reliable method of reconstruction. Using two approaches improves the chance of performing a successful reconstruction by leveraging different methods to attempt the reconstruction.
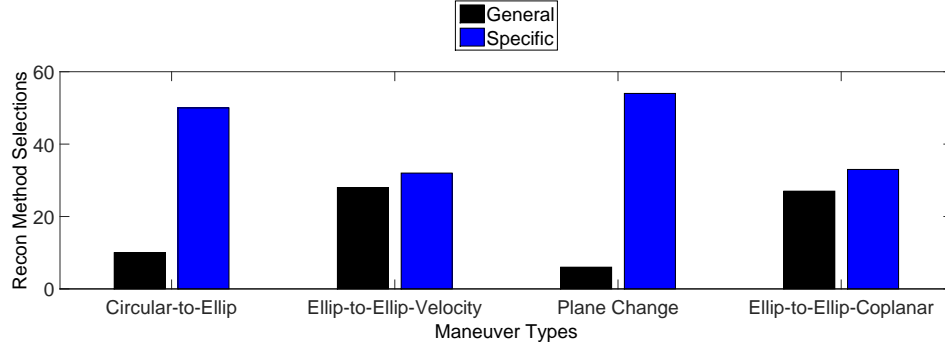
Figure 5.4: Reconstruction Method Selected Based on Maneuver Types

5.9.3   *True Error Classifier.*

The next three subsections specifically look at three different ways to classify a maneuver reconstruction attempt as successful or unsuccessful. Each method evaluates the 240 cases with all filter/smoother combinations and maneuver reconstruction strategies with the goal of determining when a reconstruction success is expected. Of all the variables considered in the scenarios, only some are truly impactful. The aim of each subsection is to determine for a specific definition of a success, the most important variables and the parameters of those variables necessary to successfully reconstruct maneuvers.

The first approach used to distinguish between successful and unsuccessful maneuver reconstructions is the average position error. This metric serves as an effective method to ensure that tracking errors remain low and the reconstruction helps predict future locations of the object of interest. Using the process described in Section 5.7 of removing the least influential variable and with the parameters discussed in Section 5.8, the neural network

97

pattern recognition tool is run over all cases. The classifier scores cases successful when the average position error is below 250 m and unsuccessful when the reconstruction results in larger errors.

The results in Table 5.5 show that the summed average residual variables are removed early in the process. This outcome is different than anticipated at the start of the research. It was expected that the most important factor in classification was the summed residuals after the reconstruction was performed as it captures whether or not observations are as expected. However, this factor is important in determining reconstruction success only when the cases considered are categorized based on the antenna type and maneuver type. The cost function provides a method to pick the optimal reconstruction as in Section 5.6, but it does not predict whether this reconstruction is successful. The local neighborhood search optimization routine provides the best solution for given conditions, but the conditions themselves determine whether or not the reconstruction is successful.

Table 5.5: Variable Influence in Classifying if Average Position Error < 250 m

Variables	Most Influential	Least Influential	% Classified Correct
7	Maneuver Type	Summed Weighted Residuals (Good Ant σ)	96%
6	Antenna Type	Maneuver Type	95%
5	Covariance	Cost Function	91%
4	Coverage Type	Antenna Type	90%
3	Post Pass #	Coverage Type	88%
2	Post Pass #	Covariance	88%

Overall, the classification provides insight into the most important variables to collect for a maneuver reconstruction. The results show that the most important variables to consider are the type of coverage, the number of passes, and the covariance.

Therefore, when performing maneuver reconstruction, these variables are good predictors of reconstruction success.

To further explain the results, Figure 5.5 shows how using the covariance and post pass number it is possible to draw a line separating the successful and failed reconstructions. A optimization classification algorithm is used to determine the best covariance line to minimize misclassification. The line in the plot is placed in the best location along the y axis to separate the successful reconstruction cases from the unsuccessful cases during each post pass. Ideally, if the covariance variable is an accurate discriminator, all success cases should fall below the line and all unsuccessful cases above the line. The success circles are placed slightly to the left and the unsuccessful triangles are placed slightly to the right for ease of visualization. Each case is placed along the y axis at the smallest primary eigenvalue of the covariance matrix achieved during that pass. The goal of the linear discriminator is to define a requirement of when a successful or unsuccessful reconstruction is expected based on the post-pass number and covariance. The ability of the line to divide the cases provides an assessment on the abilities of the requirement definition to predict success. The linear discriminator is applied for each pass and serves as a simplified form of the neural network classifier. Given 60 simulations for each pass, Figure 5.5 shows that after the first post-maneuver pass the best linear discriminator occurs at a covariance of 0.0748 km. A confidence of 72% is associated with the assertion that a covariance below 0.0748 km will result in a successful reconstruction. For the second post-maneuver pass, there is a 92% confidence in the hypothesis that a covariance below 0.2907 km will results in a successful reconstruction. The third post-maneuver pass confidence is 100% that covariances below 0.2715 km result in successful reconstruction. Finally, the last post-maneuver pass hypothesis of successful reconstruction below a covariance of 0.2894 km has a 98% confidence.
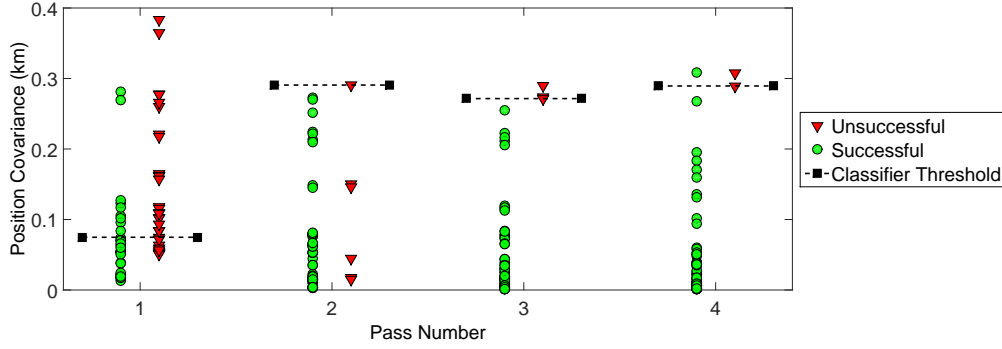
Figure 5.5: Position Error Classifier Success Based on Post Pass and Covariance

Using the average position error classifier of 250 m as a threshold, the data are further organized to show actual successful reconstructions in covariance windows. Using the important classification variables of the sum of the pre-maneuver minimum covariance primary eigenvalue and the post-maneuver minimum covariance primary eigenvalue and the post-maneuver pass number, the results are binned into three general covariance groups. Table 5.6 compares the results after each pass for all cases when reconstructing maneuvers and results in 199 total success cases. This result shows how each of the 60 cases shift into different covariance categories after each pass of observations are processed. Also, this table bounds the requirements and percent success for post passes and covariances. The data show how the combination of small covariances and more post-maneuver passes nearly guarantees successful reconstructions. This result matches with the logic that the smaller the covariance and the larger the number of post-maneuver passes, the better the estimate and the better the reconstruction. When tracking high visibility targets, the goal is to drive covariances low enough to fall into certain categories to improve chances of reconstruction. Since the covariance after a radar pass is predictable, this information allows for efficient and effective dynamic radar tasking during reconstruction. The percentages of success do

not grow in a purely increasing fashion in Table 5.6 because of the variability of using different antenna types and coverages in a single data set.

Table 5.6: Error Reconstruction Success with Post Pass Covariance Windows

	Position Covariance Primary Eigenvalue Range								
	0 to 0.05			0.05 to 0.15			0.15 to 0.4		
Pass	Success	Fail	%	Success	Fail	%	Success	Fail	%
1	10	0	100%	18	18	50%	2	12	14%
2	27	3	90%	20	1	95%	7	2	78%
3	40	0	100%	12	0	100%	5	3	63%
4	43	0	100%	9	0	100%	6	2	75%

Besides the variable detailing the number of post-maneuver passes, the difference between a full pass of data and a partial pass of data has a large effect on the ability to successfully reconstruct. If the 80 full coverage non-inclined cases are compared to the 80 partial coverage cases, the impact of coverage loss is clear. For the full coverage cases, 76 resulted in successful reconstruction achieving a 95% success rate. In the partial coverage cases, there were only 56 successful reconstruction cases for a 70% success rate. Therefore, reducing coverage to only the first quarter of the orbit decreases the ability to reconstruct a maneuver by 25%. This result is important to note as oftentimes only a smaller subset of the data during a pass is recorded to either free up antennas or reduce the volume of data. For high-priority tracking of maneuvering spacecraft, it is necessary to include full passes of data to improve chances for successful reconstruction.

Another consideration in the dynamic tasking of ground-based radars for tracking is the performance of the radar. If all cases evaluated are separated into those in which the pre- and post-maneuver orbits are determined by good, medium, and poor performance radars, the reconstruction abilities are realized. The motivation for choosing these combinations of

radars is to determine the impact of a less capable or similar radar on reconstruction. The results of sampling the five sets of 48 cases with varying radar types are shown in Table 5.7. Using a good radar for the post-maneuver reconstruction provided a 15% improvement in reconstruction ability over the medium performance class of radars. Table 5.7 also shows variability as the bad-bad case successfully reconstructs one additional case over the good-bad case. This result differs from predicted and is correlated to the fact that four pre-maneuver passes are used to achieve an accurate estimate which allows the bad-bad case to perform as well as the good-bad case. Additionally, this table shows the weakness of using the cost function in Equation 5.9 to select the best reconstructed maneuver. Generally the smallest residuals result in the best reconstruction; however, there are a few cases in which a very slightly larger cost results in a better reconstructed maneuver. Since the med-med and bad-bad cases are fairly close, an 80% success rate is expected for the bad-med case. For the med-good, bad-good, and med-bad cases, nearly identical results as their reverses (good-med, good-bad, bad-med) are expected due to the similar overall error total for the pre- and post-maneuver estimates.

Table 5.7: Reconstruction Success Based on Antenna Type

Pre-Man Ant	Post-Man Ant	Success	% Success
Good	Good	46	96%
Good	Med	39	81%
Good	Bad	37	77%
Med	Med	39	81%
Bad	Bad	38	79%

The analysis of the variables' impact on the classification supports the fact that the cost function in Equation 5.9 is not the best method to predict reconstruction success after each pass. While originally anticipated as the best delineation variable, the cost creates a false

sense of successful reconstruction. During the post-maneuver passes, the reconstruction algorithms attempt to drive down residuals, but only for the orbital observations obtained up to that point. After each pass, the cost function value often has little variability. This approach results in low errors, but only for passes that have occurred. The error for future observations can be large despite a good value for the cost function defined in Equation 5.9. As a result, a single pass is often not enough information to reconstruct a maneuver as shown in Table 5.6. The classifier used to measure success depends on the average error over all four post-maneuver passes. Oftentimes a reconstruction after a single post-maneuver pass may produce small errors during the pass, but the errors grow over subsequent passes. This increasing error effect after a single post-maneuver pass reconstruction is shown in Figure 5.6 for the bad-bad inclined circular-to-elliptical maneuver case. For this particular case, the cost function was approximately 3, indicating that the average residuals were well within normal tolerance for that antenna. However, the results show that additional passes of observations are necessary for successful reconstruction.
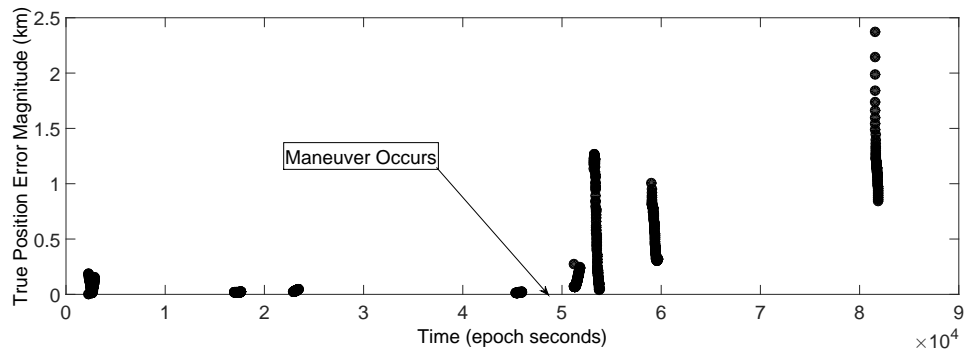
Figure 5.6: Position Error for the Bad-Bad Configuration Circular-to-Elliptical Maneuver

5.9.4 Adaptive Estimate Classifier.

Another important classifier to evaluate is whether or not a reconstructed maneuver run through a filter/smoother reduces errors below those of an adaptive filter/smoother without maneuver reconstruction. In certain cases, the output of the best adaptive filter/smoother is superior with respect to error when compared to the reconstructed cases. Using the total summed error for each case, the adaptive estimate is compared to the reconstructed maneuver and processed through the filters and smoothers. Figure 5.7 shows the results of the good antenna non-inclined circular-to-elliptical maneuver full coverage case when the maneuver is reconstructed after the third pass and compared to the IOD $\rightarrow$ BLS $\rightarrow$ EKF/smoother approach. The figure shows how successful maneuver reconstruction reduces errors below the best adaptive filter/smoother approach.
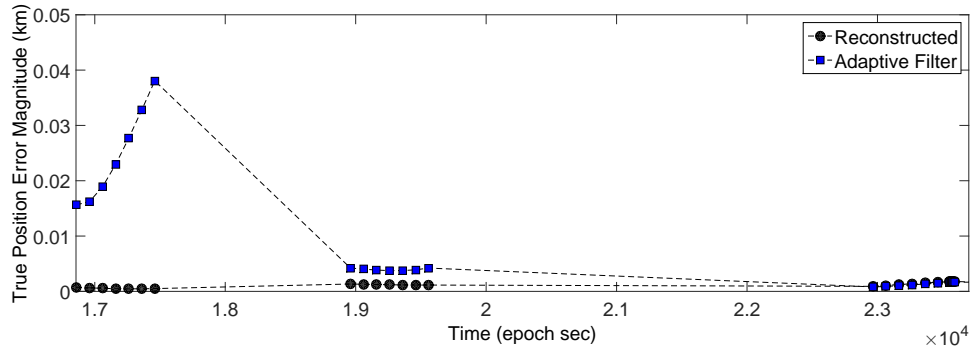
Figure 5.7: Reconstruction After Third Pass Errors Compared to the Adaptive Filter

If the goal is reducing errors, a better classifier is to determine when the reconstruction will reduce errors below the adaptive filter/smoother. Figure 5.7 shows a case where the reconstruction solution contains less error; however, this is not true for every attempted reconstruction. Using the classifier of least summed position error between the two approaches a variable analysis is performed as in Section 5.7. The results of

the classification are captured in Table 5.8. When all variables are included in the neural network pattern recognition tool, only 90% of the cases are correctly classified. Determining when the reconstruction will outperform the adaptive filter/smoother is more difficult than predicting when the average true error is below 250 m (Table 5.5). The least pertinent variables in the first two runs pertain to the residuals. As discussed above, the cost function and summed residual variables are not effective classifiers. This classification metric results in selecting the covariance and number of post passes variables as the most influential. When comparing errors of the adaptive filter/smoother to the reconstructed maneuver filter/smoother errors, the performance of the classifier fluctuates in the first two runs. This variability is a result of the fact that the neural network classification tool randomly selects the test and validation sets to calculate weights. This random selection adds a variability element to the results.

Table 5.8: Variable Influence Classifying Reconstruction vs. Adaptive Estimate

Variables	Most Influential	Least Influential	% Classified Correct
7	Post Pass #	Cost Function	90%
6	Antenna Type	Summed Weighted Residuals (Good Ant σ)	92%
5	Antenna Type	Maneuver Type	89%
4	Post Pass #	Antenna Type	85%
3	Post Pass #	Coverage Type	83%
2	Post Pass #	Covariance	83%

When determining whether or not a maneuver reconstruction will outperform an adaptive filter/smoother, only the number of post passes and covariance are necessary to achieve a classification accuracy of 83%. Using this information, a linear classifier is applied as in Section 5.9.3. The results are captured in Figure 5.8 and show the difficulty

in parsing the data. There is 92% confidence in the hypothesis that a covariance above 0.0131 km will result in a unsuccessful reconstruction during the first post pass. This delineation is a poor discriminator as no success cases are below the line; highlighting the need for a neural network classifier. The hypothesis confidence is only 62% for successful reconstruction below 0.2242 km during the second post pass. For the third post pass, there is 88% confidence in the discriminator at a covariance of 0.2896 km. Finally, there is a 91% confidence in the hypothesis that a covariance below 0.2894 km during the fourth post pass results in a successful reconstruction.
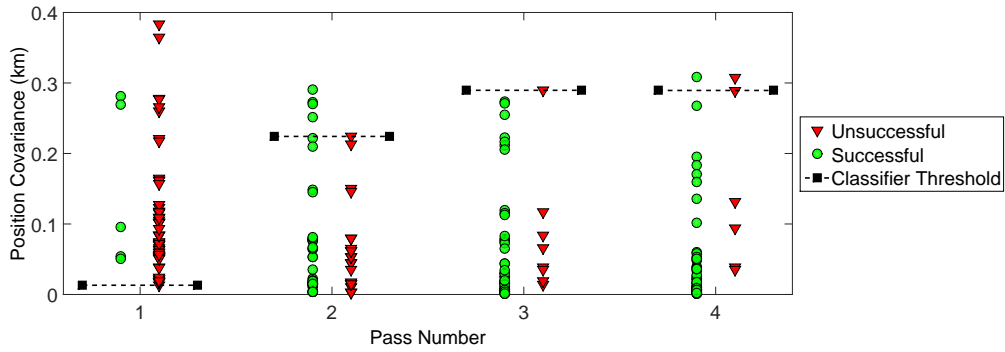
Figure 5.8: Adaptive Estimate Classifier Success Based on Post Pass and Covariances

The metric of error comparison to the best adaptive filter/smoother is the most strict definition of success evaluated. Table 5.9 displays the outcome that only 151 of 240 cases result in a successful reconstruction. Only 5 of 60 first post pass reconstruction cases are successful. This table also highlights the importance of the post passes variable when determining successful and unsuccessful cases. The percentage variability seen in the table is similar to Table 5.6 and due to the number of cases in each covariance bin and the adaptive/filter smoother performance. Overall, the results confirm the notion that

reconstruction is much more successful when smaller covariance estimates are used after multiple post passes.

Table 5.9: Adaptive Estimate Reconstruction Success with Post Pass Covariance Windows

| | Position Covariance Primary Eigenvalue Range | | | | | | | | |
| | 0 to 0.05 | | | 0.05 to 0.15 | | | 0.15 to 0.4 | | |
Pass	Success	Fail	%	Success	Fail	%	Success	Fail	%
1	0	10	0%	3	33	8%	2	12	14%
2	21	9	70%	13	8	62%	6	3	67%
3	36	4	90%	9	3	75%	7	1	88%
4	41	2	95%	7	2	78%	6	2	75%

5.9.5 *Maneuver Error Classifier.*

The analysis up to this point is dependent upon a position error metric that determines which reconstructions are successful. There is another classification metric to consider. If the reconstructed maneuver filter/smoother error does not meet the requirements discussed in Sections 5.9.3 or 5.9.4, it may still meet less stringent requirements placed only on the reconstructed maneuver vector estimate. Even though the full reconstruction does not provide the desired accuracy with respect to position error, it may still provide a general estimate of the size and timing of the maneuver. Oftentimes this estimate helps analysts understand the capabilities of the satellite and patterns of behavior, which can aid in tracking maneuvering satellites and will benefit future maneuver reconstruction efforts. A new metric is applied that considers the reconstruction a success when the estimated maneuver magnitude has less than 2% error and occurs within one minute of the actual maneuver. Table 5.10 shows successful reconstruction results by maneuver type using this metric. For many cases, the maneuver reconstructions are close enough to provide valuable details but not close enough to reduce average position errors below the desired threshold.

The classifier of position errors results in 199 success cases, as shown in Table 5.6 and 151 in Table 5.9, whereas the magnitude percent error and miss time error classifier results in 207 success cases. Table 5.10 shows how increasing the number of post passes increases the chances of success over all maneuver types.

Table 5.10: Maneuver Error Success for Maneuver Types

| | Maneuver Types | | | | | | | |
| | Circular-to-Ellip | | Ellip-to-Ellip-Velocity | | Plane Change | | Ellip-to-Ellip-Coplanar | |
Pass	Success	%	Success	%	Success	%	Success	%
1	6	40%	9	60%	12	80%	10	67%
2	13	87%	13	87%	15	100%	13	87%
3	15	100%	13	87%	15	100%	13	87%
4	15	100%	15	100%	15	100%	15	100%

5.10   Conclusions

This chapter set forth the goal of defining when precise enough orbital information was available for a maneuver reconstruction to meet defined criteria for success based on true error, outperforming an adaptive filter/smoother, and reconstructed maneuver error bounds. At the start, seven specific variables were proposed as potentially impacting the ability to define when a post-maneuver orbital solution was accurate enough for reconstruction. Based on the optimization routine used for reconstruction, it was determined that residuals were least important in classifying success or non-success for all three definitions of success. The key take away from this analysis is that if residuals are used within the cost function when selecting the best reconstruction solution, they are not a good predictor of a successful reconstruction. Instead, the results advocate against claiming reconstruction success purely based on residuals which is counter to the original notions of the authors and others.

Neural network pattern recognition with feature screening served as an initial method to reduce the number of variables while determining the impact of each. The results of the feature screening highlighted the impact of two critical variables: covariance and the number of post passes. This conclusion confirmed that a filter's covariance matrix estimates the magnitude of true error in the solution estimate. Of the 240 scenarios, the neural network classifier determines which cases result in successful maneuver reconstructions with 96% accuracy proving its effectiveness in using all variables to determine when success is expected.

The attempts made to linearly discriminate successful verses unsuccessful cases stress the lack of a concrete requirement to guarantee success in early post pass attempts. The wide variety of simulations performed show there are no clear delineations to ensure reconstruction success, but instead percentages for potential successes and general rules of thumb. Across all three classifiers the results suggest three passes are adequate to successfully reconstruct a maneuver.

While analyzing the scenarios, additional insights were gleaned. A full pass-worth of observations increases the chance of successful reconstruction by 25% when compared against a partial pass of observations. Furthermore, the results show that using good radars improves the chances of successful reconstruction by 15% when compared to tracking using medium class accuracy radars.

Overall, this chapter provides an analysis on using new adaptive filtering techniques and known reconstruction methods to predict the possibility of successful maneuver reconstructions. The results emphasize the abilities of adaptive filters in tracking maneuvering spacecraft and reconstructing maneuvers. Finally, a reconstruction is only as good as the data it is based on, and an evaluation of the number of post passes and covariance predicts the accuracy of a maneuver reconstruction.

VI.   Tracking a Continuously Maneuvering Spacecraft

6.1   Introduction

In the previous chapter, instantaneous maneuvers occurred outside of view of radars during a coverage gap. These maneuvers are easier to detect as the maneuvered orbit diverges from the predicted orbit over time. For high-priority target tracking, a maneuver could incur while in view of a ground site. For smaller continuous maneuvers, tuned logic is necessary to accurately and timely determine the start and conclusion of a maneuver. This chapter formulates an original VSD filter/smoother combination to track a spacecraft performing a continuous thrust maneuver. The approach leverages covariance inflation to ensure post-maneuver convergence [155]. A varying process noise IMM and fixed epoch smoother are applied within a VSD filter in the developed approach to track a CMS. The algorithms and analysis developed herein are designed to directly aid the SSA effort in calculating state estimates for CMS.

6.2   Filter Smoother Consistency Test

Besides the factor Ψ discussed in previous chapters, another method to determine spacecraft maneuvers is based on the filter-smoother consistency test [156; 157]. The filter-smoother consistency test was originally designed as a method to test the proper amount of process noise covariance during filtering for SOD. The test serves as a method to determine how to properly weight process noise time constants for errors in modeling perturbations, such as drag and solar radiation pressure. Overall, the test determines when a filter approach is properly capturing and modeling the dynamics. Since the filter-smoother test determines whether the orbit is fit properly, it also determines if an unknown maneuver has occurred [110]. If the filter-smoother consistency test suddenly fails after the dynamics

110

were well-modeled and previous estimates passed the test, the time of the failure is the likely start of an unknown maneuver.

The filter-smoother test declares a maneuver using Θ and a known bound. Beginning with the difference between the filter and smoother covariance at time i

$$\Delta \mathbf{P}_i = \hat{\mathbf{P}}_i - \hat{\mathbf{P}}_i^s \tag{6.1}$$

Define $\boldsymbol{\sigma}_i$ as a n x n diagonal matrix composed of indicial notation elements $\sigma_{i_{j,j}}$ which represent the square root of the diagonals in $\Delta \mathbf{P}_i$

$$\sigma_{i_{j,j}} = \sqrt{\Delta \mathbf{P}_{i_{j,j}}} \text{ for } j = 1,...n \tag{6.2}$$

where n is the number of states. The difference between the filter state, $\hat{\mathbf{x}}$, and smoother state, $\hat{\mathbf{x}}^s$ is used to complete the test.

$$\boldsymbol{\Theta}_i = \sigma_i^{-1} (\hat{\mathbf{x}}_i - \hat{\mathbf{x}}_i^s) \tag{6.3}$$

$\boldsymbol{\Theta}_i$ is a vector of length n that determines whether all states are properly estimated or if a maneuver has occurred. A maneuver is declared at t_i if the absolute value of any of the elements, Θ, in the vector $\boldsymbol{\Theta}_i$ exceed a set threshold. During simulation testing, Θ describes the largest element in $\boldsymbol{\Theta}$ at each time. In this chapter, the filter-smoother test is adapted for the use of maneuver detection, and its performance is evaluated for detecting the start and stop of small continuous thrusts.

6.3 Adaptive Variable State Dimension Filter

Increasing the filter's covariance provides a method for the filter to re-converge on the new orbital solution. When tracking a high-priority CMS, it is assumed that the post-maneuver observations are known to pertain to the target. In this case, filtering-through unknown maneuvers requires detecting the maneuver then inflating the covariance to compensate for unknown dynamics changes [155].

Nominal methods of spacecraft tracking consider a maneuver as the start of a new orbit, in which case a new initial orbit process attempts to fit the post-maneuver orbit. These approaches along with other IOD methods are designed to converge on a new post-maneuver orbit; however, in the continuous thrust case the spacecraft is still maneuvering and the orbit is still changing. The filter attempts to converge to an orbit that is changing at each observation step. Additionally, the same issue occurs when a nominal BLS approach is used to update an epoch during a continuous thrust period. If the BLS converges in the first place, the new epoch will consist of some averaged state errors caused by the maneuver. If the BLS output state epoch is propagated using a nominal EKF, the filter will quickly diverge. Clearly, a different approach is required, and the key is extending and adapting maneuver target tracking schemes designed for linear systems, i.e. aircraft, to the nonlinear discrete dynamic cases for SSA. The maneuver detection and covariance inflation approach allows a VSD to smoothly transition between added state variables.

For the continuous thrust case, the VSD filter prevents filter divergence. After a maneuver is detected when either Ψ or Θ is larger than a set tolerance, the state variable is augmented to estimate a thrust acceleration vector

$$\mathbf{x}_{Add} = \begin{bmatrix} r_I & r_J & r_K & v_I & v_J & v_K & th_{a_I} & th_{a_J} & th_{a_K} \end{bmatrix}^T \tag{6.4}$$

where $\mathbf{th}_a$ estimates the components of the thrust acceleration for the maneuver. Also, the covariance must increase in size to account for the new variables:

$$\mathbf{P}_{Add} = \begin{bmatrix} \mathbf{P} & 0 \\ 0 & \mathbf{P}_{th_a} \end{bmatrix} \tag{6.5}$$

where $\mathbf{P}_{th_a}$ is a 3×3 matrix containing the error in estimating the thrust. To estimate the new states, it is necessary to include them in the dynamics function:

$$\dot{\mathbf{x}}_{Add} = \begin{bmatrix} v_I & v_J & v_K & -\frac{\mu_\oplus r_I}{r^3} + th_{a_I} & -\frac{\mu_\oplus r_J}{r^3} + th_{a_J} & -\frac{\mu_\oplus r_K}{r^3} + th_{a_K} & 0 & 0 & 0 \end{bmatrix}^T \tag{6.6}$$

For the EKF, the error state transition matrix equation, Equation 3.5, and Jacobian, Equation 3.3, are updated to account for the added states:

$$\mathbf{A}_{Add}(t) = \frac{\partial \dot{\mathbf{x}}_{Add}}{\partial \mathbf{x}_{Add}} = \begin{bmatrix} 0 & \mathbf{I} & 0 \\ \mathbf{\Lambda} & 0 & \mathbf{I} \\ 0 & 0 & 0 \end{bmatrix} \tag{6.7}$$

where each element is a 3×3 matrix. The mapping function from one frame to the next is not changed as the thrust state variables are not used after the integration when estimating the observations. In the UKF it is also important to update the number of states, $n = 9$, in the algorithm and verify that weights and summations are calculated properly.

The thrust acceleration vector, $\mathbf{th}_a$, is purposefully selected as the additional states to generalize the approach. If $\Delta \mathbf{v}$ is selected as a state, the calculation becomes less general as defining masses and engine performance is required. The thrust acceleration state allows for calculating the maneuver as additional accelerations experienced by the spacecraft that are not modeled within the dynamics. This approach works best when the perturbing accelerations of the orbit are well known and estimated. For the scenarios, two-body equations are used, but the approach is directly applicable to any higher order propagator and estimation routine that accounts for perturbations.

When transitioning between state variables with different lengths, it is important to account for the times at which the transitions are made. The smoothing of the augmented filter outputs and nominal filter outputs must occur separately. Due to the change in size of the state, covariance, and error state transition matrices, the smoother operations cannot occur across a transition between different state variable sizes. The algorithms must track the start and stop of the additional states and store this information when determining smoothing intervals.

While estimating an unobservable thrust acceleration, the filter can at times grow overconfident in the estimate and diverge with large residuals and large Ψ values, falsely

indicating the possible conclusion of the maneuver. Improving the VSD filter is possible by tuning the filter with added uncertainty in the form of **Q** as defined in Chapter 3. Define **Q**$_{Add}$ as a 9×9 diagonal matrix composed of three, 3×3 diagonal matrices with scalar values of **Q**$_r$, **Q**$_v$, and **Q**$_{th}$. The values are separated to scale constants for the added uncertainty during the estimation of the position, velocity, and thrust. **Q** is nominally used to model propagation errors but is tunable to improve filter performance during thrust estimation. Applying the VSD to tracking CMS requires understanding and using added process noise to improve performance.

In the VSD approach it is important to only estimate the thrust when the spacecraft is thrusting; otherwise, the filter estimate is less accurate. If the approach is delayed in determining the start of the maneuver, errors build up as the spacecraft of interest maneuvers. If the conclusion of the maneuver is not detected, the filter mis-categorizes orbit errors as potential thrust accelerations causing errors to build. The start of the thrust is determined using Ψ in Algorithms 3 and 4, and Θ in Equation 6.3. The conclusion of the thrust is possible (at times) to determine using the exact same methods. While estimating the additional states during maneuvers, once Ψ or Θ exceeds a limit, the maneuver is declared complete. To use Ψ or Θ, the conclusion of the maneuver must cause errors large enough for the methods to detect.

Besides Ψ and Θ, there are other methods to determine the conclusion of the thrust. The thrust estimated as additional states during the maneuver decreases when the spacecraft concludes the maneuver. A simple way to determine the end of the maneuver is to just look at the magnitude of the estimated thrust from the VSD filter, $|\mathbf{th}_a|_2$. Once the thrust magnitude dips into the noise floor, the maneuver is declared over. This approach is typically slow in determining the conclusion of the thrust, but is fairly robust if the filter is properly tuned. Another method to determine the conclusion of the thrust uses a very

similar approach to Ψ, but instead only the thrust components are considered [57:421-488].

$$\psi_{th} = \mathbf{th}_a^T \, (\mathbf{P}_{th_a})^{-1} \, \mathbf{th}_a \qquad (6.8)$$

ψ_{th} highlights (in the form of a scalar) when the estimated thrust is insignificant and the maneuver has concluded. Once below a threshold, ψ_{th} indicates the end of the maneuver. Each method performs differently when the size of the maneuver is varied as detailed in Section 6.6.

6.3.1 Multiple Model Estimation of End of Continuous Thrust.

In the single model approach when the thrust acceleration magnitude is too small to determine the end of the maneuver by examining ψ_{th} or $|\mathbf{th}_a|_2$, a new multiple model approach is developed. The approach originated out of necessity as all reviewed methods for a single VSD filter continued to estimate thrust states long after the conclusion of the maneuver resulting in increased errors. Figure 6.1 shows the strategy for determining maneuver termination. The multiple model approach leverages the fact that Ψ indicates in real-time whether or not the filter outputs fit the orbit. Thus, if Ψ remains below a threshold when a nominal filter is run, the maneuver has ended. Similarly, Θ is another measure to use in the multiple model approach to provide a near real-time estimate of the conclusion of the thrust (with a slight delay due to the backwards running smoother).

The multiple model approach to determine the conclusion of a maneuver allows for starting nominal filters as often as accuracy requirements demand. It is necessary to inflate the covariance during the transition as it is unlikely that the orbit is perfectly estimated at the time. Next, the nominal filter will attempt to lower the covariance and converge on an orbit. If the spacecraft is not maneuvering, the filter will converge on the new orbit and Θ and Ψ will remain below their respective thresholds. However, if the conclusion is estimated prematurely, the filter will diverge as indicated by Θ and Ψ. For the approach to work, each estimate of the end of the maneuver must run for a period of time after the covariance is lowered to determine the accuracy of the prediction. The multiple model

VSD approach provides a method to estimate in real-time and near real-time the end of small magnitude continuous maneuvers using a single model. Without an effective method to determine the conclusion of the thrust, the estimation routine continues to incorrectly estimate a thrust state and the accuracy of the solution is poor.
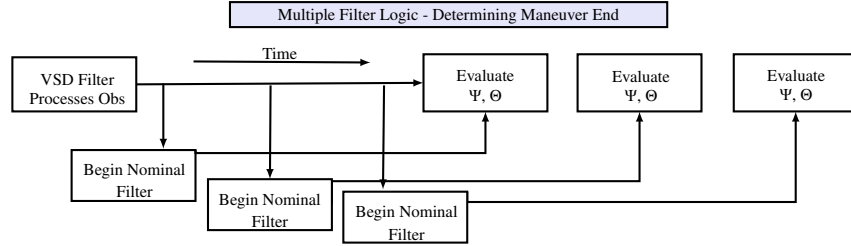
Figure 6.1: Multiple Model Estimate of Maneuver Conclusion Using Ψ and Θ

6.3.2 Variable State Dimension Tracking Filters for Maneuvering Spacecraft.

Using techniques of Kalman and VSD filtering for spacecraft tracking, this section details the logic to track a CMS. This new approach adapts the VSD filter concept for use in the spacecraft tracking problem by using covariance inflation, process noise, and estimating thrust dynamics. Additionally, the filter is adaptable to use any of the maneuver start detection and maneuver end detection methods discussed in the previous sections. This algorithm differs from traditional VSD models as it requires covariance inflation after increasing the size of the state vector to converge on the CMS. The UKF version of the adaptive VSD filter preserves the logic in Section 6.3.2 except that the UKF equations are used to estimate the state and covariance. To implement the UKF, use Algorithm 4 with the weighting scheme in Equation 3.52.

For both filters, the VSD logic begins with maneuver detection. Once a maneuver is initially detected ($\Psi_i >$ maneuver threshold), increase the states to estimate the thrust

$$\hat{\mathbf{x}}_i = \mathbf{x}_{Add} = \begin{bmatrix} r_I & r_J & r_K & v_I & v_J & v_K & 0 & 0 & 0 \end{bmatrix}^T \tag{6.9}$$

Simultaneously, add dimensions to the covariance

$$\hat{\mathbf{P}}_i = \mathbf{P}_{Add} = \begin{bmatrix} \mathbf{P}_{rr} & \mathbf{P}_{rv} & 0 \\ \mathbf{P}_{vr} & \mathbf{P}_{vr} & 0 \\ 0 & 0 & \mathbf{P}_{vv} \end{bmatrix} \tag{6.10}$$

Also, inflate the covariance until the $\text{trace}\left(\hat{\mathbf{P}}_i\right) <$ inflation threshold by repeating the operation

$$\hat{\mathbf{P}}_i = 10\hat{\mathbf{P}}_i \tag{6.11}$$

Once the maneuver concludes, reduce dimensions

$$\hat{\mathbf{x}}_i = \begin{bmatrix} r_I & r_J & r_K & v_I & v_J & v_K \end{bmatrix}^T \tag{6.12}$$

$$\hat{\mathbf{P}}_i = \begin{bmatrix} \mathbf{P}_{rr} & \mathbf{P}_{rv} \\ \mathbf{P}_{vr} & \mathbf{P}_{vv} \end{bmatrix} \tag{6.13}$$

Also, inflate the covariance again using Equation 6.11. After processing an interval of observations, filter estimates are improved with a smoother as discussed in Section 3.10.5. Ensure state dimensions are consistent throughout the smoothing interval when transitioning between maneuvering and nominal estimation.

6.4 Interacting Multiple Model

While the IMM is mostly used for tracking objects maneuvering with linear motion and objects in clutter, the approach is further tailored within the VSD filter for tracking CMS [158]. The amount of process noise added while estimating unknown thrust states in a single VSD filter impacts the performance of the filter as the thrust size varies. For larger cases, the process noise helps prevent filter divergence; whereas, the same level of noise for a smaller thrust results in an inability to accurately estimate the thrust. Since the thrust is assumed unknown a priori and during the maneuver, the IMM provides an advantage by combining the inputs of various filters that have different levels of process noise.

117

The IMM is memoryless and dependent upon certain jump probabilities, $\mathbf{Pr}_{j|k}$, at each time step. When using the IMM in tracking CMS, there is not a need to jump between varying noise models. Instead, it is more effective to use the formulation of the IMM and allow for residual based weighting of all the models. Switching in an IMM occurs according to a heuristic-based jump probability matrix at each observation and decreases performance in this application. When using a Gaussian mixture of filters to track CMS, it is best to set the probabilities of switching between models to near zero and vary the process noise levels within the filters. Existing IMM methods call for maneuver verses non-maneuver models combining at each step; however, this is very inefficient for spacecraft tracking as errors are quite large when using thrusting models to estimate a non-thrusting spacecraft. To utilize the IMM within the VSD paradigm, the IMM initiates after the maneuver is detected and terminates after the end of the maneuver. The IMM begins after covariance inflation as discussed in Section 6.3.2.

Adapting the IMM within the VSD filter after a maneuver is detected has several benefits. First, it does not limit the estimate to a single process noise filter which improves thrust estimates. Also, the weights determined by the IMM provide an initial solution for the best noise to use during post processing refinement. The outputs of the IMM are improved via a fixed lag mode matching smoother as detailed in Algorithm 6. Section 6.6 demonstrates through scenarios the benefits of the IMM when compared to a single model VSD approach.

6.5 Simulation

To test the performance of the newly developed VSD EKF, a similar VSD UKF, and a VSD multiple process noise IMM, a spacecraft is simulated in a 500 km non-inclined circular orbit. Sixteen ground-based radars are equally spaced longitudinally and placed at a latitude of $5°$. The purpose of this setup is to simulate constant coverage of the spacecraft. This orbit has a period of 5677 s and 100% of the orbit is observed after this

time. If the spacecraft is in view, each radar collects observations at 1 Hz, unless otherwise specified. Zero mean Gaussian error is added to each observation with the following standard deviations: 1 m for range, 0.01° for azimuth and elevation, and 50 mm/s for range rate. The error factors simulate the observation noise present in a very accurate mechanical tracking radar. Increasing radar noise errors will increase true position errors and thrust estimation errors; however, it will not greatly impact the maneuver detection results as the approaches are covariance based. In the EKF, $\mathbf{R}$ is a diagonal matrix containing the appropriate variances for each observation and $\mathbf{Q}$ during non-thrusting times is a matrix of zeros as only two body-assumptions are used.

After one complete orbit, the spacecraft maneuvers for 1500 seconds in the tangential direction with a thrust acceleration as detailed in Table 6.1. Then, the spacecraft is tracked for an entire orbit after maneuver completion. A maneuver is declared using limits on both Ψ and Θ and then the covariance is increased to an inflation threshold of one. The maneuver is considered complete using the various methods discussed previously, then the covariance is again increased to a threshold of one. The total $\Delta\mathbf{v}_{norm}$ values associated with Table 6.1 are 0.5, 0.25, 0.05, 0.025, and 0.005 respectively.

Table 6.1: Thrust Acceleration in the Velocity Vector Direction for Simulated Cases

	Case 1	Case 2	Case 3	Case 4	Case 5
$\mathbf{th}_a\left(\mathrm{mm/s^2}\right)$	100	50	10	5	1

A smoother is run over filter data every ten observations in the single and IMM formulations. The filter-smoother test in Equation 6.3 is conducted at every observation. Data is smoothed every ten observations as well when using the multiple filter approach to determine the conclusion of the maneuver. Each of the five maneuvers is simulated 15 times using the same observation noise. Each run is different as added random noise is

re-sampled each time. The UKF parameters are set to $\alpha = 0.1$, $\gamma = 2$, and $\kappa = -3$ within the routine (Algorithm 4).

When using the multiple model strategy from Section 6.3.1 to determine the conclusion of a maneuver, a nominal filter is run with the VSD output at ten observation intervals after the start of the maneuver. Ψ and Θ are evaluated for 1000 seconds to determine if they exceed the thresholds of 30 and 4.5, respectively. Similar to the standard VSD approach, the covariance is inflated immediately after the transition until the trace of the covariance is larger than 1. After allowing 100 seconds for the filter to settle, the first case in which Ψ or Θ remain below the threshold for the entire 1000 seconds is selected as the best guess for the conclusion of the maneuver.

The single model VSD and five model IMM values for $\mathbf{Q}_{Add}$ in the 1 Hz scenarios are detailed in Table 6.2. The values for the models were determined via sample testing of various diagonal noise vectors. The starting value for the initial weights in the IMM are $\mathbf{w} = \begin{bmatrix} 0.2 & 0.2 & 0.2 & 0.2 & 0.2 \end{bmatrix}^{T}$. Additionally, the diagonals of the $\mathbf{Pr}_{j|k}$ matrix are set to 0.999999 with all off-diagonals set to $2.5 \cdot 10^{-7}$. These starting values ensure that each model has an equal opportunity of selection and jumping between models is minimized within the IMM. Through mixing and likelihood weighting at each time step, the IMM determines the best model. For each level of thrust, the best $\mathbf{Q}_{Add}$ noise level is relatively constant; therefore, it is not necessary to jump between models at each time observation. Instead, the IMM approach is used to tune the filtering to account for various thrust sizes and process noise levels. The set of five models was determined during initial testing and deemed large enough to span the set of maneuver magnitudes simulated. Five models is also a small enough set to avoid degrading solution accuracy by averaging accurate and inaccurate model estimates. The IMM is only run after the maneuver is detected and concludes when the maneuver has ceased as determined by the methods discussed above.

Table 6.2: Process Noise Configurations for the Single Model VSD and IMM

	Single	IMM 1	IMM 2	IMM 3	IMM 4	IMM 5
$\mathbf{Q}_r$	10^{-9}	10^{-9}	10^{-10}	10^{-11}	10^{-12}	10^{-13}
$\mathbf{Q}_v$	10^{-12}	10^{-12}	10^{-13}	10^{-14}	10^{-15}	10^{-16}
$\mathbf{Q}_{th}$	10^{-12}	10^{-12}	10^{-13}	10^{-14}	10^{-15}	10^{-16}

6.6 Results

Developing tracking approaches for a CMS requires special consideration of maneuver detection approaches. The first section of the results, Section 6.6.1, compares performance of the filter-smoother test and the maneuver detection scalar Ψ in detecting the start of a maneuver. Section 6.6.2 compares the performance of four different methods to detect the end of the maneuver including the novel multiple model approach. Section 6.6.3 compares the performance of the single adaptive VSD EKF and UKF models developed in to an IMM tailored for spacecraft tracking. Next, comparisons are made by varying the frequency of observations. Finally, comments are provided for additional applications.

6.6.1 Maneuver Start Detection.

Both the maneuver detection scalar, Ψ, and filter-smoother consistency test, Θ, provide an accurate method to determine maneuvers; however, each has its advantages and disadvantages. Ψ requires tuning the limit to the orbit regime and observations. At times, large observation gaps or residuals cause a sharp increase in Ψ; therefore, for precise, small maneuver applications it is necessary to evaluate past data to determine an appropriate maneuver threshold. Additionally, if a radar is prone to spurious measurements, a window of Ψ measurements are necessary to determine the difference between the start of a maneuver and a bad data point. The benefit of this method is that it works in real-time with the filter and a maneuver is detected during the processing of the observation.

Θ is more robust because it is less susceptible to false-positives during large data gaps. The filter-smoother test requires running a smoother that works backwards in time. This feature requires the test to run on blocks of data; therefore, it is not real-time and is dependent on the frequency at which the smoother is run. The filter-smoother test can only detect maneuvers that occur within the window of the smoother. If the smoother timing is perfect, the maneuver in Case 1 is detected exactly at the start. Figure 6.2 shows the test detecting the start of the maneuver when the smoother is initiated ten seconds after the maneuver. The vertical lines in the plot define the smoother intervals and the threshold detection is set to 4.5.
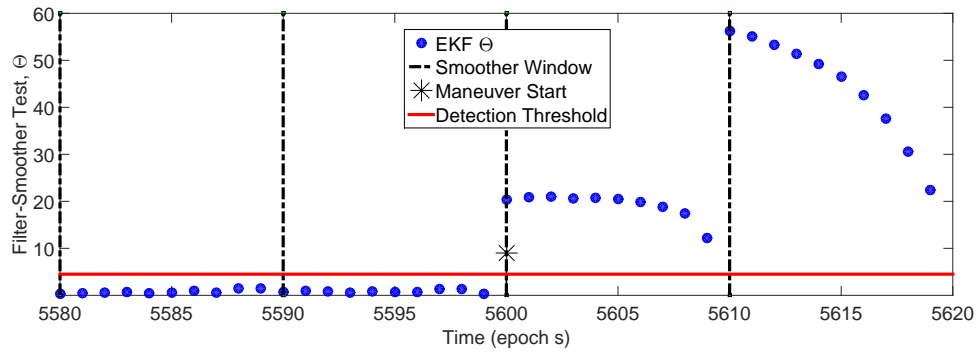
Figure 6.2: Case 1 Maneuver Detection when Smoother Window is Ideally Timed

Using the same ten second smoother window, if the start of the window is not perfectly timed, the detection of the start of the maneuver is estimated early in the smoothed block. Figure 6.3 shows how this affects when the maneuver is detected. Figures 6.2 and 6.3 show how well the filter-smoother test performs in detecting a maneuver but also how dependent the test is on the timing and length of the smoother window. The larger the smoother window, the better the smoother averages the filter. Since the smoother runs after a batch of observations is collected, a larger window results in a larger delay in detecting

a maneuver. This effect highlights a trade-off in using the filter-smoother test. During testing when observations are collected at 1 Hz, a smoother window of ten seconds is short enough to detect the maneuver quickly and large enough to improve filtered state estimates. Tuning the smoother window improves the filter-smoother test and tuning depends on the observation frequency and any observation gaps.
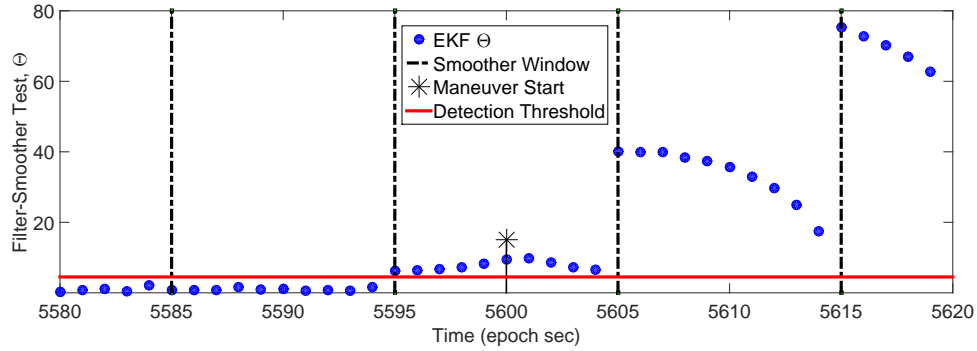
Figure 6.3: Case 1 Maneuver Detection when Smoother Window is Ill-timed

The maneuver detection scalar Ψ serves as a way to assess the error in an estimate without actually knowing the true location of the spacecraft as Ψ highlights any disparities between the covariance size and residual size. For these reasons, it proves effective in detecting maneuvers in real-time without the need to work backwards in time as the smoother does. Figure 6.4 highlights a real-time version of the VSD filter using Ψ as a transition threshold. The figure shows how Ψ grows above the threshold quickly for Case 1. At the next observation, the covariance is inflated and the states are augmented to estimate the thrust. Figure 6.4 shows how the covariance inflation drops Ψ below the threshold and the thrust estimating keeps Ψ below the threshold until the conclusion of the maneuver.

Across all five cases each simulated 15 times, Figure 6.5 shows the performance of each method using tuned detection thresholds of 30 for Ψ and 4.5 for Θ. For the filter-

123
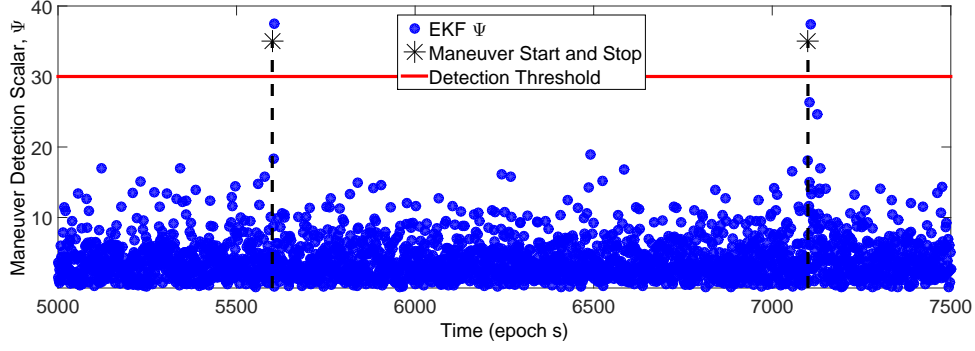
Figure 6.4: Detecting Maneuver Start and Conclusion with Ψ

smoother case, a fixed interval smoother is used after every ten observations. The filter-smoother test is perfect at detecting the start of the maneuver for the two largest test cases. This performance is linked to the fact that the smoother windows were aligned with the start of the maneuver, as in Figure 6.2. Across all cases, the filter-smoother test outperforms Ψ, which shows the strength of the proposed approach and also the benefit of using the smoother to improve filter estimates by working backwards in time. The figure also shows that as the thrust acceleration level decreases, both methods detect the start of the maneuver later and later. This trend results from the fact that the acceleration changes are so small that they are within the observation noise. As the spacecraft continues to thrust at a small acceleration, eventually the errors build up over time and the maneuver is detected.

6.6.2   *Maneuver End Detection.*

In Section 6.3.1, the multiple model approach to determine the end of a continuous maneuver was introduced to handle low thrust cases when using a single VSD model. For larger thrust cases; however, the same tests to detect the start of a maneuver can identify the conclusion of a maneuver. Figure 6.6 shows the filter-smoother test determining the end of the maneuver for Case 1 using a threshold of 4.5. The filter-smoother test detects the conclusion of the maneuver for all 15 runs of Case 1 but only for four of the 15 runs
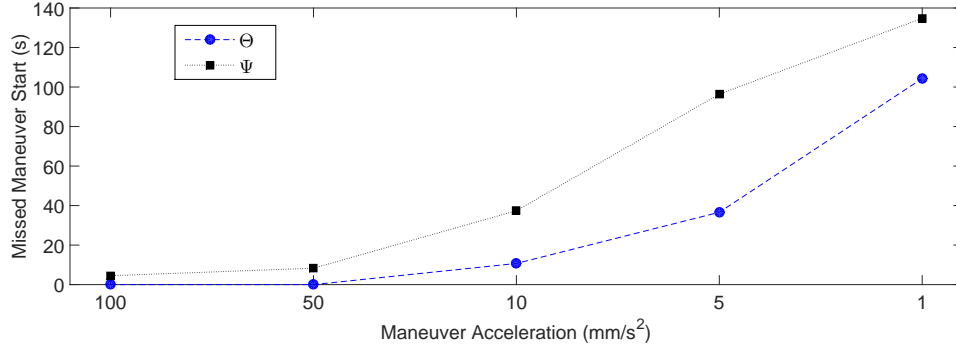
Figure 6.5: Average Error in Detecting Maneuver Start for Each Case

of Case 2. For Ψ, the end of the maneuver is more difficult to identify. While Figure 6.4 shows a single run in which the end of the maneuver is detected, out of the 15 runs of Case 1, Ψ signaled the end of the maneuver for only two of the runs.
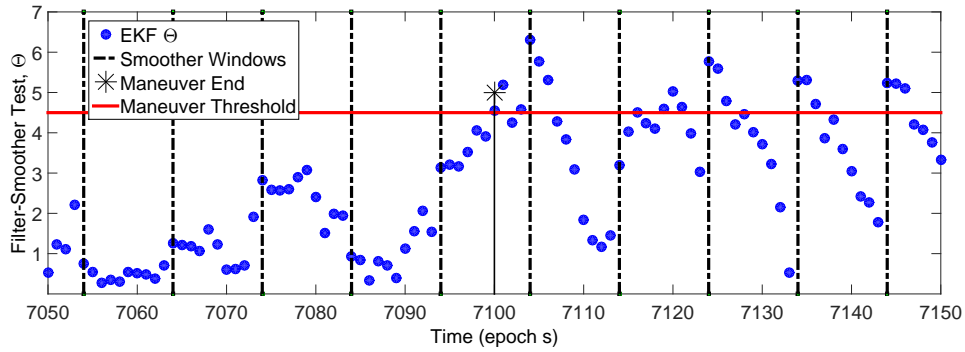
Figure 6.6: Detecting Maneuver End for Case 1 Using Filter-smoother Test

Another way to detect the end of the maneuver, as discussed in Section 6.3, is to simply evaluate the change in the estimated thrust magnitude, $|\mathbf{th}_a|_2$, to determine when the maneuver has ceased. Figure 6.7 shows how the end of the maneuver is detected by evaluating the magnitude of the thrust for one run of Case 1. The dashed square wave is the

actual thrust magnitude of the simulated spacecraft. This approach initially requires several observations for the filter to converge on the maneuver after the covariance inflation. If the covariance is not inflated, near perfect knowledge is required for the start and magnitude of the maneuver to prevent filter divergence. Once the filter locks on the maneuver, it remains locked until the spacecraft concludes the maneuver. It takes the filter over 100 seconds to begin estimating the maneuver near zero. This approach detects the end of the maneuver in a simple way, but is much slower than the filter-smoother test as shown in Figure 6.6. This method works in the exact same way for the single model approach as it does within the IMM.
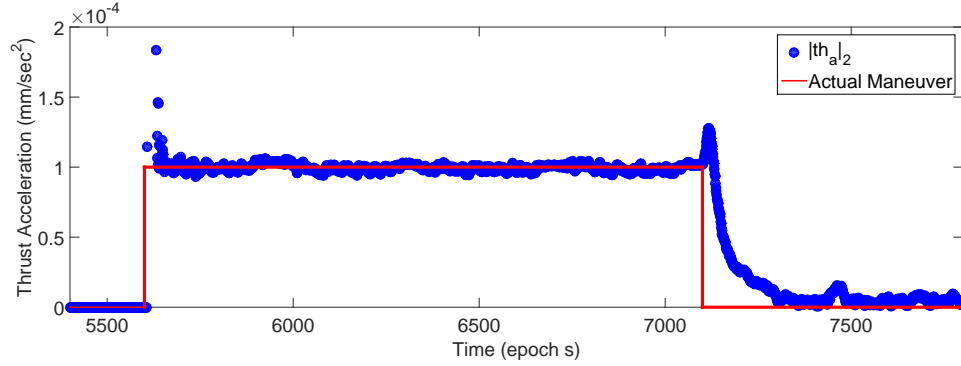
Figure 6.7: Case 1 Thrust Magnitude Estimate with Single VSD Filter.

The results for detecting the end of a Case 1 using ψ_{th}, Equation 6.8, are captured in Figure 6.8. The figure shows how this method calculates the end of the maneuver 30 seconds late, which is faster than the thrust magnitude method; however, the process still requires some tuning to declare maneuver completion. For both the thrust magnitude and ψ_{th} approaches, the tuning method is not exact. By looking at the curves shown in Figures 6.7 and 6.8, a visual inspection shows the end of the maneuver, but only after levels reach consistent near-zero values. Figure 6.8 shows a sinusoidal pattern for ψ_{th} which is a result

of the interaction between the inertial frame thrust coordinates, the thrust acceleration in the velocity direction, and the associated covariances. If the maneuver is in some combination of the radial, velocity vector, and normal directions, the shape of ψ_{th} changes, but a pattern is still easily recognizable. The pattern allows for slightly faster detection of the conclusion of the maneuver when compared to the thrust magnitude approach because once the sine wave breaks pattern, the conclusion of the thrust is realized. Additionally, this method is directly portable to the IMM approach as it relies only on the estimate thrust state and covariance.
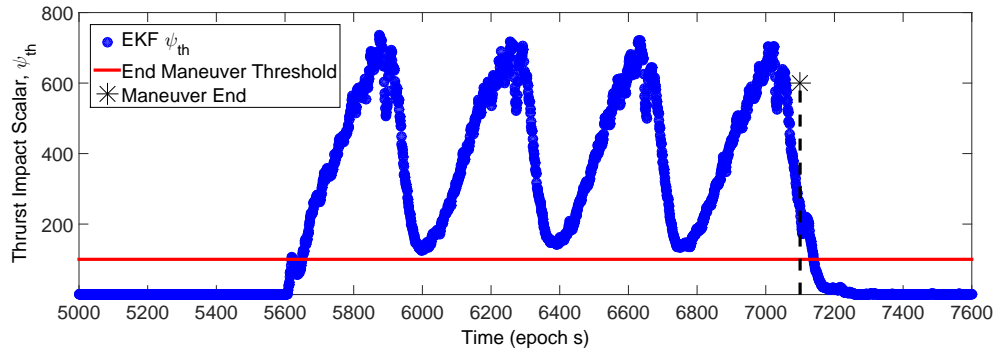
Figure 6.8: Maneuver End Detection Using Single Model ψ_{th}

Continuous thrust maneuvers are more difficult to detect than large, near-instantaneous maneuvers due to the small magnitude of continuous thrust accelerations. The conclusion of the maneuver is more difficult to determine than the start of the maneuver because the filter has a less accurate orbit fit while the maneuver is occurring. This decreased accuracy is directly related to the fact that the thrust acceleration is unobservable. Table 6.3 shows the application of each method in determining the average stop time for 15 runs of each maneuver case. The table shows that as the maneuver gets smaller, the task of estimating the end of the maneuver becomes much more difficult, especially for the single model

approaches. For all cases, an EKF is used; and for the IMM, only the $|\mathbf{th}_a|_2$ and ψ_{th} method results are listed. For the filter-smoother test, a fixed interval smoother is used after every ten observations. For Ψ and Θ, a new nominal filter is begun after every ten seconds and the first to remain under the threshold is selected as the best estimate.

Table 6.3: Errors in Determining Maneuver End; * denotes single model threshold

	Case 1		Case 2		Case 3		Case 4		Case 5	
	Limit	Miss(s)	Limit	Miss(s)	Limit	Miss(s)	Limit	Miss(s)	Limit	Miss(s)
Ψ	30	13.5	30	15.7	30	41.3	30	65.5	30	117.2
Θ	4.5	2.5*	4.5	11	4.5	23.3	4.5	33.5	4.5	105.2
ψ_{th}	125	27.8	25	35	0.15	93.4				
$\mathrm{IMM}_{\psi_{th}}$	125	31	200	10.7	50	62.2	2.0	91.5	0.25	360.5
$|\mathbf{th}_a|_2$	$5 \cdot 10^{-5}$	60.4	$2.5 \cdot 10^{-5}$	58.6	$2.5 \cdot 10^{-6}$	114.5				
$\mathrm{IMM}_{|\mathbf{th}_a|_2}$	$5 \cdot 10^{-5}$	54.3	$2.5 \cdot 10^{-5}$	55.7	$5 \cdot 10^{-6}$	73.9	$2.5 \cdot 10^{-6}$	86.9	$5 \cdot 10^{-7}$	179.7

As discussed previously, the Θ and Ψ approaches for detecting the end of the maneuver are quick to determine the end of the thrust, but only reliable for large maneuvers. The threshold approach using Θ was reliable and effective for only Case 1; whereas, the Ψ threshold was not reliable for any maneuver type once all 15 runs were considered. When small magnitude thrusting stops, the thrust level is too low to generate a large enough error to exceed the stop maneuver threshold; therefore, a multiple model strategy is necessary. Table 6.3 summarizes the results of the novel multiple model approach to determine the end of the lower acceleration continuous thrust test cases using the output from the single process noise VSD model. Based on the multiple model strategy of selecting the first case in which Θ and Ψ remained within limits, all results predict the maneuver ending prior to the actual end of the maneuver. This result is an artifact of the strategy and expected. Just as the methods take longer to detect smaller maneuvers, the multiple model strategy assumes

a good fit prior to the end of the maneuver because the thrust is too small to deviate the orbit fit. The multiple model strategy provides a more accurate initial estimate of the maneuver conclusion compared to ψ_{th} and $|\mathbf{th}_a|_2$ approaches. The method provides a way to determine the end of the smallest thrust acceleration when all other single VSD model methods fail. The multiple model approach to determine the end of the thrust can handle IMM outputs, but was not considered due to the similarities with the single model approach. The only difference is that the multiple model end thrust approach would use the state estimate from the IMM instead of from the single process noise model.

The single model ψ_{th} method is able to determine the conclusion of the thrust for the three larger maneuver cases. The level of the maneuver conclusion threshold varies for different size maneuvers. The sinusoidal wave seen in Figure 6.8 shifts lower or higher depending on the size of the maneuver and size of the process noise added. A visual inspection of the curve provides a good choice for the threshold. The different selected thresholds are shown in Table 6.3 for the 15 cases run for both the IMM and single model. Also, the table shows that ψ_{th} outperforms the thrust magnitude approach in determining the end of the maneuver for the larger cases. This trend reveals that the inclusion of the inverse covariance (information matrix) aides in detecting the end of the maneuver. Once the thrust acceleration decreases to 5 mm/s^2 the sinusoidal curve seen in Figure 6.8 becomes much less observable for the single model case and the end of the thrust is indeterminable. When using the IMM, the process noise of several models are mixed, and the method can detect the end of every thrust simulation. The smaller the thrust, the less likely the IMM$_{\psi_{th}}$ method is to outperform the IMM$_{|\mathbf{th}_a|_2}$ approach.

Table 6.3 shows that the thrust magnitude for the single model is able to determine the conclusion of the larger thrusts. Figure 6.9 shows the difference between estimating the end of the thrust using $|\mathbf{th}_a|_2$ and IMM$_{|\mathbf{th}_a|_2}$ for Case 5. The figure shows that the single model thrust magnitude estimate is far from the truth and does not change when the maneuver

129

ends. The IMM approach favors a small amount of process noise for small thrusts and is able to accurately estimate the maneuver and its conclusion. Figure 6.9 reveals the benefits of combining the IMM within the VSD for cases when the general order of magnitude of the thrust is unknown. All estimates of the conclusion of the thrust using the thrust magnitude method occur after the actual thrust conclusion. Additionally, it is important to highlight that even though the single model approach poorly models the thrust, the multiple model approach to determine the maneuver conclusion still outperforms $\text{IMM}_{|\mathbf{th}_a|_2}$.
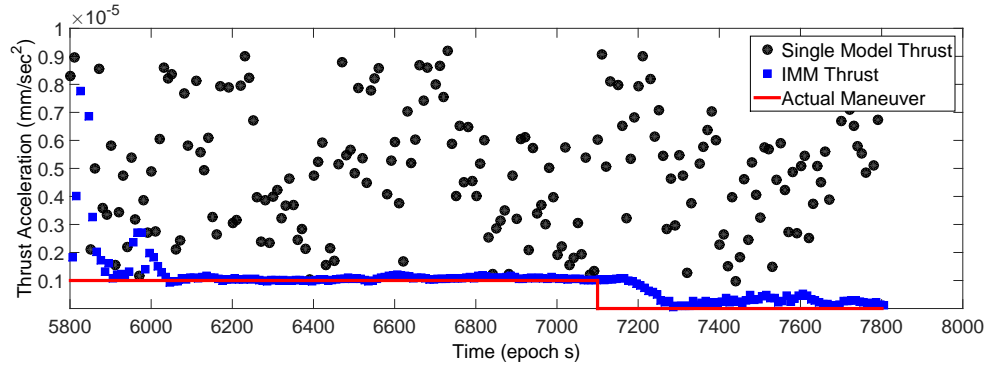
Figure 6.9: Case 5 Thrust Magnitude Estimates Using a Single Model and IMM

From the five different maneuver cases each with 15 runs, the filter-smoother approach proved most successful at determining the beginning and end of the maneuvers. Additionally, if the orbit estimation routine is tied directly to the radar and required to run in real-time, then the Ψ multiple model approach was next best in determining the beginning and end of the maneuver. Finally, the IMM approach is able to modify the level of process noise to accurately model lower thrusts.

6.6.3 Error Analysis.

The simulation results show the ability of the filter to detect the maneuver, adapt dimensions, estimate the thrust acceleration, and detect the end of the maneuver. One

method to evaluate the performance of the algorithms is to determine the RMS error between the truth orbit and the smoother estimated orbit during the maneuver as in Equation 3.58. Another metric to evaluate and assess the VSD single model and IMM approaches is to determine the percent error of the thrust estimate while the maneuver is occurring.

$$\Delta v_{err} = \sum_{i}^{N} \frac{\left| \left| \mathbf{th}_{a_i}^{true} \right|_2 - \left| \mathbf{th}_{a_i}^{est} \right|_2 \right|_1}{\left| \mathbf{th}_{a_i}^{true} \right|_2} \cdot 100 \tag{6.14}$$

There is much research effort placed on determining the start and stop of the maneuver because the orbital solution is much less accurate when estimating a thrust that is not occurring. Figure 6.10 shows the error differences that are incurred when inaccurately determining the end of the maneuver. Comparing the multiple model thrust end determination approach with the nominal single model VSD, Figure 6.10 displays the results of one of the 15 runs of Case 5. Determining the approximate end of the maneuver greatly reduces the error. The summed error for every second for the time period displayed is 53.2 km for the multiple model case and 74.9 km for the nominal VSD filter. Although the thrust is small, an inability to detect the end of the maneuver results in quickly building errors and a poor orbital solution. Without the multiple model thrust end approach, the thrust is assumed to still occur and errors continually build due to modeling a maneuver that is not occurring.

During analysis of the start and stop miss times shown in Figure 6.5 and Table 6.3, both UKFs and EKFs were initially tested. The results were nearly identical; therefore, only the EKF was used to determine the full results in the tables due to its computational speed. The UKF is reintroduced to evaluate the errors once the start and stop times of the maneuvers are estimated using the EKF. To compare the performances of the EKF to the UKF, the estimated start and stop times of the maneuver for each test case resulting from the filter-smoother tests are used to run the single model VSDs on simulated data. Additionally, the IMM approach using five models each with an EKF and different process noise as outlined
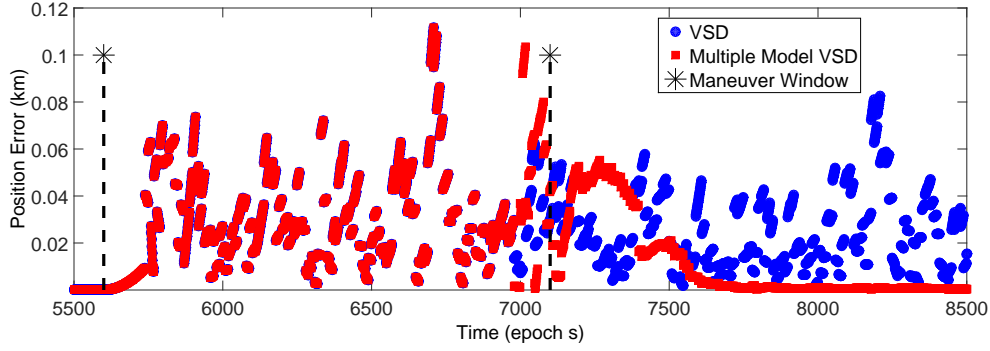
Figure 6.10: Position Error Using Multiple Model Maneuver End Detection for Case 5

in Section 6.5 is run with identical start and stop times. The errors determined from the smoother estimates are summarized in Table 6.4.

The Δv_{err} error column in Table 6.4 captures the average error in estimating the magnitude of the maneuver after the filter has settled and prior to the end of the maneuver (epoch seconds 5800 - 7100). This magnitude percent error evaluates the steady-state performance of the additional state filters and the average percent error of the magnitude of the thrust estimated. The position error column is calculated using a span of observations from 100 seconds prior to the maneuver through 400 seconds post maneuver (epoch seconds 5500 - 7500). The results pertain to an observation frequency of 1 Hz and are the average sum of the 2000 position error points across 15 cases. The table shows how closely the EKF and UKF perform. Since the observation errors are normally-distributed, it is anticipated that the filters will perform similarly. The filters are both designed and derived to minimize normally-distributed errors. The linearization of the errors performed in the EKF did not compromise the results due to the frequency of observations. The UKF avoids the linearization while sacrificing computational time, taking about ten times longer to run. For cases when radars collect observations often and at high frequencies with a high fidelity propagator, the EKF is the better choice because it is faster and errors are well approximated

132

through lineartization. If radars are of poor quality and collecting data infrequently and if a simple propagator is used, the UKF is the superior choice as it better handles un-modeled nonlinearities. The results also show that the single process noise model VSD, using either the UKF or EKF, estimates the thrust magnitude very accurately for larger thrust cases (Figure 6.7) and poorly for the low thrust cases (Figure 6.9). This result is expected as a percent error metric allows for larger errors when the thrust magnitude is larger.

Table 6.4: Thrust and Position Error Comparison Between Cases and Filters

	Case 1		Case 2		Case 3		Case 4		Case 5	
	Δv_{err}	RMS_r	Δv_{err}	RMS_r	Δv_{err}	RMS_r	Δv_{err}	RMS_r	Δv_{err}	RMS_r
EKF	2.1 %	55.1 km	3.9%	61.9 km	20.0%	56.6 km	50%	59.2 km	395.3%	54.8 km
UKF	2.1 %	55.2 km	3.9%	61.7 km	20.0%	56.6 km	50%	59.1 km	395.3%	54.9 km
IMM	1.8 %	72.5 km	2.4%	65.6 km	3.9%	52.3 km	6.6%	50.4 km	59.1%	38.9 km

For the simulations tested, the larger the maneuver, the more process noise required to prevent filter divergence. The IMM evaluates five models at each time step and weights the model based on its residual likelihood. The weights of each model, $\mathbf{w}$, for each test case and all runs are summed and normalized in Figure 6.11. As alluded to earlier, the weights clearly show the IMM favors more process noise during larger maneuver scenarios and less during smaller maneuvers. This figure supports the results in Table 6.4. The single model VSD EKF has a much larger $\mathbf{Q}$ than the weighted IMM; therefore, the EKF has larger errors for smaller thrust cases.

Additionally, Figure 6.11 shows for Case 1 that the largest weighted input does not correspond to the largest noise. The single model has a consistent position noise of $\mathbf{Q}_r = 10^{-9}$ and lower overall error. Yet, the IMM better estimates the thrust and has larger position errors. The IMM, in a sub-optimal way, selects the best weights at
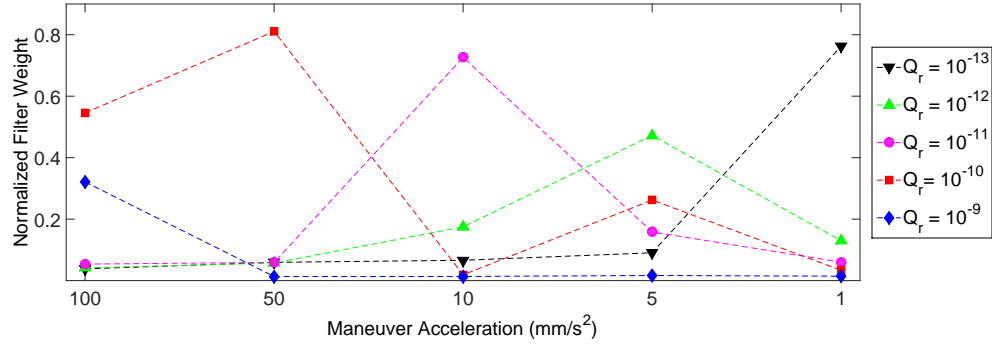
Figure 6.11: VSD IMM Normalized Filter Weights for Each Case

each observation in a memoryless fashion. Therefore, slightly growing errors over many observations are not realized, as opposed to a large error between two observations. Figure 6.12 shows how the IMM fails to add enough process noise to decrease errors as compared to a larger constant noise source. The results in Table 6.4 show the abilities of the IMM to accurately estimate thrusts at all levels. Overall, the IMM provides more flexibility to handle a wider range of thrusts; however, a properly tuned, single model approach can provide better results.
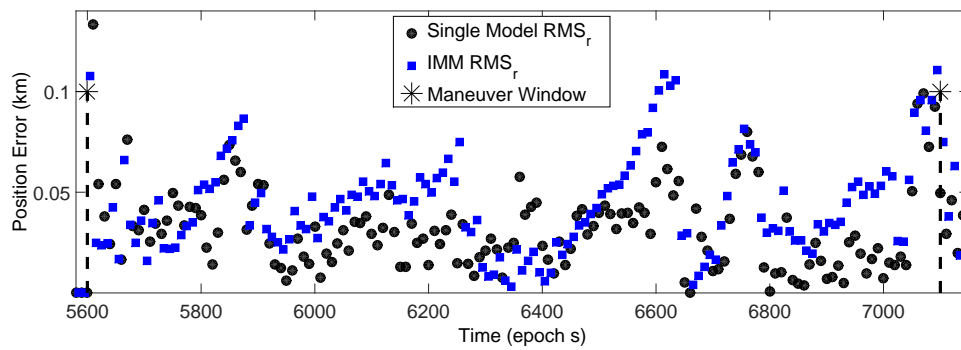
Figure 6.12: Case 1 Position Errors for a Single Model Compared to an IMM

6.6.4 Observation Frequency.

For high-priority, non-cooperative orbit determination, it is critical to utilize as much data as possible to improve the orbit estimate. To illustrate the impact of high frequency observations, the single model VSD Case 5 is performed 15 times for several different observation frequencies. Each observation frequency required tuning the added process noise $\mathbf{Q}$. The values of $\mathbf{Q}$ are determined by scaling the noise based on the observation frequency to achieve an equal comparison amongst the different approaches.

Proceeding in a similar fashion as performed in previous sections, first the start and stop maneuver times are evaluated. Table 6.5 reveals that increasing the observation frequency does not correspond to a faster maneuver detection; in fact it is slower. This result is a product of the KF routine and the very small thrust accelerations. With more frequent observations, the state is continually updated while averaging the errors associated with the undetected maneuver. With less frequent observations, the thrust accelerations cause larger errors resulting in an earlier maneuver detection. For each frequency, ten observations are processed prior to running a smoother. Therefore, for the 0.1 frequency case, one second of observations are processed; 100 seconds of observations are processed prior to smoothing for the ten second observation frequency case. The larger smoothing window allows the less-frequent observation approach to outperform the short frequency case in detecting the start of the maneuver. The short frequency case outperforms the less-frequent observation case when using the multiple model approach in Figure 6.1 at ten observation intervals to detect the conclusion of the maneuver. Overall, adding more frequent observations does not improve the filter's ability to determine the start of the maneuver; however, the ability to determine the end of the maneuver using multiple models is improved when the time between observation decreases as is evident when comparing Table 6.3 to Table 6.5.

Table 6.5: Maneuver Detection for Case 5 with Varying Observation Frequencies

Obs Freq (s)	Method	Limit	Start Miss(s)	Stop Miss(s)
10	Ψ	30	143	215.7
10	Θ	4.5	91	174.3
0.1	Ψ	30	123.2	94.1
0.1	Θ	5	104.7	81.5

Next, the errors of each approach are compared in Table 6.6 using the results from Table 6.5. The position error is the magnitude error from the smoother for Case 5 for a period of 2000 seconds that include the entire maneuver (epoch seconds 5500 - 7500). The error is determined by summing the RMS position error every ten seconds. The Δv_{err} is the average percent error from epoch seconds 5800-7100, which is the time after the filter settles until the end of the thrust. The results for the position error for Case 5 are not exactly 1/10th of the error displayed in Table 6.4 due to the fact that the error is not evenly distributed and points were selected every ten seconds. Increasing the observation frequency was not intended to improve the Δv estimation as was accomplished with the IMM; instead, the results compare the position error impact of increasing the observation frequency. The error decreases significantly as the observations increase. The higher frequency 10 Hz (0.1 s) case outperforms the 1 Hz case for nearly the entire period of the thrust estimation. The results in Table 6.6 solidify the proposal that increasing the observation frequency from the same radar improves the tracking solution when all other variables are held constant. Therefore, when available, it is best to use as much of the data as possible from the radar to track the non-cooperative spacecraft.

6.6.5 Additional Applications.

The simulations tested all provided constant coverage of the CMS which is not likely in operational tracking. The scenarios were purposefully designed to test the abilities

Table 6.6: Position and Thrust Error when Observation Frequency is Varied

Observation Frequency(s)	$\mathbf{Q}_p$	$\mathbf{Q}_v$ & $\mathbf{Q}_{th}$	Δv_{err}	RMS_r
10	10^{-8}	10^{-11}	393%	8.3
1	10^{-9}	10^{-12}	390%	5.3
0.1	10^{-10}	10^{-13}	326%	3.0

of the VSD and IMM approaches in a simple environment. Due to limited ground site resources and observation geometry, a realistic orbit determination routine for a high-priority spacecraft will contain coverage gaps as sensors are sparse. The new multiple model approach developed and tested can also serve as a way to handle coverage gaps. If the spacecraft is maneuvering as it exits coverage, the multiple model approach can use a baseline model that assumes the thrust continues and then use other models to estimate the end of the thrust at different intervals. This approach provides a set of possible thrust durations and locations of the spacecraft. Once the radar reacquires the spacecraft, the closest of the multiple models is selected as the best guess for the thrust that occurred outside of view.

Additionally, the VSD and IMM can process data from observations made by any sensor, as long as the observation errors are understood. Both methods are directly portable to higher fidelity orbit propagators and estimation routines. Once the maneuver is estimated via the smoother, some assumptions may improve the solution quality. If it is assumed that the maneuver is constant over the time window, the filter-smoother combination can reprocess the data while assuming a constant thrust. Also during post-processing, different optimization and input estimation routines are implementable to further reduce errors now that the VSD approach detected start times, stop times, an initial estimate of the maneuver, and an IMM provided process noise estimate.

6.7   Conclusion

Overall, the newly developed VSD IMM algorithm is successful at performing orbit determination on a CMS, and the new maneuver end multiple model method provides accurate estimates of maneuver end times. Where traditional IOD and BLS methods fail to converge on an orbit, the VSD IMM with covariance inflation provides a new approach to perform tracking and orbit determination in real-time for high-priority cases.

While the IMM approach provides the flexibility to handle maneuvers of all magnitudes, a well-tuned single model filter can outperform the multiple model approach. The research shows that if the magnitude of potential maneuvers is known, the best solution is to tune a single VSD model for tracking. If little data is available on a spacecraft that can quickly throttle maneuvers, an IMM approach is recommended during initial real-time processing and tracking. The initial thrust and state estimates from the VSD models provide excellent starting values for further analysis using optimization and refinement tools during post-processing.

The algorithm developed in this chapter extends and improves existing filtering methods in the literature from their generic forms into a method to meet the SSA demands for tracking a high-priority non-cooperative spacecraft.

VII.   Short Arc Covariance Intersection

7.1   Introduction

Focused on SSA, McCall and Darrah propose the need for companion satellites in LEO to monitor other satellites and/or debris [159]. This approach would require the ability to quickly determine the orbit of a non-cooperative satellite then estimate and propagate its covariance. The research in this chapter is motivated by this same idea and focuses on short arc orbit determination and short-term covariance propagation. The goal of this chapter is to develop a method and metrics to determine a minimum pass length for orbit fitting and estimating to meet a projected covariance requirement. The driving question is "what is the confidence in the short-term propagation of a short arc orbit fit using radar observations?" More specifically, "how many observations from a radar are needed to fit an orbit so that the propagated covariance meets an error requirement defined by a six dimensional manifold or three dimensional ellipsoid?" While previous chapters focused on the filter-through and reconstruction approaches, this chapter focuses on the new IOD method.

This chapter considers the need to quickly place an object within an n-dimensional hypervolume to interact with a non-cooperative object of which only a small portion of the orbital information is known. Consider the mission example of a failed spacecraft in a critical orbit that requires removal. Outgassing and a lack of ephemeris has made long term orbit predictions difficult for the damaged satellite. This research investigates the accuracy of the orbit fit needed prior to launching a servicing satellite. The primary concern is the time required to reach the vicinity of the failed spacecraft. Focusing on LEO objects, the purpose of this work is to evaluate whether a short orbit fit is sufficient to meet a covariance requirement. While others focused on the probability of collision, this chapter examines the percentage of shared n-dimensional hypervolumes between a covariance requirement

and a propagated non-cooperative object covariance [13; 95; 98]. For simplicity, manifolds greater than three dimensions are referred to as n-dimensional ellipsoids.

This effort strives for covariance realism by using an IOD→BLS→UKF to process observations and a UKF to propagate orbital states and covariances over short periods of time. The UKF is chosen as it was shown to preserve covariance realism better than an EKF [160]. The test statistics originate from the propagation step only in which Monte Carlo points are distributed according to a starting mean and covariance. Confirming results by Horwood et al., initial testing verified covariance realism is achieved using an IOD then BLS filter to update the epoch and covariance [89]. Combining this approach with a UKF, covariance realism is preserved, but only for a single instance of the estimation chain. This chapter evaluates the entire estimation chain for realism multiple times for varying orbits.

Given a specified number of observations, this chapter desires to determine the probability that a predicted state meets an accuracy requirement. A straightforward method to determine this probability is to perform the entire estimation chain multiple times in a Monte Carlo fashion. The probability of success is then just the percentage of successful final estimates. In the next sections, other methods involving covariances are developed to compare against the Monte Carlo full estimation chain probability.

7.2 Ellipsoids from Gaussians

For collision avoidance, the top three by three section of the covariance matrix is visualized as a position ellipsoid [94]. Consider an n-D ellipsoid requirement defined by a multivariate Gaussian $\mathcal{N}(\mu, \mathbf{P})$. This chapter seeks a method to determine the percentage of the propagated pdf n-D ellipsoids that lie within a n-D requirement ellipsoid. Additionally, the paper considers p standard deviations of the propagated pdf n-D ellipsoid that lies within the n-D requirement ellipsoid. The number of states is generalized to allow for a three dimensional position or velocity analysis and an overall six dimensional analysis. The squared Mahalanobis distance for Gaussian pdfs is identical to a $(p\sigma)^2$ surface of an n-D

ellipsoid. Given the center $\boldsymbol{\mu}_{ell}$ and the shape matrix $\mathbf{P}_{ell}$, an n-D ellipsoid conforms to the equation

$$(\mathbf{x} - \boldsymbol{\mu}_{ell})^T \, \mathbf{P}_{ell}^{-1} \, (\mathbf{x} - \boldsymbol{\mu}_{ell}) \leq 1 \tag{7.1}$$

The covariance approximates errors represented by σ^2 components. Substituting an orbital state and covariance, the surface of an n-D ellipsoid consists of the locus of points, $\mathbf{b}$, that satisfy the equation

$$(p\sigma)^2 = \left[(\mathbf{b} - \boldsymbol{\mu})^T \, \mathbf{P}^{-1} \, (\mathbf{b} - \boldsymbol{\mu}) \right] \tag{7.2}$$

Therefore, the set of all vectors $\mathbf{b}$ with a squared Mahalanobis distance equal to $(p\sigma)^2$ represent the surface of the $p\sigma$ n-D ellipsoid. Any vector with a squared Mahalanobis distance greater than $(p\sigma)^2$ lies outside the error ellipsoid and any vector with a smaller Mahalanobis squared distance lies within the error ellipsoid. Given that ellipsoids are preserved under the affine transformation, if the ellipsoid 1σ boundary points are known, multiplying them by p^2 scales the ellipsoid to the desired error size.

Alfano and Greer transform the ellipsoid equation into a matrix formulation [94]. This development is well suited to determine if ellipsoids intersect. Begin with a position $\boldsymbol{\mu}_r$ and covariance $\mathbf{P}_r$ corresponding to a multivariate Gaussian. Take the inverse of the position covariance via $\mathbf{L} = \mathbf{P_r}^{-1}$

$$\mathbf{L_r} = \begin{bmatrix} L_{11} & L_{12} & L_{13} & 0 \\ L_{21} & L_{22} & L_{23} & 0 \\ L_{31} & L_{32} & L_{33} & 0 \\ 0 & 0 & 0 & -1 \end{bmatrix} \tag{7.3}$$

Define the translation matrix

$$\mathbf{T} = \begin{bmatrix} 1 & 0 & 0 & 0 \\ 0 & 1 & 0 & 0 \\ 0 & 0 & 1 & 0 \\ -\boldsymbol{\mu}_{r_1} & -\boldsymbol{\mu}_{r_2} & -\boldsymbol{\mu}_{r_3} & 1 \end{bmatrix} \tag{7.4}$$

Describe a vector, $\boldsymbol{\gamma}$, as any point in 3-D Cartesian space

$$\boldsymbol{\gamma} = \begin{bmatrix} x & y & z & 1 \end{bmatrix} \tag{7.5}$$

Given this formulation, any position represented by $\boldsymbol{\gamma}$ that lies within or on the ellipsoid meets the condition that

$$\boldsymbol{\gamma}\mathbf{T}\mathbf{L_r}\mathbf{T}^T\boldsymbol{\gamma}^T p^2 \leq 0 \tag{7.6}$$

in which p^2 describes the preferred σ sizing. This matrix derivation provides a straightforward effective way to determine if a given point, $\boldsymbol{\gamma}$, lies within a defined requirement ellipsoid. Additionally, this method is well-suited for a numerical Monte Carlo evaluation of test points. Finally, the derivation above is specific for the 3-D case, but expands to n-D without loss of generality when $\boldsymbol{\gamma}$ is defined as a $1 \times (n + 1)$ vector and $\mathbf{T}$ and $\mathbf{L}_S$ are defined as $(n+1) \times (n+1)$ matrices. The expansion to matrices in n-D follows the same format as shown above. An example of the matrix formulation to determine interior ellipsoid points is shown in Figure 7.1.

7.2.1 Ellipsoid Surface Points.

For visualization and analysis, it is often necessary to numerically determine a locus of n-D points, **b**, that lie on the surface of an ellipsoid. Randomly sampling points can create a uniform distribution of points on the surface of the unit N-sphere [161]. Begin by generating a vector **g** composed of n components that are each sampled independently from the standard normal distribution. Then, divide each sample by the magnitude of the vector

(2-norm)

$$\mathbf{x}_s = \frac{\mathbf{g}}{|\mathbf{g}|_2} \tag{7.7}$$

Specifically, $\mathbf{g}$ is a $n \times 1$ vector with the elements $g \sim \mathcal{N}(0, 1)$. This process is repeatable until an adequate amount of vectors numerically represent the surface of the N-sphere [161]. Next, transform the points to the desired N-ellipsoid with center $\boldsymbol{\mu}$ and shape matrix $\mathbf{P}$. The transformation is performed via an eigen decomposition [13:21-26]. In orbital dynamics the covariance matrix is defined as positive definite and symmetric with six real eigenvalues. To perform the transformation of a single point lying on the N-sphere, determine the eigenvalues and eigenvectors of the covariance matrix. Define the eigenvalues as λ and the eigenvectors as $\mathbf{v}$. Also, denote $\mathbf{V}$ as the matrix composed of the eigenvectors. Create a rotated and translated ellipsoid of desired $p\sigma$ size using the sampled vectors $\mathbf{x}_s$ each with elements $\mathbf{x}_s^j$ for $j = 1...n$

$$\mathbf{x}_e^j = p \sqrt{\lambda_j} \cdot \mathbf{x}_s^j \tag{7.8}$$

$$\mathbf{x}_b = \mathbf{V}\mathbf{x}_e + \boldsymbol{\mu} \tag{7.9}$$

The set of vectors $\mathbf{x}_b$ lie on the desired ellipsoid and are sizable to any desired $p\sigma$ confidence. Figures 7.1 and 7.2 use the discussed transformations to visually represent ellipsoids.

7.2.2 *Covariance Intersection.*

With defined expressions of n-D ellipsoids and the ability to determine when states lie within ellipsoids, Monte Carlo testing can determine the percentage of propagated states that lie within a covariance requirement. Using Equation 7.6 analysis will determine if a state lies within an ellipsoid that is generated from a required covariance. As discussed above, the simplest method to determine the probability of success for a scenario is to run the entire estimation chain multiple times and determine the percentage of end state

successes. This approach is time consuming and does not necessarily correlate to a real-time tracking operation, however, it does provide a benchmark to compare against.

Another way to determine the probability of success is to find the extent to which the final two covariances intersect. Generally speaking, the goal is to estimate a set of intersection states $\mathbf{x}_{int}$ such that $\mathbf{x}_{int} \in \mathcal{E}(\boldsymbol{\mu}_{est}, \mathbf{P}_{est}) \cap \mathcal{E}(\boldsymbol{\mu}_{req}, \mathbf{P}_{req})$ in which $\mathcal{E}$ describes an ellipsoid with mean $\boldsymbol{\mu}$ and covariance $\mathbf{P}$. There is not a simple analytical solution to the describe the shape and hypervolume resulting from the intersection of two n-D overlapping ellipsoids. Alfano projects the intersection onto a 2-D plane and integrates to solve for the shared volume [97]. The motivation for this research is to maintain the generality of a n-D intersection case. To capture the probabilistic hypervolume shared by the intersections of two ellipsoids, a straightforward numerical approach is developed.

The intersection between the propagated covariance ellipsoid and the requirement covariance ellipsoid represents the probability of success that the propagated states lie within the requirement. Consider numerically representing the propagated covariance by sampling the multivariate Gaussian distribution via a large set of points

$$\mathbf{x}_{est}^{mc} = \boldsymbol{\mu}_{est} + \mathbf{A}_{est}(\boldsymbol{\psi}) \tag{7.10}$$

in which $\mathbf{A}_{est}^T \mathbf{A}_{est} = \mathbf{P}_{est}$ and $\mathbf{A}_{est}$ is determined via a Cholesky decomposition. The vector $\boldsymbol{\psi}$ is $n \times 1$ with elements $\psi_i \sim \mathcal{N}(0, 1)$. A large set of these points numerically capture the propagated multivariate Gaussian. The probability of success is then the number of sampled points that fall within the requirement covariance ellipsoid divided by the total number of sampled points. This approach allows for sampling across the entire distribution in any number of dimensions. Figure 7.1 visualizes position samples from the 5σ propagated ellipsoid used to determine intersection with the required ellipsoid. Samples within the intersection are colored black.

There are optimization routines which can find an ellipsoid that approximates the volume shared by the intersection of two ellipsoids [162]. The intersection of two ellipsoids

144
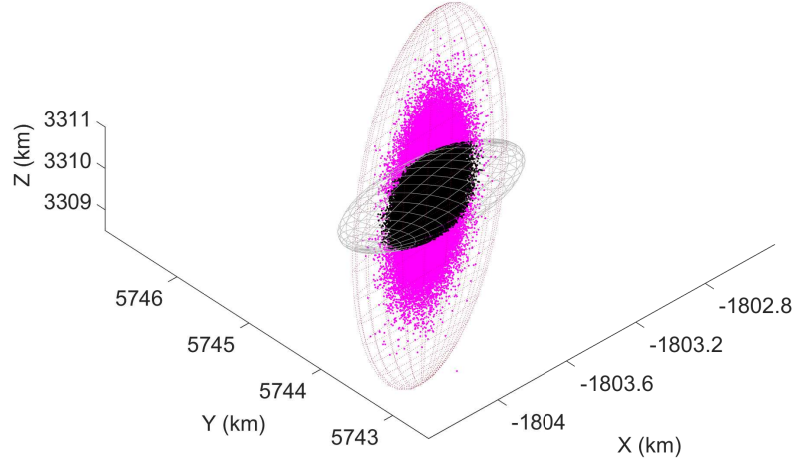
Figure 7.1: Approximating Ellipsoid Intersection with Numeric Sampling

is not necessarily an ellipsoid; however, an ellipsoid can approximate the intersection. The difficulty of the ellipsoidal approximation is reduced when assuming the intersection ellipsoid shares the same orientation as one of the ellipses. This intersection approach lends itself as a worst case probability estimate. Instead of using an optimization routine to solve for the ellipsoidal approximation of the intersection, consider the sampled points in Equation 7.10. Provided that at least one of the sampled points from the propagated state covariance lies outside the required covariance, the propagated covariance is sized so that the outlying point is a boundary point of a new ellipsoid that approximates the intersection. Using Equation 7.6 and sampled states from Equation 7.10, it is possible to find the state outside the intersection with the smallest p value

$$\mathbf{x}_{out} \in \left(\mathcal{E}\left(\boldsymbol{\mu}_{est}, \mathbf{P}_{est}\right) \cap \mathcal{E}\left(\boldsymbol{\mu}_{req}, \mathbf{P}_{req}\right) \right)^{C} \tag{7.11}$$

$$p_{app}\sigma = \min\left[\sqrt{\left(\mathbf{x}_{out} - \boldsymbol{\mu}_{est}\right)^{T} \mathbf{P}_{est}^{-1} \left(\mathbf{x}_{out} - \boldsymbol{\mu}_{est}\right)} \right] \tag{7.12}$$

The intersection approximating ellipsoid is $\mathcal{E}(\boldsymbol{\mu}_{est}, \mathbf{P}_{est})$ sized according to p_{app} with a locus of boundary points specified by Equations 7.8 and 7.9. Using Equations 3.61 and 3.62 with the resulting p value from Equation 7.12, a probability of the state lying within the intersection approximating ellipsoid is determined. Given enough samples in Equation 7.10, a point is found just outside the intersection to size the approximating ellipsoid, and the results are similar to an optimization routine. Figure 7.2 shows the approximating ellipsoidal capturing the intersection of a required and propagated covariance. Notice that the approximating ellipsoid approach does not capture the full intersecting volume when compared to the sampling approach in Figure 7.1. Both approaches are independent of the dimension choice.
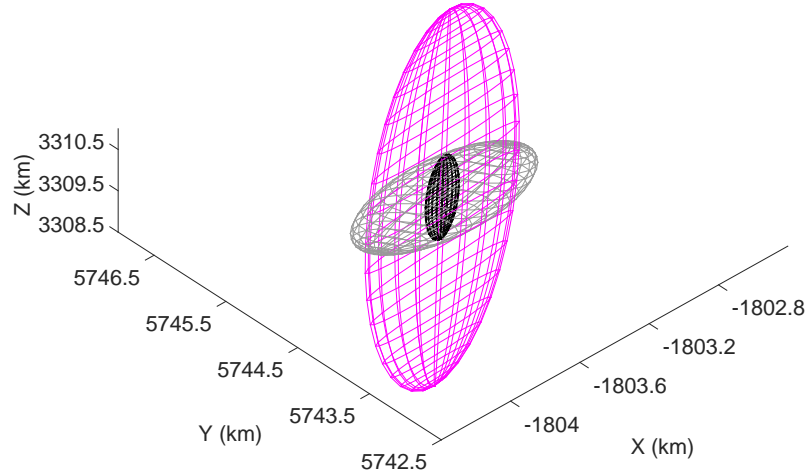
Figure 7.2: Approximating Ellipsoid Intersection with an Ellipsoid

Three methods are presented to estimate the probability of success that an orbit fit meets a required covariance: run the entire estimation chain multiple times and determine the percentage of propagated states that meet the requirement, sample the propagated

covariance and determine the percentage of samples that meet the requirement, and use an ellipsoidal approximation of the intersection to determine the probability of success.

7.3 Simulation

The goal of the research is to analyze the probability that a short arc orbit determination meets a predetermined covariance requirement as detailed in Figure 7.3. To test the covariance intersection methods, the full estimation chain is run in Monte Carlo fashion across a set of scenarios and success probabilities are compared. The set of scenarios chosen are designed to determine the number of observations necessary to meet a given covariance requirement. To further breakdown this problem, four parameters of the simulation are selected as design variables: radar performance, altitude, inclination, and observations processed.

To vary radar performance, simulated perfect observations are perturbed by adding random noise based on the radar's estimated error σ values, $\mathbf{R}$. Three specific profiles are selected based off of actual performance data and are listed in Table 7.1. In the simulation, a single ground site is placed at 0 deg longitude, 5 deg latitude and 0 km altitude and begins collecting observation vectors at 1 Hz once the satellite is above 5 deg elevation. For this research, it is assumed that the radar successfully finds, fixes, and acquires observations from the desired object.

Table 7.1: Radar Measurement Standard Deviations

Radar	σ_ρ (m)	σ_β (deg)	σ_{el} (deg)	$\sigma_{\dot{\rho}}$ (m/s)
Good	5	0.01	0.01	0.05
Average	25	0.03	0.03	0.2
Poor	100	0.05	0.05	10

The following orbital altitudes are simulated: 350, 500, 750, and 1000 km. Additionally, the orbital inclinations of 30, 60, and 90 deg are considered. Finally, six different thresholds of observations are considered for evaluation: 15, 30, 60, 120, 180, and 240 observations. The eccentricity of all orbits is fixed at 0.002 and the remaining classical orbital element angles are all set to 0 deg. With all combinations of radar performance, altitude, inclination, and observations, 216 test cases are considered. For Monte Carlo purposes, each simulation is run 100 times varying the observation noise randomly. For each orbit test case, the percentages based on the observation amounts are provided in Table 7.2.

Table 7.2: Percentage of Orbit Observed

	Observations					
Altitude (km)	15	30	60	120	180	240
350	0.3	0.6	1.1	2.2	3.3	4.4
500	0.3	0.5	1.1	2.1	3.1	4.2
750	0.3	0.5	1.0	2.0	3.0	4.0
1000	0.2	0.5	1.0	1.9	2.9	3.8

The estimation chain of IOD→BLS→UKF detailed in Chapter 3 processes the simulated observations. The first three available observations are selected for the Herrick-Gibbs IOD (Equation 3.37). Up to 150 observations (when available) are used for the BLS filter to update the epoch state and covariance (Algorithm 2). The UKF then processes every other observation from the epoch until the final observation as determined by the scenario (Algorithm 4). There is no noticeable performance degradation in processing only every other observation in the UKF compared to every observation. Every other observation is selected for computational speed purposes. After the final observation, the covariance

is propagated for 10 minutes and then compared to the required covariance. The scenario formulation is captured in Figure 7.3.

For the covariance sampling, $k = 5 \times 10^5$ samples are selected to numerically represent the distribution of the propagated covariances using Equation 7.10. The k value was determined during initial testing by varying the number of points until the change to the next greater number of points was indistinguishable. As stated previously, 100 state vectors are considered for testing the entire estimation chain to determine whether the final state lies within the requirement. The covariance requirement $\mathbf{P}_{req} = \mathbf{A}_{req}^T \mathbf{A}_{req}$ is defined as a 6-D diagonal matrix in km and km/s centred on the simulated true final location of the tracked object. Table 7.3 lists the standard deviations for three requirement covariances of interest.

Table 7.3: Requirement Accuracy Levels

Accuracy	σ_{r_I}	σ_{r_J}	σ_{r_K}	σ_{v_I}	σ_{v_J}	σ_{v_K}
Low	10	10	10	0.01	0.01	0.01
Medium	1	1	1	0.001	0.001	0.001
High	0.5	0.5	0.5	0.0005	0.0005	0.0005

The required covariance is provided in the RSW frame. To compare to an inertially propagated covariance, the required covariance is rotated to the inertial frame via the transformation $\mathbf{P}_{ECI} = \mathbf{ROT}\,(\mathbf{P}_{RSW})\,\mathbf{ROT}^T$ [12:818-819].

7.4   Results

7.4.1   Full Estimation Chain Covariance Realism.

A main goal of this section is to verify the covariance intersection methods discussed above. These methods are advantageous for mission operations as they avoid running Monte Carlo trials to determine a probability of success. The intersection methods require a single realistic propagated covariance centered around a propagated state. During
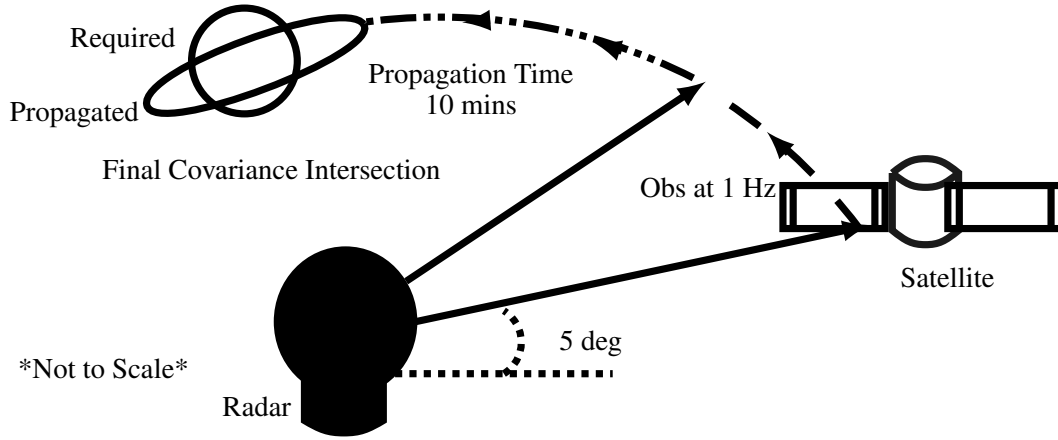
Figure 7.3: Scenario Diagram

simulation testing, the estimation chain is run 100 times for each scenario resulting in 100 estimated states and 100 estimated covariances. The estimated states represent a distribution that is captured by a covariance. To use the covariance intersection methods described in Section 7.2 to determine the probability of success, it is necessary to consolidate all propagated covariances to a single realistic covariance. To leverage the UKF routines and avoid the need of running Monte Carlo trials in the future, the goal is to find a Gaussian to capture the distribution of the propagated states. Given all the states, an iterative EM algorithm is run to solve for a covariance [102]. This algorithm is discussed in further detail in Chapter 9. Define the maximum expectation mean and covariance for each scenario case as $\boldsymbol{\mu}_{EM}$ and $\mathbf{P}_{EM}$. This new covariance meets realism requirements in all cases except for two of the shortest observation run cases for the poor radar. One case achieves realism by removing an outlier, while the other requires a Gaussian mixture to preserve realism.

While the maximum expectation covariance can validate the covariance intersection sampling approach, it requires knowledge of all propagated Monte Carlo trial states. The expectation of a run of the full estimation chain is the mean of the propagated states, $\boldsymbol{\mu}_{est}$. "Fattening" the average propagated covariance, $\mathbf{P}_{est}$, around the mean propagated state can

result in achieving realism. The average covariance of all runs has the proper orientation but is too small to capture the spread of all propagated states. For a single mean and covariance propagated from the final observation time, realism is preserved. However, this work is addressing the entire estimation chain and searching for a final covariance to capture a distribution of states from the orbit estimation chain.

Using the EM Gaussian ($\boldsymbol{\mu}_{EM}$, $\mathbf{P}_{EM}$) for each test case, a scalar constant, ξ, is tested to fatten the average propagated covariance to form a Gaussian ($\boldsymbol{\mu}_{est}$, $\xi\mathbf{P}_{est}$). A static optimization routine is run to determine the optimal value of ξ to minimize the Kullback-Leibler divergence between the two distributions for each case [163].

To make the approach applicable to all cases, the resulting ξ values are averaged and a new, single ξ value is considered. Sampling around the average and testing, the best ξ value for achieving covariance realism was found to be 1.5. This value results in achieving covariance realism in 95.4% of the cases. Therefore, when using covariance intersection methods to determine probabilities for a single case, fatten the final propagated covariance by a factor of 1.5. Fattening will increase the likelihood of achieving covariance realism and account for the variability in the full estimation chain. This testing is the first attempt at preserving covariance realism across an entire estimation chain. When Monte Carlo runs are available, the EM covariance is recommended as it is more effective in achieving realism. When using a single estimation chain run, fattening the final covariance by $\xi = 1.5$ is recommended.

7.4.2 Covariance Intersection Validation.

Using the EM covariance, $\mathbf{P}_{EM}$, the probability of success using the Monte Carlo propagated states is compared against sampling the propagated covariance intersection (Equation 7.10) and estimating the intersection using an ellipsoid (Equation 7.12). Figure 7.4 displays the differences in the calculated position probabilities of success using the three approaches for the high accuracy, average radar cases. The figure clearly

151

shows the close relationship between covariance sampling and the Monte Carlo runs. Additionally, it shows that estimating the intersection with an ellipsoid results in a worst-case estimate of the success probability. This result is due to the inability of an ellipsoid to properly capture the intersection. For the full six dimensional covariance requirement, comparing the same cases of the two intersection approaches with the Monte Carlo state success probabilities matches trends in Figure 7.4. In the figure, the scenarios are sorted to start with the largest observation case then vary inclination and altitude prior to moving to the next observation number case. This organization eases comparability between the three methods. The covariance sampling has a maximum error of 9.2% and an average error of 1.2% while approximating the intersection with an ellipsoid has a maximum error of 77.5% and an average error of 12.7%. The results validate that given a realistic covariance, sampling the covariance and determining the intersection percentage provides an accurate representation of the probability of meeting a requirement. This approach of intersection sampling results in an efficient and accurate way to determine success probabilities given a realistic propagated covariance.
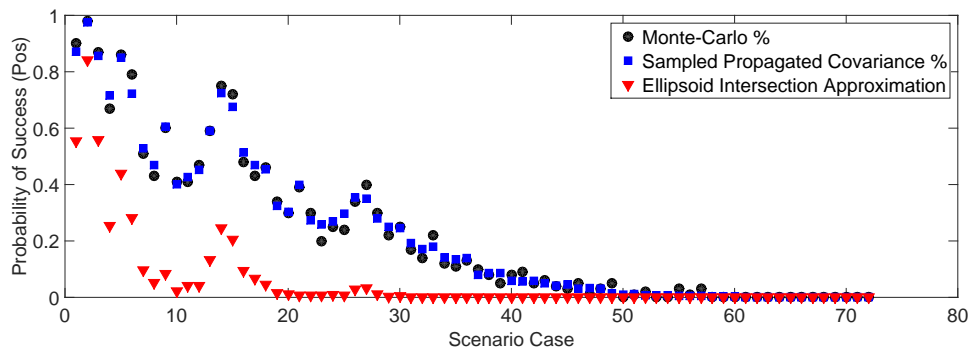
Figure 7.4: Probability Comparison for Position Requirement using Average Radar

7.4.3 Mission Analysis.

Using the final Monte Carlo state samples for all cases, it is now possible to answer the motivating question of the research: "What is the minimum number of observations necessary to meet an accuracy requirement of the orbital solution?" The answer primarily depends on the dimension of the requirement, the accuracy of the requirement, the type of radar used, and the altitude of the object of interest. For purposes of a definitive "go, no-go" decision, consider the threshold of a 90% probability of success. In Table 7.4, the results are averaged across inclination cases and the intersection percentages are provided for the 3-D position and 6-D overall cases. A color coding is used such that red indicates not meeting either requirement above a 90% probability of success, yellow represents meeting the position requirement only, and green represents meeting both. Several trends are noticeable in the table and discussed in the next paragraphs. Overall, these results show the difficulties in determining the future location of an object when so little is known of its orbital arc.

The table's organization helps highlight variables that decrease the probability of achieving the accuracy requirements. First, the smaller the accuracy requirement, the more observations necessary to achieve it. Second, reducing the requirement dimension shows that the velocity requirement is much more difficult to meet than the position requirement. This result is a product of the radar observation vector. The full position is observable while only the magnitude of the velocity is observed through the range rate. The percentages of achieving the 3-D position requirement are greater in all cases when compared to the full 6-D requirement. The results captured in Table 7.4 also reveal the significant performance decline when transitioning between different radar performance levels. These results reveal the importance of a highly accurate radar for the short arc mission of error estimation. Additionally, the results highlight the difficulty of accurately estimating an orbit given only a short observation time.

153

Table 7.4: Percent Success Meeting Accuracy Requirements (3-D | 6-D)

Accuracy	Radar	Altitude	Observations					
			15	30	60	120	180	240
Low	Good	350	49 | 25	99 | 73	100 | 100	100 | 100	100 | 100	100 | 100
		500	47 | 22	95 | 66	100 | 100	100 | 100	100 | 100	100 | 100
		750	34 | 16	82 | 52	100 | 98	100 | 100	100 | 100	100 | 100
		1000	29 | 17	79 | 46	100 | 96	100 | 100	100 | 100	100 | 100
	Average	350	19 | 7	58 | 27	100 | 82	100 | 100	100 | 100	100 | 100
		500	13 | 4	51 | 24	96 | 66	100 | 100	100 | 100	100 | 100
		750	9 | 4	36 | 17	88 | 57	100 | 100	100 | 100	100 | 100
		1000	7 | 3	31 | 16	81 | 54	100 | 96	100 | 100	100 | 100
	Poor	350	1 | 1	16 | 5	76 | 27	100 | 96	100 | 100	100 | 100
		500	2 | 0	10 | 1	62 | 27	100 | 89	100 | 99	100 | 100
		750	0 | 0	7 | 1	44 | 14	98 | 75	100 | 98	100 | 99
		1000	0 | 0	4 | 2	29 | 7	93 | 63	100 | 92	100 | 99
Medium	Good	350	5 | 3	18 | 9	58 | 33	99 | 90	100 | 100	100 | 100
		500	5 | 1	16 | 8	46 | 22	98 | 78	100 | 98	100 | 100
		750	2 | 1	10 | 4	35 | 17	93 | 61	100 | 92	100 | 100
		1000	2 | 0	12 | 4	33 | 19	79 | 48	98 | 85	100 | 98
	Average	350	0 | 0	5 | 3	19 | 7	61 | 34	96 | 69	100 | 95
		500	0 | 0	4 | 0	16 | 8	52 | 27	84 | 49	99 | 80
		750	0 | 0	5 | 2	12 | 4	37 | 18	65 | 35	87 | 53
		1000	0 | 0	0 | 0	11 | 3	28 | 12	51 | 27	76 | 46
	Poor	350	0 | 0	0 | 0	1 | 0	20 | 5	52 | 17	75 | 40
		500	0 | 0	0 | 0	1 | 0	9 | 2	33 | 11	62 | 27
		750	0 | 0	0 | 0	1 | 0	6 | 2	14 | 5	37 | 13
		1000	0 | 0	0 | 0	0 | 0	4 | 1	16 | 5	28 | 10
High	Good	350	3 | 1	9 | 3	33 | 13	88 | 51	100 | 96	100 | 100
		500	1 | 0	8 | 3	21 | 9	75 | 47	98 | 79	100 | 99
		750	1 | 0	4 | 1	18 | 9	60 | 34	90 | 61	100 | 88
		1000	0 | 0	3 | 1	17 | 8	45 | 25	80 | 48	96 | 77
	Average	350	0 | 0	2 | 0	8 | 3	33 | 11	69 | 30	92 | 56
		500	0 | 0	1 | 0	7 | 1	26 | 9	46 | 20	77 | 41
		750	0 | 0	2 | 1	4 | 2	18 | 5	34 | 16	51 | 23
		1000	0 | 0	0 | 0	3 | 0	12 | 4	25 | 12	43 | 21
	Poor	350	0 | 0	0 | 0	0 | 0	4 | 0	14 | 3	35 | 10
		500	0 | 0	0 | 0	0 | 0	1 | 0	10 | 2	25 | 6
		750	0 | 0	0 | 0	0 | 0	3 | 0	5 | 1	12 | 4
		1000	0 | 0	0 | 0	0 | 0	1 | 0	5 | 0	9 | 2

The altitude of the satellite of interest impacts the solution of short arc orbital fits. The trend is clear that the lower the altitude, the better the estimation chain performs in placing the final state within the requirement ellipsoid. The data trend relates back to the simulation set-up outlined in Figure 7.3. Each run is only afforded a set number of observations dictated by a cut-off time. A lower altitude object moves faster and sweeps

out a larger arc length in a given time than a slower, higher object. Therefore, better orbital knowledge is known for lower objects than higher objects when the collection time is fixed (Table 7.2). For this reason, the initial orbit estimation string has a higher probability of success for the lower altitude cases.

In Table 7.4, each cell is the average success of three different inclination cases as discussed in Section 7.3. Varying the inclination does result in different success percentages; however, there is not a clear trend across all cases. One possible explanation for the inclination's impact on the final probability of success is estimability. Estimability is the degree of observability of the states and is characterized by the covariance output of the Kalman Filter [164]. The size of the eigenvalues of the covariance matrix represent the estimability (larger is worse) in each eigenaxis. To test this concept, the covariance matrix eigenvalues for multiple varying inclination cases are summed. In some instances, the average eigenvalue for the 60 deg orbit configuration is less than the other inclinations for the 120, 180, and 240 observation cases. However, the size of the covariance does not always correlate to performance. There are instances in which the inclination case with the largest summed averaged eigenvalues has the best performance. The orientation of the propagated covariance, not just size, is important in evaluating the intersection. This reason motivates using the numerical intersection probability approach. The inclination that performs best for one observation case does not necessarily perform best for another number of observations. In general, the performances are close when inclination is varied. There is not a best inclination when considering all observation quantities, orbit altitudes, and radar performances. Since the ground radar collects an equal number of observations to fit each orbit, inclination variation does not noticeably impact solution accuracy.

7.5   Conclusion

This chapter sought to determine the number of observations needed to meet a user-defined orbital accuracy requirement. To accomplish this, an approach to approximate the

covariance intersection produced from a particular orbit estimation strategy is developed. Determining a realistic covariance results in discovering a fattening factor to capture the expected distribution of the state after an estimation chain. The intersection approach proves accurate at predicting the number of Monte Carlo simulations that meet a defined covariance accuracy requirement. While other works focus on just the propagation itself, this research evaluates the entire estimation string including observation errors. By preserving covariance realism through the estimation strategy, numerically estimating ellipsoid intersections successfully captures the percentage of states that fall within the requirement. Using the fattening covariance inflation factor and numerical intersection sampling methods, the probability of success is realized without the need to run Monte Carlo trials.

The mission evaluation reveals several trends in the short arc orbital fit analysis. The more accurate the requirement, the lower the probability of success. The radars with less observational noise outperform those with greater noise. Estimating the full state is far more difficult than estimating just the position. Relaxing the requirement to a 3-D position covariance ellipsoid results in far more cases with a probability of success above 90%. Finally, when considering the number of observations and time in view of the radar as design variables, a lower altitude satellite is tracked more accurately than a higher satellite.

This chapter provides a straightforward numerical approach for predicting the percentages of orbital state estimates from a full estimation chain that fall within a user-defined covariance accuracy requirement in any n dimensions.

VIII. Evaluating the Unscented Transform for Cartesian and Equinoctial Elements

8.1 Introduction

This short chapter considers using the UT discussed in Section 3.10.3.1 to transform states and covariances between Equinoctial and Cartesian coordinate frames. In many operations, covariances are provided in Cartesian elements; however, new research recommends representing uncertainties in the Equinoctial frame. As discussed, Equinoctial elements have only one fast-moving variable that describes the angular location of the satellite within its orbit. For this reason, Equinoctial elements are useful for perturbation studies as well as avoiding nonlinear growth causing non-Gaussian error covariances. Cartesian elements are all fast moving. While they are easier to visualize and contain no singularities, covariances expressed in this frame can depart from Gaussian distributions during longer propagation times. Due to nonlinearties in the transformation between these two coordinate frames, the UT is studied as a method to complete this transformation as it is known to preserve the first two moments of a distribution (mean and covariance) [89; 165].

If the covariance is provided in the RSW frame, a transformation to the ECI frame is performed via the transform ($\mathbf{P}_2 = \mathbf{ROT}\,(\mathbf{P}_1)\,\mathbf{ROT}^T$). This approach is not possible for the transition back and forth between Equinoctial and Cartesian elements as it requires a sequence of coupled, nonlinear equations [166]. In Section 3.10.3.1, two different methods are discussed for use in the UT. The weighting values are customizable for certain transformations. Given the demand of the Equinoctial to Cartesian transformation (and vice versa), a full examination of sigma point weights in the UT are evaluated in this chapter.

The motivation for this research is to enable the freedom of transitioning covariances between coordinate systems as accurately as possible using the UT. Additionally, a goal of the transformation is to compare propagation methods and provide a better visualization

of Equinoctial covariances. To test the effectiveness of the transformation consider the following metrics

$$\left[\hat{\mathbf{x}}_{ECI}, \hat{\mathbf{P}}_{ECI}\right] = UT_{Eq \to ECI}\left(UT_{ECI \to Eq}\left([\mathbf{x}_{ECI}, \mathbf{P}_{ECI}]\right)\right) \tag{8.1}$$

$$e_{\mathbf{x}} = \sum_{i=1}^{n} |\hat{\mathbf{x}}_{ECI} - \mathbf{x}_{ECI}|_1 \tag{8.2}$$

$$e_{\mathbf{P}} = \sum_{j=1}^{n} \sum_{i=1}^{n} \left|\hat{\mathbf{P}}_{ECI} - \mathbf{P}_{ECI}\right|_1 \tag{8.3}$$

where n is the dimension and i and j are matrix indicial notation. The reverse of the metrics are of interest as well to determine errors when beginning with an Equinoctial state and covariance.

8.2   Simulation

With the full details of the coordinate transformations provided in Appendix A and the UT explicitly defined in Section 3.10.3, routines are implementable to test various parameters for different orbits and covariances. Tables 8.1 - 8.4 list a test set of states and covariances. These sets are then run through equations 8.1 - 8.3. If the initial values are provided in Equinoctial elements, the reverse of 8.1 - 8.3 is performed. With each test, the errors are calculated and iterated using an optimization routine until a best solution is determined using both the symmetric and additional parameters UTs. The best values for the weighting parameters are then compared for each test case.

Following recommendations from Horwood et al., five test cases are examined for the Equinoctial to Cartesian transformation [160]. Additionally, some common orbit regimes are implemented as test cases with Cartesian means and covariances. These cases emulate a Geosynchronous (GEO) orbit, sun-synchronous orbit, launch vehicle insertion orbit, Mid-Earth Orbit (MEO), and Molniya orbit, respectively.

158

Table 8.1: Equinoctial Element State Cases

Case	a (km)	h	k	p_e	q_e	ℓ (rad)
1	7136.6	0.00104138	-0.00943269	0.66386	-0.323786	4.87296
2	7136.6	10^{-8}	10^{-8}	10^{-8}	10^{-8}	10^{-8}
3	7136.6	0.00104138	-0.00943269	0.66386	-0.323786	4.87296
4	42164.1	10^{-8}	10^{-8}	10^{-8}	10^{-8}	4.363323
5	26628.1	0.642591	-0.371	0.534868	-0.308806	4.607669

Table 8.2: Equinoctial Element Covariance Cases

Case	σ_a (km)	σ_h	σ_k	σ_{p_e}	σ_{q_e}	σ_ℓ (rad)
1	20	10^{-3}	10^{-3}	10^{-3}	10^{-3}	$1.74528 \cdot 10^{-4}$
2	20	10^{-3}	10^{-3}	10^{-3}	10^{-3}	$1.74528 \cdot 10^{-4}$
3	0.5	10^{-5}	10^{-5}	10^{-5}	10^{-5}	$9.696 \cdot 10^{-5}$
4	2	10^{-4}	10^{-4}	10^{-4}	10^{-4}	$1.35744 \cdot 10^{-4}$
5	2	10^{-4}	10^{-4}	10^{-4}	10^{-4}	$1.35744 \cdot 10^{-4}$

Consider starting covariances such that $\mathbf{P} = \mathbf{A}^T \mathbf{A}$ and

$$\mathbf{A}_{Eq} = \text{diag} \begin{bmatrix} \sigma_a & \sigma_h & \sigma_k & \sigma_{p_e} & \sigma_{q_e} & \sigma_\ell \end{bmatrix} \tag{8.4}$$

$$\mathbf{A}_{ECI} = \text{diag} \begin{bmatrix} \sigma_{\mathbf{r}_I} & \sigma_{\mathbf{r}_J} & \sigma_{\mathbf{r}_K} & \sigma_{\mathbf{v}_I} & \sigma_{\mathbf{v}_J} & \sigma_{\mathbf{v}_K} \end{bmatrix} \tag{8.5}$$

While Equinoctial elements are effective in SOD, they also come with a few challenges when implemented within a UT and UKF. Equinoctial elements contain a single angular element which requires additional care within the UT's determination of the propagated mean and covariance. Since $\ell \in [0, 2\pi]$, the UT must compute the average of 359 deg and 1 deg as 0 deg and not 180 deg. Therefore, some form of averaging or a branch cut is recommended when determining means and covariances. A straight forward branch cut

Table 8.3: Cartesian State Test Cases

Case	$\mathbf{r}_I$ (km)	$\mathbf{r}_J$ (km)	$\mathbf{r}_K$ (km)	$\mathbf{v}_I \left(\frac{km}{sec}\right)$	$\mathbf{v}_J \left(\frac{km}{sec}\right)$	$\mathbf{v}_K \left(\frac{km}{sec}\right)$
1	-32965.6	-26291.9	0	1.91446	-2.40042	0.160911
2	6535.7	-429.417	3017.24	-3.14188	-0.949466	6.6713
3	5658.59	3660.65	1371.2	-4.31888	5.69185	2.62914
4	25998.7	2596.56	3778.01	-0.674741	2.16746	3.15367
5	-1920.31	2407.75	-6150.12	-7.85281	-6.26305	0

Table 8.4: Cartesian Test Covariance Cases

Case	$\sigma_{\mathbf{r}_I}$ (km)	$\sigma_{\mathbf{r}_J}$ (km)	$\sigma_{\mathbf{r}_K}$ (km)	$\sigma_{\mathbf{v}_I} \left(\frac{km}{sec}\right)$	$\sigma_{\mathbf{v}_J} \left(\frac{km}{sec}\right)$	$\sigma_{\mathbf{v}_K} \left(\frac{km}{sec}\right)$
1	20	20	20	0.012	0.012	0.012
2	2	2	2	0.0012	0.0012	0.0012
3	0.5	0.5	0.5	0.0005	0.0005	0.0005
4	2	2	2	0.0012	0.0012	0.0012
5	2	2	2	0.0012	0.0012	0.0012

method is to represent all angles in the mean and covariance calculation in the UT via a 2π multiple such that $\ell \in [b, b + 2\pi]$ [167].

$$b = \ell_1 - \pi \tag{8.6}$$

$$\ell_i = \ell_i + 2\pi \left\lceil \frac{b - \ell_i}{2\pi} \right\rceil \tag{8.7}$$

After the branch cut, the mean and covariances are ready for use within the UT. Figure 8.1 highlights the affect on the estimated covariance if the angular quantity is handled improperly. If necessary, the average is transformable back via a 2π modification such that if $\ell \geq 2\pi$ then subtract 2π prior to the propagation routine. If the modified $\ell < 0$, add 2π.

(a) Proper   (b) Improper
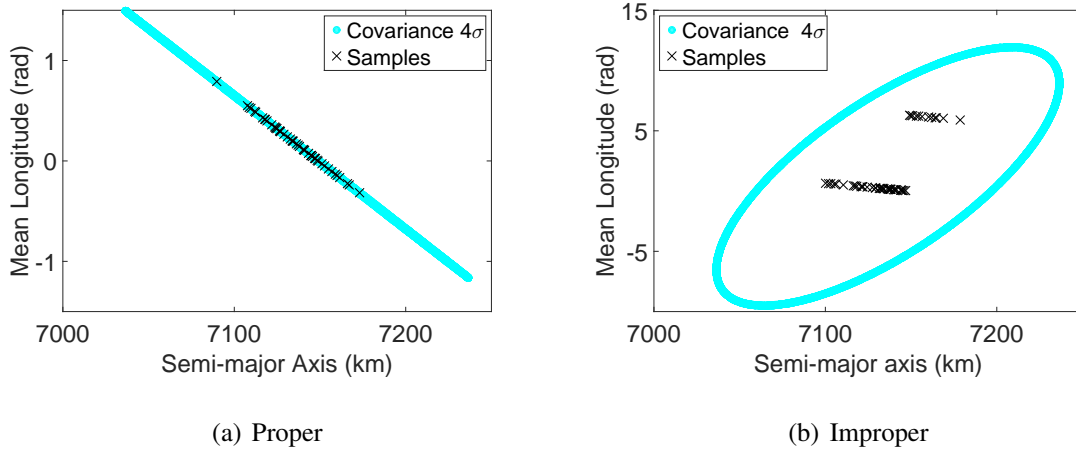
Figure 8.1: Handling ℓ in UKF Propagation

8.2.1 Optimization Formulation.

In Equations 8.2 and 8.3 the performance tests are outlined. There are two values of the transform to consider, the state and covariance. A choice of α, γ, λ or κ within the UT may reduce errors in the covariance of the transformation at the cost of accuracy of the mean. Initial testing revealed, in general, that a change in an input value has far more effect on the covariance cost measure than the state measure. When using the covariance comparison cost to determine the optimal input, the best or nearly best state results from the transformation. Since the covariance cost function is more sensitive to changes and produces accurate means, it is selected for use in the optimization routine for all simulations.

The symmetric transformation only has one variable, κ, to modify to impact the cost function in Equation 8.3. Finding the optimal value of κ for each case requires searching the solution space of possible values. A lower boundary value is necessary on κ within the optimization formulation, $\kappa > -n$. A discrete static optimization interior-point search method is performed to determine the optimal κ value, κ^*, for each test case. Interior-point searching is necessary as sampled values of κ below the boundary results in complex sigma

161

points which are not permitted to obtain a real, positive definite covariance matrix with the UT. Using the same optimization approach, the additional parameter transformation requires determining three optimal values: α^*, γ^*, and λ^*. From Chapter 3, $\alpha \in (0, 1]$, γ is any real number, and $\lambda > -n$.

The risk of a local optimization is a concern for both transformations. For the symmetric case, functional evaluation differences are small between varying κ values. For the additional parameter case, sampling three variables can result in converging on different optimal solutions when the initial guess is modified. To combat the local minimum problem for both transformations, three different starting values that lie near the boundaries are used in the optimization routines. The best of the local optimum solutions is selected as the global optimum.

8.3 Results

Using the test cases in Tables 8.3 and 8.4, $\kappa^*, \alpha^*, \gamma^*$ and λ^* are determined using an optimization routine with Equation 8.3 as the cost function. Additionally, the optimal transform is evaluated for the state transform (Equation 8.2). The results are compared against the fixed symmetric transform where $\kappa = -3$. The results in Figures 8.2 and 8.3 show several trends worth discussing.

First and foremost, the figures show that a traditional UT (not optimized) does a fair job at preserving the state and covariance through the transform. The triangle lines show generally small values across all cases examined. The traditional approach produces the most error during the low accuracy cases. Next, notice that the optimized additional value transform is the best, or very close to the best, in every case. This trend reveals that adding variables to control the covariance can increase performance.

It is worth noting as well that the optimized symmetric transform results are not better than the simplified constant symmetric approach in several cases. This result shows that the optimization routine did not search the entire solution space. This feature did not occur

for all cases; however, it did for three of the ten cases considered. Adding more starting cases and increasing convergence accuracy requirements could improve the optimization routine's ability to search the full solution space. However, this would only improve performance for the specified cost function. The results also show that the best covariance configuration is not the best at the state transform. While all methods perform generally well for the transform, the results show that the optimization configuration can improve transformation results for most cases but not all. The results from the additional parameter transformation are very encouraging as they show a way to improve upon traditional transformation methods. Overall, the optimal UT is a viable method to transition means and covariances for SSA applications, and the basic fixed symmetric value transform can meet accuracy needs for most cases.
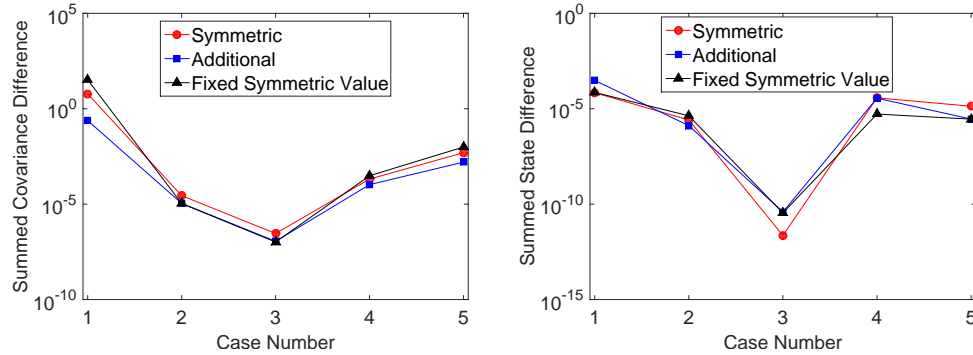
Figure 8.2: ECI→Eq→ECI Transformation Errors

The optimal values of the transform parameters for each case provide additional insight and are displayed in Figure 8.4. The first trend worth noting is that all κ^* values are negative. This result is expected for Gaussians because as κ approaches $-n$, greater weight is placed upon the original mean instead of the sigma points. However, κ^* does not show a noticeable trend when the accuracy of the solution is varied in different scenarios.
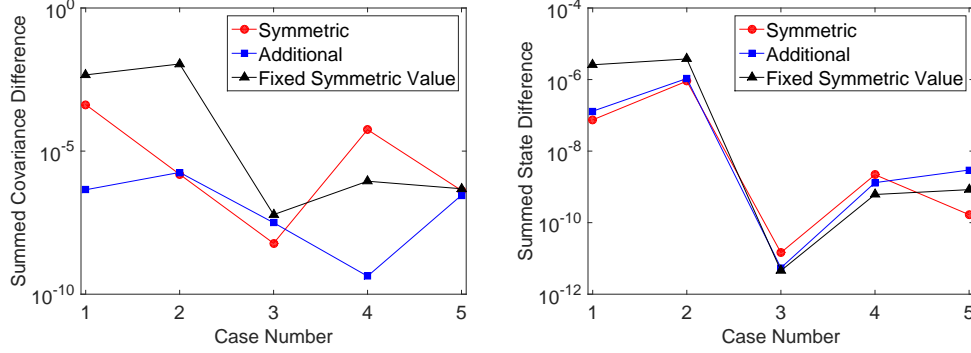
Figure 8.3: Eq→ECI→Eq Transformation Errors

In Figure 8.4, the trends of the other parameters are also displayed. There is an inverse relationship between α and λ. Additionally, α tends to remain low for lower accuracy cases. The figure shows that there is not a constant optimal value for each variable across all cases. The optimal values vary as does the performance, and there is not a noticeable simplistic analytical equation to determine optimal parameters for the transform.

Overall, the results show that the traditional method is effective, but additional optimal parameters can improve performance. Furthermore, there is not a straightforward method to determine or predict optimal parameter values as they are uncorrelated to specific orbits or accuracy levels.

8.4 Conclusions

The UT is shown to successfully transform means and covariances between Cartesian and Equinoctial orbital element sets. This chapter developed a method to improve the performance of the traditional transformation by varying sigma point weighting factors. Furthermore, an optimal approach is detailed to determine the best parameters to use in the transformation. The additional parameter transform approach is the most accurate when input values are optimized. Using optimal values, the UT now preserves the mean

Figure 8.4: Optimal Transform Parameter Values

and covariance more accurately between coordinate frames. Since Equinoctial elements preserve covariance realism longer, an optimal UT can convert an Equinoctial covariance to a more visually appealing Cartesian covariance.

IX.   Preserving Covariance Realism with Gaussian Mixtures

9.1   Introduction

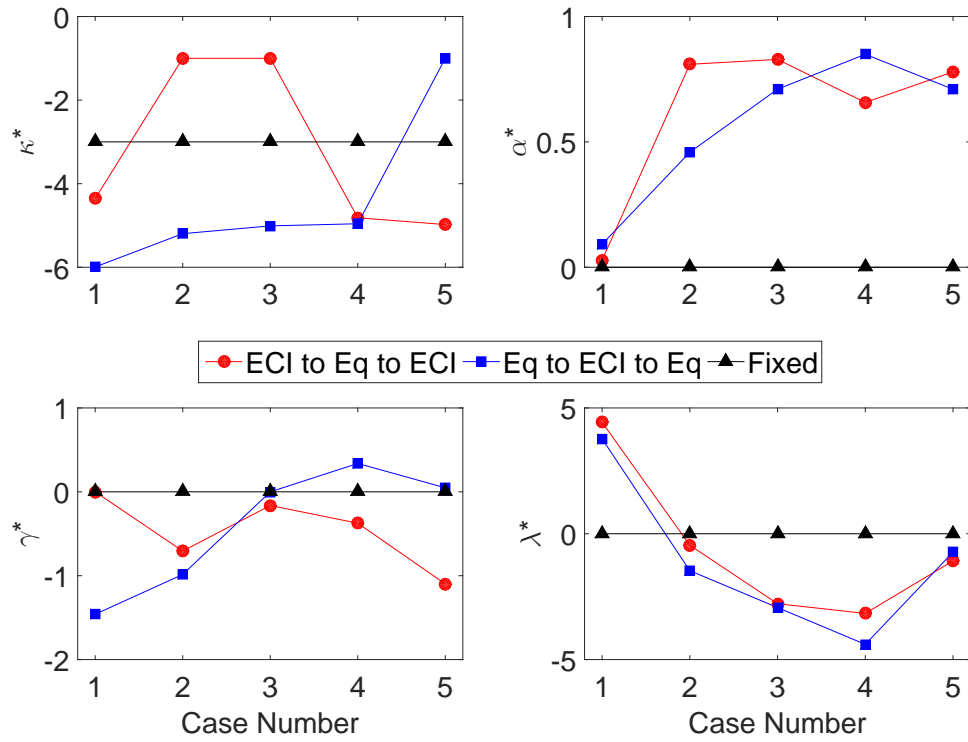Covariance realism becomes a greater concern as objects with larger associated covariances are propagated over longer periods of time. Casting the estimation routine in the Equinoctial element systems aides in achieving realism for longer periods of time. If realism is not met during a propagation, a Gaussian mixture is created through the splitting process to meet realism requirements. Given a distribution of points, an EM routine can fit a mixture to achieve realism. In this chapter, both the EM and splitting methods are implemented within a Gaussian mixture UKF. The UKF is used in coordination with a high fidelity orbital propagator to leverage commercial routines for high precision orbit determination analyses. Due to large covariances and long propagation times, a precise propagator is required. After propagating with a mixture, processing observations can collapse a Gaussian mixture back to a single Gaussian to represent errors. There is direct similarity between processing observations with a Gaussian mixture and the more general IMM [84]. Within an IMM routine, the model that best captures the dynamics with Gaussian residuals is weighted heaviest. This chapter develops new techniques to use the IMM to adaptively weight the best model in the mixture, coalesce the mixture into a single Gaussian, and prune off incompatible models.

9.2   Equinoctial Element Unscented Kalman Filter

Recent research reveals that longer propagation times of large initial covariances, $\mathbf{P}$, in Cartesian coordinates results in non-Gaussian distributions [87]. A Gaussian pdf has the form detailed in Equation 3.7. Recall that $\mathbf{x}$ and $\boldsymbol{\mu}$ are $n \times 1$ in the range $[-\infty, \infty]$, and $\mathbf{P}$ is $n \times n$ where n is the dimension of the multivariate Gaussian.

A single Gaussian KF in Cartesian ECI coordinates often improperly characterizes the underlying error distribution. In this frame, Monte Carlo samples form a "banana shape" uncertainty distribution. To demonstrate and motivate the need for mixtures, define the state vector of the spacecraft, $\mathbf{x}$, in the Cartesian frame as is done in Equation 3.1.

Starting with a state and covariance, $\mathbf{x}_0$ and $\mathbf{P}_0$, sample the normal distribution to create a set of Monte Carlo points such that $\mathbf{x}_{mc} = \boldsymbol{\mu} + \mathbf{A}(\boldsymbol{\psi})$. The mean $\boldsymbol{\mu}$ is the starting state $\mathbf{x}_0$ and $\mathbf{A}$ is the Cholesky decomposition of the covariance such that $\mathbf{P} = \mathbf{A}^T\mathbf{A}$. The vector $\boldsymbol{\psi}$ is $n \times 1$ and composed of random samples $\psi \sim \mathcal{N}(0, 1)$. Using a two body orbital propagator for a simple scenario, all Monte Carlo points are propagated for 24 hours. Next, the propagation step of a UKF (Algorithm 4) is run to determine the expected final single Gaussian error distribution. Figure 9.1 displays the final distribution results. The 2-D plot shows rings for one through five σ values from the UKF Gaussian, and the 3-D plot shows the 4σ position ellipsoid from the same Gaussian. Both figures clearly show that a single Gaussian does not capture the underlying distribution. A 4σ bound should encompass 98.6% of a 6-D normal distribution; this is clearly not the case. A similar figure is provided in other works [3; 91].

(a) $\mathbf{r}_I, \mathbf{r}_J$ Position   (b) Position
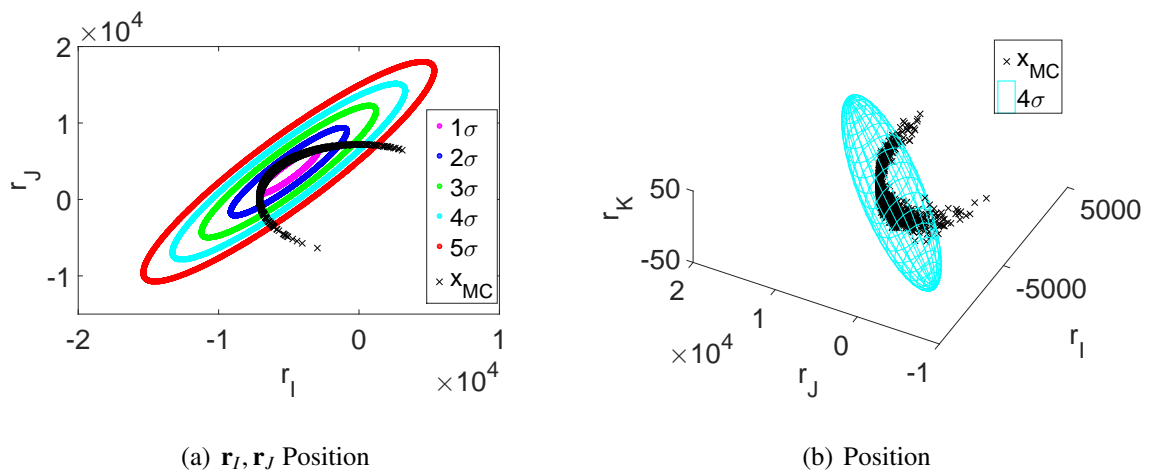
Figure 9.1: 24 Hour Point Distribution and UKF Covariance σs

Horwood and Aristoff lobby to abandon Cartesian based covariances and opt for Equinoctial elements with the single fast moving angular variable ℓ (mean longitude). Although the uncertainty is difficult to visualize as the elements are not intuitive, mathematically, the elements better match a Gaussian distribution during propagation. The Equinoctial orbital elements are defined in Equation 3.68. The transformation details and UT for covariances between element sets is discussed in Chapter 8. Performing the same full day propagation as done in Figure 9.1, the Equinoctial elements prove far more effective in capturing the underlying distribution with a single Gaussian UKF. Figure 9.2 highlights all the combinations of the fast moving variable, ℓ, with the rest of the elements and displays the same σ bounds as Figure 9.1. All combinations show Gaussian distributions except for the semi-major axis comparison. In Cartesian elements, every combination suffers from fast moving variables and non-Gaussian distributions; whereas, the Equinoctial approach must only handle one instance of a potential non-Gaussian distribution. Handling the non-Gaussian portion is the subject of the next section.

Figure 9.2: Cross Sections of Equinoctial Elements after 24 Hour Propagation

When including observation processing in the Equinoctial element UKF, the transformation from Equinoctial elements to ground radar based observations necessitates

168

solving Kepler's problem (iteratively). Since the solution to Kepler's problem converges quadratically, this computational time is of little concern with modern computers. Additionally, as discussed previously in Chapter 8, the angular variable, ℓ, requires special treatment with the UT.

9.3 Gaussian Mixture

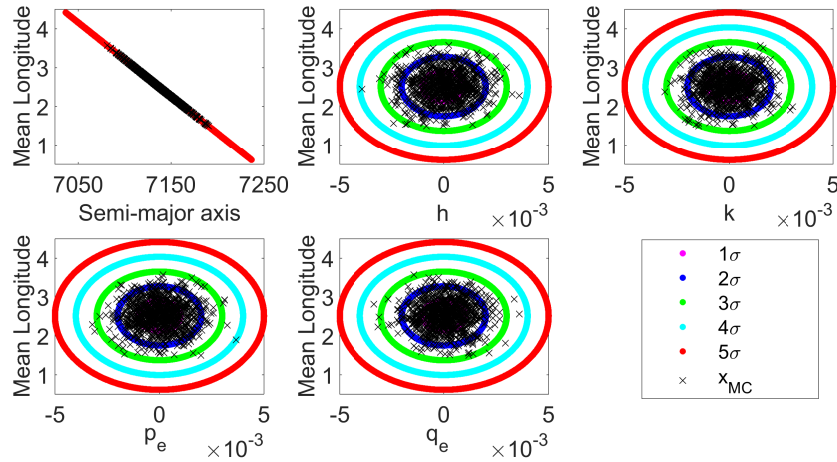A Gaussian mixture combines several Gaussian distributions to model an underlying distribution that is non-Gaussian. In pioneering work, it was shown that given enough components, a mixture can model any distribution sufficiently close given a distance metric [90]. Define a Gaussian mixture as the sum of multiple weighted Gaussians

$$p_{\mathbf{x}}^M = \sum_{i=1}^N w_i \mathcal{N}(\mathbf{x}; \boldsymbol{\mu}_i, \mathbf{P}_i) = \sum_{i=1}^N w_i p_{\mathbf{x}_i} \tag{9.1}$$

where $w \in [0, 1]$.

9.3.1 Splitting Techniques.

Single multivariate Gaussians with larger covariances can fail to meet realism requirements under a nonlinear transformation. However, in a small neighborhood, nonlinear transformations are approximately linear. Therefore, a Gaussian with smaller covariances remains more Gaussian after a nonlinear transformation as compared to a larger Gaussian. The process of splitting or refining a Gaussian can preserve realism by approximating the original distribution with smaller Gaussians along a refinement direction. The refinement direction is wisely chosen as the direction in which the nonlinearity is most severe. Define the multi-dimensional splitting approximation as [168]

$$\mathcal{N}(\mathbf{x}; \boldsymbol{\mu}, \mathbf{P}) \approx \sum_{i=1}^N w_i \mathcal{N}(\mathbf{x}; \boldsymbol{\mu} + f_i u; \mathbf{P}_i) \tag{9.2}$$

where a unit vector u is the refinement direction and a scalar, f, defines how far along the vector to displace the mean. Solving the univariate Gaussian refinement problem is far easier than the full dimension problem. With the refinement direction, u, the univariate results are applicable for the multivariate case. Specifically, the splitting solution

approximates the standard Gaussian with a mixture

$$\mathcal{N}(x; 0, 1) \approx \sum_{i=1}^{N} w_i \mathcal{N}\left(x; \mu_i, \sigma_i^2\right) \tag{9.3}$$

Formulating an optimization problem, potential weights, means, and variances are selected to minimize a cost function that captures the differences between the standard normal distribution and the Gaussian mixture. The pdf version of the L_2 metric provides a scalar to compare how well the mixture approximates a single Gaussian. Define the cost function as the L_2 metric.

$$J = \int_{-\infty}^{\infty} \left[\mathcal{N}(x; 0, 1) - \sum_{i=1}^{N} w_i \mathcal{N}\left(x; \mu_i, \sigma_i^2\right)\right]^2 dx \tag{9.4}$$

The cost function is reducible to the matrix form

$$J = \mathbf{w}^T \mathbf{M} \mathbf{w} - 2\mathbf{w}^T \mathbf{n} + \frac{1}{2\sqrt{\pi}} \tag{9.5}$$

with vectors $\mathbf{w} = w_1, .., w_n$, $(\mathbf{n})_i = \mathcal{N}\left(\mu_i; 0, \sigma_i^2 + 1\right)$ and the $N \times N$ component matrix $\mathbf{M}$ is defined by $(\mathbf{M})_{ij} = \mathcal{N}\left(\mu_i - \mu_j; 0, \sigma_i^2 + \sigma_j^2\right)$. The mathematical reduction is shown in Appendix B.1. Given a set number of components, N, the optimization routine must determine the mixture's set of weights, $w_i, ..w_N$, means, $\mu_i, ..\mu_N$, and standard deviations $\sigma_i, ..\sigma_N$. The optimization problem contains the constraints that the weights must sum to one, $\sum_{i=1}^{N} w_i = 1$, and all weights must be positive, $w_i >= 0$ [168]. Gaussian mixtures are defined only for positive weights that sum to 1 to preserve the definition of a pdf.

The goal of the mixture it to reduce the size of the variance such that $\sigma_i < 1$. To limit the possible solutions, a set number of components are defined prior to solving the optimization problem. Even still, the optimization routine is computationally challenging as the cost function contains a large set of means and standard deviations. Adding a constraint that the standard deviations of all mixture components be equivalent aids in solving the problem [91]. Once the optimization problem is solved, the same solution can continually re-split Gaussians as necessary to assemble a more accurate mixture. The three mixture split solution by DeMars et al. is detailed in Appendix B.2.

Horwood et al. developed a sub-optimal method to increase computational efficiency by equally spreading the means according to a user-defined input $\hat{\sigma}$ where $\hat{\sigma} \in [0, 1]$. Additionally, $\hat{\sigma}$ specifies the number of components within the algorithm [168]. This approach reduces the optimization to a quadratic programming problem in which only the weight vector, **w**, is optimized. This approach affords a method to quickly determine a mixture of a desired component size. The details of the method are specified in B.2. For $\hat{\sigma} = 0.5$ and $\hat{\sigma} = 0.2$, the solutions are plotted in Figure 9.3.

(a) 17 components　　　　　　(b) 61 components
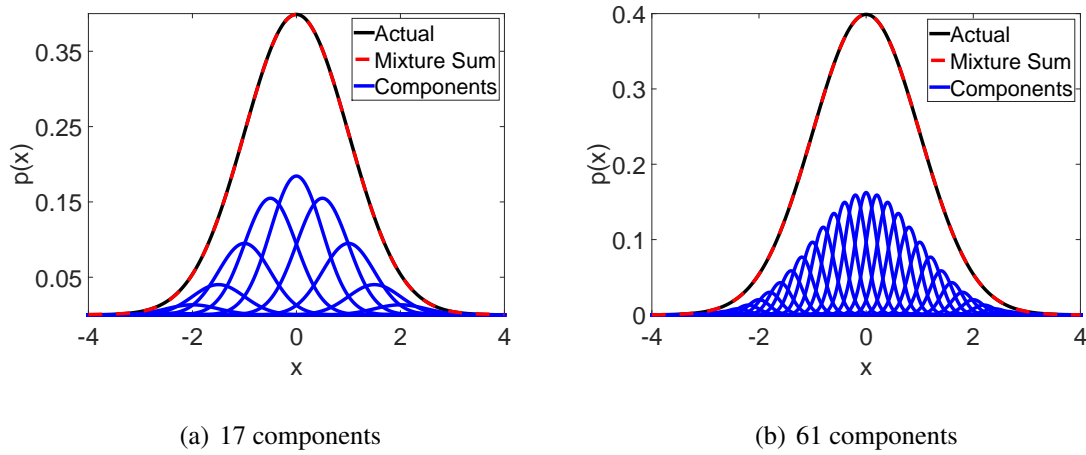
Figure 9.3: Mixture Approximation of Standard Gaussian

The univariate splitting should occur in the direction in which the nonlinearity is most severe to preserve covariance realism. To determine this direction, begin by performing a spectral decomposition of the starting covariance

$$\mathbf{P} = \mathbf{V}\mathbf{\Lambda}\mathbf{V}^{T} \tag{9.6}$$

where **V** is a matrix with eigenvectors $\mathbf{v}_i$ as columns and $\mathbf{\Lambda}$ is a diagonal matrix with eigenvalues λ_i. In Cartesian coordinates, splits occur along the largest eigenvalue; however, for Equinoctial elements it is best to split along the eigenvector, $\mathbf{v}_f$, corresponding to the largest semi-major axis change as shown in Figure 9.2. Choose the eigenvector associated

with the largest first element of the product $\sqrt{\lambda_i}\mathbf{v}_i$. Using the univariate splitting results $\widetilde{w}_i, \widetilde{\mu}_i, \widetilde{\sigma}_i$ and a previous Gaussian with mean $\boldsymbol{\mu}$ and covariance $\mathbf{P}$, split along the $\mathbf{v}_f$ vector. Define the mean and covariance for each mixture component

$$\boldsymbol{\mu}_i = \boldsymbol{\mu} + \sqrt{\lambda_f}\widetilde{\mu}_i\mathbf{v}_f \tag{9.7}$$

$$\boldsymbol{\Xi}_i = \text{diag}\left[\lambda_1, ...\lambda_f\widetilde{\sigma}^2, ...\lambda_N\right] \tag{9.8}$$

$$\mathbf{P}_i = \mathbf{V}\boldsymbol{\Xi}_i\mathbf{V}^T \tag{9.9}$$

and assign the weights found performing the previous optimization routine.

Given an input $\hat{\sigma}$ that defines the number of components, N, and a splitting direction, a state and covariance beginning at an initial time, t_0, is split into components. The splitting allows for smaller covariance Gaussians that remain more Gaussian over a long propagation. As the covariances approach zero, the weighting scheme preserves a mixture through a transformation [92]. Thus, incorporating a mixture into a UKF orbit estimation routine is straightforward. Each component of the mixture is propagated independently using the UKF propagation step in Algorithm 4. Given a starting mixture, $\sum_{i=1}^{N} w_{i_0}\mathcal{N}\left(\mathbf{x};\boldsymbol{\mu}_{i_0};\mathbf{P}_{i_0}\right)$, the propagated weights are equivalent to the initial weights $\left(w_{t_0} = w_{t_f}\right)$ and the final mixture is $\sum_{i=1}^{N} w_{i_f}\mathcal{N}\left(\mathbf{x};\boldsymbol{\mu}_{i_f};\mathbf{P}_{i_f}\right)$. When the propagation is complete, it is necessary to answer whether or not enough components were used to achieve covariance realism. Each added component increases computational demands; therefore, it best to find a mixture with the fewest number of components necessary.

9.3.2 Mixture Mode.

To use the covariance realism test described in Section 3.12, it is necessary to determine the mode of a Gaussian mixture, $\hat{\mathbf{x}}$. There is not an analytical solution to the mode of a mixture; instead, it requires solving a nonlinear optimization problem. Using the negative log likelihood of the mixture pdf as a cost function, J, improves convergence on

the mode

$$J = -\ln\left(p_{\mathbf{x}}^M\right) \tag{9.10}$$

where $p_{\mathbf{x}}^M$ is a mixture as defined in Equation 9.1. In most optimization routines, providing the gradient and Hessian of the cost function also improves convergence speeds; the derivations are provided in Appendix B.3. A good initial guess for the optimization routine, $\hat{\mathbf{x}}_0$, is the mean of the most heavily weighted mixture component such that $w_k = \max[\mathbf{w}]$ and the initial guess is $\mathbf{x}_0 = \boldsymbol{\mu}_k$. This guess for a mixture with a smaller number of components is often the mode itself. Once the optimization routine determines the mode, the mixture is testable for covariance realism using Equation 3.66. If the mixture does not meet covariance realism, a larger number of components are necessary in the mixture.

9.3.3 Expectation Maximization Mixture.

The longest computational draw is not the optimization routines to determine a mixture, it is the propagation over long times especially as the number of components in the mixture increases. A mixture with 78 components requires propagating 1000+ sample points. This propagation is just as computationally taxing as simply propagating 1000 Monte Carlo samples. If the samples are known at the final time, a different approach to splitting is proposed to fit a mixture to a point distribution. Borrowing from signal processing and pattern matching research, fitting a set of points with the near optimal EM algorithm results in a mixture meeting realism requirements [102; 104]. Determining the optimal mixture for a set of points is considered a class NP-Hard problem. The EM routine was developed as a fast and effective way to determine a near optimal solution; however, the routine is highly dependent upon the initial mixture guess that seeds the algorithm.

Continuing from Equation 9.1, the EM algorithm requires an initial mixture guess. There are several seeding methods to determine the starting means for the EM approach including random selection, k-means++, furthest distance, etc. The k-means++ approach is selected for use in this application based on its accuracy and efficiency. The k++ means

seeding requires specification of the number of mixture components, *N*, prior to running the algorithm [105].

The EM algorithm is a clustering method similar to k-means and uses a two step process [103]. Given *N* starting means from the k++ algorithm, identical weights and covariances form an initial mixture guess. The first step is called the expectation step and consists of defining membership weights for each point to each component. Next, the maximization step uses the weights from the previous step to calculate updated weights, means, and covariances for the mixture. The process is iterated until convergence and summarized in Appendix B.4. If covariance realism is not achieved with the initial number of mixture components, the number is increased and the process repeated until realism requirements are met.

9.3.4 *Interacting Multiple Models.*

In the update step of a single model orbit estimation UKF, ground observations are used to update the state and covariance estimates. Consider a ground radar that captures an observation vector $\mathbf{y}_t$ at time *t* and that the error is $\mathcal{N}(0, \mathbf{R})$ where $\mathbf{R}$ is diagonal with the error variance of each observation. Within the UKF, the function *G* maps the state in Equinoctial elements into a projected observation. The conversion between Equinoctial and Cartesian elements is discussed in Appendix A. The process for converting from Cartesian elements to observations of range, azimuth, elevation, and range rate is discussed in Section 3.8.

The IMM directly correlates to the Gaussian mixture process discussed thus far except that Markovian switching constants for mixing components are unnecessary. By adapting the IMM approach to the propagated mixture, it is possible to update the orbital estimates of a mixture with new observations provided proper association. Throughout this chapter, target to track association is assumed correct. Processing observations with a mixture requires more effort as there are *N* propagated components each with a mean, covariance,

and weight. The IMM methodology updates mixture weights, means, and covariances, and prunes unfit components to calculate a new mixture with an overall mean and covariance. Then, the new mixture is propagated to the time of the next observation and the updating process is repeated. For this application, the IMM in Algorithm 5 is implemented with $\mathbf{Pr}_{j|k} = \mathbf{I}$ and pruning logic (Equation 3.72).

It is worth noting that a covariance represented in Equinoctial elements can suffer from a poor condition number due to the large numerical differences in error between the semi-major axis and mean longitude. This problem typically occurs when processing the first observation after a long propagation of a large covariance. Within the UKF update step of a mixture component, the resulting covariance can lose positive definiteness. To resolve this error while minimizing disruption to the UKF process, the covariance is made positive definite through $\mathbf{P} = \mathbf{P} + \xi\mathbf{I}$ where ξ is on the order of 10^{-12}. This approach improves the condition number with minimal effort and modification of the covariance.

Additionally, to cut down on computational propagation demands, it is advantageous to return to representing the covariance by a single Gaussian whenever possible. Pruning unnecessary Gaussians within the IMM affords computational savings; however, there are situations in which two or three models remain with relevant weights after processing several observations. In this case, coalescing models into a single Gaussian is performed by forming a single Gaussian model from the overall IMM mean and covariance, $\underline{\mathbf{x}}$ and $\underline{\mathbf{P}}$. Using the IMM output as the input to process the next observation for these cases results in reducing computational resources while minimizing estimation errors.

9.4 Simulation

To test and compare the approaches discussed in the previous sections, a set of simulations are designed, coded, and analyzed. The scenarios start with a provided initial state and covariance, $\mathbf{x}_0$ and $\mathbf{P}_0$. In operational terms, this value is the result from a previous orbit fit or covariance propagation. The starting values are then propagated using the UKF

propagation step until visible by a ground radar. The radar collects observations with known uncorrelated errors. Similar to previous chapters, a modern mechanical tracking radar is simulated with error standard deviation σ values of 5 m for range, 0.01 deg for azimuth and elevation, and 0.05 m/s for range rate. Perfect observations are simulated every 60 seconds while in view of the radar and then perturbed with errors $\mathcal{N}(0, \sigma^2)$ according to the σ values. A set of four ground radars equally spaced longitudinally at a latitude of 5 deg are simulated to track the spacecraft. The locations of the radars do not impact the results as the main variable evaluated is the length of propagation time.

The truth orbit of the simulations are modeled with the following steps. Sample the initial distribution $\mathbf{x}_{0_s} = \mathbf{x}_0 + \mathbf{A}\varpi$ where $\mathbf{P} = \mathbf{A}^T\mathbf{A}$ and ψ is a vector of n dimensions with each element distributed $\psi \sim \mathcal{N}(0, 1)$. This step varies the initial starting value such that it is not the mean, but some value consistent with the starting distribution. The initial value is then propagated and observations are simulated with applicable errors. These steps provide the simulated truth to which the IMM attempts to fit using the perturbed observations.

To implement the splitting mixture approach discussed in Section 9.3.1, create 1000 Monte Carlo points from the initial distribution and propagate each to the initial observation. Next, check the propagated covariance for realism using the Monte Carlo points. If realism is not achieved, split the initial covariance into a mixture. Propagate the mixture and check for realism again. Continue the splitting and propagation process until a realistic covariance is achieved at the time of the first observation. The following $\hat{\sigma}$ values are attempted in order until covariance realism is achieved

$$\hat{\sigma} = \begin{bmatrix} 0.7 & 0.5 & 0.4 & 0.3 & 0.2 & 0.15 & 0.1 & 0.07 & 0.05 \end{bmatrix} \tag{9.11}$$

For the EM approach, the propagated 1000 Monte Carlo points are used to fit a mixture with the EM process. First, attempt a single Gaussian fit. If this does not meet realism requirements, increment the number of components by two and fit the Monte Carlo points again. Continue the process until a realistic covariance is achieved. Since the EM approach

is known to produce different solutions for different initial conditions, the approach is run three times prior to increasing the number of components. The first instance that achieves covariance realism ends the EM process and the mixture output from the algorithm is then used to process observations.

Once realism is achieved with both approaches, begin processing observations using the pruning IMM until the end of the pass. A pruning constant of 10^{-10} is used within the IMM. Additionally, if several models remain after processing 5 observations, the models are combined and a single model with the IMM mean and covariance is used within the UKF. The results of each mixture IMM are also compared to a single traditional UKF. Each simulated truth orbit is determined using Microcosm Inc.'s HPOP [150]. HPOP uses numerical integration of orbit dynamics with 21×21 spherical harmonic expansion of the Geopotential, atmospheric drag, lunar gravity, and solar radiation pressure perturbations. Additionally, the same propagator is used with the UKF estimation routine and for all Monte Carlo points.

9.5 Results

9.5.1 Method Comparison.

In this work, the EM routine is introduced as a way to form a mixture that meets covariance realism requirements for orbit propagation. To compare this approach to the previously developed splitting algorithm, four initial orbits are considered. The four starting orbits are detailed Table 9.1. Additionally, two different starting covariance sizes are evaluated and the values for the diagonals of $\mathbf{A}$ are listed in Table 9.2. The initial covariance is formed via $\mathbf{P} = \mathbf{A}^T \mathbf{A}$. The first two orbits and covariance sizes repeat those in other works [87]. The motivation for using these orbits is to ensure the coded methods work by confirming results and also to establish benchmarks to compare against the EM approach. The second two orbits are similar to operational orbits of interest for

177

LEO spacecraft including both a sun-synchronous orbit (Orbit C) and a lower altitude orbit at a launch insertion inclination (Orbit D).

Table 9.1: Equinoctial Element State Cases

Orbit	a (km)	h	k	p_e	q_e	ℓ (rad)
A	7136.6	$1.042 \cdot 10^{-3}$	$-9.43269 \cdot 10^{-3}$	0.6639	-0.32379	4.87296
B	7136.6	10^{-8}	10^{-8}	10^{-8}	10^{-8}	10^{-8}
C	7178.13	0	$9.98540 \cdot 10^{-5}$	0	-1.15240	3.14159
D	6878.14	0	$-9.98540 \cdot 10^{-5}$	0	-0.25397	3.14159

Table 9.2: Equinoctial Element Covariance Accuracies

Accuracy	σ_a (km)	σ_h	σ_k	σ_{p_e}	σ_{q_e}	σ_ℓ (rad)
Low	20	10^{-3}	10^{-3}	10^{-3}	10^{-3}	$1.74528 \cdot 10^{-4}$
Med	2	10^{-4}	10^{-4}	10^{-4}	10^{-4}	$1.35744 \cdot 10^{-4}$

A key metric in comparing the splitting and EM methods is the number of mixture components necessary to meet realism requirements. Figure 9.4 compares the number of components within the mixture at the first post propagation observation for each of the eight test cases. Clearly, the EM method achieves realism with far fewer components. This result is expected as the EM method occurs outside of the UKF dynamics and evaluates only the set of propagated Monte Carlo points. The EM approach does not evenly space component means as is done in the splitting approach. Figure 9.5 shows the semi-major axis and mean longitude cross section for each mixture at the first observation of the medium accuracy Orbit B test case. The figure resembles the initial results shown in Figure 9.2, and clearly displays the differences between the splitting and EM approaches. Both approaches properly align component means with the Monte Carlo points; however, the EM means are

not symmetric nor evenly spaced. Also, note that different initial guesses input into the EM algorithm result in different EM means. Although the EM approach achieves realism with far fewer components, the components themselves are not necessarily known in advance as k++ means seeding is based on distribution sampling.

The splitting approach is much different than the EM method as it does not consider the Monte Carlo points. Instead, it focuses on splitting the initial covariance and propagating smaller covariance components until realism is achieved. The benefit of the EM approach is that it achieves realism with far fewer components as shown in Figure 9.4. The disadvantage with the EM approach is that it requires a set of propagated Monte Carlo points. The benefit of the splitting approach is that a look-up table could provide a required number of components for an orbit, covariance, and propagation time. If the number of components necessary to achieve realism are known prior to propagation, it is possible to avoid propagating 1000+ Monte Carlo points for each satellite and instead just propagate the mixture components. The disadvantage of splitting is that the number of components can grow very large and outweigh the cost of propagating a set of Monte Carlo points.
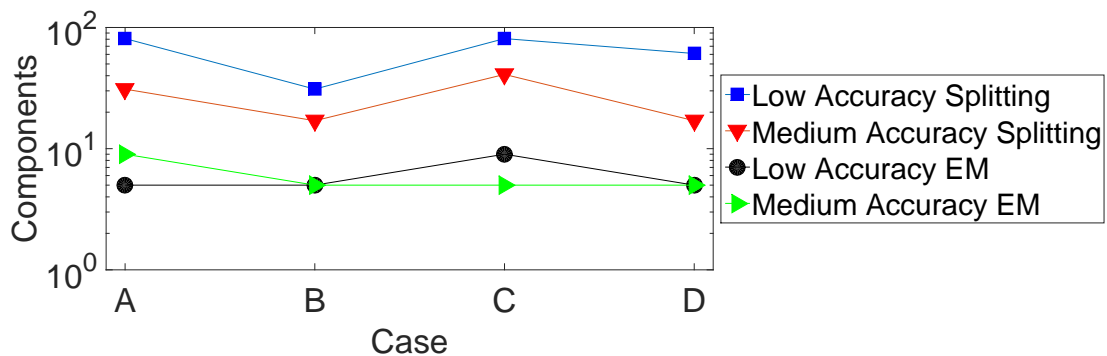

Figure 9.4: Mixture Component Comparison

Given that each method requires different numbers of components, the next question to answer is "which method is better at estimating the orbit?" Although computational
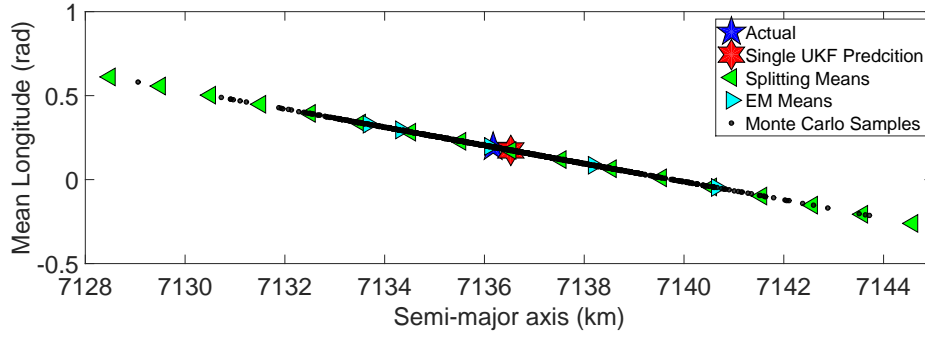
Figure 9.5: Medium Accuracy Orbit B at First Observation

demands may vary, the most important factor to consider is the mixture's ability to process observations and accurately estimate the orbit. To evaluate the performance of each approach, the mixtures are included within an IMM and process the same set of observations defined by each orbit case. Instead of evaluating each residual within the IMM, Ψ is analyzed (Algorithm 5). A larger value of Ψ indicates a poor orbit fit and possible filter divergence. The benefit of analyzing Ψ is that it assess the orbit fit without knowledge of the simulated truth state vector. In addition to Ψ, the more easily visualized position error is evaluated (Equation 3.58). The values for Ψ and RMS_r at each observation are averaged over the pass and compared in Tables 9.3 and 9.4. The tables also detail the propagation times and the number of observations in each pass. As stated previously, observations occur every minute once the satellite is in view of the radar after the defined propagation time.

The time row of Tables 9.3 and 9.4 reveals that a much longer propagation time of the medium accuracy cases is required to necessitate a mixture due to a failure of the covariance realism test. This result is expected and confirms other published results. Specific testing was not performed to detect the exact propagation time when a mixture was needed as this has already been researched [87]. Instead, covariance realism tests are performed at certain observation times to check for realism until it is determined a mixture is required.

180

Of interest, the medium accuracy Orbit B case shows that a near circular non-inclined LEO orbit does not require a mixture unless the propagation time is fairly long. The need for the mixture is based on the nonlinearities in the equations of motion, mainly the effect of Earth's non-uniform gravity field. When compared to other orbits, Orbit B experiences less non-spherical perturbations and the initial distribution remains Gaussian for longer.

Tables 9.3 and 9.4 also compare the newly developed mixture approaches with a nominal single Gaussian UKF. The results reinforce the need to use mixtures and an IMM. The single model UKF is greatly outperformed by the IMM. The values of Ψ for the single model UKF are extremely large showing a poor orbit fit, and the average position errors confirm the inadequacy of a single model approach. In fact, most values of Ψ are large enough to either miss-tag the observation to the wrong satellite or declare the detection of a false maneuver. The performance of the EM is fairly similar to the performance of the splitting approach. The differences between the two methods are minimal for most cases expect for the low accuracy Orbit D and the medium accuracy Orbit B cases. These cases both reveal a weakness of the IMM that warrants further discussion.

Table 9.3: Simulation Results Low Accuracy Cases

Orbit	A	B	C	D
Time (min)	552	502	609	503
Observations	7	15	3	6
Orbit %	7.0	15.0	3.0	6.3
Single Ψ	8136	120.05	$1.4 \cdot 10^4$	$2.4 \cdot 10^4$
Split Ψ	0.84	3.471	2.275	39.44
EM Ψ	1.92	1.201	1.703	104.49
Single RMS_r	0.3082	0.04934	4.2076	1.098
Split RMS_r	0.0048	$1.54 \cdot 10^{-4}$	0.0409	0.2325
EM RMS_r	0.0106	$1.63 \cdot 10^{-4}$	0.0228	0.0370

Table 9.4: Simulation Results Medium Accuracy Cases

Orbit	A	B	C	D
Time (min)	1796	4092	1756	1789
Observations	5	15	13	12
Orbit %	5.0	15.0	12.9	12.7
Single Ψ	33.16	291.8	18.75	60.88
Split Ψ	1.42	41.65	0.6952	0.549
EM Ψ	1.12	1.97	0.7300	0.489
Single RMS_r	0.0076	0.0042	0.000342	0.00226
Split RMS_r	0.0042	0.0002152	0.000500	0.000468
EM RMS_r	0.0036	0.0002714	0.000495	0.000546

The approach developed in this chapter begins pruning models after the first observation. Depending on the errors within the first observation processed, it is possible that the wrong Gaussian is heavily weighted. Since the covariances of each model are relatively small (compared to the single model case), converging to the non-optimal model solution causes an increase in errors and potential filter divergence. The IMM strategy was developed based on the frequency of observations and the potential size of the mixture resulting from the splitting case. If observations occurred more frequently, performance of the IMM may improve if the weighting is delayed until several observations are processed in a batch form. This approach allows for analysis of the residuals and covariance over several observations prior to weighting and pruning. Also, with a large number of components, it is advantageous to quickly shed known unfit models to reduce computational overhead. For this reason, pruning began at the first step; however, performance could improve by optimizing the pruning constant. The IMM formulation is advantageous in SSA operations due to its generality; however, one can carefully tune the pruning and weighting steps to optimize performance for a specific orbit or set of

observations. Additionally, if the observations occur more frequently, it is possible to use covariance inflation techniques to converge on the orbit with a single Gaussian [169]. This single model solution can serve as a comparison to the coalesced single model solution from the IMM. Overall, performance variability between mixture approaches within the IMM is expected in the general formulation and performance may improve by specific tuning of the IMM approach for a given orbit and observation scenario.

9.5.2 Unknown Maneuver Scenario.

An interesting application of the developed techniques is in handling unknown maneuvers in orbit estimation. The scenarios in the previous sections have large covariances when compared to satellites that are observed frequently. The low accuracy cases are consistent with objects very low on the prioritized collection list such as debris in harmless orbits. For the active satellites with maneuver capabilities, unknown maneuvers are known to cause issues with tracking and orbit estimation. The techniques developed and tested thus far in this chapter are directly transferable to handle unknown maneuvers through large covariance orbit estimation.

If there is intelligence or knowledge of a potential maneuver, a worst case inflated covariance can capture the uncertainty in a maneuver. Consider an active satellite that is tracked frequently whose solution contains a high accuracy covariance with $\mathbf{A} =$ $\mathrm{diag}\begin{bmatrix} 0.05 & 10^{-5} & 10^{-5} & 10^{-5} & 10^{-5} & 9.696 \cdot 10^{-5} \end{bmatrix}$.

Given that a satellite frequently maneuvers, it is possible to plan for a potential maneuver by inflating the covariance prior to a long observation time gap. Since many optimal maneuvers occur in the velocity or anti-velocity vector directions, we will consider scenarios with this type of maneuver [9]. That said, the approach is applicable to a maneuver in any direction. The worst case scenario approach assumes that the maneuver occurs just after observations cease. Given estimation of the satellite's engine performance, a possible maneuver size is then hypothesized.

With this information, the initial covariance is increased to capture the potential maneuver. First, determine a new orbit if the instantaneous maneuver occurs by transforming the initial state in Equinoctial elements to Cartesian ECI coordinates. Next, transform the expected maneuver from the RSW frame to Cartesian ECI coordinates. Add the velocity change to the initial orbit and rotate the sum back to Equinoctial elements. Now, the potential maneuver is expressed as a difference between two Equinoctial state vectors. To capture the maneuver in the covariance, set the 1σ covariance bound equivalent to the state difference in each direction such that $\mathbf{A}_{man} =$ diag $[|a_{nom} - a_{man}|, ..., |\ell_{nom} - \ell_{man}|]$. This formulation assumes the maneuver is equally likely in both the velocity and anti-velocity vector directions. To determine the new initial covariance, add the uncertainty from the maneuver to the previously defined covariance such that $\mathbf{A} = \mathbf{A} + \mathbf{A}_{man}$ and $\mathbf{P} = \mathbf{A}^T\mathbf{A}$. This approach is used for three maneuver test cases of Orbit D which are outlined in Table 9.5. The respective Δv_{norm} values for the maneuver cases are 0.003, 0.017, and 0.033.

Table 9.5: Orbit D Maneuver Covariance Accuracies

Δv	σ_a (km)	σ_h	σ_k	σ_{p_e}	σ_{q_e}	σ_ℓ
10 (m/s)	18.13	10^{-5}	0.0026	10^{-5}	10^{-5}	$9.696 \cdot 10^{-5}$
5 (m/s)	9.05	10^{-5}	0.0013	10^{-5}	10^{-5}	$9.696 \cdot 10^{-5}$
1 (m/s)	1.81	10^{-5}	$2.63 \cdot 10^{-4}$	10^{-5}	10^{-5}	$9.696 \cdot 10^{-5}$

The cases are tested using a similar approach as discussed in the previous subsection. The simulated truth orbit conducts the maneuver and observations of the truth orbit are perturbed with errors. The simulation results are captured in Table 9.6. The final column of the table shows that a smaller potential maneuver does not equate to a large enough covariance to necessitate a mixture as a single Gaussian passes the covariance realism test. A single model is able to keep the position errors low and properly update the orbital

solution with new observations. The table also reveals again the differences between the split and EM approaches as discussed in the previous section. Overall, the results show that a large covariance formulation of mixtures within an IMM can estimate orbital solutions even when unknown maneuvers occur. The approach taken for these test cases assumed a worst case scenario and large covariance inflation. If the maneuver occurred later in the coverage gap or never occurred, the approach is general enough to weight the proper model once observations are processed. The IMM can converge on the solution regardless of timing or maneuver size provided a worst case initial covariance inflation is used. The generality of the approach can help improve collision avoidance routines when there is potential for an unknown maneuver.

Table 9.6: Simulation Results Maneuver Cases

ΔV	10 m/s	5 m/s	1 m/s
Time (min)	581	580	579
Observations	5	5	5
Orbit %	5.3	5.3	5.3
Split Components	61	31	
EM Components	7	3	
Single Ψ	$8.6255 \cdot 10^5$	$2.0263 \cdot 10^4$	13.4198
Split Ψ	0.4295	109.6450	
EM Ψ	587.33	1.6069	
Single RMS_r	1.5613	0.4532	0.0022
Split RMS_r	$1.9395 \cdot 10^{-4}$	0.0128	
EM RMS_r	0.0181	0.0024	

9.6 Conclusion

The research in this chapter presented a fully-functional orbit estimation routine to ensure realistic error propagation and convergence on an accurate orbit estimate using MMAE. The merging of mixture propagation routines with a pruning IMM to process observations and update state estimates results in accurate orbit fits. This combination is an effective way to estimate orbits with large associated errors and long propagation times. The results show that the EM approach can achieve realism with far fewer components than the splitting approach. However, the EM method requires that the propagated Monte Carlo points are simulated or known; whereas, the splitting approach need not simulate all Monte Carlo points if a look up table is used to specify the required number of components. Both methods show significant accuracy improvements when compared to a single model approach.

By representing potential maneuvers with an inflated covariance, the results provide a new real-time methodology for orbit estimation of maneuvering spacecraft. The methods developed are a direct solution to the SSA problem currently facing the JSpOC. Overall, the state of the art mixture covariance propagation routines are improved through the addition of the EM formulation, the inclusion of the IMM in processing observation, and the adaptation of the covariance to capture potential unknown maneuvers.

X.   Conclusion

10.1   Contributions

This dissertation investigated a multitude of different approaches to track a non-cooperative maneuvering spacecraft using MMAE. Each chapter studied the overall general problem using different techniques catered to the type and timing of the maneuver. All chapters provided concrete examples with results that supported the use of MMAE for handling maneuvers in orbit estimation. Chapters 4-9 each provide a specific contribution to the state-of-the-art for orbital estimation of maneuvering spacecraft.

In Chapter 4, filtering-through an instantaneous maneuver using a covariance inflation IMM was explored. The maneuver detection metric, Ψ, indicated when to inflate the estimated covariance allowing for real-time detection of maneuvers and the ability to prevent filter divergence. Without adapting the filter to handle maneuvers, past information on the orbit fit is discarded and a new IOD is necessary which requires batching observations to develop an accurate estimate. The key feature of the developed algorithm is using the IMM as a method to select the degree to which the covariance is inflated. A single inflated covariance model is too specific to handle a wide variety of orbits and results in either false detections or increased errors due to over inflation. Using a pruning IMM presents an original way to solve the problem of choosing the amount of covariance inflation necessary while continuing to estimate the orbit in real-time.

In Chapter 5, the results highlight that even without knowledge of the true orbit, the covariance and number of post passes serve as adequate predictors of when performing maneuver reconstruction is worthwhile. Confidence in a reconstruction attempt must consider and account for the number of post passes and covariance. The neural network pattern recognition results highlight the need for integrating higher fidelity analysis techniques when analyzing non-cooperative orbital data. For SSA the goal is often catalog

accuracy, and the results highlight the impacts of each variable on the estimation accuracy. The results show that the output of an adaptive filter/smoother is more accurate when compared to the reconstruction solution after a single pass. Across all tests, the results suggest three passes are adequate to successfully reconstruct a maneuver. This information is useful in dynamic sensor tasking when determining the amount of coverage needed in high-priority maneuvering spacecraft tracking operations. Overall, a reconstruction is only as good as the data it is based on, and an evaluation of the number of post passes and covariance predicts the accuracy of a maneuver reconstruction.

In Chapter 6, a CMS is tracked using the VSD MMAE approach. Equipping orbit determination routines with the ability to detect a maneuver and transition to track a spacecraft as it accelerates is critical for updating location estimates of maneuvering satellites. This improvement will assist in determining the orbital solution in real-time and help pass accurate state estimates to additional radars. An increase in the frequency of observations for tracking a CMS will also help decrease the errors. Implementing dynamic real-time maneuver estimation through MMAE will surely improve responsiveness and accuracy.

Chapter 7 highlights the impact of short passes on accurate orbit predictions. Using the fattening covariance inflation factor and numerical intersection sampling methods, the probability of success is realized without the need to run Monte Carlo trials. This discovery is key as most operational tracking missions do not get 100 trials to characterize the error, but instead only one chance and a single data set. While the chapter focuses on the short propagation IOD, the full dimensional analysis approach is applicable to any situation in which two covariance ellipsoids are considered (collision avoidance, rendezvous, etc.). By posing the problem differently through a covariance requirement, the developed intersection method provides more information than simply determining if an intersection occurs. The sampling method determines the percentage of intersection and

the probability of success in meeting the accuracy requirement. The results revealed that a high accuracy short IOD mission is simply infeasible using a poor performing radar with limited orbital arc information.

The developments in Chapter 8 directly correlate to operational orbit propagation routines. Since it is known that Equinoctial element covariance propagations are more accurate, it is prudent to enable simple transformations between the element sets. Cartesian covariances from the JSpOC special perturbation catalog are easily convertible to Equinoctial covariances for use in propagation routines to preserve realism. Additional degrees of accuracy are very important when determining error bounds for orbital solutions. A more accurate transformation allows for improved collision avoidance routines and prevents catastrophic collisions or unnecessary avoidance maneuvers. The optimal UT provides an additional layer of accuracy to the traditional transformation approach.

Finally, in Chapter 9 methods are presented to ensure accurate orbital covariances that will surely improve collision avoidance routines. The inclusion of unknown maneuvers within the formulation can assist radars in expanding the search area to effectively track a satellite that maneuvered unknowingly. The mixture and IMM formulation is versatile and adaptable to almost any tracking situation. The results become more accurate when more observations are processed and the IMM coalesces to a single Gaussian model. The developed methods combine the filtering-through approach with multiple models and covariance realism.

All chapters revealed that the real-time orbit determination of high-priority maneuvering spacecraft requires a change in thinking about traditional tracking. It is not sufficient to gather a minimal number of observations with large spacing and then later piece together the maneuvers and orbits. Instead, a spacecraft that maneuvers often demands ground site resources and the ability to quickly discern the radar observations from those of another spacecraft. Tactical spacecraft missions are likely in the near future as spacecraft

and launch costs decrease. Using the developed filtering approaches with prioritized radar collections is an effective way to perform orbit determination and the SSA mission in the future.

Maneuvering spacecraft are most critical to track as unknown maneuvers may result in failing to locate the spacecraft at a future time or cross-tagging the observation to the incorrect satellite. An important step in the future of improving SSA is understanding which satellites have the potential to maneuver and equipping orbit determination routines with the abilities to track these spacecraft as they maneuver. The covariance inflation IMM with maneuver start and end detection abilities is an implementable tool to help improve SSA of high-priority targets.

The examples in the dissertation support initiatives in handling 'big data' at the JSpOC. At times, passes are reduced to only several observations to limit processing and storage. The results in each chapter show that the accuracy of the orbit estimate improves with higher frequency data. Also, the results support the need to accurately calibrate and upgrade radars, and consider the abilities of a radar when tasking it for collection. Certain radars are more accurate, and the performance of a radar must be considered during tasking for high-priority missions.

10.2 Future Work

It is the hope of every researcher that his or her work is recognized and continued by others in the future. There are multiple areas covered in this dissertation that could benefit from additional work. First and foremost, the implemented methods could benefit from increased testing through additional scenarios and orbital regimes. A neural network tool was implemented for reconstruction. The research could benefit from evaluating other multivariate methods of classification and researching the impact of using different neural network configurations (layers, neurons, test case sizes, etc.).

The topic of how to handle a spacecraft that is maneuvering as it exits coverage was not fully evaluated. Using the multiple model approach, one could use a baseline model that assumes the thrust continues and then use other models to estimate the end of the thrust at different intervals. This approach would provide a set of possible thrust durations and locations of the spacecraft. Once the radar reacquires the spacecraft, the closest of the multiple models is selected as the best guess for the thrust that occurred outside of view. Research in this area is necessary to transition the VSD IMM for operational use. Additionally, the multiple filter logic approach to determine a continuous maneuver end was not optimized to calculate the frequency with which to begin a nominal filter. This approach could benefit from additional research on how to time the start of the nominal filter to minimize computational time while improving the models performance.

The optimal UT between element set results were promising, but might benefit from further testing. One could consider a weighted cost function or a multi-objective optimization formulation. Additional optimization routines such as particle swarm may assist in preventing a local optimal solution. Tightening convergence tolerances and adding additional starting values could also increase the accuracy of the optimization routines.

Lastly, future developments of the large covariance long propagation study should consider varying radar data frequencies, tuning the pruning constant, and potentially adjusting the timing of component weighting to increase the robustness of the IMM.

To meet the future needs of SSA, it is necessary to perform orbit estimation fast and accurately while adapting to unpredicted maneuvers. This dissertation implemented and outlined orbit estimation routines while developing new tactics and techniques to keep pace with the ever changing world of commercial and military satellite operations.

Algorithm 9: Transition from ECI to Equinoctial Coordinates [12:116-127]

---

1 Given $\mathbf{x_{ECI}} = \begin{bmatrix} r_I & r_J & r_K & v_I & v_J & v_K \end{bmatrix}^T = \begin{bmatrix} \mathbf{r} & \vdots & \mathbf{v} \end{bmatrix}^T \qquad v = |\mathbf{v}|_2 \qquad r = |\mathbf{r}|_2$

2 Specific mechanical energy: $\varepsilon = \frac{1}{2}v^2 - \frac{\mu_\oplus}{r}$

3 Angular momentum: $\mathbf{h} = \mathbf{r} \times \mathbf{v}$ semi-major axis: $a = -\frac{\mu_\oplus}{2\varepsilon}$

4 Eccentricity: $\mathbf{e} = \frac{1}{\mu_\oplus}\left(\mathbf{v} \times \mathbf{h} - \frac{\mu_\oplus \mathbf{r}}{r}\right) \qquad e = |\mathbf{e}|_2$

5 Line of nodes direction $\mathbf{n} = \frac{\mathbf{k} \times \mathbf{h}}{|\mathbf{k} \times \mathbf{h}|_2}$ where $\mathbf{k} = \begin{bmatrix} 0 & 0 & 1 \end{bmatrix}^T$

6 Right Ascension of Ascending Node: $\Omega = \cos^{-1}(\mathbf{n}_I)$

    Quad check: if $\mathbf{n}_J \geq 0 \to 0 \leq \Omega \leq 180$ deg else $180 < \Omega < 360$ deg

7 Inclination: $i = \cos^{-1}\left(\frac{\mathbf{k} \cdot \mathbf{h}}{|\mathbf{h}|_2}\right) \qquad 0 \leq i \leq 180$ deg

8 Argument of perigee: $\omega = \cos^{-1}\left(\frac{\mathbf{n} \cdot \mathbf{e}}{|\mathbf{e}|_2}\right)$

    Quad check: if $\mathbf{e}_K \geq 0 \to 0 \leq \omega \leq 180$ deg else $180 < \omega < 360$ deg

9 True anomaly $\upsilon = \cos^{-1}\left(\frac{\mathbf{e} \cdot \mathbf{r}}{e \cdot r}\right)$

    Quad check: if $\mathbf{r} \cdot \mathbf{v} \geq 0 \to 0 \leq \upsilon \leq 180$ deg else $180 < \upsilon < 360$ deg

10 COEs: $\mathbf{x}_{COE} = \begin{bmatrix} a & e & i & \Omega & \omega & \upsilon \end{bmatrix}^T$

11 Eccentric anomaly: $E = 2\tan^{-1}\left[\sqrt{\frac{1-e}{1+e}}\tan\left(\frac{\upsilon}{2}\right)\right] \qquad$ Mean anomaly: $M = E - e\sin E$

12 $k = e\cos(\omega + \Omega) \qquad h = e\sin(\omega + \Omega) \qquad \ell = M + \omega + \Omega$

13 $p_e = \tan\left(\frac{i}{2}\right)\sin(\Omega) \qquad q_e = \tan\left(\frac{i}{2}\right)\cos(\Omega)$

14 Equinoctial elements: $\mathbf{x}_{Eq} = \begin{bmatrix} a & h & k & p_e & q_e & \ell \end{bmatrix}^T$

Algorithm 10: Transition from Equinoctial to ECI [12:116-127]

1 Given $\mathbf{x}_{Eq} = \begin{bmatrix} a & h & k & p_e & q_e & \ell \end{bmatrix}^T$

2 $e = \sqrt{h^2 + k^2}$ $i = 2\tan^{-1}\left(\sqrt{p_e^2 + q_e^2}\right)$ where $0 \leq i \leq 180$. If $i < 0$ then

   $i = 180 \text{ deg} + i$

3 Using a four-quadrant inverse tangent $\Omega = \tan^{-1}\left(\frac{p_e}{q_e}\right)$ $\zeta = \tan^{-1}\left(\frac{h}{k}\right)$

4 $\omega = \zeta - \Omega$ where $0 \leq \omega < 360 \text{ deg}$ $M = \ell - \omega - \Omega$ where $0 \leq M < 360 \text{ deg}$

5 $M = E - e\sin E$ is Kepler's problem. Reference Algorithm 11.

6 $\upsilon = \tan^{-1}\left(\frac{\sin(\upsilon)}{\cos(\upsilon)}\right)$ where $\cos(\upsilon) = \frac{\cos(E)-e}{1-e\cos(E)}$ and $\sin(\upsilon) = \frac{\sin(E)\sqrt{1-e^2}}{1-e\cos(E)}$

7 COEs: $\mathbf{x}_{COE} = \begin{bmatrix} a & e & i & \Omega & \omega & \upsilon \end{bmatrix}^T$

8 $p = a(1 - e^2)$

9 $\mathbf{r}_{PQW} = \begin{bmatrix} \frac{p\cos(\upsilon)}{1+e\cos(\upsilon)} & \frac{p\sin(\upsilon)}{1+e\cos(\upsilon)} & 0 \end{bmatrix}$ $\mathbf{v}_{PQW} = \begin{bmatrix} -\sqrt{\frac{\mu_\oplus}{p}}\sin\upsilon & \sqrt{\frac{\mu_\oplus}{p}}(e+\cos(\upsilon)) & 0 \end{bmatrix}$

10 $\mathbf{ROT}_{PQW \to ECI} =$

$$\begin{bmatrix} \cos(\Omega)\cos(\omega) - \sin(\Omega)\sin(\omega)\cos(i) & -\cos(\Omega)\sin(\omega) - \sin(\Omega)\cos(\omega)\cos(i) & \sin(\Omega)\sin(i) \\ \sin(\Omega)\cos(\omega) + \cos(\Omega)\sin(\omega)\cos(i) & -\sin(\Omega)\sin(\omega) + \cos(\Omega)\cos(\omega)\cos(i) & -\cos(\Omega)\sin(i) \\ \sin(\omega)\sin(i) & \cos(\omega)\sin(i) & \cos(i) \end{bmatrix}$$

11 $\mathbf{r}_{ECI} = \mathbf{ROT}_{PQW \to ECI}\left(\mathbf{r}_{PQW}\right)^T$ $\mathbf{v}_{ECI} = \mathbf{ROT}_{PQW \to ECI}\left(\mathbf{v}_{PQW}\right)^T$

12 $\mathbf{x}_{ECI} = \begin{bmatrix} \mathbf{r}_{ECI}^T & \vdots & \mathbf{v}_{ECI}^T \end{bmatrix}^T$

Algorithm 11: Kepler's Problem ($M \to E$) [12:73]

1 Given M, Guess that $E_0 = M$

2 $E_{n+1} = E_n + \frac{M - (E_n - e\sin(E_n))}{1 - e\cos E_n}$

3 **if** $\left|\frac{E_{n+1}-E_n}{E_{n+1}}\right|_1 >$ *Tolerance* **then**
   | $E_n = E_{n+1}$ return to step 2

   else
   | $E = E_{n+1}$

   end

Appendix B: Gaussian Mixtures

B.1 Univariate Splitting Cost Function Derivation

To break down the cost function into a more friendly form, use some properties of Gaussian multiplications and integrations [91].

$$\Gamma\left(\mu_1, \mu_2, \sigma_1^2, \sigma_2^2\right) = \frac{1}{\sqrt{2\pi\left(\sigma_1^2 + \sigma_2^2\right)}} e^{-\frac{(\mu_1 - \mu_2)^2}{2\left(\sigma_1^2 + \sigma_2^2\right)}} \tag{B.1}$$

$$= \mathcal{N}\left(\mu_1 - \mu_2; 0, \sigma_1^2 + \sigma_2^2\right) \tag{B.2}$$

$$= \int_{-\infty}^{\infty} \mathcal{N}\left(x; \mu_1, \sigma_1^2\right) \mathcal{N}\left(x; \mu_2, \sigma_2^2\right) dx \tag{B.3}$$

$$J = \int_{-\infty}^{\infty} [\mathcal{N}(x; 0, 1)]^2 \, dx - \int_{-\infty}^{\infty} \mathcal{N}(x; 0, 1) \sum_{i=1}^{N} w_i \mathcal{N}\left(x; \mu_i, \sigma_i^2\right) dx \tag{B.4}$$

$$- \int_{-\infty}^{\infty} \left[\sum_{i=1}^{N} w_i \mathcal{N}\left(x; \mu_i, \sigma_i^2\right)\right]^2 dx \tag{B.5}$$

$$\int_{-\infty}^{\infty} [\mathcal{N}(x; 0, 1)]^2 \, dx = \Gamma(0, 0, 1, 1) = \frac{1}{2\sqrt{\pi}} \tag{B.6}$$

$$\int_{-\infty}^{\infty} \mathcal{N}(x; 0, 1) \sum_{i=1}^{N} w_i \mathcal{N}\left(x; \mu_i, \sigma_i^2\right) dx = \sum_{i=1}^{N} w_i \Gamma\left(0, \mu_i, 1, \sigma_i^2\right) \tag{B.7}$$

$$\int_{-\infty}^{\infty} \left[\sum_{i=1}^{N} w_i \mathcal{N}\left(x; \mu_i, \sigma_i^2\right)\right]^2 dx = \sum_{i=1}^{N} \sum_{j=1}^{N} w_i w_j \Gamma\left(\mu_i, \mu_j, \sigma_i^2, \sigma_j^2\right) \tag{B.8}$$

With the weights vector $\mathbf{w} = w_1, .., w_n$, define

$$(\mathbf{n})_i = \mathcal{N}\left(\mu_i; 0, \sigma_i^2 + 1\right) \qquad (\mathbf{M})_{ij} = \mathcal{N}\left(\mu_i - \mu_j; 0, \sigma_i^2 + \sigma_j^2\right) \tag{B.9}$$

$$J = \mathbf{w}^T \mathbf{M} \mathbf{w} - 2\mathbf{w}^T \mathbf{n} + \frac{1}{2\sqrt{\pi}} \tag{B.10}$$

194

B.2 Mixture Approximation of Standard Gaussian

Algorithm 12: Gaussian Mixture Approximation of Standard Gaussian [168]

input : $\hat{\sigma} \in [0, 1]$

output: $\widetilde{\mathbf{w}}, \widetilde{\boldsymbol{\mu}}, \widetilde{\boldsymbol{\sigma}}$ for a mixture $p_x^M = \sum_{i=1}^{N} \widetilde{w}_i \mathcal{N}\left(\mathbf{x}, \widetilde{\mu}_i, \widetilde{\sigma}_i^2\right)$

1 **if** $\hat{\sigma} \geq 2/3$ **then**
  | Set $N = 3$ use solution from Table B.1 **end routine**

  end

2 **if** $\hat{\sigma} \geq 1/2$ **then**
  | Set $m = 4$ and $\widetilde{\sigma}_i = 1/2$

  else
  | $m = 6$, and $\widetilde{\sigma}_i = \hat{\sigma}$

  end

3 $N = \lceil 1 + 2\frac{m}{\hat{\sigma}} \rceil$

4 **for** $i = 1$ *to* N **do**
  | $\widetilde{\mu}_i = -m + \widetilde{\sigma}(i - 1)$

  end

  Solve optimization problem $J = \widetilde{\mathbf{w}}^T \mathbf{M} \widetilde{\mathbf{w}} - 2\widetilde{\mathbf{w}}^T \mathbf{n}$ for $\mathbf{w}$ as in Equation 9.5

  $\widetilde{\mathbf{w}}$ is the vector of the weights $\widetilde{w}_i$, $\widetilde{\boldsymbol{\mu}}$ is a vector of the means $\widetilde{\mu}_i$, and $\widetilde{\boldsymbol{\sigma}}$ is a vector of

  $\widetilde{\sigma}_i$, which are equivalent.

Table B.1: DeMars' Three Component Mixture Solution [91]

Component	$\widetilde{w}_i$	$\widetilde{\mu}_i$	$\widetilde{\sigma}_i$
1	0.225224624913675	-1.057515461475881	0.671566288664076
2	0.549550750172650	0	0.671566288664076
3	0.225224624913675	1.057515461475881	0.671566288664076

B.3 Mixture Mode Gradient and Hessian

Begin with the cost function and take the partial derivative

$$J = -\ln\left(p_{\mathbf{x}}^M\right) \tag{B.11}$$

$$\mathcal{N}\left(\mathbf{x}; \boldsymbol{\mu}_i, \mathbf{P}_i\right) = \frac{e^{-\frac{1}{2}(\mathbf{x}-\boldsymbol{\mu}_i)^T \mathbf{P}_i^{-1}(\mathbf{x}-\boldsymbol{\mu}_i)}}{(2\pi)^{n/2}\,|P_i|^{1/2}} = p_{\mathbf{x}_i} \tag{B.12}$$

$$\frac{\partial J}{\partial \mathbf{x}} = -\frac{1}{\sum_{i=1}^{N} w_i \mathcal{N}\left(\mathbf{x}; \boldsymbol{\mu}_i, \mathbf{P}_i\right)} \frac{\partial \sum_{i=1}^{N} w_i \mathcal{N}\left(\mathbf{x}; \boldsymbol{\mu}_i, \mathbf{P}_i\right)}{\partial \mathbf{x}} \tag{B.13}$$

$$\frac{\partial J}{\partial \mathbf{x}} = -\frac{1}{p_{\mathbf{x}}^M} \sum_{i=1}^{N} w_i \left(\frac{e^{-\frac{1}{2}(\mathbf{x}-\boldsymbol{\mu}_i)^T \mathbf{P}_i^{-1}(\mathbf{x}-\boldsymbol{\mu}_i)}}{(2\pi)^{n/2}\,|P_i|^{1/2}} \frac{\partial}{\partial \mathbf{x}} \left[-\frac{1}{2}(\mathbf{x}-\boldsymbol{\mu}_i)^T \mathbf{P}_i^{-1}(\mathbf{x}-\boldsymbol{\mu}_i) \right] \right) \tag{B.14}$$

$$-\mathbf{P}_i^{-1}(\mathbf{x}-\boldsymbol{\mu}_i) = \frac{\partial}{\partial \mathbf{x}} \left[-\frac{1}{2}(\mathbf{x}-\boldsymbol{\mu}_i)^T \mathbf{P}_i^{-1}(\mathbf{x}-\boldsymbol{\mu}_i) \right] \tag{B.15}$$

$$\frac{\partial J}{\partial \mathbf{x}} = \frac{1}{\sum_{i=1}^{N} w_i \mathcal{N}\left(\mathbf{x}; \boldsymbol{\mu}_i, \mathbf{P}_i\right)} \sum_{i=1}^{N} w_i \left(\frac{e^{-\frac{1}{2}(\mathbf{x}-\boldsymbol{\mu}_i)^T \mathbf{P}_i^{-1}(\mathbf{x}-\boldsymbol{\mu}_i)}}{(2\pi)^{n/2}\,|P_i|^{1/2}} \left[\mathbf{P}_i^{-1}(\mathbf{x}-\boldsymbol{\mu}_i) \right] \right) \tag{B.16}$$

$$\frac{\partial J}{\partial \mathbf{x}} = \frac{1}{p_{\mathbf{x}}^M} \sum_{i=1}^{N} w_i p_{\mathbf{x}_i} \left[\mathbf{P}_i^{-1}(\mathbf{x}-\boldsymbol{\mu}_i) \right] \tag{B.17}$$

Now to find the Hessian:

$$\frac{\partial^2 J}{\partial \mathbf{x} \partial \mathbf{x}^T} = \frac{\partial}{\partial \mathbf{x}} \frac{\Lambda}{\Xi} \tag{B.18}$$

$$\Lambda = \sum_{i=1}^{N} \left(w_i p_{\mathbf{x}_i} \left[\mathbf{P}_i^{-1}(\mathbf{x}-\boldsymbol{\mu}_i) \right] \right) \tag{B.19}$$

$$\Xi = \sum_{i=1}^{N} w_i p_{\mathbf{x}_i} = p_{\mathbf{x}}^M \tag{B.20}$$

$$\frac{\partial \Xi}{\partial \mathbf{x}} = -\sum_{i=1}^{N} w_i p_{\mathbf{x}_i} \left[\mathbf{P}_i^{-1} (\mathbf{x} - \boldsymbol{\mu}_i) \right] \tag{B.21}$$

$$\frac{\partial \Lambda}{\partial \mathbf{x}} = \sum_{i=1}^{N} \left(w_i p_{\mathbf{x}_i} \left[\mathbf{P}_i^{-1} \right] - w_i p_{\mathbf{x}_i} \left[\mathbf{P}_i^{-1} (\mathbf{x} - \boldsymbol{\mu}_i) \right] \left[\mathbf{P}_i^{-1} (\mathbf{x} - \boldsymbol{\mu}_i) \right]^T \right) \tag{B.22}$$

$$\frac{\partial \Lambda}{\partial \mathbf{x}} = \sum_{i=1}^{N} w_i p_{\mathbf{x}_i} \left(\mathbf{P}_i^{-1} - \mathbf{P}_i^{-1} (\mathbf{x} - \boldsymbol{\mu}_i) (\mathbf{x} - \boldsymbol{\mu}_i)^T \mathbf{P}_i^{-1} \right) \tag{B.23}$$

Combining all terms, the Hessian is

$$\frac{\partial^2 J}{\partial \mathbf{x} \partial \mathbf{x}^T} = \frac{\sum_{i=1}^{N} w_i p_{\mathbf{x}_i} \left(\mathbf{P}_i^{-1} - \mathbf{P}_i^{-1} (\mathbf{x} - \boldsymbol{\mu}_i) (\mathbf{x} - \boldsymbol{\mu}_i)^T \mathbf{P}_i^{-1} \right)}{\sum_{i=1}^{N} w_i p_{\mathbf{x}_i}}$$
$$+ \frac{\left(\sum_{i=1}^{N} w_i p_{\mathbf{x}_i} \left[\mathbf{P}_i^{-1} (\mathbf{x} - \boldsymbol{\mu}_i) \right] \right) \left(\sum_{i=1}^{N} w_i p_{\mathbf{x}_i} \left[\mathbf{P}_i^{-1} (\mathbf{x} - \boldsymbol{\mu}_i) \right] \right)^T}{\left(\sum_{i=1}^{N} w_i p_{\mathbf{x}_i} \right)^2} \tag{B.24}$$

B.4 K-means++ Expectation Maximization

Algorithm 13: K-means++ Seeding [105]

input : k, $d \times 1$ Monte-Carlo samples $\mathbf{x}_{MC_i}$, predefined number of components N

output: Means $\boldsymbol{\mu}_1 \dots \boldsymbol{\mu}_N$

1 Select a random point as first mean: $\boldsymbol{\mu}_1 = \mathbf{x}_{MC_i}$

2 Calculate D^2 for each sample as the minimum squared distance to a mean defined thus far $D_i^2 = \min \left[|\mathbf{x}_{MC} - \boldsymbol{\mu}_i|_2^2 \right], \forall \boldsymbol{\mu}_i$

3 Sample next mean from probability distribution: $Pr(i) = \frac{D_i^2}{\sum_j D_j^2}$

4   Create cdf by summing Pr element wise

5   Sample distribution by finding first cdf element $< rand$ where $rand \sim \mathcal{U}[0, 1]$

6   Set the corresponding $\mathbf{x}_{MC}$ value from the cdf as the next mean, $\boldsymbol{\mu}_i$

7 Return to step 2 until N means are selected

Algorithm 14: Expectation Maximization [103]

input : k, $d \times 1$ Monte-Carlo samples: $\mathbf{x}_{MC}$, Component means $\boldsymbol{\mu}_1...\boldsymbol{\mu}_N$

output: $\mathbf{w}$, $\boldsymbol{\mu}_1...\boldsymbol{\mu}_N$, $\mathbf{P}_1...\mathbf{P}_N$

1 Determine d variances for each element of the sample set:

$$\sigma_j^2 = \text{var}\left(\mathbf{x}_{MC_{j1}}, ..., \mathbf{x}_{MC_{jk}}\right) \text{ for } j = 1...d$$

2 Set initial component covariances equal: $\mathbf{P}_i = \text{diag}\left[\sigma_1^2, ..., \sigma_d^2\right]$

3 Set initial component weights equal $w_i = \frac{1}{N}$

4 Form initial mixture with input means: $p_{\mathbf{x}_0}^M = \sum_{i=1}^N w_i \mathcal{N}\left(\mathbf{x}; \boldsymbol{\mu}_i, \mathbf{P}_i\right)$

Expectation Step:

5 Compute $k \times N$ membership weight matrix for each sample to each component:

$$\mathbf{M}_{ij} = \frac{w_j \mathcal{N}\left(\mathbf{x}_{MC_i}; \boldsymbol{\mu}_j, \mathbf{P}_j\right)}{\sum_{z=1}^N w_z \mathcal{N}\left(\mathbf{x}_{MC_i}; \boldsymbol{\mu}_z, \mathbf{P}_z\right)}$$

Maximization Step:

6 Determine new weights with $1 \times N$ vector $\mathbf{m}$

$$\mathbf{m}_j = \sum_{i=1}^k \mathbf{M}_{ij} \qquad w^{new} = \frac{1}{k}\mathbf{m}$$

7 Determine new means and covariances for $j = 1, ..., N$

$$\boldsymbol{\mu}_j^{new} = \frac{1}{\mathbf{m}_j} \sum_{i=1}^k \mathbf{M}_{ij} \mathbf{x}_{MC_i}$$

$$\mathbf{P}_j^{new} = \frac{1}{\mathbf{m}_j} \sum_{i=1}^k \mathbf{M}_{ij} \left(\mathbf{x}_{MC_i} - \boldsymbol{\mu}_j^{new}\right)\left(\mathbf{x}_{MC_i} - \boldsymbol{\mu}_j^{new}\right)^T$$

8 Form updated mixture: $p_{\mathbf{x}_{new}}^M = \sum_{i=1}^N w_i^{new} \mathcal{N}\left(\mathbf{x}; \boldsymbol{\mu}_i^{new}, \mathbf{P}_i^{new}\right)$

9 Calculate negative log likelihood: $q_{new} = -\ln\left(p_{\mathbf{x}_{new}}^M\right)$

10 Iterate, returning to step 5 until $(q_{new} - q_{old}) <$ tolerance

Bibliography

[1] Department of Defense & Office of the Director of National Intelligence, *National Security Space Strategy Unclassified Summary*, Arlington, VA, January 2011.

[2] Hyten, J., "Gen. John Hyten, Commander of U.S. Air Force Space Command, in Conversation with SpaceNews," December 2014, https://www.youtube.com/watch?v=G1-I-_Y1An0#t=372, Accessed 22 Decemeber, 2014.

[3] National Research Council, *Continuing Kepler's Quest: Assessing Air Force Space Command's Astrodynamics Standards*, The National Academies Press, 2012.

[4] NASA, "Space Debris and Human Spacecraft," Sep 2013, http://www.nasa.gov/mission_pages/station/news/orbital_debris.html, Accessed 22 Decemeber, 2014.

[5] Vishwajeet, K., Singla, K., and Jah, M., "Nonlinear Uncertainty Propagation for Perturbed Two-Body Orbits," *Journal of Guidance, Control, and Dynamics*, April 2014, accessed July 29, 2014. doi: 10.2514/1.G000472.

[6] Baird, M. A., "Maintaining Space Situational Awareness and Taking It to the Next Level," *Air & Space Power Journal*, Vol. 27, No. 5, Sep 2013, pp. 50–73.

[7] Pawlikowski, E., "Disruptive Challenges, New Opportunities, and New Strategies," *Strategic Studies Quarterly*, Vol. 6, No. 1, Spring 2012, ADA557401.

[8] Wasson, M., "Space Situational Awareness in the Joint Space Operations Center," *Proceedings of the Advanced Maui Optical and Space Surveillance Technologies Conference*, Maui Economic Development Board, Inc., Sep 2011.

[9] Showalter, D. J. and Black, J. T., "Responsive Theater Maneuvers via Particle Swarm Optimization," *Journal of Spacecraft and Rockets*, 2014, doi: 10.2514/1.A32989, Accessed 24 Jun 2014.

[10] Co, T. C., *Operationally Responsive Spacecraft Using Electric Propulsion*, Ph.D. thesis, Air Force Institute of Technology (AU), Wright-Patterson AFB OH, Sep 2012, ADA564646.

[11] Abbot, R. I. and Wallace, T. P., "Decision Support in Space Situational Awareness," *Lincoln Laboratory Journal*, Vol. 16, No. 2, 2007, pp. 297–335.

[12] Vallado, D. A., *Fundamentals of Astrodynamics and Applications*, Springer, New York, NY, 3rd ed., 2007.

[13] Wiesel, W. E., *Modern Orbit Determination*, Aphelion Press, Beavercreek, OH, 2003.

[14] Tapley, B., Schutz, B., and Born, G. H., *Statistical Orbit Determination*, Elsevier, Burlington, MA, 2004.

[15] Wiesel, W. E., *Spaceflight Dynamics*, Aphelion Press, Beavercreek, OH, 3rd ed., 2010.

[16] Wiesel, W. E., *Modern Astrodynamics*, Aphelion Press, Beavercreek, OH, 2010.

[17] Casella, G. and Berger, R. L., *Statistical Inference*, Duxbury Press, Belmont, CA, 2nd ed., 2002.

[18] Ackleh, A. S., Allen, E. J., Kearfott, R. B., and Seshaiyer, P., *Classical and Modern Numerical Analysis: Theory, Methods and Practice*, CRC Press, Boca Raton, FL, 2011.

[19] Kalman, R. E., "Contributions to the Theory of Optimal Control," *Boletn de la Sociedad Matemtica Mexicana*, Vol. 5, No. 2, 1960, pp. 102–119.

[20] Kalman, R. E., "A New Approach to Linear Filtering and Prediction Problems," *Journal of Fluids Engineering*, Vol. 82, No. 1, 1960, pp. 35–45, doi: 10.1115/1.3662552.

[21] Welch, G. and Bishop, G., "An Introduction to the Kalman Filter," Tech. Rep. TR 95-041, University of North Carolina, Department of Computer Science, 1995.

[22] Wright, J., "Optimal Orbit Determination," *12th AAS/AIAA Spaceflight Mechanics Meeting*, No. 192, Univelt, Inc., Jan 2002.

[23] Wright, J. R., "Sequential Orbit Determination with Auto-Correlated Gravity Modeling Errors," *Journal of Guidance, Control, and Dynamics*, Vol. 4, No. 3, May 1981, pp. 304–309, doi: 10.2514/3.56083.

[24] Hujsak, R., "Orbit Determination During High Thrust and Low Thrust Maneuvers," *15th AAS/AIAA Spaceflight Mechanics Meeting*, No. 136, Univelt, Inc., Jan 2005.

[25] Hujsak, R., "OD for Non-Cooperative Maneuvering Satellites," *AGI User Exchange*, Analytical Graphics, Inc., Aug 2007.

[26] Wright, J. R., "Nonlinear Variable Lag Smoother," *18th AAS/AIAA Spaceflight Mechanics Meeting*, No. 303, Univelt, Inc., Jan 2008.

[27] Woodburn, J., Carrico, J., and Wright, J. R., "Estimation of Instantaneous Maneuvers Using a Fixed Interval Smoother," *Advances in the Astronautical Sciences*, Vol. 116, 2003, pp. 243–260.

[28] Raol, J. and Sinha, N., "On the Orbit Determination Problem," *Aerospace and Electronic Systems, IEEE Transactions on*, Vol. 21, No. 3, May 1985, pp. 274–291, doi: 10.1109/TAES.1985.310558.

[29] Li, X. R. and Jilkov, V. P., "Survey of Maneuvering Target Tracking: III. Measurement Models," *Signal and Data Processing of Small Targets*, Vol. 4473, International Society for Optics and Photonics, November 2001, pp. 423–446, doi: doi:10.1117/12.492752.

[30] Julier, S. J. and Uhlmann, J. K., "Reduced Sigma Point Filters for the Propagation of Means and Covariances through Nonlinear Transformations," *American Control Conference, Proceedings of the*, Vol. 2, Institute of Electrical and Electronics Engineers, 2002, pp. 887–892, doi: 10.1109/ACC.2002.1023128.

[31] Simon, D., *Optimal State Estimation: Kalman, H Infinity, and Nonlinear Approaches*, John Wiley & Sons, Hoboken, NJ, 2006.

[32] Julier, S. J. and Uhlmann, J. K., "Unscented Filtering and Nonlinear Estimation," *Proceedings of the IEEE*, Vol. 92, No. 3, Mar 2004, pp. 401–422, doi: 10.1109/JPROC.2003.823141.

[33] Teixeira, B. O. S., Santillo, M. A., Erwin, R. S., and Bernstein, D. S., "Spacecraft Tracking Using Sampled-Data Kalman Filters," *Control Systems, IEEE*, Vol. 28, No. 4, Aug 2008, pp. 78–94, doi: 10.1109/MCS.2008.923231.

[34] Lee, D.-J. and Alfriend, K. T., "Sigma Point Filtering for Sequential Orbit Estimation and Prediction," *Journal of Spacecraft and Rockets*, Vol. 44, No. 2, Mar 2007, pp. 388–398, doi: 10.2514/1.20702.

[35] Pardal, P. C. P. M., Kuga, H. K., and de Moraes, R. V., "Robustness Assessment Between Sigma Point and Extended Kalman Filter for Orbit Determination," *Journal of Aerospace Engineering, Sciences, and Applications*, Vol. 3, No. 3, Sep 2011, pp. 35–44, doi: 10.7446/jaesa.0303.04.

[36] Cheon, Y.-J., "Fast Convergence of Orbit Determination using Geomagnetic Field Measurement in Target Pointing Satellite," *Aerospace Science and Technology*, Vol. 30, No. 1, October 2013, pp. 315–322, doi: 10.1016/j.ast.2013.08.016.

[37] Särkkä, S., "Continuous-time and Continuous-discrete-time Unscented Rauch–Tung–Striebel Smoothers," *Signal Processing*, Vol. 90, No. 1, January 2010, pp. 225–235, doi: 10.1016/j.sigpro.2009.06.012.

[38] Särkkä, S., "Unscented Rauch–Tung–Striebel Smoother," *Automatic Control, IEEE Transactions on*, Vol. 53, No. 3, Apr 2008, pp. 845–849, doi: 10.1109/TAC.2008.919531.

[39] Hough, M. E., "Recursive Bias Estimation and Orbit Determination," *Journal of Guidance, Control, and Dynamics*, Vol. 32, No. 2, Mar 2009, pp. 645–653, doi: 10.2514/1.39955.

[40] Hough, M. E., "Orbit Determination with Improved Covariance Fidelity, Including Sensor Measurement Biases," *Journal of Guidance, Control, and Dynamics*, Vol. 34, No. 3, May 2011, pp. 903–911, doi: 10.2514/1.53053.

[41] Ichikawa, T., "The Orbit Estimation For Low Thrust Spacecraft," *41st Society of Instruments and Control Engineers Annual Conference, Proceedings of the*, Vol. 3, Institute of Electrical and Electronics Engineers, Aug 2002, pp. 1839–1844, doi: 10.1109/SICE.2002.1196601.

[42] Melvin, P. J., "A Kalman Filter For Orbit Determination With Applications to GPS and Stellar Navigation," *6th AAS/AIAA Spaceflight Mechanics Meeting*, No. 145, Univelt, Inc., Feb 1996.

[43] Cloutier, J., Lin, C.-F., and Yang, C., "Maneuvering Target Tracking via Smoothing and Filtering Through Measurement Concatenation," *Journal of Guidance, Control, and Dynamics*, Vol. 16, Mar 1993, pp. 377–384, doi: 10.2514/3.21013.

[44] Stallard, D., "An Angle-only Tracking Filter for a Maneuvering Target," *Guidance, Navigation and Control Conference*, No. 3343, American Institute of Aeronautics and Astronautics, Aug 1990, doi: 10.2514/6.1990-3343.

[45] Bekir, E., "Adaptive Kalman Filter for Tracking Maneuvering Targets," *Journal of Guidance, Control, and Dynamics*, Vol. 6, No. 5, Sep 1983, pp. 414–416, doi: 10.2514/3.19852.

[46] Gelb, A., *Applied Optimal Estimation*, MIT press, Cambridge, MA, 1974.

[47] Sorenson, H. W. and Sacks, J. E., "Recursive Fading Memory Filtering," *Information Sciences*, Vol. 3, No. 2, Apr 1971, pp. 101–119, doi: 10.1016/0020-0255(73)90003-0.

[48] Lee, T. S., "Theory and Application of Adaptive Fading Memory Kalman Filters," *Circuits and Systems, IEEE Transactions on*, Vol. 35, No. 4, Apr 1988, pp. 474–477, doi: 10.1109/31.1769.

[49] Lin, C.-F., *Modern Navigation, Guidance, and Control Processing*, Vol. 2, Prentice Hall, Englewood Cliffs, NJ, 1991.

[50] Magill, D., "Optimal Adaptive Estimation of Sampled Stochastic Processes," *Automatic Control, IEEE Transactions on*, Vol. 10, No. 4, Oct 1965, pp. 434–439, doi: 10.1109/TAC.1965.1098191.

[51] Chan, Y., Hu, A. G., and Plant, J., "A Kalman Filter Based Tracking Scheme with Input Estimation," *Aerospace and Electronic Systems, IEEE Transactions on*, Vol. 15, No. 2, Mar 1979, pp. 237–244, doi: 10.1109/TAES.1979.308710.

[52] Bogler, P. L., "Tracking a Maneuvering Target Using Input Estimation," *Aerospace and Electronic Systems, IEEE Transactions on*, Vol. 23, No. 3, May 1987, pp. 298–310, doi: 10.1109/TAES.1987.310826.

[53] Lee, H. and Tahk, M.-J., "Generalized Input-Estimation Technique for Tracking Maneuvering Targets," *Aerospace and Electronic Systems, IEEE Transactions on*, Vol. 35, No. 4, Oct 1999, pp. 1388–1402, doi: 10.1109/7.805455.

[54] Wang, T. C. and Varshney, P. K., "A Tracking Algorithm for Maneuvering Targets," *Aerospace and Electronic Systems, IEEE Transactions on*, Vol. 29, No. 3, Jul 1993, pp. 910–925, doi: 10.1109/7.220939.

[55] Park, Y.-H., Seo, J., and Lee, J.-G., "Maneuvering Target Tracking Using the Variable Dimension Filter with Input Estimation," *AAS/AIAA Astrodynamics Conference*, No. 4600, American Institute of Aeronautics and Astronautics, 1992, doi: 10.2514/6.1992-4600.

[56] Bar-Shalom, Y. and Birmiwal, K., "Variable Dimension Filter for Maneuvering Target Tracking," *Aerospace and Electronic Systems, IEEE Transactions on*, Vol. 18, No. 5, Sep 1982, pp. 621–629, doi: 10.1109/TAES.1982.309274.

[57] Bar-Shalom, Y., Li, X. R., and Kirubarajan, T., *Estimation with Applications to Tracking and Navigation: Theory Algorithms and Software*, John Wiley & Sons, Hoboken, NJ, 2004.

[58] Soken, H. E. and Hajiyev, C., "Adaptive Unscented Kalman Filter with Multiple Fading Factors for Pico Satellite Attitude Estimation," *4th International Conference on Recent Advances in Space Technologies*, Institute of Electrical and Electronics Engineers, Jun 2009, pp. 541–546, doi: 10.1109/RAST.2009.5158254.

[59] Ramachandra, K., *Kalman Filtering Techniques for Radar Tracking*, CRC Press, Boca Raton, FL, 2000.

[60] Li, W.-C., Wei, P., and Xiao, X.-C., "An Adaptive Nonlinear Filter of Discrete-Time System with Uncertain Covariance Using Unscented Kalman Filter," *IEEE International Symposium on Communications and Information Technology*, Vol. 2, Institute of Electrical and Electronics Engineers, Oct 2005, pp. 1436–1439, doi: 10.1109/ISCIT.2005.1567140.

[61] Mehra, R., "Approaches to Adaptive Filtering," *Automatic Control, IEEE Transactions on*, Vol. 17, No. 5, Oct 1972, pp. 693–698, doi: 10.1109/TAC.1972.1100100.

[62] Myers, K. and Tapley, B., "Adaptive Sequential Estimation with Unknown Noise Statistics," *Automatic Control, IEEE Transactions on*, Vol. 21, No. 4, Aug 1976, pp. 520–523, doi: 10.1109/TAC.1976.1101260.

[63] Shi, Y., Han, C., and Liang, Y., "Adaptive UKF for Target Tracking with Unknown Process Noise Statistics," *Information Fusion, 12th International Conference on*, Institute of Electrical and Electronics Engineers, Jul 2009, pp. 1815–1820.

[64] Burkhart, P. D. and Bishop, R. H., "Adaptive Orbit Determination for Interplanetary Spacecraft," *Journal of Guidance, Control, and Dynamics*, Vol. 19, No. 3, May 1996, pp. 693–701, doi: 10.2514/3.21676.

[65] Kumar, K., Yadav, D., and Srinivas, B. V., "Adaptive Noise Models for Extended Kalman Filter," *Journal of Guidance, Control, and Dynamics*, Vol. 14, No. 2, Mar 1991, pp. 475–477, doi: 10.2514/3.20665.

[66] Wright, J. R., Woodburn, J., Truong, S., and Chuba, W., "Orbit Gravity Error Covariance," *18th AAS/AIAA Spaceflight Mechanics Meeting*, No. 157, Univelt, Inc., Jan 2008.

[67] Singer, R. A., "Estimating Optimal Tracking Filter Performance for Manned Maneuvering Targets," *Aerospace and Electronic Systems, IEEE Transactions on*, Vol. 6, No. 4, Jul 1970, pp. 473–483, doi: 10.1109/TAES.1970.310128.

[68] Hujsak, R., "Process Noise," *AGI Users' Conference*, Analytical Graphics, Inc., October 2005.

[69] Han, J., Song, Q., and He, Y., "Adaptive Unscented Kalman Filter and its Applications in Nonlinear Control," *Kalman Filter Recent Advances and Applications*, edited by V. M. Moreno and A. Pigazo, InTech, Apr 2009, pp. 1–24, doi: 10.5772/6799.

[70] Lee, D.-J. and Alfriend, K. T., "Adaptive Sigma Point Filtering for State and Parameter Estimation," *AAS/AIAA Astrodynamics Specialist Conference*, Vol. 2, 2004, pp. 897–916, doi: 10.2514/6.2004-5101.

[71] Busse, F. D., How, J. P., and Simpson, J., "Demonstration of Adaptive Extended Kalman Filter for Low Earth Orbit Formation Estimation Using CDGPS," *Navigation*, Vol. 50, No. 2, Jun 2003, pp. 79–93, doi: 10.1002/j.2161-4296.2003.tb00320.x.

[72] Sage, A. P. and Husa, G. W., "Algorithms for Sequential Adaptive Estimation of Prior Statistics," *IEEE 8th Adaptive Processes Decision and Control Symposium*, Vol. 8, Institute of Electrical and Electronics Engineers, Nov 1969, pp. 61–61, doi: 10.1109/SAP.1969.269927.

[73] Mohamed, A. H. and Schwarz, K. P., "Adaptive Kalman Filtering for INS/GPS," *Journal of Geodesy*, Vol. 73, No. 4, May 1999, pp. 193–203, doi: 10.1007/s001900050236.

[74] Li, X. R. and Jilkov, V. P., "Survey of maneuvering target tracking. Part V. Multiple-model methods," *Aerospace and Electronic Systems, IEEE Transactions on*, Vol. 41, No. 4, Oct 2005, pp. 1255–1321, doi: 10.1109/TAES.2005.1561886.

[75] Amirzadeh, A., Karimpour, A., and Moeini, A., "An IMM Algorithm Based on Augmented Kalman Filter for Maneuvering Target Tracking," *Scientific Research and Essays*, Vol. 6, No. 34, Dec 2011, pp. 6787–6797, doi: 10.5897/SRE10.980.

[76] Rago, C. and Mehra, R. K., "Robust Adaptive Target State Estimation for Missile Guidance Using the Interacting Multiple Model Kalman Filter," *IEEE Position Location and Navigation Symposium*, Institute of Electrical and Electronics Engineers, Mar 2000, pp. 355–362, doi: 10.1109/PLANS.2000.838325.

[77] Xiong, Z., Jang, H., Li, Q., Liu, W., and Chen, T., "The Research of Maneuvering Target Tracking based on Interacting Multiple Model," *Automatic Control and Artificial Intelligence, International Conference on*, IET, Mar 2012, pp. 2171–2174, doi: 10.1049/cp.2012.1429.

[78] Hanlon, P. D. and Maybeck, P. S., "Multiple-Model Adaptive Estimation Using a Residual Correlation Kalman Filter Bank," *Aerospace and Electronic Systems, IEEE Transactions on*, Vol. 36, No. 2, Apr 2000, pp. 393–406, doi: 10.1109/7.845216.

[79] Bizup, D. F. and Brown, D. E., "Maneuver Detection Using the Radar Range Rate Measurement," *Aerospace and Electronic Systems, IEEE Transactions on*, Vol. 40, No. 1, Jan 2004, pp. 330–336, doi: 10.1109/TAES.2004.1292169.

[80] Shetty, S. and Alouani, A. T., "A Multisensor Tracking System with an Image-Based Maneuver Detector," *Aerospace and Electronic Systems, IEEE Transactions on*, Vol. 32, No. 1, Jan 1996, pp. 167–181, doi: 10.1109/7.481259.

[81] Yun, J. and Ryoo, C.-K., "Missile Guidance Law Estimation Using Modified Interactive Multiple Model Filter," *Journal of Guidance, Control, and Dynamics*, Vol. 37, No. 2, Feb 2014, pp. 484–496, doi: 10.2514/1.61327.

[82] Helmick, R. E., Blair, W. D., and Hoffman, S. A., "Fixed-interval Smoothing for Markovian Switching Systems," *Information Theory, IEEE Transactions on*, Vol. 41, No. 6, Nov 1995, pp. 1845–1855, doi: 10.1109/18.476310.

[83] Nandakumaran, N., Sutharsan, S., Tharmarasa, R., Lang, T., McDonald, M., and Kirubarajan, T., "Interacting Multiple Model Forward Filtering and Backward Smoothing for Maneuvering Target Tracking," *Signal and Data Processing of Small Targets, Proceedings 7445*, No. 744503, International Society for Optics and Photonics, Aug 2009, doi: 10.1117/12.826549.

[84] Blom, H. A. P. and Bar-Shalom, Y., "The Interacting Multiple Model Algorithm for Systems with Markovian Switching Coefficients," *Automatic Control, IEEE Transactions on*, Vol. 33, No. 8, Aug, pp. 780–783.

[85] Vallado, D. A. and Seago, J. H., "Covariance Realism," *AAS/AIAA Astrodynamics Specialist Conference*, No. 304, Univelt, Inc., Aug 2009, pp. 49–67.

[86] Folcik, Z., Lue, A., and Vatsky, J., "Reconciling Covariances with Reliable Orbital Uncertainty," *Proceedings of the Advanced Maui Optical and Space Surveillance Technologies Conference*, Maui Economic Development Board, Inc., Sep 2011.

[87] Aristoff, J. M., Horwood, J. T., Singh, N., and Poore, A. B., "Nonlinear Uncertainty Propagation in Orbital Elements and Transformation to Cartesian Space Without Loss of Realism," *SPACE Conferences & Exposition*, No. 4167, American Institute of Aeronautics and Astronautics, Aug 2014, doi: 10.2514/6.2014-4167.

[88] Horwood, J. T., Aristoff, J. M., Singh, N., Poore, A. B., and Hejduk, M. D., "Beyond Covariance Realism: A New Metric for Uncertainty Realism," *Signal and Data Processing of Small Targets, Proceedings 9092*, No. 90920F, International Society for Optics and Photonics, Jun 2014, doi: 10.1117/12.2054268.

[89] Horwood, J. T., Aragon, N. D., and Poore, A. B., "Covariance Consistency for Track Initiation Using Gauss-Hermite Quadrature," *Signal and Data Processing of Small Targets, Proceedings 7698*, No. 76980T, International Society for Optics and Photonics, Apr 2010, doi: 10.1117/12.851880.

[90] Alspach, D. L. and Sorenson, H. W., "Nonlinear Bayesian Estimation Using Gaussian Sum approximations," *Automatic Control, IEEE Transactions on*, Vol. 17, No. 4, Aug 1972, pp. 439–448, doi: 10.1109/TAC.1972.1100034.

[91] DeMars, K. J., Bishop, R. H., and Jah, M. K., "Entropy-Based Approach for Uncertainty Propagation of Nonlinear Dynamical Systems," *Journal of Guidance, Control, and Dynamics*, Vol. 36, No. 4, May 2013, pp. 1047–1057, doi: 10.2514/1.58987.

[92] Terejanu, G., Singla, P., Singh, T., and Scott, P. D., "Uncertainty Propagation for Nonlinear Dynamic Systems Using Gaussian Mixture Models," *Journal of Guidance, Control, and Dynamics*, Vol. 31, No. 6, Nov 2008, pp. 1623–1633, doi: 10.2514/1.36247.

[93] Horwood, J. T., Aragon, N. D., and Poore, A. B., "Gaussian Sum Filters for Space Surveillance: Theory and Simulations," *Journal of Guidance, Control, and Dynamics*, Vol. 34, No. 6, Nov 2011, pp. 1839–1851, doi: 10.2514/1.53793.

[94] Alfano, S. and Greer, M. L., "Determining if Two Solid Ellipsoids Intersect," *Journal of Guidance, Control, and Dynamics*, Vol. 26, No. 1, Jan 2003, pp. 106–110, doi: 10.2514/2.5020.

[95] Gottlieb, R. G., Sponaugle, S. J., and Gaylor, D. E., "Orbit Determination Accuracy Requirements for Collision Avoidance," *AAS/AIAA Spaceflight Mechanics Meeting*, No. 181, Univelt, Inc., February 2001, pp. 1105–1121.

[96] Yim, H., Jung, I., and Chung, D., "Enhancement of Collision Probability Accuracy Using Improved Orbit Prediction Methods," *SpaceOps Conference*, No. 1275488,

American Institute of Aeronautics and Astronautics, Jun 2012, doi: 10.2514/6.2012-1275488.

[97] Alfano, S., "Satellite Conjunction Monte Carlo Analysis," *AAS/AIAA Spaceflight Mechanics Meeting*, Feb.

[98] Alfano, S., "A Numerical Implementation of Spherical Object Collision Probability," *The Journal of Astronautical Sciences*, Vol. 53, No. 1, 2005, pp. 103–109.

[99] Kahle, R., Weigel, M., Kirschner, M., Spiridonova, S., Kahr, E., and Letsch, K., "Relative Navigation to Non-Cooperative Targets in LEO: Achievable Accuracy from Radar Tracking Measurements," *International Journal of Space Science and Engineering*, Vol. 2, No. 1, 2014, pp. 81–95, doi: 10.1504/IJS-PACESE.2014.060112.

[100] Xu, W., Liang, B., Li, C., and Xu, Y., "Autonomous Rendezvous and Robotic Capturing of Non-Coperative Target in Space," *Robotica*, Vol. 28, No. 5, Aug 2010, pp. 705–718, doi: 10.1017/S0263574709990397.

[101] Vallado, D. A. and Carter, S. S., "Accurate Orbit Determination from Short-Arc Dense Observational Data," *Journal of the Astronautical Sciences*, Vol. 46, No. 2, Apr 1998, pp. 195–213.

[102] McLachlan, G. and Krishnan, T., *The EM Algorithm and Extensions*, Vol. 382, John Wiley & Sons, Hoboken, NJ, 2007.

[103] Lloyd, S., "Least Squares Quantization in PCM," *Information Theory, IEEE Transactions on*, Vol. 28, No. 2, Mar 1982, pp. 129–137, doi: 10.1109/TIT.1982.1056489.

[104] Moon, T. K., "The Expectation-Maximization Algorithm," *Signal processing magazine, IEEE*, Vol. 13, No. 6, Nov 1996, pp. 47–60, doi: 10.1109/79.543975.

[105] Arthur, D. and Vassilvitskii, S., "k-means++: The Advantages of Careful Seeding," *18th Annual ACM-SIAM symposium on Discrete algorithms, Proceedings of the*, Society for Industrial and Applied Mathematics, Jan 2007, pp. 1027–1035.

[106] Ingraham, S. P., *Dynamic Constellation Tasking and Management*, Master's thesis, Air Force Institute of Technology (AU), Wright-Patterson AFB OH, Mar 2013, ADA583235.

[107] Hujsak, R., Woodburn, J., and Seago, J., "The Orbit Determination Tool Kit (ODTK), Version 5," *17th AAS/AIAA Spaceflight Mechanics Meeting*, No. 125, Univelt, Inc., Jan 2007.

[108] Li, X. R. and Jilkov, V. P., "Survey of Maneuvering Target Tracking. Part I. Dynamic Models," *Aerospace and Electronic Systems, IEEE Transactions on*, Vol. 39, No. 4, Oct 2003, pp. 1333–1364, doi: 10.1109/TAES.2003.1261132.

[109] Oltrogge, D., "Determination Of Orbit Cross-Tag Events And Maneuvers With Orbit Detective," *AAS/AAIA Astrodynamics Specialist Conference*, No. 413, Univelt, Inc., Jul 2011.

[110] Kelecy, T. and Jah, M., "Detection and Orbit Determination of a Satellite Executing Low Thrust Maneuvers," *Acta Astronautica*, Vol. 66, No. 5, Mar 2010, pp. 798–809, doi: 10.1016/j.actaastro.2009.08.029.

[111] Kelecy, T., Hall, D., Hamada, K., and Stocker, D., "Satellite Maneuver Detection Using Two-Line Element (TLE) Data," *Proceedings of the Advanced Maui Optical and Space Surveillance Technologies Conference*, Maui Economic Development Board, Inc., Sep.

[112] Lemmens, S. and Krag, H., "Two-Line-Elements-Based Maneuver Detection Methods for Satellites in Low Earth Orbit," *Journal of Guidance, Control, and Dynamics*, Vol. 37, No. 3, May 2014, pp. 860–868, doi: 10.2514/1.61300.

[113] Patera, R. P., "Space Event Detection Method," *Journal of Spacecraft and Rockets*, Vol. 45, No. 3, May 2008, pp. 554–559, doi: 10.2514/1.30348.

[114] Mehrotra, K. and Mahapatra, P. R., "A Jerk Model for Tracking Highly Maneuvering Targets," *Aerospace and Electronic Systems, IEEE Transactions on*, Vol. 33, No. 4, Oct 1997, pp. 1094–1105, doi: 10.1109/7.624345.

[115] Oltrogge, D., "Maneuver Event Detection and Reconstruction Using Body-Centric Acceleration/Jerk Optimization," *AAS/AAIA Astrodynamics Specialist Conference*, No. 578, Univelt, Inc., Jul 2011.

[116] Johnson, T. M., "Post-Maneuver Orbit Accuracy Recovery Analysis," *20th AAS/AIAA Spaceflight Mechanics Meeting*, No. 155, Univelt, Inc., Feb 2010.

[117] Storch, T. R., *Maneuver Estimation Model for Relative Orbit Determination*, Master's thesis, Air Force Institute of Technology (AU), Wright-Patterson AFB OH, Mar 2005, ADA434307.

[118] Huang, J., Hu, W.-D., Xin, Q., and Du, X.-Y., "An Object Correlation and Maneuver Detection Approach for Space Surveillance," *Research in Astronomy and Astrophysics*, Vol. 12, No. 10, Sep 2012, pp. 1402–1416, doi: 10.1088/1674-4527/12/10/003.

[119] Bishop, C. M. et al., *Neural Networks for Pattern Recognition*, Oxford University Press, Oxford, UK, 1996.

[120] Haith, G. and Bowman, C., "Data Driven Performance Assessment and Process Management for Space Situational Awareness," *Infotech @ Aerospace Conferences*, American Institute of Aeronautics and Astronautics, April 2010, doi: 10.2514/6.2010-3483.

[121] Beale, M. H., Hagan, M. T., and Demuth, H. B., *Neural Network Toolbox™*, MathWorks Inc., Natick, MA, Sep 2012, Revision 2012b.

[122] Hagan, M. T., Demuth, H. B., and Beale, M. H., *Neural Network Design*, PWS Publishing Company, Boston, MA, 1996.

[123] Bauer Jr., K. W., Alsing, S. G., and Greene, K. A., "Feature Screening Using Signal-to-Noise Ratios," *Neurocomputing*, Vol. 31, No. 1, Mar 2000, pp. 29–44, doi: 10.1016/S0925-2312(99)00147-2.

[124] Vallado, D. A. and Griesbach, J. D., "Simulating Space Surveillance Networks," *AAS/AIAA Astrodynamics Specialist Conference*, No. 580, Univelt, Inc., Jul 2011.

[125] Weeden, B. C. and Cefola, P. J., "Computer Systems and Algorithms for Space Situational Awareness: History and Future Development," *Advances in the Astronautical Sciences*, Vol. 138, No. 420, Jul 2010, pp. 205–227.

[126] Cefola, P., Weeden, B., and Levit, C., "Open Source Software Suite for Space Situational Awareness and Space Object Catalog Work," *4th International Conference on Astrodynamics Tools Techniques*, European Space Agency, May 2010, pp. 3–6.

[127] Richmond, D., "Space Situational Awareness (SSA) Research Findings," *Proceedings of the Advanced Maui Optical and Space Surveillance Technologies Conference*, Maui Economic Development Board, Inc., Sep 2008.

[128] Butkus, A., Roe, K., Mitchell, B. L., and Payne, T., "Space Surveillance Network and Analysis Model (SSNAM) Performance Improvements," *DoD High Performance Computing Modernization Program Users Group Conference*, Institute of Electrical and Electronics Engineers, Jun 2007, pp. 469–473, doi: 10.1109/HPCMP-UGC.2007.67.

[129] Stauch, J., Jah, M., Baldwin, J., Kelecy, T., and Hill, K., "Mutual Application of Joint Probabilistic Data Association, Filtering, and Smoothing Techniques for Robust Multiple Space Object Tracking," *SPACE Conferences & Exposition*, No. 4365, American Institute of Aeronautics and Astronautics, August 2014, doi: 10.2514/6.2014-4365.

[130] Kelecy, T., Jah, M., and DeMars, K., "Application of a Multiple Hypothesis Filter to Near GEO High Area-to-Mass Ratio Space Objects State Estimation," *Acta Astronautica*, Vol. 81, No. 2, Dec 2012, pp. 435–444, doi: 10.1016/j.actaastro.2012.08.006.

[131] Hecker, M., "Expert System for Processing Uncorrelated Satellite Tracks," *Journal of Guidance, Control, and Dynamics*, Vol. 18, No. 5, Sep 1995, pp. 1139–1144, doi: 10.2514/3.21516.

[132] Singh, N., Horwood, J. T., Aristoff, J. M., and Poore, A. B., "Multiple Hypothesis Tracking (MHT) for Space Surveillance: Results and Simulation Studies," *Proceedings of the Advanced Maui Optical and Space Surveillance Technologies Conference*, Maui Economic Development Board, Inc., Sep 2013.

[133] Sabol, C., Segerman, A., Hoskins, A., Little, B., Schumacher, P. W., and Coffey, S., "Search and Determine Integrated Environment (SADIE) for Space Situational Awareness," *Proceedings of the Advanced Maui Optical and Space Surveillance Technologies Conference*, Maui Economic Development Board, Inc., Sep 2012.

[134] Blackman, S. S., "Multiple Hypothesis Tracking for Multiple Target Tracking," *Aerospace and Electronic Systems Magazine, IEEE*, Vol. 19, No. 1, Jan 2004, pp. 5–18, doi: 10.1109/MAES.2004.1263228.

[135] Benoudnine, H., Keche, M., Ouamri, A., and Woolfson, M. S., "New Efficient Schemes for Adaptive Selection of the Update Time in the IMMJPDAF," *Aerospace and Electronic Systems, IEEE Transactions on*, Vol. 48, No. 1, Jan 2012, pp. 197–214, doi: 10.1109/TAES.2012.6129630.

[136] Reid, D. B., "An Algorithm for Tracking Multiple Targets," *Automatic Control, IEEE Transactions on*, Vol. 24, No. 6, Dec 1979, pp. 843–854, doi: 10.1109/TAC.1979.1102177.

[137] Cox, I. J. and Hingorani, S. L., "An Efficient Implementation of Reid's Multiple Hypothesis Tracking Algorithm and its Evaluation for the Purpose of Visual Tracking," *Pattern Analysis and Machine Intelligence, IEEE Transactions on*, Vol. 18, No. 2, Feb 1996, pp. 138–150, doi: 10.1109/34.481539.

[138] Poore, A. B. and Horwood, J. T., "Multiple Hypothesis Correlation for Space Situational Awareness," Tech. rep., Numerica Corp., Aug 2011, ADA563914.

[139] Singh, N., Horwood, J. T., and Poore, A. B., "Space Object Maneuver Detection via a Joint Optimal Control and Multiple Hypothesis Tracking Approach," *22nd AAS/AIAA Spaceflight Mechanics Meeting*, No. 159, Univelt, Inc., Jan 2012.

[140] Erwin, R. S., Albuquerque, P., Jayaweera, S., and Hussein, I., "Dynamic Sensor Tasking for Space Situational Awareness," *American Control Conference (ACC)*, Institute of Electrical and Electronics Engineers, Jun 2010, pp. 1153–1158, doi: 10.1109/ACC.2010.5530989.

[141] Williams, P. S., Spencer, D. B., and Erwin, R. S., "Coupling of Estimation and Sensor Tasking Applied to Satellite Tracking," *Journal of Guidance, Control, and Dynamics*, Vol. 36, Jul, pp. 993–1007.

[142] Williams, P. S., Spencer, D. B., and Erwin, R. S., "Utilizing Stability Metrics to Aid in Sensor Network Management Solutions for Satellite Tracking Problems," *22nd AAS/AIAA Spaceflight Mechanics Meeting*, No. 111, Univelt, Inc., Jan 2012.

[143] Miller, J. G., "A New Sensor Allocation Algorithm for the Space Surveillance Network," *Military Operations Research*, Vol. 12, No. 1, Dec 2007, pp. 57–70, doi: 10.5711/morj.12.1.57.

[144] Betts, J. T., "Survey of Numerical Methods for Trajectory Optimization," *Journal of Guidance, Control, and Dynamics*, Vol. 21, No. 2, Mar 1998, pp. 193–207, doi: 10.2514/2.4231.

[145] Bryson, A. E., *Dynamic Optimization*, Addison Wesley Longman, Boston, MA, 1999.

[146] Jiang, Z., Song, Q., He, Y., and Han, J., "A Novel Adaptive Unscented Kalman Filter for Nonlinear Estimation," *Decision and Control, 46th IEEE Conference on*, Institute of Electrical and Electronics Engineers, Dec 2007, pp. 4293–4298, doi: 10.1109/CDC.2007.4434954.

[147] Holzinger, M. J. and Scheeres, D. J., "Object Correlation, Maneuver Detection, and Maneuver Characterization Using Control Effort Metrics with Uncertain Boundary Conditions and Measurements," *Guidance, Navigation, and Control and Co-located Conferences*, No. 8347, American Institute of Aeronautics and Astronautics, Aug 2010, doi: 10.2514/6.2010-8347.

[148] Holzinger, M. J., Scheeres, D. J., and Alfriend, K. T., "Object Correlation, Maneuver Detection, and Characterization Using Control Distance Metrics," *Journal of Guidance, Control, and Dynamics*, Vol. 35, No. 4, Jul 2012, pp. 1312–1325, doi: 10.2514/1.53245.

[149] MATLAB, *Version R2104b*, MathWorks Inc., Natick, MA, 2014.

[150] Microcosm Inc., "High Precision Orbit Propagator," Jan 2015, http://smad.com/space-systems/software/high-precision-orbit-propagator/, Accessed 19 Jan 2015.

[151] Adurthi, N., Singla, P., and Singh, T., "Conjugate Unscented Transform and its Application to Filtering and Stochastic Integral Calculation," *Guidance, Navigation, and Control and Co-located Conferences*, No. 4934, American Institute of Aeronautics and Astronautics, Aug 2012, doi:10.2514/6.2012-4934.

[152] Hartikainen, J., Solin, A., and Särkkä, S., *Optimal Filtering with Kalman Filters and Smoothers a Manual for the MATLAB toolbox EKF/UKF*, Aalto Univertsity School of Science, August 2011, Version 1.3.

[153] Orbital ATK, "Orbital ATK Series of Small Satellite Buses," Oct 2014, https://www.orbitalatk.com/space-systems/science-national-security-satellites/science-environment-satellites/docs/A-Series_Satellites_Fact_Sheet.pdf, Accessed 13 May 2015.

[154] Broucke, R. A. and Cefola, P. J., "On the Equinoctial Orbit Elements," *Celestial Mechanics*, Vol. 5, No. 3, May 1972, pp. 303–310, doi: 10.1007/bf01228432.

[155] Goff, G. M., Showalter, D., Black, J. T., and Beck, J. A., "Parameter Requirements for Noncooperative Satellite Maneuver Reconstruction Using Adaptive Filters," *Journal of Guidance, Control, and Dynamics*, Vol. 38, No. 3, Jan 2015, pp. 361–374, doi: 10.2514/1.G000941.

[156] McReynolds, S. R., "Fixed Interval Smoothing-Revisited," *Journal of Guidance, Control, and Dynamics*, Vol. 13, No. 5, Sep 1990, pp. 913–921, doi: 10.2514/3.25419.

[157] Wright, J. R., Woodburn, J., Truong, S., and Chuba, W., "Sample Orbit Covariance Function and Filter/Smoother Consistency Tests," *18th AAS/AIAA Spaceflight Mechanics Meeting*, No. 159, Univelt, Inc., Jan 2008.

[158] Williams, J. L., *Gaussian Mixture Reduction for Tracking Multiple Maneuvering Targets in Clutter*, Master's thesis, Air Force Institute of Technology (AU), Wright-Patterson AFB OH, Mar 2003, ADA415317.

[159] McCall, G. H. and Darrah, J. H., "Space Situational Awareness: Difficult, Expensive–and Necessary," *Air & Space Power Journal*, Vol. 28, No. 6, Nov 2014, pp. 6–16.

[160] Horwood, J. T., Aristoff, J. M., Singh, N., and Poore, A. B., "A Comparative Study of New Non-linear Uncertainty Propagation Methods for Space Surveillance," *Signal and Data Processing of Small Targets, Proceedings 9092*, No. 90920H, International Society for Optics and Photonics, Jun 2014, doi: 10.1117/12.2051353.

[161] Marsaglia, G., "Choosing a Point from the Surface of a Sphere," *The Annals of Mathematical Statistics*, Vol. 43, No. 2, Apr 1972, pp. 645–646, doi: 10.1214/aoms/1177692644.

[162] Kurzhanskiy, A. A. and P., V., "Ellipsoidial Toolbox (ET)," *Decision and Control, 45th IEEE Conference on*, Institute of Electrical and Electronics Engineers, Dec 2006, pp. 1489–1503, doi: 10.1109/CDC.2006.377036.

[163] Kullback, S. and Leibler, R., "On Information and Sufficiency," *The Annals of Mathematical Statistics*, Vol. 22, No. 1, Mar 1951, pp. 79–86, doi: 10.1214/aoms/1177729694.

[164] Kassas, Z. and Humphreys, T., "Observability Analysis of Collaborative Opportunistic Navigation With Pseudorange Measurements," *Intelligent Transportation Systems, IEEE Transactions on*, Vol. 15, No. 1, Feb 2014, pp. 260–273, doi: 10.1109/TITS.2013.2278293.

[165] Julier, S., Uhlmann, J., and Durrant-Whyte, H. F., "A New Method for the Nonlinear Transformation of Means and Covariances in Filters and Estimators," *Automatic Control, IEEE Transactions on*, Vol. 45, No. 3, Mar 2000, pp. 477–482, doi: 10.1109/9.847726.

[166] Wasson, M. S., *Data Reduction with Least Squares Differential Correction Using Equinoctial Elements*, Master's thesis, Air Force Institute of Technology (AU), Wright-Patterson AFB OH, Dec 1992, ADA259004.

[167] Horwood, J. T., personal communications, Dec 2014, Numerica Corp, Fort Collins, CO.

[168] Horwood, J. T. and Poore, A. B., "Adaptive Gaussian Sum Filters for Space Surveillance," *Automatic Control, IEEE Transactions on*, Vol. 56, No. 8, Aug 2011, pp. 1777–1790, doi: 10.1109/TAC.2011.2142610.

[169] Goff, G. M., Black, J. T., and Beck, J. A., "Orbit Estimation of a Continuously Thrusting Spacecraft Using Variable Dimension Filters," *Journal of Guidance, Control, and Dynamics*, March 2015, pp. 1–14, Accessed April 4, 2015, doi: 10.2514/1.G001091.

REPORT DOCUMENTATION PAGE

Form Approved
OMB No. 0704–0188

1. REPORT DATE (DD–MM–YYYY)	2. REPORT TYPE	3. DATES COVERED (From — To)
18–06–2015	Dissertation	October 2012 - June 2015

4. TITLE AND SUBTITLE

Orbit Estimation of Non-Cooperative Maneuvering Spacecraft

5a. CONTRACT NUMBER

5b. GRANT NUMBER

5c. PROGRAM ELEMENT NUMBER

6. AUTHOR(S)

Goff, Gary M., Captain, USAF

5d. PROJECT NUMBER

5e. TASK NUMBER

5f. WORK UNIT NUMBER

7. PERFORMING ORGANIZATION NAME(S) AND ADDRESS(ES)

Air Force Institute of Technology
Graduate School of Engineering and Management (AFIT/EN)
2950 Hobson Way
Wright-Patterson AFB, OH 45433-7765

8. PERFORMING ORGANIZATION REPORT NUMBER

AFIT-ENY-DS-15-J-051

9. SPONSORING / MONITORING AGENCY NAME(S) AND ADDRESS(ES)

Intentionally Left Blank

10. SPONSOR/MONITOR'S ACRONYM(S)

11. SPONSOR/MONITOR'S REPORT NUMBER(S)

12. DISTRIBUTION / AVAILABILITY STATEMENT

Distribution Statement A:
Approved for Public Release; Distribution Unlimited

13. SUPPLEMENTARY NOTES

This work is declared a work of the U.S. Government and is not subject to copyright protection in the United States.

14. ABSTRACT

Due to the ever increasing congestion of the space environment, there is an increased demand for real-time situation awareness of all objects in space. An unknown spacecraft maneuver changes the predicted orbit, complicates tracking, and degrades estimate accuracies. Traditional orbit estimation routines are implemented, tested, and compared to a multiple model format that adaptively handles unknown maneuvers. Multiple Model Adaptive Estimation is implemented in an original way to track a non-cooperative satellite by covariance inflation and filtering-through a maneuver. Parameters for successful instantaneous maneuver reconstruction are analyzed. Variable State Dimension estimation of a continuously maneuvering spacecraft is investigated. A requirements based analysis is performed on short arc orbital solutions. Large covariance propagation of potential maneuvers is explored. Using ground-based radars, several thousand simulations are run to develop new techniques to estimate orbits during and after both instantaneous and continuous maneuvers. The new methods discovered are more accurate by a factor of 700 after only a single pass when compared to non-adaptive methods. The algorithms, tactics, and analysis complement on-going efforts to improve Space Situational Awareness and dynamic modeling.

15. SUBJECT TERMS

Maneuver Detection, Orbit Determination, Multiple Model Adaptive Estimation

16. SECURITY CLASSIFICATION OF:			17. LIMITATION OF ABSTRACT	18. NUMBER OF PAGES	19a. NAME OF RESPONSIBLE PERSON
a. REPORT	b. ABSTRACT	c. THIS PAGE			Dr. Jonathan T. Black, AFIT/ENY
U	U	U	UU	239	19b. TELEPHONE NUMBER (include area code) (540)231-0037 jonathan.black@afit.edu

Standard Form 298 (Rev. 8–98)
Prescribed by ANSI Std. Z39.18